Tunable photonics based on whispering gallery resonators on an all-polymeric chip-scale platform

Zur Erlangung des akademischen Grades eines

DOKTORS DER NATURWISSENSCHAFTEN (Dr. rer. nat.)

von der KIT-Fakultät für Physik
des Karlsruher Instituts für Technologie (KIT)

genehmigte

DISSERTATION

von

M.Sc. Simon Woska
aus Mühlacker

Tag der mündlichen Prüfung : 03.12.2021
Referent : Prof. Dr. Heinz Kalt
Korreferent : Priv.-Doz. Dr. Michael Hetterich

Prüfungskomission:
Prof. Dr. H. Kalt
Priv.-Doz. Dr. M. Hetterich
Prof. Dr. D. Hunger
Prof. Dr. C. Rockstuhl
Prof. Dr. J. Schmalian

Karlsruhe Institute of Technology (KIT)
Institute of Applied Physics
Wolfgang-Gaede-Straße 1
76131 Karlsruhe
Germany

Research group Prof. Dr. Heinz Kalt: http://www.aph.kit.edu/kalt

Simon Woska
simon.woska@kit.edu

This work has been financially supported by the Karlsruhe School of Optics and Photonics (KSOP).

http://www.ksop.de

Contents

Chapter 1

Introduction

The term '*photonics*' is derived from the Greek word '*photo-*' (or '*phos*', meaning 'light') and resembles the commonly known '*electronics*'. In line therewith, it comprises the general processing of signals of light, including, e.g., their generation, detection and modulation [1]. Over the last decades, the field of photonics has attracted increasing attention from both academic research and industry [2,3]. Modern advances in micro- and nano-scale fabrication technologies enable to realize such photonic applications more and more on chip scale [4]. These chip-scale photonic systems often are composed of several building blocks with different specific purposes.

For various photonic building blocks, an effective temporal and spatial confinement of light is required. Such a confinement is feasible using different kinds of micro-scale optical resonators [5,6], including so-called whispering gallery mode (WGM) cavities. These WGM cavities are able to confine light for a comparably long time in a small volume and can be realized with an overall footprint of only tens of square micrometers [7,8].
Numerous WGM-based micro-scale photonic building blocks have been demonstrated, including low-threshold lasers or spectral filters [9–12]. Furthermore, phenomena of cavity-quantum electro dynamics (cQED) like an enhancement of light-matter interaction have been observed in such resonators [13–15]. The area of possible applications of WGM-based building blocks is further increased by introducing a tunability of the spectral position of the underlying optical modes. Following this route, e.g., tunable low-threshold lasers can be realized [16,17]. In the context of cQED, such a spectral tunability is indispensable, as the WGMs must be tuned to match the optical transition of the emitter of interest [18,19].

An optical coupling of ensembles of cavities in close spatial proximity to so-called photonic molecules (PMs) is feasible due to the evanescent field of WGM resonators [20, 21]. Based on such PMs, spectral higher-order filters or optical delays in coupled resonator optical waveguides (CROWs) have been realized [22, 23]. Also, topologically protected single-mode lasing and robust lasing at exceptional points in hybrid PMs have been reported [24–26].
A tunability of the coupling among the individual WGM cavities of a PM facilitates additional possible applications as, e.g., CROWs with a tunable optical delay [27]. PMs at exceptional points can be driven in and out of their state of broken parity-time symmetry via a change of the inter-cavity coupling [28].

WGM-based photonic building blocks are mostly fabricated from materials such as semiconductors or silica which enable the realization of high-quality cavities with a strong temporal and spatial confinement [29, 30]. However, a distinct tunability of the key characteristics of the underlying optical modes is usually not feasible due to the inflexibility of these materials. At that point, photonic building blocks on an all-polymeric platform come into play. The vast field of existing polymers with different material properties significantly extents the range of possible designs of photonic building blocks. Including polymers with an elastomeric character, also highly tunable photonic building blocks are conceivable [31, 32].
Conventional non-polymeric materials are usually structured using electron-beam lithography [29, 30]. The fabrication of polymeric building blocks on the other hand is often feasible employing cost-efficient and parallelizable methods such as deep-UV lithography, nano-imprint lithography or 3D laser printing [33–35]. Also, the general material costs are often significantly reduced. Hence, an all-polymeric approach does not only enable the tunability of optical key characteristics of photonic elements, but also promises a cost-efficient future upscaling of their fabrication processes.

The present thesis aims at a realization of a chip-scale and all-polymeric platform for WGM-based tunable photonic building blocks. The intended tunability is achieved by incorporating a special class of smart polymers, so-called liquid crystal elastomers (LCEs). Due to their molecular order, these elastomers undergo a strong and reversible anisotropic actuation behavior under various external stimuli [36]. Therefore, this exotic material class paves the way for even more elaborate designs of tunable building blocks. In the scope of the present thesis, all chip-scale polymeric structures are fabricated using upscalable optical methods. High-quality WGM cavities are realized using novel processes based on 3D laser printing [37].
The potential of the all-polymeric chip-scale platform is demonstrated by tuning two exemplary key characteristics of WGM-based photonic building blocks: the spectral positions of the resonances of an individual WGM cavity as well as the inter-cavity coupling of a PM consisting of two WGM resonators in close spatial proximity.

To realize spectrally tunable WGMs, disk-shaped cavities entirely made from LCE are 3D laser printed. The in-plane expansion of the LCE is used to increase the radius of the cavity's disk and thereby tune its resonance wavelength. Herein, also the reversibility of this tuning mechanism is investigated. Comparable approaches have already been reported but lack either a sufficient spectral tuning of the optical modes [38] or a fabrication process suitable for future upscaling [16].

The tunable evanescent coupling of a PM is achieved by printing polymeric but rigid disk-shaped WGM resonators onto a chip-scale LCE substrate. The reversible contraction of the LCE is used to decrease the distance between the cavity disks and therefore increase their degree of evanescent coupling. The potential of this building block as a tunable add-drop filter is demonstrated.

Organization of this thesis

The present thesis is subdivided into seven chapters. Following the introduction, the fundamentals of the physical concept of whispering gallery modes are addressed in Chapter 2. Important figures of merits are introduced. The spatial and spectral mode structure of WGMs in disk-shaped cavities is presented. Incongruous differences of spatial mode structures obtained from analytical effective-index calculations and finite-element simulations are found. Based thereon, an alternative classification scheme of WGMs in disk-shaped cavities is derived and its advantages are discussed. Finally, a short overview of photonic applications of WGMs is given. Herein, both individual WGM cavities as well as PMs are addressed. The impact of a spectral tunability of single WGMs and a tunable evanescent coupling of PMs on possible applications is included.

The experimental investigations of the spectral mode structure of WGMs in this thesis are based on fiber-transmission spectroscopy. Hence, this method is introduced in Chapter 3. Its fundamentals are recapitulated, the intensity transfer between fiber and WGM resonator is analytically described using coupled-mode theory (CMT) and the established experimental methodology is outlined. Afterwards, two newly developed extensions to the investigation scheme are presented. Firstly, fiber-transmission spectroscopy using two tapered optical fibers simultaneously is introduced. This includes a CMT-based analytical description of the modified measurement configuration, a fabrication process of bent tapered optical fibers and the required modifications of the experimental setup. Secondly, two approaches of polarization-sensitive fiber-transmission spectroscopy are introduced and compared. One of these methods analyzes the polarization of the fiber transmission, while the other employs the directional radiation of the WGM of interest.

In Chapter 4, the fabrication processes of all-polymeric tunable photonic building blocks are outlined. At first, the material class of liquid crystal elastomers is introduced, including their chemical composition and mechanical and optical properties as well as possible approaches to manipulate their molecular order. Then, the fabrication of chip-scale LCE substrates is demonstrated. The actuation of these substrates is evaluated using a novel investigation scheme based on polymeric micro-scale markers. Afterwards, the 3D laser printing of micro-scale rigid photonic elements onto such substrates is demonstrated. The quality of these structures is evaluated based on scanning-electron micrographs as well as their optical key characteristics. Finally, the 3D laser printing of chip-scale photonic elements entirely made from LCE is introduced. The quality of the structures is again assessed based on scanning-electron micrographs and optical key characteristics.

The spectral tunability of WGM resonators entirely made from LCE is demonstrated in Chapter 5. The fundamentals of the spectral tuning of WGMs are introduced and the expected tunability of such LCE cavities is estimated. Afterwards, their spectral tuning is experimentally investigated and compared to these expectations. The impact of the advancements of the respective fabrication process presented in Chapter 4 is evaluated. Also, the reversibility of the spectral tuning of the LCE resonators as well as a possible adjustment of their absolute tuning response via a change of the LCE's chemical composition are addressed.

In Chapter 6, the tunable coupling of WGMs in photonic molecules on LCE substrates is demonstrated. The fundamentals of this evanescent coupling are recapitulated and the tunability of the inter-cavity gap is demonstrated using optical micrographs. The evanescent coupling is then analytically described based on CMT. Herein, optical waveguides are introduced into the calculations and expected signatures of a tunably coupled PM in fiber-transmission spectra using one or two tapered optical fibers are computed. Experimentally obtained single-fiber transmission spectra of a tunable PM are compared to the respective calculations. The PM's tunable coupling strength is derived from the resonance splitting of delocalized supermodes. Finally, the controllable intensity transfer through a tunably coupled PM in add-drop configuration is demonstrated. The enhancement of the transferred intensity is compared to the expectations based on CMT.

Finally, Chapter 7 concludes the results presented in this thesis and evaluates the potential of the developed chip-scale and all-polymeric platform of WGM-based tunable photonic building blocks for future applications. An outlook on possible prospective research activities building on the results of the present thesis is given.

Chapter 2

Whispering gallery modes in photonic building blocks

In this chapter, the fundamental concept of whispering gallery mode (WGM) cavities as well as important figures of merit are recapitulated in Sec. 2.1. Within this context, a short analytical description of a WGM resonance derived from a harmonic oscillator is given. In Sec. 2.2, the spectral and spatial mode structure of such cavities is covered in more detail. Therein, spatial mode structures obtained using the analytical effective index method are compared to those derived from finite element simulations. Based thereon, the systematic of WGM resonances in disk-shaped cavities is discussed and a novel classification scheme of these modes contradicting the established classification is proposed. This novel scheme takes the inseparability and non-orthogonality of such WGMs into account. Finally, a short overview of different possible applications of WGM resonators in the context of photonic systems is given in Sec. 2.3.

2.1 Whispering gallery modes and their figures of merit

Whispering gallery resonators confine light by the total internal reflection of light that propagates within a dielectric resonator material [7,8]. If the refractive index of the resonator material n_r is larger than the one of its surrounding n_s and light hits the interface under a sufficiently small angle, it is totally internally reflected. If the interface between the resonator material and its surrounding forms a closed path, the light is guided along that path. If furthermore the optical length of that path matches an integer of the wavelength of the guided light, constructive interference after one round trip leads to confined optical resonances. In the present work, rotationally

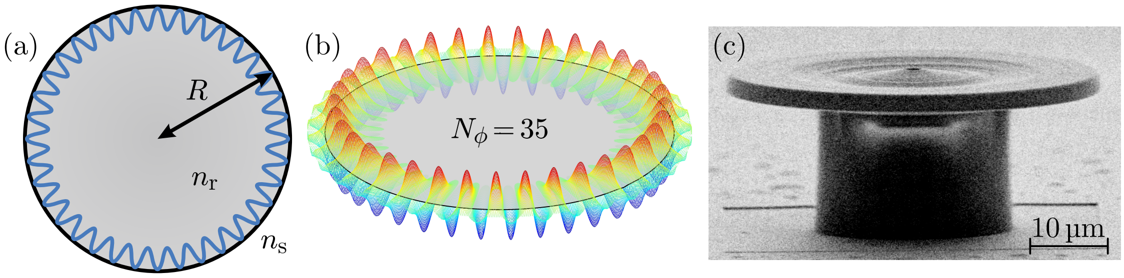

Figure 2.1: (a) illustrates a WGM resonance in a rotationally symmetric structure of radius R with a refractive index n_r larger than the one of its surrounding n_s. The requirement of constructive interference leads to solutions with an integer number N_ϕ of field maxima along the outer rim. Since the light is confined by total internal reflection, a part of the mode is evanescently guided outside the cavity. This effect is demonstrated in (b), where the electric-field distribution of a WGM resonance with $N_\phi = 35$ is depicted. The exponential tails reaching beyond the edge of the cavity (black line) are visible. In (c), an SEM micrograph of a polymeric disk-shaped WGM cavity with a radius of $R = 25\,\mu\mathrm{m}$ is depicted. (a)/(b) adapted from [39]/[40], sample in (c) fabricated by Roman Oberle [41].

symmetric, disk-shaped WGM cavities (as exemplary depicted in Fig. 2.1(c)) are investigated. For such cavities, a resonance condition in the form of

$$2\pi R \times n_\mathrm{eff} = N_\phi \lambda_0 \text{ with } N_\phi \in \mathbb{N} \tag{2.1}$$

holds. Herein, R is the radius of the rotationally symmetric cavity and N_ϕ is the number of field maxima along the azimuthal direction ϕ of the cavity. In Fig. 2.1(a), a rotationally symmetric refractive-index distribution and the formation of resonant modes due to constructive interference is illustrated.

Due to the guiding of light by total internal reflection within the dielectric cavity, a non-vanishing but exponentially decaying part of the electromagnetic field is located in the cavity's surrounding. This evanescent part of the mode leads to an effective refractive index n_eff of the WGM, for which the condition

$$n_\mathrm{s} < n_\mathrm{eff} < n_\mathrm{r} \tag{2.2}$$

holds. In the case of tightly confined modes in polymeric cavities surrounded by air, the approximation $n_\mathrm{eff} \approx n_\mathrm{r}$ is mostly sufficient. Nevertheless, the evanescent field of the WGMs is of high importance, since it enables an efficient evanescent coupling between such cavities and tapered optical fibers within the scope of fiber-transmission spectroscopy [8, 42] (see Ch. 3). Figure 2.1(b) depicts an exemplary distribution of the electric field component of a WGM resonance obtained from finite-element method (FEM) simulations. The evanescent tails of the mode reaching into the cavity's surrounding are evident.

The time dependence of the field amplitude within a WGM cavity can be determined from the differential equation of a lossy harmonic oscillator [43,44]

$$\frac{\mathrm{d}}{\mathrm{d}t}a(t) = \left(\mathrm{i}\omega_0 - \frac{1}{2\tau}\right) a(t), \tag{2.3}$$

where $a(t)$ represents one of the field components, ω_0 is the resonance frequency of the mode and τ is the lifetime of a photon limited by the cavity's loss mechanisms. Solving this equation leads to a time dependence of

$$a(t) = a_0 \exp\left(\mathrm{i}\omega_0 t\right) \exp\left(-\frac{t}{2\tau}\right). \tag{2.4}$$

As expected for a lossy harmonic oscillator, the field amplitudes in the cavity oscillate with frequency ω_0 and an exponentially decaying envelope.
Via a Fourier transformation, the spectral dependence of the intensity $I(\omega)$ inside a cavity can be calculated from Eq. (2.4):

$$I(\omega) = |a(\omega)|^2 \propto \frac{1}{(\omega - \omega_0)^2 + \frac{1}{4\tau^2}}. \tag{2.5}$$

Hence, the WGM resonances are expected to show a Lorentzian line shape centered at ω_0 with a full width half maximum (FWHM) equal to the inverse photon lifetime:

$$\Delta\omega_{\mathrm{FWHM}} = \tau^{-1}. \tag{2.6}$$

Quality factor

The capability of a cavity to confine light over time is often described using the so-called quality factor Q. It is defined as the ratio of the energy stored in the cavity to the power dissipated from the cavity within one period of the mode's oscillation:

$$Q := \omega_0 \frac{\text{stored energy}}{\text{dissipated power}}. \tag{2.7}$$

As the stored energy is given by $|a(t)|^2$ (with the field amplitude $a(t)$ in Eq. (2.4)) and the dissipated energy by its time derivative, this leads to a quality factor of

$$Q = \omega_0 \tau, \tag{2.8}$$

meaning the quality factor is directly proportional to the photon lifetime of the cavity. The highest quality factors achieved in WGM resonators up to date have been found by Grudinin *et al.*, who showed values larger than $Q = 6 \times 10^{10}$ in

cylindrical cavities made from CaF_2 [45]. This corresponds to a photon lifetime in the order of 35 µs.
All loss mechanisms of a WGM cavity directly connected to the material or shape of the resonator itself are combined in the so-called intrinsic quality factor Q_i. There are mainly three different loss channels contributing to this combined intrinsic quality factor Q_i:

- **Radiation losses**
  Within a WGM cavity, the light is forced to travel along a bent path. This leads to radiation losses, which can be understood in both a wave as well as a particle picture.
  To preserve the rotational symmetry of the system, the wavelength of the evanescent part of a WGM mode increases with larger distance from the cavity. This also leads to an increasing phase velocity. At a certain distance from the outer rim of the cavity, this phase velocity exceeds the speed of light c_0/n_s. Therefore, this part of the mode is not guided anymore, but radiated from the cavity. [42]
  Considering photons within the WGM cavity, the contrast of the refractive index at the boundary of the cavity can be seen as a finitely high potential wall trapping the photons inside the cavity. Hence, the photons are able to tunnel through that potential wall and leave the cavity. The height and shape of this barrier are both mainly depending on the radius of the cavity as well as the refractive index contrast to its surrounding. As it can be shown from calculations using the Wentzel-Kramers-Brillouin approximation, the quality factor depends exponentially on the cavity's radius. [46–49]
  The cavities investigated in this work are made of polymeric materials with refractive indices of around 1.5 and radii of 20 µm to 30 µm. For light near the infrared (IR) c-band, this leads to an expected radiation limit of the quality factor in the order of 10^{23} [47].

- **Absorption losses**
  As in linear waveguides, a part of the light propagating in a WGM cavity is lost due to intrinsic absorption as well as scattering within the dielectric bulk [44,47]. These processes are combined in the material-specific absorption coefficient α and also limit the quality factors of WGM resonators. This limit can be calculated using [50,51]:

  $$Q_\mathrm{mat} = \frac{2\pi n_\mathrm{r}}{\lambda\alpha}. \tag{2.9}$$

  Besides the explicit dependency of Q_mat on λ, the absorption coefficient α also changes with wavelength.

The rigid polymeric cavities in this work are made from the commercially available photoresist IP-S (see Sec. 4.3 for further information). For this material, only very few absorption measurements are found in literature. To estimate the quality factor near the IR c-band, a value of α measured at a wavelength of 1100 nm in [52, 53] is assumed. Using Eq. (2.9), this leads to an estimate of the absorption-limited quality factor of $Q_{\text{mat}} \approx 6.5 \times 10^4$.
The flexible resonators investigated in this work are fabricated from a custom-mixed liquid-crystal resist. Hence, there is no absorption data available and the respective limitation on the quality factor can not be estimated.

- **Scattering losses**
  The third important loss mechanism limiting the intrinsic quality factor of WGM cavities is scattering due to surface roughness. The imperfections of the surface act as scatterers and couple intensity out of the cavity. The extent of this effect is mainly influenced by the degree of surface roughness [54, 55] and is described by the scattering-limited quality factor Q_{scat}. In contrast to both other contributions to the intrinsic quality factor, the influence of this loss channel can be reduced via an improvement of the fabrication process of the respective cavities.

The combined intrinsic quality factor Q_{i} of a cavity is calculated as the inverse sum of all of its single contributions [44]:

$$Q_{\text{i}}^{-1} = Q_{\text{rad}}^{-1} + Q_{\text{mat}}^{-1} + Q_{\text{scat}}^{-1}. \tag{2.10}$$

Comparing the magnitude of the different contributions to the intrinsic quality factor, radiation losses can be neglected in the case of the polymeric cavities in this work. As the influence of surface scattering should be controllable by the applied fabrication method, the material-specific quality factor Q_{mat} acts as a fundamental limit of the investigated cavities. Regarding the optimization of the cavities' fabrication processes (see Ch. 4), it is one of the main goals to achieve a small surface roughness. If the surfaces are sufficiently smooth, the scattering-induced quality factor is large compared to the absorption-induced one ($Q_{\text{scat}} \gg Q_{\text{mat}}$) and the cavities' overall quality factor is given by their absorption limit: $Q_{\text{i}} \approx Q_{\text{mat}}$.
As described in Sec. 3.1.1, the FWHM of the Lorentzian of a WGM resonance is broadened if an optical fiber is coupled to the cavity. This also holds for other kinds of light-guiding structures as, e.g., prisms. Such a broadening of the resonance can be described with an additional coupling quality factor Q_{c}. This leads to an overall quality factor of

$$Q^{-1} = Q_{\text{i}}^{-1} + Q_{\text{c}}^{-1} = Q_{\text{rad}}^{-1} + Q_{\text{mat}}^{-1} + Q_{\text{scat}}^{-1} + Q_{\text{c}}^{-1}. \tag{2.11}$$

Mode volume

Besides the confinement over a certain time, WGMs are also tightly confined in space. The spatial extent of the respective field distributions is hereby described using the so-called mode volume V_m. It is defined as the ratio of the total energy stored in the cavity to the maximum energy density within the cavity [29, 56]:

$$V_\mathrm{m} = \frac{\int \epsilon(\mathbf{r}) \left|\mathbf{E}(\mathbf{r})\right|^2 \mathrm{d}V}{\max\left[\epsilon(\mathbf{r}) \left|\mathbf{E}(\mathbf{r})\right|^2\right]}. \tag{2.12}$$

Herein, $\mathbf{E}(\mathbf{r})$ is the electric field strength and $\epsilon(\mathbf{r})$ is the dielectric function. In close spatial proximity of the WGM cavity (so $\epsilon(\mathbf{r}) = 1$), $|\mathbf{E}(\mathbf{r})|$ is non-zero due to the evanescent part of the modes. Hence, also these evanescent fields contribute to the mode volume.

Free spectral range

Another important characteristic of WGM cavities is the periodicity of their mode spectrum. This periodicity results from the recurrence of the WGMs with their azimuthal mode number N_ϕ and is described using the so-called free spectral range (FSR) $\Delta\lambda_\mathrm{FSR}$. The FSR is defined as the spectral distance between two modes with identical mode characteristics except a difference in the azimuthal mode number of $|\Delta N_\phi| = 1$. This leads to [42]

$$\Delta\lambda_\mathrm{FSR} = \frac{\lambda_0^2}{2\pi R \times n_\mathrm{eff} + \lambda_0} \approx \frac{\lambda_0^2}{2\pi R \times n_\mathrm{eff}}, \tag{2.13}$$

wherein the approximation holds in the case of $R \gg \lambda_0$. In the case of the polymeric cavities ($n_\mathrm{r} \approx 1.5$) with radii of $R = 20\,\mu\mathrm{m}$ to $30\,\mu\mathrm{m}$ in this work, the free spectral range is in the order of $\Delta\lambda_\mathrm{FSR} \approx 8\,\mathrm{nm}$ to $12\,\mathrm{nm}$.

The free spectral range of a WGM cavity is of particular importance regarding their spectral tunability. A resonator is called fully tunable, if the spectral positions of its modes can be shifted over more than one FSR. In this case, it is possible to tune a fundamental mode of the cavity to any spectral position of interest. [57]

2.2 Spatial mode structure of WGMs in disk-shaped resonators

As already introduced and illustrated in Fig. 2.1, WGM resonances can be characterized by their integer number of field maxima N_ϕ along the azimuthal ϕ-direction of the cavity. To fully understand the spectral and spatial mode structure of disk-shaped WGM resonators, the radial (ρ) and axial (z) field distributions also need to be considered.
In the following section, the spatial mode structure is analytically derived from the cylindrical Helmholtz equations following an established approach using a separation ansatz. Afterwards, the mode classification resulting from these calculations is compared to numerical simulations of spatial field distributions and the validity of the underlying assumptions of the analytical calculations is assessed. Based on the found incongruous differences of the spatial field distributions, a classification scheme of WGMs contradicting the established classification is proposed. This novel scheme takes the inseparability and non-orthogonality of such WGMs into account.

The results presented in this section have been obtained in close cooperation with Lukas Rebholz within his Master's thesis [40] and can be found there in further detail.

Analytical calculation of modes in disk-shaped resonators

An analytical description of the spatial field distributions in the case of disk-shaped WGM cavities is well-established in literature [58–60] and is also covered in more detail in [40, 61, 62]. It is based on the cylindrical scalar Helmholtz equations:

$$\left[\partial_\rho^2 + \frac{1}{\rho}\partial_\rho + \frac{1}{\rho^2}\partial_\phi^2 + \partial_z^2 + k^2 n^2(\rho, z)\right] \mathcal{F}(\rho, \phi, z) = 0. \tag{2.14}$$

This differential equation containing the wave number k as well as the refractive index n holds for all six components of the electromagnetic field: $\mathcal{F} = \{\mathbf{E}, \mathbf{H}\}$. The cylindrical symmetry has been taken into account by the spatial distribution of the refractive index $n(\rho, z)$.
In analogy to the analytical solution of modes in slab waveguides [58, 59], two classes of approximately independent field components have been assumed: $\{E_\rho, H_\phi, H_z\}$ and $\{H_\rho, E_\phi, E_z\}$. These solutions are called modes with transverse-electric (TE) and transverse-magnetic (TM) polarization, respectively.

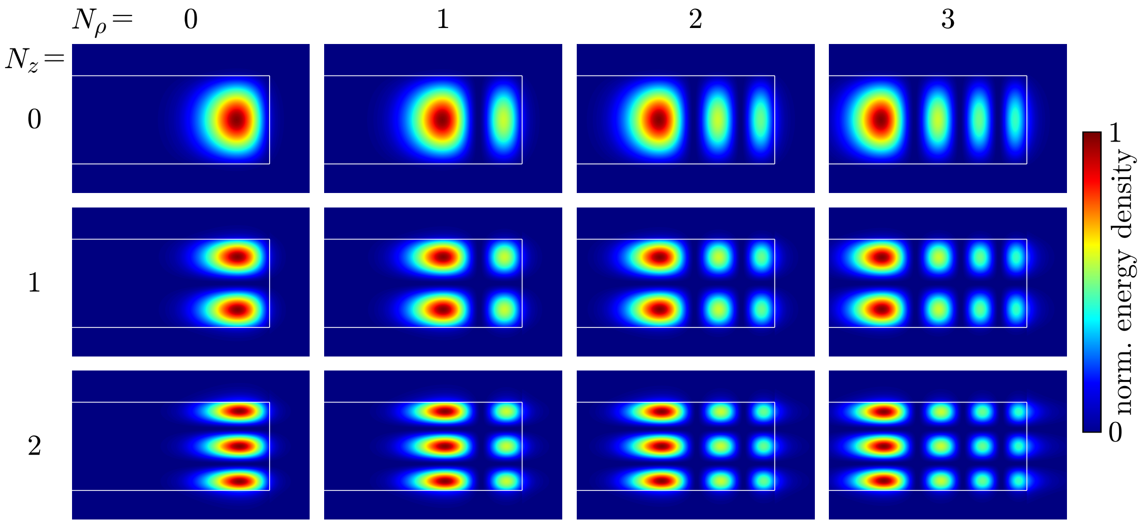

Figure 2.2: Contour plots of analytically obtained intensity distributions in the (ρ, z)-plane of WGM resonances in a disk-shaped resonator. All depicted modes share an azimuthal mode number of $N_\phi = 139$ and TE polarization. The different intensity distributions can be described as a two-dimensional array of maxima with $(N_\rho + 1)$ being the number of columns and $(N_z + 1)$ the number of lines. TM modes as well as modes with differing N_ϕ show a similar behavior. Adapted from [40].

Using the separation ansatz $\mathcal{F}(\rho, \phi, z) = \Phi(\phi) \cdot \mathcal{G}(\rho, z)$, as well as the periodicity $\Phi(\phi) = \Phi(\phi + 2\pi)$, the solution in azimuthal direction

$$\Phi(\phi) = \exp\left[\pm \mathrm{i} N_\phi \phi\right] \text{ with } N_\phi \in \mathbb{N} \tag{2.15}$$

has been found. For the remaining part of the differential equation $\mathcal{G}(\rho, z)$, a separation ansatz is not feasible since the spatial distribution of the refractive index can not be split into independent components. Approximate solutions have been calculated using the so-called effective-index method (EIM). Therein, such a separation ansatz is done despite the inseparability of the refractive index. The mutual dependency of the two differential equations has been considered by means of an effective refractive index. Via this effective quantity, the influence of the spatial distribution of the refractive index in z-direction has been incorporated into the differential equation describing the field distribution in ρ-direction, and vice versa. Numerical solutions to these mutually dependent equations can be found in an iterative approach. [58–60]

The solutions in z-direction $\mathcal{Z}(z)$ are given by standing waves within the resonator disk and exponentially decaying tails in its close surrounding. From the mirror symmetry of the system with respect to the plane perpendicular to its rotational axis, a set of solutions with different integer numbers of field extrema along the z-direction $(N_z + 1)$ has been found.

The solutions in ρ-direction $\mathcal{R}(\rho)$ have been calculated to be given by oscillating Bessel functions within the cavity as well as exponentially decaying Hankel functions of the second kind in its surrounding. Again, the solutions can be characterized by their integer number of field extrema along the ρ-direction $(N_\rho + 1)$.
Summing up these results, the spatial field distribution of a WGM within a disk-shaped cavity can be fully described using the three mode numbers N_ϕ, N_ρ, N_z as well as their polarization state (TE or TM). To illustrate the influence of N_ρ and N_z therein, the intensity profile within the (ρ, z)-plane of exemplary TE modes with $N_\phi = 139$ and differing mode numbers N_ρ and N_z are depicted in Fig. 2.2. As it is evident from these mode profiles, the intensity distribution is given by a two-dimensional array of maxima with the numbers $(N_\rho + 1)$ and $(N_z + 1)$ describing the number of columns and rows, respectively. These intensity distributions can also be understood as a superposition of the individual solutions $\mathcal{R}(\rho)$ and $\mathcal{Z}(z)$. TM modes show similar intensity distributions with only slight variations. The classification of WGMs in disk-shaped cavities based on N_ϕ, N_ρ, N_z and their polarization state is well-established in literature [39, 61, 63–67].

Modes in disk-shaped resonators obtained from finite-element simulations

An alternative approach to calculate the field distributions in disk-shaped WGM cavities is given by numerical simulations using the finite-element method (FEM). Herein, the rotational symmetry of the system has again been used to separately determine the ϕ-dependency of the solution in the form of Eq. (2.15).

To calculate the remaining electromagnetic field components, the (ρ, z)-plane of the WGM cavity has been triangulated and Maxwell's equations have been solved within the finite area elements. Then, boundary conditions have been applied to determine the overall field distribution of interest as well as the respective resonance frequency. Although the results have been obtained numerically, no approximations despite the triangulation into finite area elements itself have been done within the calculations. Especially, neither a separability of the spatial distribution of the refractive index nor the existence of two independent classes of field components (meaning TE and TM modes) has been assumed. FEM simulations have been extensively used in this research group to determine the field distribution of resonances in WGM cavities, hence a more comprehensive description of this numerical approach can be found elsewhere [40, 61, 68, 69].

In this work as well as in [40], FEM simulations are used to test the validity of the analytical field distributions calculated using EIM. This is done based on a qualitative comparison of the spatial intensity distributions. In Fig. 2.3, exemplary intensity profiles in the (ρ, z)-plane of modes with $N_\phi = 139$ obtained from FEM are depicted.

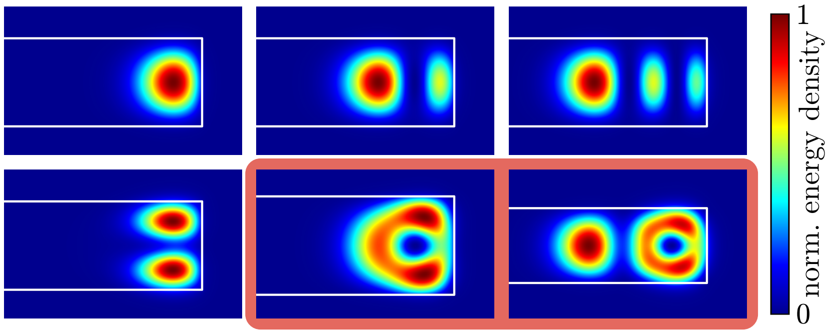

Figure 2.3: Contour plots of the intensity distributions in the (ρ, z)-plane of WGM resonances in a disk-shaped resonator obtained from FEM simulations. Most of the modes show a strong similarity to those obtained using EIM. These modes are found in two versions with a preferential electric-field orientation along either the ρ- or the z-direction, corresponding to analytical TE and TM modes. However, some of the modes (highlighted in red) are not within the set of the analytical solutions and do not show a preferential field orientation. Under close inspection, these modes can be identified as a superposition of analytical solutions. Adapted from [40].

For most of the calculated modes, a strong similarity to the results obtained from the analytical EIM calculations is found. These modes also show preferential field orientations corresponding to either TE or TM polarization. Nevertheless, some of the modes (highlighted in red) do not show a two-dimensional array of maxima and, hence, cannot be described as a superposition of a single radial $\mathcal{R}(\rho)$ and axial analytical solution $\mathcal{Z}(z)$. Therefore, these modes are not within the set of solutions obtained from EIM. Furthermore, these modes do not show a preferential orientation of the electromagnetic fields and, hence, cannot be allocated to a TE or TM polarization [40]. Under further inspection however, these modes can be understood as a superposition of two modes that are within the set of analytical solutions (meaning each of these modes $j = 1, 2$ is a superposition of its own radial $\mathcal{R}_j(\rho)$ and an axial part $\mathcal{Z}_j(z)$). In the depicted case, the highlighted modes are identified as a superposition of the mode on their left-hand side (corresponding to the analytical mode with $(N_\rho, N_z) = (0, 1)$) with the respective mode above (corresponding to $(N_\rho, N_z) = (1, 0)$ and $(2, 0)$). Herein, these two contributions again show either a TE- or TM-like polarization. This observation suggests the assumption of a coupling of the modes obtained from analytical EIM calculations.

The deviation between the numerical FEM simulations and the analytical solutions is expected to be caused by the underlying assumptions of the analytical calculations. By assuming a separability of the differential equation (2.14), possible solutions with a non-separable field distribution (as the ones highlighted in Fig. 2.3) have been ignored. Additionally, the existence of independent TE and TM modes adapted from slab waveguides does not generally hold. Therefore, these assumptions lead to an

incomplete picture of the mode structure of disk-shaped WGM cavities. Furthermore, they demonstrate the limited utility of the description of WGMs based on the mode numbers N_ϕ, N_ρ, N_z and their polarization state.
In the following, a classification of WGMs in disk-shaped cavities based on properties that are conserved under the coupling of single modes is proposed.

Alternative classification scheme of WGMs in disk-shaped cavities

In both EIM and FEM, the azimuthal dependency of the field distribution of WGM resonances is derived from the separation ansatz given by Eq. (2.15). This separation is not based on any approximation but only harnessing the rotational symmetry of the problem. Hence, N_ϕ is conserved and therefore a useful number to characterize the respective WGM resonances.
Another symmetry of the system is the mirror symmetry with respect to the plane perpendicular to its rotational axis. Based thereon, the regarding z-parity P_z of a WGM, meaning the eigenvalue of the field distribution under the mirror transformation $z \mapsto -z$, is expected to be conserved. Regarding the modes from analytical EIM calculations, TE modes with an even N_z and TM modes with an odd N_z share the same z-parity, and vice versa. Based on the symmetry of the underlying problem, no further conserved quantity can be expected.

To further understand the structure of WGM resonances in disk-shaped cavities, the interaction of the modes (as indicated in Fig. 2.3) has been investigated in detail. To that end, the resonance frequencies of several modes obtained from FEM simulations have been taken into account. As the extent of such mode interactions is expected to depend on the spectral distance between the contributing modes, this distance has been tuned via the change of a geometrical parameter of the cavity. In Fig. 2.4, the resonance frequency of 12 WGMs is depicted versus the thickness of the cavity. Herein, the expected conservation of N_ϕ and P_z is already considered: All depicted modes share the same azimuthal mode number of $N_\phi = 139$. Modes with a z-parity of $P_z = 1$ and $P_z = -1$ have been divided into the two separate plots Fig. 2.4(a) and Fig. 2.4(b), respectively.
In both plots in Fig. 2.4, several points of spectral degeneracy between two WGMs seem to arise. Under close inspection however, the resonance frequencies of the contributing modes always show an avoided-crossing behavior which is a typical characteristic of optical coupling. The only modes not showing any avoided crossings (gray lines) are the fundamental modes with analytical mode numbers $(N_\rho, N_z) = (0, 0)$ that have a large spectral distance to all other WGMs over the whole investigated range of the disk's thickness. The modes of highest angular frequency (blue lines) also undergo avoided crossings with modes of even higher frequency, that are not shown here. This causes the single kinks of these lines. Beyond that, there seem to

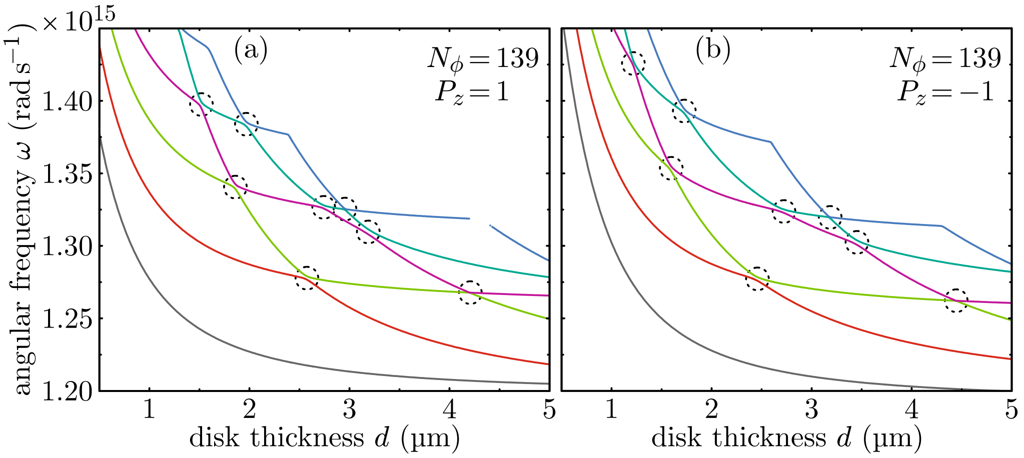

Figure 2.4: Resonance frequency of 12 WGMs versus the disk's thickness. All modes share the same azimuthal mode number N_ϕ and are divided into two plots regarding their z-parity of (a) $P_z = 1$ and (b) $P_z = -1$. In both plots, several potential crossing points arise (black circles). Taking a closer look, an avoided-crossing behavior is found for each of these points. This finding indicates an optical coupling between all modes of one plot that are spectrally close. (For the mode in (a) with highest frequency, some data points are missing due to numerical issues.) Partly adapted from [40].

be no avoided crossings with a missing coupling partner. Thus, an avoided crossing is observed if and only if two modes of the same N_ϕ and P_z come spectrally close. This observation strongly indicates that a mode with pre-defined N_ϕ and P_z couples to all other modes sharing these characteristics but to no other modes. As the contributing modes gradually interchange their characteristics along an avoided crossing, this also demonstrates the conservation of the mode numbers N_ϕ and P_z as well as the absence of any additional conserved quantities. In particular, the mode numbers N_ρ and N_z are not conversed.

These findings can also be related to the spatial mode profiles depicted in Fig. 2.2 and Fig. 2.3: If the resonance frequency of a WGM in Fig. 2.4 is far from that of any other resonance of the same N_ϕ and P_z, a spatial mode profile similar to that of an analytical solution is found. In these cases, the modes also show a preferential electric-field orientation in either ρ- or z-direction. In the following, such modes are referred to as modes with a TE-like or TM-like polarization, respectively. Changing the disk's thickness and thus getting closer to an avoided crossing, the mode profiles of both modes gradually interchange and are thereby losing their preferential field orientation. The exemplary profiles highlighted in Fig. 2.3 correspond to the points of minimum spectral distance between the coupling modes. Changing the disk's thickness even further, the mode profiles gradually change into those of the respective coupling partner. A detailed discussion of all these phenomena is given in [40].

Regarding a reliable classification scheme of WGMs in disk-shaped cavities, the spectral order of the modes can be utilized. Since for a given set of N_ϕ and P_z the modes only show avoided crossings, this order does not change. Hence, the integer spectral order number N_s starting with $N_\mathrm{s} = 1$ for the mode corresponding to the fundamental mode with analytical mode numbers $(N_\rho, N_z) = (0, 0)$ (gray lines) is conserved. Consequently, a whispering gallery mode in a disk-shaped cavity can be fully characterized by the three mode numbers N_ϕ, P_z and N_s.

Compared to the established system based on N_ρ and N_z, this classification is beneficial as its completeness and correctness do not depend on the dimensions of the cavity. Additionally, it incorporates the modes with a complex spatial field distribution and missing preferential field orientation that are not covered by the analytical solutions from EIM calculations. In the future, a more thorough understanding and treatment of these modes and their coupling might be useful to realize various novel WGM-based devices as for instance chip-scale polarization converters.

2.3 Photonic applications based on WGMs

Whispering gallery resonators are of great use within various fields of modern photonics. Their field of application reaches from simple building blocks like filters and switches to topical research in quantum and topological photonics. Herein, both single cavities as well as ensembles of coupled resonators are deployed. (A detailed introduction into the physical concept of coupled WGM cavities is given in Sec. 6.1.) For both cases, a non-comprehensive overview of established photonic applications is given in the following.

In line with the experimental results presented in Ch. 5, the potential impact of a spectral tunability is emphasized in case of single cavities. Regarding the application of ensembles of coupled resonators, the advantage of a tunable coupling strength is highlighted in accordance with the experimental results presented in Ch. 6. A more comprehensive overview of established areas of application of WGM resonators can be found elsewhere [42, 63, 70, 71].

Applications of individual WGM resonators

The first experimental proof of WGMs was found by Garrett *et al.* in 1961 in the tangential emission of CaF_2-spheres doped with Sm^{++}-ions [72]. This was also the first realization of a WGM-based micro laser. To enable laser emission of a WGM cavity, the dielectric resonator material is doped with an emitter in which population inversion and hence stimulated emission is generated. Various systems, e.g., rare-earth ions [9, 72], quantum dots [73–75] or organic dyes [10, 16, 17] have been employed as an emitter. Following this approach, micro lasers with very low lasing thresholds have been realized [9, 10, 76]. Regarding these micro lasers, a potential tunability of the WGM's wavelength directly implies a tunability of the laser's output wavelength.

Another established application of WGM cavities utilizes their wavelength selectivity. Using the narrow-band resonances, optical signals in waveguides can be filtered based on their wavelength [11,12,77,78]. Such spectral filters have also been realized in an add-drop configuration [79,80]. Alternatively, a switching of optical signals is feasible [81, 82]. This switching is often achieved using nonlinear optical effects as the Kerr effect [30, 83–85]. In the context of filtering/switching, a tunability of the spectral position of the WGM resonance gives direct control over the wavelength of the signal to be filtered/switched.

Due to their large quality factors and small mode volumes, WGM cavities are suitable to enhance light-matter interaction in the context of so-called cavity-quantum electrodynamics (cQED) [5, 13–15, 86–89]. One popular example thereof is the so-called Purcell effect: the enhancement of spontaneous emission of a source within an optical cavity [90–92]. This effect can also be observed in micro lasers based on dye-doped WGM cavities under continuous-wave excitation [39, 93]. Employing a parametric down-conversion process, various single-photon sources based on WGM cavities have been realized [18,19,94,95]. Within these cQED applications, the tunability of the wavelength of the regarding WGM resonance is of critical importance, as it has to be tuned to match the optical transition of the investigated emitter of interest. Recently, also a modulation of the Purcell enhancement via a detuning of the respective WGM resonance has been demonstrated [96].

Applications of ensembles of coupled cavities

Spectral filters can also be realized using more than one WGM cavity. Such higher-order filters provide a steeper slope of their transfer function as well as a stronger attenuation of signals with non-resonant wavelengths [97–102]. An additional degree of freedom herein is the arrangement of the coupled cavities which allows for filters with various characteristics [42]. Additionally, the group velocity of an optical pulse through a series of coupled WGM cavities depends on the cavities' coupling strength [103–105]. By sending optical signals through such coupled resonator optical waveguides (CROWs), delay lines can be fully realized on chip scale [22,23,106–108]. A control of the coupling strength between the cavities would enable a tunability of the delay time in the order of picoseconds [27].

Within recent years, the research field of exceptional-point photonics has gained high interest [109, 110]. Herein, the $\mathcal{PT}$-symmetry of non-hermitian photonic systems is intentionally broken. In this context, exceptional points (EPs) describe points in the parameter space of the system, at which at least two eigenstates as well as their eigenvalues coalesce and exotic properties of the photonic system arise [111–113]. In pairs of coupled WGM cavities, EPs can be realized comparably easy by a balancing of optical gain and loss [28]. Following this route, high-power single-mode micro lasers [26], micro lasers with reversed pump dependence [114], and robust lasing modes [115] as well as a significant enhancement of the sensitivity of WGM-based sensors [116–118] have been realized. By tuning the coupling strength of the two WGM cavities, the system can be driven in and out of its EPs [28]. EPs have recently also been observed in CROWs [119–121].

Furthermore, WGM cavities are of major interest in the upcoming field of topological insulator photonics. Therein, it is made use of topologically protected edge states in periodic structures with a photonic bulk bandgap [122–124]. Hafezi *et al.* demonstrated topological edge states in a periodic ensemble of WGM cavities on a silicon platform [125]. Robust and single-mode lasing from such topologically protected edge states has been reported [24, 25]. Recently, even electrically pumped topological insulator lasers [126] have been demonstrated.

Chapter 3

Fiber-transmission spectroscopy of whispering gallery modes

This chapter covers the investigation of whispering gallery modes using so-called fiber-transmission spectroscopy (FTS). In Sec. 3.1, the fundamentals of FTS including an analytical description based on coupled-mode theory as well as the established experimental methodology are given. Afterwards, two extensions to the established method that have been realized within the scope of this work are presented: In Sec. 3.2, fiber-transmission spectroscopy using two tapered optical fibers is introduced. Herein, again a short analytical description of the system, as well as necessary adaptions of the experimental methods are covered. This includes the fabrication of bent tapered optical fibers. In Sec. 3.3, polarization-sensitive FTS is addressed. The polarization analysis of the fiber transmission itself as well as of the directional radiation of the investigated WGMs is introduced.

3.1 Basics of fiber-transmission spectroscopy

For WGM cavities to be included into more complex photonic systems, an efficient method for the incoupling and outcoupling of light is required. Hereby, the coupling to free-space light is not feasible in an efficient manner due to the cavities' rotational symmetry [8, 127]. One of the most popular methods to achieve an efficient coupling is the evanescent coupling to an optical waveguide in plane of the whispering gallery mode [128–130]. If the propagation constant of the modes guided in both resonator and waveguide match and so-called critical coupling is achieved, theoretically the whole intensity of a mode propagating in the waveguide is coupled to the WGM cavity for resonant wavelengths, and vice versa.

Regarding the detection of whispering gallery modes in disk-shaped cavities within the fundamental investigations in this work, evanescent coupling to a waveguide is the method of choice. Instead of lithographically structured and substrate-bound waveguides as used in integrated photonic systems [131, 132], tapered optical fibers are used. This approach offers a higher flexibility, as the propagation constant of the fiber and the coupling to different WGMs can be chosen on the spot. This method of fiber-transmission spectroscopy allows for the investigation of the spectral mode structure of WGM cavities and has been extensively used within the scope of this work. Additionally, this investigation method has been further developed to give access to additional measurands beyond the spectral distribution of the WGMs.

Within the measurement method of FTS, the tapered part of an optical fiber is brought into close spatial proximity of the WGM cavity of interest to enable an evanescent coupling between the modes propagating in the fiber and the resonator [128–130]. In this state, light from a tunable laser source is fed to the optical fiber and the wavelength of the mode propagating in the fiber is changed with time. If the wavelength of the fiber mode fulfills the resonance condition of a WGM, it is evanescently coupled to the cavity and dissipated there by the intrinsic losses. Therefore, this light is missing in the transmission of the fiber and appears as a Lorentzian dip, if the optical output at the end of the fiber is detected using a photo diode. Following this approach, the spectral position of WGM resonances is given by the center wavelength of the Lorentzian dips and the quality factor of the modes can be calculated from the full width half maximum (FWHM).

To achieve an efficient evanescent coupling of a tapered fiber to a WGM cavity, several conditions have to be fulfilled. One important aspect is the so-called phase matching, which describes the degree of agreement of the propagation constants of the fiber and resonator modes [133]. Since the propagation constant of a WGM is fixed by the geometrical properties and the refractive index of the regarding cavity, a sufficient phase matching has to be ensured via a precise control of the diameter of the tapered optical fiber. This diameter is typically slightly smaller than the vacuum wavelength of the propagating laser mode [59, 133]. Since FTS is usually performed using light in the visible or near-IR spectral regime, this requirement corresponds to a fiber diameter in the order of hundreds of nanometers. The tapering of such fibers is done in a semi-automated fashion, as further described in Sec. 3.1.2.

Another condition for the efficient evanescent coupling is a large and time-stable coupling coefficient due to a sufficient spatial overlap of the evanescent fields of the two modes. This fiber-resonator coupling coefficient $|\mu_{\mathrm{in}}|$ mainly depends on the relative position of fiber and resonator. To ensure a sufficient and stable coupling, the position of the fiber needs to be precisely controlled in the order of ten nanometers. This is done using a 6-axis positioning unit based on a 3D piezo stage. A description of the established FTS measurement setup is given in Sec. 3.1.2.

In the following, first a short analytical description of the coupling of fiber and resonator mode is given using so-called coupled-mode theory (CMT). Afterwards, the established experimental methods to meet the necessary requirements of FTS listed above are presented.

3.1.1 Intensity transfer between resonator and fiber in coupled-mode theory

The analytical description of the intensity transfer between resonator and waveguide is based on coupled-mode theory [59, 97, 133–135] and is also found in more detail in the Master's thesis of Osman Karayel [62].

The transfer of electromagnetic energy between a waveguide and a WGM cavity is possible by means of an evanescent coupling of the propagating optical modes. The coupling mechanism is hereby based on the fact that the evanescent part of an unperturbed waveguide mode penetrates the bulk of the cavity, and vice versa. Within the cavity, the waveguide mode induces a polarization of the material and hence also a propagating cavity mode. The extent of this effect is strongly depending on the spatial overlap of the field distributions of waveguide and cavity mode within the cavity and thus on the relative position of waveguide and cavity. This is also illustrated by the schematic depiction of the cross section of the coupling region in Fig. 3.1(a). The coupling coefficient $|\mu_\mathrm{in}|$ can be calculated by integrating the product of the electric-field distributions of the unperturbed waveguide and cavity mode over the cross section of the WGM cavity. Therein, also the relative orientation of the modes' polarizations needs to be taken into account. This aspect is however ignored in the following, as it is covered in detail in Sec. 3.3.

Assuming the coupling coefficient $|\mu_\mathrm{in}|$ to be known, the coupling of waveguide and cavity mode can be calculated based on the differential equation used earlier to generally describe WGM resonances. As presented in Sec. 2.1, the field amplitude $a(t)$ within a whispering gallery resonator can be described using the differential equation of a lossy harmonic oscillator with eigenfrequency ω_0 and photon lifetime τ_i due to its intrinsic losses (see Eq. (2.3)). Within this concept, the intensity transfer from and to a waveguide can be described as a perturbation in the following manner:

$$\frac{\mathrm{d}}{\mathrm{d}t}a(t) = \left(\mathrm{i}\omega_0 - \frac{1}{2\tau_\mathrm{i}} - \frac{1}{2\tau_\mathrm{in}}\right) a(t) - \mathrm{i}\mu_\mathrm{in} s_\mathrm{i}(t). \tag{3.1}$$

Here,

$$s_\mathrm{i}(t) = S_0 \exp \mathrm{i}\omega t \tag{3.2}$$

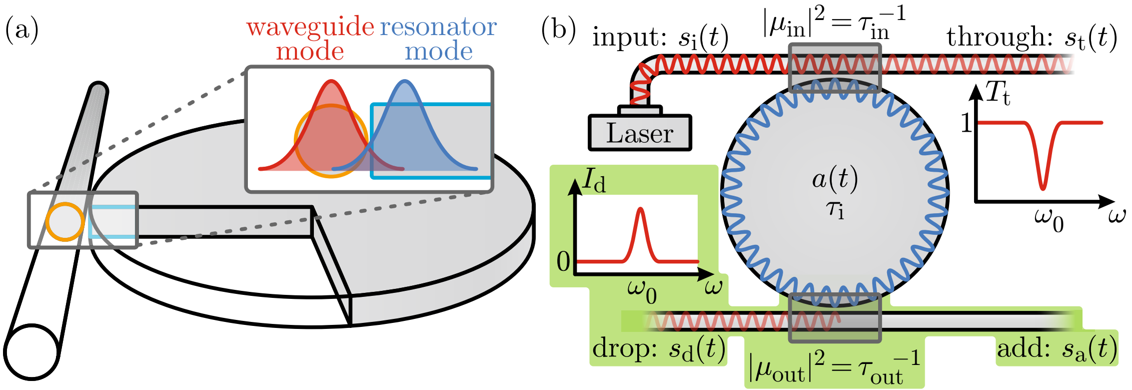

Figure 3.1: Schematic illustration of the concept of FTS. (a) depicts the spatial overlap of the unperturbed field distributions of fundamental waveguide (red) and cavity mode (blue) in the coupled case. The coupling coefficient $|\mu_\mathrm{in}|$ is proportional to the spatial overlap of the modes within the cavity (cyan rectangle). (b) demonstrates the investigation of WGMs using FTS. Laser light is coupled to the input port and propagates as waveguide mode with field amplitude $s_\mathrm{i}(t)$ in the fiber. If the frequency of $s_\mathrm{i}(t)$ matches that of a WGM ω_0, the light is coupled to the cavity within the coupling region (gray box) by $|\mu_\mathrm{in}|$ and excites a mode with field amplitude $a(t)$. The WGM is dissipated by its intrinsic losses with a photon lifetime of τ_i. The additional loss due to fiber coupling is accounted for by the photon lifetime τ_in. In the transmission T_t of the waveguide mode with field amplitude $s_\mathrm{t}(t)$ propagating from the coupling region to the through port, a Lorentzian dip centered at ω_0 is found. Elements with green background illustrate measurements using two fibers (see Sec. 3.2): The second waveguide is coupled to the cavity via a coupling coefficient $|\mu_\mathrm{out}|$, introducing another photon lifetime τ_out. Light coupled to the second waveguide travels towards the drop port with field amplitude $s_\mathrm{d}(t)$. A Lorentzian peak of the transferred intensity I_d centered at ω_0 is detected. Due to the directionality of the coupling, the waveguide mode at the add port usually carries a field amplitude of $s_\mathrm{a}(t) \approx 0$.

is the field amplitude of the mode coupled to the input port and propagating in the waveguide towards the coupling region. This mode is coupled to the WGM with a coupling coefficient μ_in. The additionally introduced photon lifetime τ_in of the cavity accounts for the loss channel of a possible intensity transfer from the resonator back to the waveguide. Based on the assumption of a stationary state of equal energy flows into and out of the cavity, a relation between μ_in and τ_in is found [62]:

$$\frac{1}{\tau_\mathrm{in}} = |\mu_\mathrm{in}|^2 \,. \tag{3.3}$$

A schematic depiction of waveguide and resonator including the discussed loss channels and coupling region is given in Fig. 3.1(b).

Using a continuous-wave laser source, the WGM resonator under waveguide excitation with frequency ω is an approximately stationary system. Hence, only the particulate solution of Eq. (3.1) is of interest:

$$a(t) = \frac{-\mathrm{i}\mu_{\mathrm{in}}}{\mathrm{i}(\omega - \omega_0) + \frac{1}{2}\tau_{\mathrm{i}}^{-1} + \frac{1}{2}\tau_{\mathrm{in}}^{-1}} s_{\mathrm{i}}(t). \tag{3.4}$$

In the context of fiber-transmission spectroscopy, the transmission detected at the through port at the end of the waveguide can be calculated from the amplitude of waveguide mode $s_{\mathrm{t}}(t)$ propagating away from the coupling area. Assuming the propagation directions in waveguide and resonator to be equal within the coupling region, this mode amplitude can be calculated using [136]

$$s_{\mathrm{t}}(t) = s_{\mathrm{i}}(t) - \mathrm{i}\mu_{\mathrm{in}}^{*} a(t). \tag{3.5}$$

Combining Eq. (3.2) to (3.5), the transmission of the waveguide at the through port is given by:

$$T_{\mathrm{t}}(\omega) = \left| \frac{s_{\mathrm{t}}(t)}{s_{\mathrm{i}}(t)} \right|^2 = 1 - \frac{|\mu_{\mathrm{in}}|^2 \tau_{\mathrm{i}}^{-1}}{(\omega - \omega_0)^2 + \frac{1}{4}\left(\tau_{\mathrm{i}}^{-1} + \tau_{\mathrm{in}}^{-1}\right)^2}. \tag{3.6}$$

Equation (3.6) describes a Lorentz-shaped dip in the waveguide's transmission spectrum. This dip is centered at the resonance frequency of the WGM ω_0 and can therefore be used to identify the mode. The transmission at the minimum of this resonance dip in the case of $\omega = \omega_0$ is given by:

$$T_{\mathrm{t}}(\omega = \omega_0) = \left(\frac{\tau_{\mathrm{i}}^{-1} - \tau_{\mathrm{in}}^{-1}}{\tau_{\mathrm{i}}^{-1} + \tau_{\mathrm{in}}^{-1}} \right)^2 \tag{3.7}$$

and can hence vanish in the case of the critical coupling coefficient

$$|\mu_{\mathrm{in}}|^2_{\mathrm{crit}} = \tau_{\mathrm{in}}^{-1} = \tau_{\mathrm{i}}^{-1}. \tag{3.8}$$

In this case, the external losses due to the coupling to the waveguide are equal to the intrinsic losses of the WGM resonator. Since the coupling coefficient $|\mu_{\mathrm{in}}|$ strongly depends on the distance between resonator and cavity, there is a certain critical coupling distance. If the distance between waveguide and resonator is larger than this critical value, not the whole intensity propagating in the waveguide can be coupled to the cavity. If this distance is smaller than the critical distance (and the coupling coefficient therefore larger than the critical coupling coefficient), some of the intensity is coupled back from the resonator to the waveguide within the coupling region. In both cases, the waveguide transmission does not completely vanish.

As derived in Sec. 2.1, the quality factor Q of a WGM is directly proportional to the lifetime τ, that is given by the inverse FWHM of the mode's Lorentz-shaped resonance peak. Due to the high spectral resolution of FTS, these quality factors can be investigated employing this method. However, the FWHM of a resonance dip described by Eq. (3.6) is given by

$$\Delta\omega_{\mathrm{FWHM}} = \tau_{\mathrm{i}}^{-1} + \tau_{\mathrm{in}}^{-1}. \tag{3.9}$$

Therefore, the determination of the intrinsic quality factor would only be possible in the theoretical limit of $|\mu_{\mathrm{in}}| = 0$, where no resonance dip is present. Thus, all quality factors derived from FTS measurements can be taken as lower limit to the cavities' intrinsic quality factor. In the case of critical coupling, the measured quality factor equals half the intrinsic quality factor of the cavity.

In summary, FTS offers access to the spectral position as well as a lower limit of the quality factor of the WGM modes within a cavity. The precision of the determined quantities is mainly limited by the resolution of the used tunable laser source. Hence, this method is well-suited to reliably and flexibly investigate the spectral mode structure of WGM resonators within this work.

3.1.2 Established methodology of fiber-transmission spectroscopy

The investigation method of FTS has been introduced into the research group the present work has been done in more than 10 years ago [64] and used extensively since [10,16,33,39,64,66,137,138]. In this time, well-developed experimental setups for both the fabrication of tapered optical fibers as well as for the conduction of FTS itself have been established. Since these methods have been used to investigate the spectral mode structure of various WGM cavities within the scope of this work, they are shortly introduced here. These sections also lay a foundation for the description of realized extensions to the method of FTS given in Sec. 3.2 and 3.3.

Fabrication of tapered optical fibers

The home-built setup used to fabricate tapered optical fibers has been adapted from [139,140] and built by Philipp Brenner within his Bachelor's thesis [141].

Tapered optical fibers are produced from commercially available single-mode fibers suited for the intended wavelength range. In the case of FTS near the infrared c-band, the fiber *SMF-28* (Corning, Inc.) is used. As a first step, the fiber's polymeric coating layer is mechanically removed, leaving back the core and cladding material with a combined diameter of 125 µm. Then, the fiber is clamped to two opposing linear motors. The taper of the fiber is produced by using the linear motors to pull both ends of the fiber in opposing directions while a small part of the

coating-free fiber is heated above its glass transition temperature using a gas flame. The used combination of the actual values of gas flow and pulling speed of the linear motors has been thoroughly engineered [39, 141].
The thinning of the fiber can be observed in a live fashion from the transmission of laser light through the fiber. Under the decreasing fiber width, the diameter of the core gets too small to guide any modes. Therefore, the core and cladding can be treated as one effective medium with the refractive index of the cladding. The light is then guided by the refractive-index contrast between the cladding and the surrounding air and higher-order modes are excited. Due to the sightly shifted resonance wavelengths of these non-fundamental modes, this leads to a slow beating of the fiber's transmission. As the fiber gets thinned further, the higher-order wavelengths slowly diverge, increasing the beating frequency. This process ends, as soon as the tapered part is too thin to still guide any higher-order modes. From that point on, the fiber promptly switches back to a single-mode propagation. At that point, the final thickness of the tapered single-mode fiber is controlled by the time the fiber is further tapered after the transition to single-mode propagation. Following this approach, the propagation constant of the tapered fiber can be precisely controlled and thus adapted to any specific needs. In the context of FTS of polymeric WGM cavities near the IR c-band, a relative intensity transfer to the cavity of more than 90 % is feasible (also see Fig. 3.3(a)), demonstrating a strong phase matching.

Established measurement setup

The fiber-transmission spectroscopy setup used in this work has been designed and built by Mario Hauser [64] and slightly modified within the following years. The description given here comprises the current version of the setup, excluding the extensions realized within the scope of this work, since they are covered separately in Sec. 3.2 and 3.3.

A schematic illustration of the FTS setup is shown in Fig. 3.2. Therein, all components without colored background constitute the established FTS setup. The physical basis of FTS is the precisely controlled spatial overlap of the evanescent fields of a tapered optical fiber and the WGM cavity. To that end, the tapered optical fiber is attached to a nano-positioning unit via a custom-built fiber mount. The positioning unit enables a precise control of the fiber position in all six spatial degrees of freedom, including a resolution of all three translations in the order of 10 nm due to closed-loop piezo actuators (*NanoMax*, Thorlabs, Inc.). The WGM sample is mounted to a copper-made sample holder, which can be heated from room temperature to around 80 °C (100 °C) with a resolution of 0.1 K using a Peltier element (heating resistor) in combination with a Pt100 temperature sensor and a PID temperature control unit. The sample as well as the tapered optical fiber can addi-

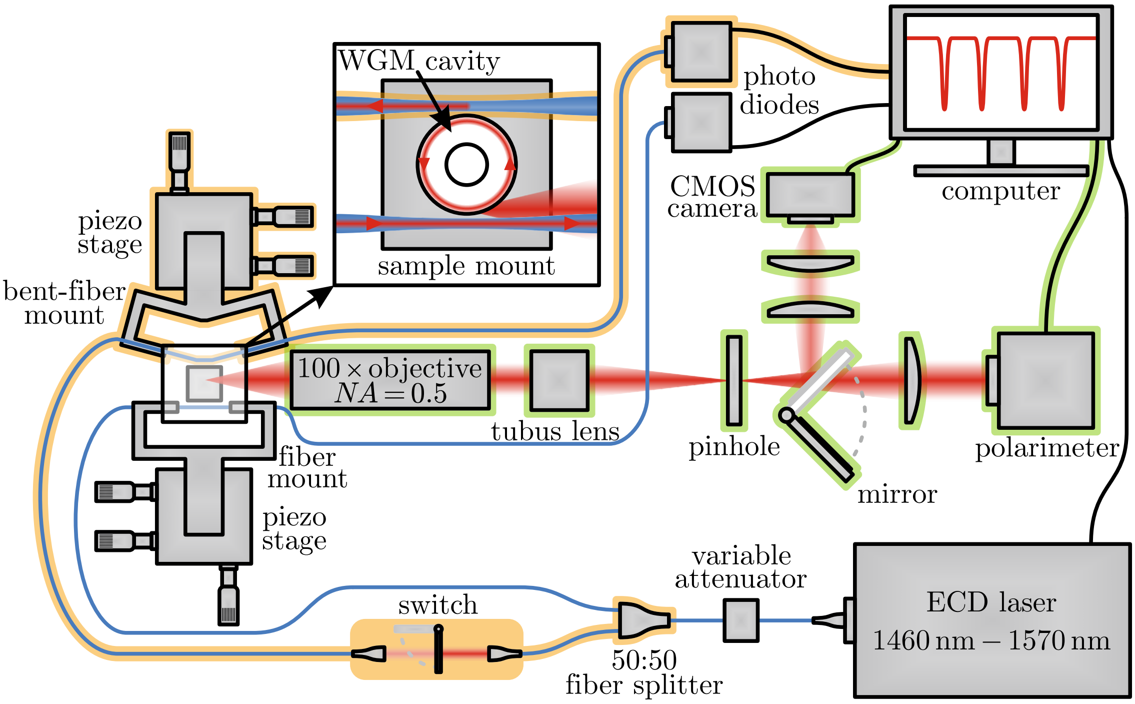

Figure 3.2: Components without colored background schematically visualize the established FTS measurement setup: Light from a widely tunable ECD laser is coupled to a single-mode optical fiber (blue). After passing a variable attenuator, the fiber is mounted to a piezo stage via a custom-built fiber mount. The tapered part of the optical fiber is brought into coupling distance to the WGM cavity of interest (also see magnified inset). The sample is placed on a heatable sample mount. At the end of the fiber, its transmission is detected using a photo diode and sent to a computer for further processing. WGM resonances appear as Lorentz-shaped dips in the fiber's transmission spectrum. Components with an orange background are part of the 2FTS extension of the setup described in Sec. 3.2, those with a green background are part of the polarization-dependent setup extension described in Sec. 3.3.2.

tionally be observed using two microscope cameras, one above the sample and one near the plane of the resonator disk. These cameras are not shown in Fig. 3.2.
As a light source, a continuously tunable external-cavity diode laser (*CTL*, TOPTICA Photonics AG) with a tuning range of 1460 nm to 1570 nm, a linewidth of 10 kHz, an absolute wavelength precision of 150 pm and a relative precision of 10 pm is used. The laser light is coupled to the input port of the single-mode fiber and the intensity is controlled using a variable optical attenuator.
Behind the coupling region to the WGM cavity, the transmission at the through port at the end of the fiber is detected using an InGaAs photo diode. The intensity at the photo diode as well as the wavelength of the light (given as output from the

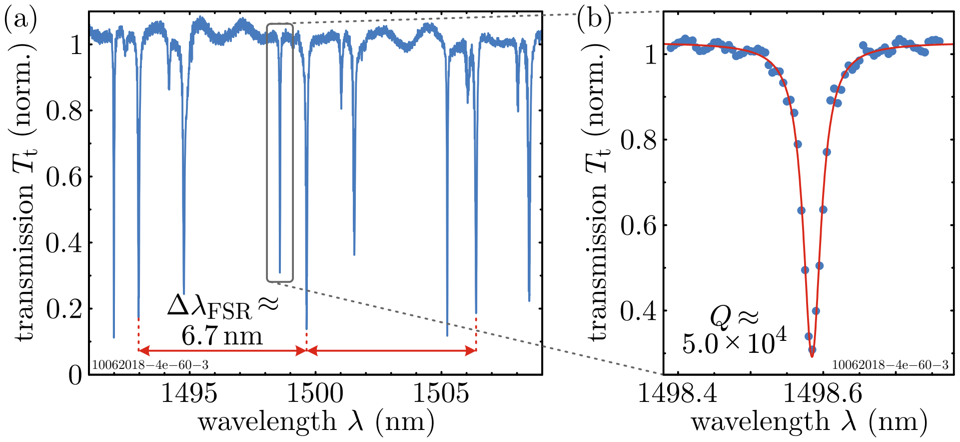

Figure 3.3: Exemplary fiber-transmission spectrum of a WGM cavity. (a) depicts the fiber transmission over a large spectral region. The FSR is evident from the periodicity of the spectrum. Within one FSR, four to five resonances are found. In (b), the dip of a single WGM resonance (also indicated in (a)) is shown. A quality factor Q of approximately 5×10^4 is estimated from the applied Lorentzian fit.

laser itself) are sent to a computer for further processing. During a measurement, the wavelength is continuously tuned with an approximately constant speed of a few nanometer per second. The allocation of the intensity signal to the wavelength is then done using the point of time of each measurement.

Regarding the detected intensity, one has to account for the wavelength dependency of both the intensity of the laser source as well as the transmission of the fiber due to material-intrinsic attenuation as well as imperfections of the taper and possible scatterers attached to the fiber. Therefore, a background measurement is performed for which a fiber-resonator distance of several 10 µm is chosen to prevent any coupling to the cavity. Afterwards, the intensity of the measurement under coupling conditions is normalized to that background measurement to obtain the Lorentz-shaped transmission dips due to the evanescent coupling to the WGM resonances.

Figure 3.3 depicts an exemplary fiber-transmission spectrum of a polymeric WGM cavity. In (a), a measurement over a large spectral region is shown. Within the plotted spectral region, several Lorentzian dips with varying depth are found. From the periodicity of the spectrum, a free spectral range $\Delta\lambda_{FSR}$ (also see Sec. 2.1) of around 6.7 nm can be concluded. In this exemplary measurement, $4-5$ WGMs are detected within one FSR. This demonstrates the existence of higher-order modes within the investigated cavities. The varying, but also approximately periodic depth of the different WGM resonances is expected to be mainly due to a differing fiber-resonator coupling. This differing coupling is mainly influenced by varying spatial mode profiles of the regarding (partly higher-order) modes and therefore changing spatial overlaps with the evanescent field of the mode within the tapered fiber. Figure 3.3(b) shows the transmission dip induced by a single WGM resonance, including an applied Lorentzian fit. A spectral position of the resonance of 1498.58 nm is determined from the fit with a relative precision in the order of 10^{-7}. This precision is therefore mainly limited by the absolute and relative wavelength precision of the used laser source. A lower limit of the quality factor can be estimated from the FWHM of the applied fit to be around 5×10^4.

3.2 Fiber-transmission spectroscopy using two optical fibers

In Ch. 6, FTS is used to investigate the tunable coupling of a photonic molecule made from two WGM cavities with changing inter-cavity distance. Although this is feasible using the resonance splitting of bonding and anti-bonding supermodes (for example see Fig. 6.4), this method also yields several drawbacks. The most essential of these drawbacks is the fact, that resonant supermodes in an FTS spectrum can not be directly distinguished from single-cavity WGMs. Therefore, an identification of supermodes is only possible performing a thorough comparison of FTS spectra detected from both coupled cavities consecutively.

A more sophisticated approach is the investigation of the intensity transferred from the tapered fiber through the coupled photonic molecule into a second tapered fiber. In such a configuration, only resonant supermodes contribute to this intensity transfer and appear as Lorentz-shaped peaks. Hence, it allows for a direct and isolated detection of delocalized supermodes. Furthermore, several potential applications of a tunably coupled photonic molecule, such as filters or switches (also see Sec. 2.3), base on that so-called add-drop configuration using two optical fibers. In analogy to such add-drop systems, the four ports and two optical fibers are also labeled here: Light is coupled into the input port of the incoupling fiber, the end of this fiber is the through port. The signal is then coupled through the cavity/photonic molecule to the outcoupling fiber and detected at the drop port. The other end of this fiber is the add port. These definitions are also given in Fig. 3.1(b).

Parts of the experimental methods presented in this section have been developed in close cooperation with Pascal Rietz [142].

In this section, the basic functionality of fiber-transmission spectroscopy using two tapered optical fibers (2FTS) is demonstrated by coupling both fibers to a single WGM cavity. This configuration is described using CMT by applying minor changes to the formulas presented in Sec. 3.1.1. This is done under the assumption, that the second fiber is coupled to the WGM cavity with a coupling coefficient $|\mu_{\text{out}}|$.

The underlying differential equation (3.1) has to be extended by an additional photon lifetime $\tau_{\mathrm{out}} = |\mu_{\mathrm{out}}|^{-2}$, which accounts for the loss channel of an intensity transfer from the cavity to the outcoupling waveguide. This additional loss channel leads to the substitution $1/(2\tau_{\mathrm{in}}) \rightarrow 1//2\tau_{\mathrm{in}}) + 1/(2\tau_{\mathrm{out}})$ in Eq. (3.1). This substitution also applies to the particulate solution of the field amplitude inside the cavity in Eq. (3.4). In analogy to Eq. (3.5), the field amplitude at the drop port at the end of the outcoupling waveguide is given by:

$$s_{\mathrm{d}}(t) = -\mathrm{i}\mu_{\mathrm{out}}^{*} a(t). \tag{3.10}$$

This leads to a relative transferred intensity from the input port of the incoupling waveguide to the drop port of

$$I_{\mathrm{d}}(\omega) = \left|\frac{s_{\mathrm{d}}(t)}{s_{\mathrm{i}}(t)}\right|^{2} = \frac{|\mu_{\mathrm{in}}|^{2}\,|\mu_{\mathrm{out}}|^{2}}{(\omega-\omega_0)^{2} + \frac{1}{4}\left(\tau_{\mathrm{i}}^{-1} + \tau_{\mathrm{in}}^{-1} + \tau_{\mathrm{out}}^{-1}\right)^{2}}. \tag{3.11}$$

As evident from Eq. (3.11), Lorentz-shaped intensity peaks centered at the spectral position of WGM resonances are expected at the drop port. Consequently, also 2FTS measurements are suited to investigate the mode structure of WGM cavities. The FWHM of the resonances is however further broadened in comparison to single-fiber FTS due to the additional loss channel. Hence, the determination of quality factors from such measurements is not reasonable. An analytical description based on coupled-mode theory of 2FTS of a photonic molecule consisting of two coupled WGM cavities is given in Sec. 6.2.3.

Within the scope of this work, the existing FTS setup has been extended by a second tapered optical fiber to enable 2FTS measurements. Apart from the obvious necessary adjustments to the overall setup discussed in Sec. 3.2.2, this also requires the fabrication of bent tapered optical fibers. The reason for this requirement as well as the realization of such fibers is discussed in the following.

3.2.1 Fabrication of bent tapered optical fibers

The requirement of bent optical fibers in the context of 2FTS can be understood by comparing the diameter of the fiber prior to tapering of 125 µm to that of a tapered fiber of around 1 µm. This means that even if two tapered fibers were in direct mechanical contact of their untapered parts, their tapered parts would still be more than 100 µm apart. Hence, such two fibers can not be used to simultaneously couple to two different sides of a PM (or similar photonic system) with an overall dimension in the order of tens of µms.

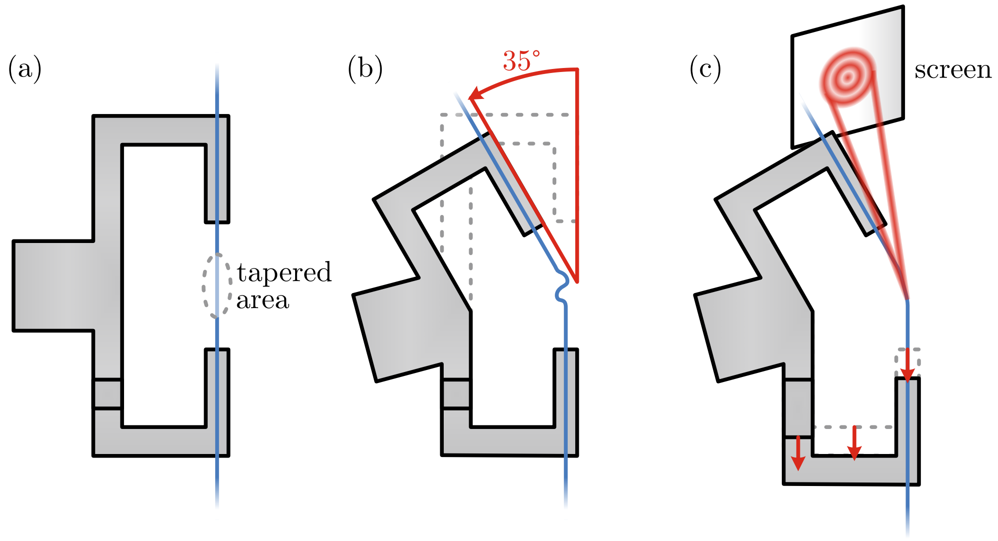

Figure 3.4: Schematic illustration of the fabrication process of bent tapered optical fibers. (a) The tapered fiber (blue) is glued to its mount in an unbent state. (b) The two sides of the fiber mount are rotated with respect to each other by 35°. This reduces the mechanical stress of the fiber and therefore leads to the taper to be free to move. (c) The mechanical stress is restored by stretching the fiber. The reduction of the motion of the fiber during this process is monitored using the radiation pattern of laser light coming from the taper.

This issue can be solved by introducing at least one bending radius within the tapered area to one of the optical fibers. To that end, a new fiber mount (inspired by [143]) has been designed, that allows for a bending of the optical fiber after the tapering process. A schematic depiction of this working principle is demonstrated in Fig. 3.4.
As a first step, a tapered optical fiber is clued to the fiber mount in its unbent state using a UV-responsive adhesive. As for a standard fiber mount, this is done with the fiber under mechanical stress to reduce the possible motion of the tapered part of the fiber. After the adhesive is hardened under UV illumination, the two sides of the fiber mount (to which the fiber is fixed on the two sides of the taper) are rotated against each other by 35°. The rotational axis is at the center of the taper of the optical fiber. Due to this rotation, the mechanical stress on the fiber is significantly reduced. This leaves the tapered part to move freely under motion of the whole fiber mount as well as drafts of air. Since such motion of the taper is inconvenient regarding FTS measurements, the mechanical stress is restored by slowly pulling the two sides of the fiber mount apart using a micrometer screw. Thereby, enough stress has to be applied to reduce the possible motion of the taper to the order of 10 nm. However if too much stress is applied, the fiber easily breaks. Therefore, the stretching process is monitored using the pattern of the forward

radiation coming from the tapered part if laser light is sent through the fiber. This radiation pattern is qualitatively investigated on a screen in several meters distance. Light is emitted from different areas of the taper due to the emission of higher-order modes, imperfections of the fiber and possible scatterers. All these single emissions show approximately rotationally symmetric patterns on the screen. The motion of the taper can therefore by estimated from the dynamically changing relative displacement of these single patterns. The bent and tapered optical fiber is gradually stretched until no further dynamical change of the relative displacement of the single patterns is observed. Assuming a distance of 5 m between the tapered fiber and the screen, the radiation pattern has to be stable in the order of single millimeters to ensure a sufficiently reduced motion of the tapered fiber. Following this process, a reproducible fabrication of bent tapered optical fibers without the need of any additional hardware has been realized.

3.2.2 Extension of the established measurement setup

To enable 2FTS measurements, not only a second tapered optical fiber, but also additional instruments have been included into the established FTS setup. In Fig. 3.2, these additional components are highlighted via a light orange background.
The bent tapered optical fiber is mounted to an additional piezo stage, which is used to precisely control the coupling distance to the WGM cavity. The intensity at the drop port at the end of the outcoupling fiber is detected using an additional InGaAs photo diode. During a 2FTS measurement, the coupling coefficient of the incoupling fiber can be estimated from the depth of the transmission dips at the through port. For the outcoupling fiber, this is not possible. Hence, this coupling has to be determined from a previously performed single-fiber FTS measurement using only the outcoupling fiber. To that end, light from the external-cavity diode laser is sent through that fiber only for the single-fiber measurement. To realize this while preventing any mechanical disturbance of the overall setup, the signal from the laser is split using a 50:50 fiber splitter. One of these parts of the signal is permanently coupled to the incoupling fiber, while the other one is coupled to free-space and then coupled into the outcoupling fiber. This way, a free-space shutter can be used to turn the coupling of laser light to the outcoupling fiber on and off. In Fig. 3.2, this configuration is labeled as *switch*.

3.2.3 2FTS measurement procedure

The 2FTS measurement is performed as follows: First, both fibers are not coupled to the cavity/photonic molecule and laser light is sent trough both of them. The

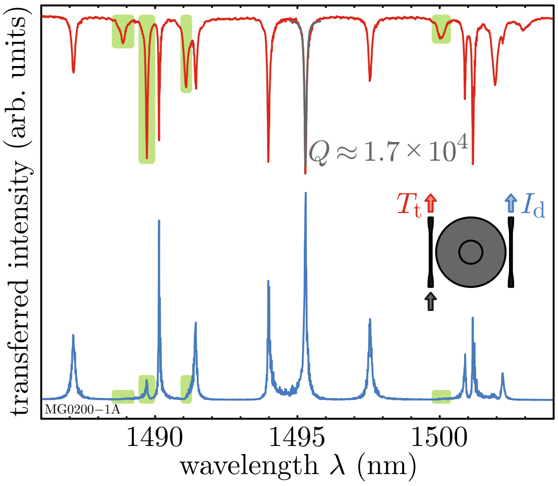

Figure 3.5: Exemplary 2FTS measurement of a single WGM cavity. The transmission to the through port T_t is depicted in red, the intensity transfer to the drop port I_d in blue. Distinct Lorentzian peaks of transferred intensity appear at the spectral position of most of the WGMs. For some of the modes, only very little or no transferred intensity is detected (highlighted in green). This finding is attributed to a weak coupling of these WGMs to the outcoupling fiber. The decrease of the quality factor of the modes in comparison to the FTS measurement depicted in Fig. 3.3 is in accordance with an additional loss channel induced by the second optical fiber.

outcoupling fiber is coupled to the cavity/photonic molecule and the coupling is estimated from the depth of the transmission dips at the drop port. Afterwards, the signal fed to the outcoupling fiber is switched off and the incoupling fiber is brought into coupling while observing the transmission dips at the through port. Hereby, the intensity transferred through the cavity/photonic molecule is simultaneously detected.

Figure 3.5 depicts an exemplary measurement of the intensities detected at both the through port T_t and the drop port I_d for both fibers being coupled to a single WGM cavity. Lorentz-shaped peaks of intensity transferred to the drop port coinciding with dips of transmission at the through port are found. This demonstrates the basic functionality of 2FTS measurements as they are used to investigate the controllability of the intensity transfer through a photonic molecule with tunable coupling in Sec. 6.4.

3.3 Polarization-sensitive FTS

Using both FTS as well as 2FTS measurements, the spectral distribution and quality factors of both single-cavity resonances as well as supermodes in photonic molecules can be investigated. Nevertheless, no information about the polarization of light within the cavities can be drawn from such spectra. As described in Sec. 2.2, the polarization state is an important characteristic of WGM resonances in disk-shaped cavities. It is indispensable to understand coupling phenomena between WGMs with varying spatial field distribution (also see Fig. 2.3). Even if neglecting such coupling effects, the spectral position of WGM resonances still depends on their polarization [144]. This dependency gets even more important, if intrinsically birefringent resonator materials as liquid crystal elastomers (see Sec. 4.1) come into play.
Within the scope of this work, two different approaches to investigate the polarization of WGM resonances while performing FTS measurements have been developed. The first of these approaches bases on the analysis of the polarization of the fiber transmission at the through port, while the other one harnesses the directional in-plane radiation of the WGM of interest. In the following, both these approaches are shortly introduced and the preferential field orientation of exemplary WGMs is determined. Hereby, both the potential of these methods as well as their limitations are discussed.

Parts of the experimental methods presented in this section have been developed in close cooperation with Evelyn Kaiser and Lukas Rebholz. Comprehensive technical descriptions can be found their respective theses [40, 145].

3.3.1 Polarization analysis of the fiber transmission

To investigate the azimuth angle of the preferential field orientation of WGMs in disk-shaped cavities within an FTS measurement, the polarization of the light at the through port at the end of the tapered fiber is analyzed. To that end, the light is coupled to free space and split by a 30:70 beam splitter. While the large fraction of the intensity is reflected onto an InGaAs photo diode, the smaller part travels directly to a polarimeter (*PAX1000IR2/M*, Thorlabs, Inc.). Within the polarimeter, a rotating $\lambda/4$-waveplate in combination with a fixed polarizer is used to convert the polarization state of the light into a temporal modulation of its intensity. This intensity is detected using a photo diode and the polarization by means of the azimuth angle ψ and ellipticity angle χ as well as the degree of polarization DOP is determined from a fast Fourier transformations. For a detailed description of the working principle of the polarimeter as well as the definition of the polarization parameters, see [40, 145].

By combining the polarization of the transmitted light with the depth of the transmission dip corresponding to a WGM resonance, the preferential field orientation of the mode can be estimated: The smaller the angle between the polarization of the fiber mode and the field orientation of the WGM, the more intensity is coupled to the cavity. To determine the preferential field orientation of a WGM of interest, the azimuth angle ψ of the polarization of the fiber mode is tuned. This is done using a manual fiber polarization controller (*FPC560*, Thorlabs, Inc.). Therein, the polarization within the fiber is changed using the birefringence of the fiber under the application of mechanical stress [146–150]. Performing FTS measurements with different polarizations of the fiber mode, the amplitude of the transmission dips is expected to follow $\cos^2(\psi - \vartheta)$, where ϑ is the preferential field orientation of the mode within the cavity.

To demonstrate the basic potential of this measurement approach, the preferential field orientation of two spectrally close WGMs within a cavity made from liquid crystal elastomer (also see Sec. 4.4) has been investigated. The amplitudes of their transmission dips have been determined from Lorentzian fits and are depicted versus the azimuth angle of the fiber polarization in Fig. 3.6(a). The amplitudes of the transmission dips are approximately following the expected $\cos^2$-like behavior, as indicated by the applied fits. The angles of the preferential field orientation of the two modes are deduced from these fits to be $\vartheta_1 \approx -28.5°$ and $\vartheta_2 \approx 62.5°$. So although these angles significantly deviate from the expected values of a TE-like ($\vartheta = 0°$) or TM-like ($\vartheta = 90°$) polarization, they differ by around 90°, indicating an orthogonality of these two modes. The significant deviation from a TE- or TM-like polarization is assumed to be induced by either the geometrical imperfections of the LCE cavity causing WGMs without preferential field orientation (see App. B.2) or a rotation of the polarization of the fiber's mode within its tapered part (see below).
Despite this successful determination of the preferential field orientation of WGMs, there are several limitations that have to be taken into account. At first, the expectation of a $\cos^2$-like behavior of the amplitude of the transmission dips is only justified in case of a linear polarization of the fiber mode, meaning an ellipticity of $\chi = 0°$. Although this can be achieved employing the polarization controller, it limits the ease of use of the presented method. Furthermore, the conservation of polarization within the optical fiber itself has to be taken into account. As mentioned earlier, a stress-induced birefringence of the fiber can alter the polarization of the fiber mode [146–150]. This influence of mechanical stress can be minimized by limiting the distance between the coupling region and the free-space coupler to a few centimeters without any bending of the fiber. Still, the polarization of the fiber mode within the tapered part of the fiber is usually not controllable [152–154]. Nevertheless, the change of the polarization of the fiber mode within the tapered part is expected to be representable by an overall rotation of the Poincaré sphere [155, 156].

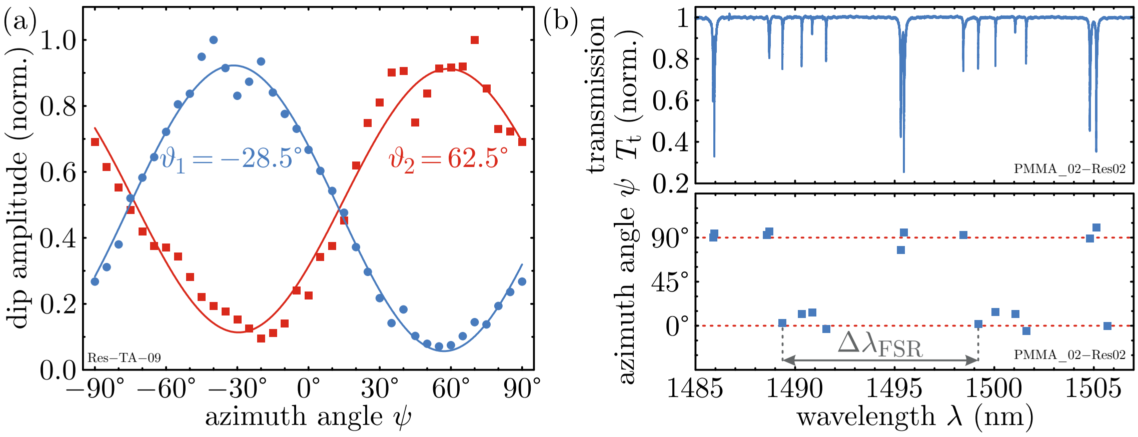

Figure 3.6: Exemplary investigation of the preferential field orientation of WGMs using two different measurement approaches. (a) The normalized amplitude of the Lorentzian transmission dips of two spectrally close WGMs is depicted versus the azimuth angle of the polarization og the fiber mode. For both WGMs, the amplitude approximately follows the expected $\cos^2$-like behavior. The angles of preferential field orientation $\vartheta_{1,2}$ of the two WGMs differ by approximately 90°, indicating orthogonality of the modes. (b) The polarization of the directional radiation of a WGM is detected in parallel with conventional fiber-transmission spectra. For each dip in the fiber's transmission spectrum (top), the azimuth angle of the cavity's radiation is determined (bottom). A clear separation into two groups of orthogonal modes with azimuth angles around 0° and 90° (dotted red lines) is evident. The small deviations from these angles show a periodicity with the free spectral range $\Delta\lambda_{\mathrm{FSR}}$. Sample in (a) fabricated by Stefan Pfleging [151], (b) adapted from [40].

Thus, modes with different polarizations should all undergo the same change of their polarization angles $\Delta\psi$ and $\Delta\chi$. Hence, this influence could be eradicated via an angle calibration based on the coupling of the tapered fiber to a WGM cavity with modes of well-defined and known preferential field orientation.

Even under the considerations mentioned above, the exemplary results depicted in Fig. 3.6(a) demonstrate the basic potential of this method to investigate the preferential field orientation of WGMs within FTS measurements.

3.3.2 Polarization analysis of the directional radiation of WGMs

In contrast to the previously discussed investigation of the polarization at the through port of the fiber, the analysis of the directional radiation of WGMs gives a more direct access to the orientation of the fields of these modes. On the other hand, a more elaborate extension of the FTS measurement setup as well as a thorough analysis of the obtained data is required.

The necessary adaptions to the established FTS setup are highlighted in Fig. 3.2 via a light green background. The radiation from the WGM cavity of interest is collected using a 100× microscope objective (*100X Mitutoyo Plan Apo NIR*, Mitutoyo Corporation) with a numerical aperture of 0.5 and a large working distance of 12 mm. After a matching tubus lens, a pinhole in the virtual image plane is used to crop the region of interest from which the radiation is analyzed. Afterwards, the light is collimated and sent to a polarimeter (*PAX1000IR2/M*, Thorlabs, Inc., for further information see Sec. 3.3.1). Alternatively, a foldable mirror in combination with a CMOS camera can be used to observe the region of interest and evaluate its cropping as well as the focusing. The polarimeter data is processed together with the remaining FTS data using a computer.
The region of interest from where the radiation is analyzed is that part of the outer rim of a WGM cavity, from which the tangential radiation is collected by the objective (also see magnified inset of Fig. 3.2). Since mainly traveling waves with a common propagation direction (counterclockwise in Fig. 3.2) are excited in the cavity [64, 157], the signal detected in the expected forward direction of these traveling waves is significantly larger than that from the counter-propagating direction [40]. Contrary to the illustration in Fig. 3.2, the radiation is not actually collected from the region where the fiber is coupled to the cavity, but in a configuration rotated by 90° with respect to the fiber. Regarding the depicted case, the radiation of the right-hand side edge of the cavity to the top of the image is collected using the microscope objective. This way it is ensured that all collected light is solely coming from WGMs guided within the cavity.
Due to the simultaneous detection of the fiber transmission and the polarization of the far field, a direct allocation of the polarization parameters of the detected radiation to the WGM resonances at different spectral positions is possible. To that end, the azimuth angle ψ, the ellipticity angle χ and the degree of polarization DOP are each averaged over the FWHM of a detected WGM. For WGMs with a preferential field orientation, the dominating direction of the electric field of the mode within the cavity directly coincides with the dominant polarization of the light at the polarimeter. This has been shown by investigating the far-field radiation of WGM resonances in FEM simulations in [40]. Hereby, an azimuth angle of 0°(90°) corresponds to a WGM with a TE-(TM-)like polarization within the cavity. A detailed discussion of the ellipticity as well as the degree of polarization within this context are spared here but can be found elsewhere [40].

The possible determination of the preferential field orientation of WGMs based on the analysis of the directional radiation from the cavity is apparent from exemplary measurements shown in Fig. 3.6(b). All WGM resonances in the investigated spectral region show azimuth angles of their far field of around 0° or 90° (dotted red lines) with deviations of a few degree and are therefore identified as modes with

TE-like or TM-like polarization, respectively. The deviations of the azimuth angle show a periodicity with the free spectral range $\Delta\lambda_{\mathrm{FSR}}$ as pointed out in Fig. 3.6(b), indicating a physical origin of these deviations.

In summary, the exemplary results shown in Fig. 3.6(b) demonstrate the potential of this method to reliably distinguish between WGMs with a TE- and TM-like polarization, which is not possible using only the established FTS measurement approach. Furthermore, this determination can be conducted in a semi-automated manner and includes the ellipticity angle χ as well as the degree of polarization DOP of the far-field radiation. These advantages justify the required elaborate extension of the FTS measurement setup in comparison to the polarization analysis of the fiber transmission introduced in Sec. 3.3.1.
In App. B.2, the polarization analysis of the directional radiation of WGMs is used to investigate the preferential field orientation of modes in tunable LCE cavities.

Both measurement approaches demonstrated in this section are suited to investigate the preferential field orientation of WGMs with a TE- or TM-like polarization. To investigate WGMs without a preferential field orientation (as those highlighted in Fig. 2.3), a more sophisticated approach is necessary. To that end, the directional radiation of WGMs under a variation of the temperature of the cavity is compared to expectations based on the far field of such modes calculated using FEM simulations in [40].

Chapter 4

Fabrication of chip-scale tunable photonic building blocks

The present chapter covers the fabrication of tunable photonic building blocks based on liquid crystal elastomers. A comprehensive overview of the fabrication methods used to realize the exemplary tunable photonic building blocks demonstrated in Ch. 5 and Ch. 6 is given.

In Sec. 4.1, the material class of liquid crystal elastomers (LCEs) is introduced. Herein, their chemical composition and mechanical and optical properties as well as possible approaches to manipulate their molecular order are addressed. Actuating chip-scale substrates made from LCE are introduced in Sec. 4.2. After the requirements for such substrates in the context of tunable photonics are discussed, the applied fabrication process is presented. Herein, the substrates are produced using mask-based UV lithography. The molecular order of the substrates is verified by polarizing optical microscopy and their actuation behavior is evaluated using micro-scale markers. In Sec. 4.3, the method of 3D laser printing is introduced and its advantages over conventional 2D lithographic methods are demonstrated using the example of printing rigid polymeric three-dimensional structures onto chip-scale LCE substrates. The quality of the fabricated structures is shortly assessed. Afterwards, the 3D laser printing of tunable micro-scale photonic structures from LCE itself is addressed in Sec. 4.4. The challenges of printing birefringent LCE as well possible approaches to overcome these issues are discussed. The quality of the obtained LCE structures is shortly evaluated. Finally, the applied fabrication methods are assessed and their suitability for a potential future upscaling to larger photonic circuits is evaluated in Sec. 4.5.

Within this chapter, fabrication processes of chip-scale tunable photonic systems in general are presented. However, the illustration of these methods as well as the evaluation of the quality of the fabricated structures is done using the example of WGM-based building blocks in accordance with the experimental results in Ch. 5 and Ch. 6.
Parts of the methods presented in this chapter have been developed in cooperation with Jannis Hessenauer, Lukas Mall, Roman Oberle, Osman Karayel, Stefan Pfleging and Pascal Rietz within the scope of their respective theses [41,62,142,151,158,159] and are published in [37].

4.1 Liquid crystal elastomers as chip-scale actuators

The focus of the present works lays on the realization of tunable photonic building blocks based on liquid crystal elastomers. Herein, the mechanical actuation of the flexible elastomer is used to modulate the configuration of the photonic building blocks and thereby tune at least one of their optical key characteristics.
Within recent years, several tunable photonic systems based on flexible substrates have been realized: By modulating the period of gratings, distributed feedback (DFB) lasers with a tunable emission frequency have been demonstrated [160–163]. Such resonance tuning via a flexible substrate has also been achieved for WGM resonances in both self-assembled polymer droplets [31] and nano membrane-based micro tube cavities [164]. Also, a resonance tuning of the optical response of meta surfaces [165] as well as photonic-crystal nano lasers is feasible [32,166]. Furthermore, more complex and tunable photonic circuits including ring resonators and coupled waveguides have been realized [167]. Beyond the tuning of resonance frequencies, flexible substrates are applied for beam steering and efficiency enhancement of second-harmonic generation in nano-wire arrays [168]. A comprehensive review on photonics employing flexible materials is given by Geiger *et al.* [169].
At the Institute of Applied Physics, flexible substrates have been used to realize both full spectral tunability of so-called split-disk WGM resonators [17] as well as a tunable coupling of several WGM micro lasers [170].

The results mentioned above are typically achieved by applying direct mechanical stress to macroscopic substrates from polydimethylsiloxane (PDMS). Despite the obvious great potential of this approach, it is rather inconvenient regarding a future integration into more complex photonic circuits: The direct application of mechanical stress is a comparably slow process that requires large and complex mechanical tools. Thus, such PDMS-based tunable photonic building blocks can not be fully transferred onto chip scale.

These issues can be overcome by using micro-scale structures made from alternative elastomers with an active actuation behavior under an external stimulus. Within recent years, several novel material classes providing such an actuation behavior have emerged [171]. In the context of photonic building blocks, the class of liquid crystal elastomers is one of the most promising candidates, as they can be operated at ambient conditions, are composed of a single material with a homogeneous refractive index and can react to various external stimuli as heat, illumination and electric/magnetic fields [36, 172, 173]. Furthermore, high-quality structures from LCE on micro scale can be realized employing single- or multi-photon absorption polymerization [174]. Besides various applications in soft robotics [175, 176] and micro robotics [177, 178], micro-scale actuators from LCE have been used in photonics to achieve spectral tuning of WGM resonances [16, 38] and optical gratings with adjustable deflection angles and polarization output [179–181]. Herein, illumination of the LCE has been used as external stimulus.

In the presented work, microscopic substrates from LCE are employed to achieve a tunable coupling of WGM cavities fully on chip scale in Ch. 6. Furthermore, a precise and full spectral tunability of WGMs is realized using resonators entirely made from LCE in Ch. 5. All the proof-of-principle investigations in these chapters as well as the characterization of material properties in the following sections use local heating as external stimulus.

4.1.1 Chemical composition of LCEs

Liquid crystal elastomers were first predicted by de Gennes in 1997 [182] and can be roughly understood as a polymerized version of liquid crystals (LCs) as they are used in commonly known LC displays. Such LCs are liquids that consist of strongly anisotropic molecules called mesogens. The mesogens' anisotropy is usually induced by their strongly calamitic shape, which can lead to a directional molecular order of the mesogens on macroscopic scale. Due to this ordering, LCs show strongly anisotropic optical characteristics that are employed in modern display technology. [183]

A liquid crystal elastomer is composed of LC mesogens that usually share the approximately same spatial orientation and are loosely crosslinked into a polymeric network with high elasticity [36, 184]. The polymeric LCE networks in the presented work have been adapted from [177] and fabricated using an illumination-induced polymerization process of an LC mixture. This mixture consists of at least three constituents that are schematically depicted in Fig. 4.1(a). Both monomer (red) and crosslinker (blue) mainly consist of several benzene rings that determine the strongly anisotropic character of the molecules. These calamitic conformations are the LCE's

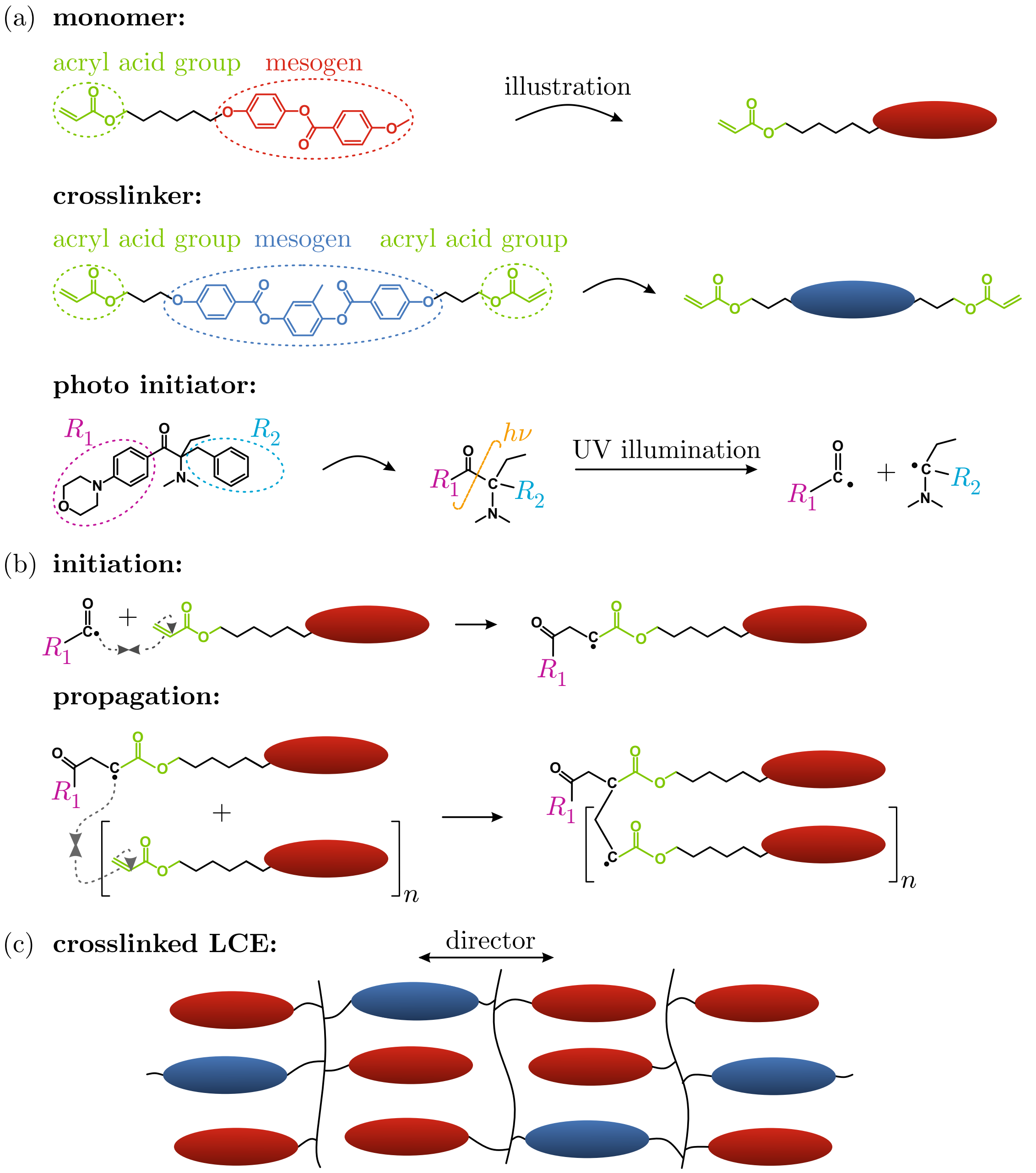

Figure 4.1: In (a), the different constituents of an LCE resist including the production of free radicals due to a fission of the photo initiator under UV illumination are shown. (b) illustrates the radical chain reaction of monomers into an LCE polymer. In (c), a crosslinked LCE polymer consisting of monomer and crosslinker molecules is depicted. All mesogens share the same spatial orientation along the director. Adapted from [142].

mesogens. While in case of the monomer one end of the mesogen is connected to an acryl acid group (green) by a carbon chain, two acryl acid groups are attached to the mesogen of the crosslinker. As these acryl acid groups form the crosslinked backbone of the LCE after polymerization, the ratio of monomer and crosslinker of the mixture is mainly responsible for the degree of crosslinking and therefore the elasticity of the polymerized LCE. The third important molecule is the photo initiator, which is split into two radicals under UV illumination. These radicals initiate a radical chain polymerization of the acryl acid groups as illustrated in Fig. 4.1(b). This chain reaction is usually terminated by a reaction of two radicals.
Figure 4.1(c) represents a crosslinked liquid crystal elastomer with a strong directional order. The calamitic mesogens all share the same spatial orientation along their so-called director and are connected to chains by a polymeric backbone (black). The crosslinker molecules link these single chains to a three-dimensional polymeric network due to their two acryl acid groups. In the following, the unpolymerized mixture is referred to as (LCE) resist. Despite its name, this resist is usually solid at room temperature.

A detailed listing of all used chemicals is given in App. A.1, a more detailed presentation of the underlying chemical processes can be found in Pascal Rietz' Master's thesis [142].

4.1.2 Mechanical and optical properties of LCEs

Both the mechanical as well as optical properties of LCs and LCEs strongly depend on the degree and orientation of the directional order of their mesogens.
The state of perfect directional order along a director (as depicted in Fig. 4.1(c)) is the so-called nematic phase. In case the mesogens carry a non-zero electric/magnetic dipole moment, the orientation of this director can be reversibly altered via the application of electric/magnetic fields [185,186]. Using local heating as external stimulus, the degree of directional order of an LC can be decreased until no preferential orientation of the mesogens is present anymore in the isotropic phase. Including an absorber dye into the LC, the degree of order can also be altered using illumination as an external stimulus. Due to their polymeric backbone, LCE's under heating usually do not transition into an isotropic phase, but into a paranematic phase of decreased but non-vanishing directional order [187].
For the LCE used in the present work, this continuous transition starts at a temperature of $T_{\mathrm{tr}} \approx 35\,°\mathrm{C}$ and goes on beyond temperatures of 100 °C [188]. As soon as the applied stimulus is disabled, the polymeric backbone forces the LCE back into its initial nematic phase, leading to a reversibility of the stimulus-induced change of directional order [36]. The overall extent of this behavior depends on the degree

of polymeric crosslinking of the elastomer network. This degree of crosslinking is controlled by changing the share of crosslinker molecules in the used LCE resist. Microscopic actuators made from LCE have been shown to react to temperature changes within a few milliseconds, allowing for maximum switching frequencies in the order of 1 kHz [177].

The reversible control of the molecular order of the LCE facilitates specific adjustments of their mechanical and optical properties that yield high potential for various applications in tunable photonic elements. These properties are summarized in the following for LCEs in general.

Mechanical properties

LCEs are soft elastomers with Young's moduli in the order of 0.1 MPa to 5 MPa [36]. Under the application of local heating as external stimulus, they show a strongly anisotropic actuation behavior. The decrease of the degree of directional order of the mesogens in combination with the polymeric backbone of the LCE leads to a contraction in the direction parallel to the director as well as an expansion in the perpendicular plane. The magnitude of these effects strongly depends on the applied temperature and has been shown up to a contraction(expansion) of a factor of 400 %(200 %) [189].

While an expansion under thermal treatment is a common property for polymeric materials, LCE is of special interest regarding the application as actuator in photonic building blocks due to its comparably large expansion in plane perpendicular to the director. The potential of this approach is also demonstrated by the temperature-induced radius increase of a WGM resonator entirely made from LCE that is used to reversibly tune the cavity's resonant wavelength in Ch. 5.

The larger temperature-induced contraction of LCE along its director is a property that is not typically found for conventional polymers. Therefore, it opens up a wide field of new applications in photonic building blocks. Especially substrates from LCE can be used to precisely reduce the distance between various photonic elements using local heating as an external stimulus. Such LCE substrates are used in Ch. 6 to realize the tunable evanescent coupling of two WGM cavities.

Optical properties

Due to the strongly anisotropic character of the calamitic mesogens, LCEs are birefringent in their nematic phase. The extraordinary axis is given by the director of the mesogens. For the LCE used in the presented work, the refractive indices as well as their dependency on temperature have been investigated on macroscopic films in [190]: At room temperature, the ordinary(extraordinary) refractive index is

given by $n_\mathrm{o} \approx 1.52 (n_\mathrm{e} \approx 1.68)$. With elevating temperature, both of these refractive indices decrease. As the molecular order reduces towards an isotropic state, also the birefringence itself slightly decreases and the refractive indices approach each other. At a temperature of 180 °C, they have been measured to be $n_\mathrm{o} \approx 1.49$ and $n_\mathrm{e} \approx 1.62$. The non-vanishing mismatch of the two indices also demonstrates the non-isotropic but paranematic state of the LCE even at high temperatures.
The optical properties of LCE come into play, if the LCE itself is used as light-guiding element. Within the context of resonance tuning via the temperature-induced change of the radius of a WGM cavity in Ch. 5, the impact of the changing refractive indices has to be taken into account.

4.1.3 Manipulation of the molecular order of LCEs

As mentioned in Sec. 4.1.2, the fundamental functionality of LCE as an actuator in photonic building blocks depends on the degree of directional order of its mesogens. Without an externally defined preferential orientation, LCs and LCEs form domains of independent director orientation with sizes in the order of 10 µm [167]. Therefore, a directional order of the LCE resist has to be induced by an external definition of a preferential director orientation prior to its polymerization. Usually, this manipulation of molecular order is performed at elevated temperatures with the resist being in its isotropic phase. By then slowly cooling down the resist, it first transitions from the isotropic into a nematic phase. Herein, its mesogens align along the externally pre-defined direction. Cooling further, the temperature passes the resist's melting point and the mesogen alignment is frozen into the solid resist.
Several methods to align the mesogens within the LCE resist using different alignment mechanisms have been established [177, 178, 180, 191–196]. In the following, only the two methods applied within the scope of this work are covered.

Both approaches used in the presented work base on surface-mediated alignment mechanisms. Herein, LCE mesogens which are in direct contact to a macroscopic surface are aligned due to special properties of that surface. Due to a self-ordering of the mesogens [167], this leads to a macroscopic ordered domain with a thickness in the order of 10 µm covering the whole macroscopic alignment surface. By sandwiching the LCE resist between two alignment surfaces with a pre-defined distance of several 10 µm, a homogeneous alignment of all mesogens is feasible [177]. That configuration of LCE resist encapsulated by two surfaces (which are usually carried by glass cover slips) is called a cell and is widely established [177, 193]. Although this approach enables a reliable and homogeneous director alignment, it does limit the overall height of LCE structures to a few 10 µm. In the context of micro-scale photonic elements however, this limitation is usually irrelevant.

The two alignment methods used in this work differ not only by their alignment mechanism, but also by the orientation of the induced alignment: To fabricate WGM resonators from LCE with a director orientation along their axis of rotational symmetry (see Sec. 4.4), a mesogen alignment perpendicular to the plane of the cell is necessary. This is achieved employing silanized glass surfaces. The fabrication of contracting LCE substrates on the other hand requires an in-plane mesogen alignment (also see Sec. 4.2) which is realized using mechanically treated polymer layers.

Initiation of the mesogen alignment using silanized glass surfaces

To realize a mesogen alignment perpendicular to the plane of the resist-filled cell, the surfaces of the cover slips are silanized. Herein, a mixture of long-chain and short-chain silane molecules is attached to the glass surfaces. The short-chain silane 3-(trimethoxysilyl)propyl methacrylate does not only bind to the glass surface, but can also bind to the mesogens of the polymeric network of the LCE within the polymerization process due to its methacrylate group. Thus, it enhances the adhesion of the LCE to the glass surface. The long-chain silane molecules dimethyloctadecyl[3-(trimethoxysilyl)propyl]ammoniumchloride (DMOAP) do not bind to the polymer matrix, but their long carbon chains stand perpendicular on the glass surface. If the concentration of these long-chain silanes is correct, the calamitic LCE mesogens align in between the carbon chains of the silane molecules, creating a macroscopic domain with a director orientation perpendicular to the surface [197]. Prior to the wet-chemical silanization treatment, a thorough cleaning of the glass surfaces of the cover slips is performed.

The silanization process used within the scope of this work has been established in close cooperation with Jannis Hessenauer and Stefan Pfleging [151, 158] as well as Alexander Münchinger at the Institute of Applied Physics and has been partly adapted from [198]. It is partly published in [37]. A detailed listing of all used chemicals as well as process steps and parameters is given in App. A.1 and App. A.2.

Initiation of the mesogen alignment using polymeric orientation layers

To initiate a macroscopic domain with a homogeneous director alignment in plane of the resist-filled cell, polymeric orientation layers with a special mechanical treatment are employed. These polymeric layers are first fabricated onto glass cover slips using a state-of-the-art spin-coating process. Afterwards, a preferential orientation is introduced to these layers. This is done using a so-called rubbing process: The polymeric layers are repeatedly rubbed along a constant direction (the later director of the LCE) using a suitable velvet cloth. This technique is widely established in the context of LC display fabrication [199, 200].

The mechanisms due to which the preferential orientation of the polymeric layers is passed onto the LCE mesogens in contact with that surface is manifold [201]: On the one hand, the polymer chains of the orientation layers are aligned along the rubbing direction. Investigations suggest that the mesogens attach to these aligned polymer chains in a parallel manner [202]. Further, an influence of a possible anisotropy of the charge distribution of these polymer chains is discussed [203]. On the other hand, the rubbing process introduces a directional topology to the polymer layers. If the size of these microscopic grooves is in the order of the dimension of the mesogens, they are expected also to contribute to the alignment of the mesogens [204, 205].
The rubbing-based alignment process used within the scope of this work has been partly adapted from [188, 206] and advanced in close cooperation with Lukas Mall and Pascal Rietz within their respective Master's theses [142, 159]. In close cooperation with Pascal Rietz, a mechanical tool for the automated rubbing of polymeric orientation layers along the lines of [207] has been built. A detailed description of that tool is given in the respective Master's thesis [142]. A detailed listing of all used chemicals as well as process steps and parameters is given in App. A.1 and App. A.4.

4.2 Fabrication of chip-scale substrates from LCE

Micro-scale substrates from LCE enable the precise control of the distance between different photonic elements fully on chip scale under an external stimulus like local heating. Therefore, they are promising candidates as actuators in tunable photonic building blocks. In the following section, first the requirements of such LCE substrates in the context of tunable photonics are addressed. Afterwards, a fabrication process of these substrates using a mask-based UV illumination is covered. The mesogen alignment of the fabricated LCE substrates is verified using polarizing optical microscopy. Finally, the temperature-induced actuation behavior is evaluated based on an automated image processing of micro-scale markers and compared to the requirements derived earlier.

4.2.1 Requirements for actuating substrates in the context of tunable photonics

The fundamental requirement of LCE substrates in the context of tunable photonics is a sufficient actuation mechanism under a moderate temperature change. It obviously depends on the specific use case, what this exactly means. Nevertheless, the consequences of this requirement regarding the performance of an actuating substrate can be estimated in a general manner.

In the following, only the contraction mechanism of the LCE is considered due to several reasons: First, this contraction is the more exotic actuation behavior and therefore opens up various new potential applications that are not feasible using conventional polymers. Furthermore, by decreasing the distance between single photonic elements, potential gaps between them due to the resolution limitation inherent to all (i.e. optical) lithographic methods can be bypassed. Finally, the temperature-induced contraction is the stronger of the two actuation mechanisms, making it more likely to be utilised.
To estimate a sufficient contraction behavior of an LCE substrate, the necessary distance change between single elements is compared to the typical overall dimension of photonic building blocks. Regarding various potential applications of such substrates, e.g., tunable DFB [160–163] or photonic crystal lasers [32, 166] as well as (tunably) coupled WGM cavities [17, 31, 170] (see Sec. 4.1), the distance change between the respective photonic elements needs to be in the order of the wavelength of the employed light. Assuming this light to range from the visible spectral region to the IR c-band ($\lambda = 400\,\mathrm{nm}$ to $1550\,\mathrm{nm}$), this leads to a necessary distance change in the order of $1\,\mu\mathrm{m}$. Compared to the typical dimension of photonic building blocks in the order of $10\,\mu\mathrm{m}$ to $100\,\mu\mathrm{m}$, the LCE substrate needs to provide a contraction of around $1\,\%$ to $10\,\%$. These values are obviously smaller than the maximum achieved contraction factor of around $400\,\%$ [189].
However, these maximum values have been achieved by heating LCE from room temperature above its nematic to isotropic phase transition temperature of (in case of [189]) $T_{\mathrm{ni}} \approx 96\,°\mathrm{C}$. Such large temperature changes are inconvenient regarding future applications as they are hard to realize and significantly limit the switching frequency of tuning mechanisms. Nevertheless, it can be drawn from [189], that also at temperatures significantly lower than T_{ni} the LCE yields a strong contraction behavior. The contraction furthermore depends approximately linear on the temperature in the order of $1\,\%\,\mathrm{K}^{-1}$. This strong temperature dependency demonstrates the great potential of LCE substrates in the context of tunable photonics, as it should be possible to tune the optical characteristics of photonic building blocks by temperature changes of only a few Kelvin.

A second critical factor regarding the application of LCE substrates in photonic building blocks is their planarity. While the modulation of the configuration of such a building block in three dimensions might enable various new applications, usually a controlled modulation within the two-dimensional plane of the substrate is favored. Regarding chip-scale LCE substrates with a thickness of only a few $10\,\mu\mathrm{m}$ as used in the presented work, this planarity is not inherent. This is due to the general softness of the LCE material as well as potential deviations in the LCE's mesogens alignment leading to an out-of-plane actuation behavior. To circumvent these potential issues, the LCE substrates stay attached to the rigid, macroscopic

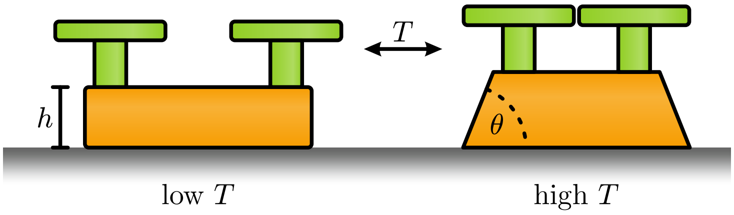

Figure 4.2: Illustration of a contracting LCE substrate (orange) with two WGM resonators (green) at different temperatures. The adhesion to a rigid substrate (gray) limits the contraction of the LCE substrate. As the maximum achievable contraction is expected to be limited by the angle of the substrate at its outer edges θ, an increase of the substrate thickness h should lead to an enhanced contraction of its surface. However, h is limited to a few 10 µm by the fabrication process. Using micro-scale substrates, a larger relative actuation between two photonic elements is feasible compared to macroscopic substrates. Adapted from [206].

surface of the glass cover slip after fabrication. This configuration however strongly limits the possible contraction of the substrate [206], as illustrated in Fig. 4.2 for an exemplary substrate with two WGM resonators. The maximum achievable contraction is expected to be limited by the angle θ at the outer edge of the substrates. Hence, a larger contraction of the substrate's surface should be feasible for a larger thickness h. This thickness is however limited to a few 10 µm by the reach of the surface-mediated mesogen alignment (see Sec. 4.1.3). To still realize a sufficient contraction between two photonic elements, micro-scale substrates are of advantage compared to macroscopic LCE substrates.
Although LCE yields a sufficiently strong actuation behavior in general, their contraction under the adhesion to a rigid surface has to be evaluated in detail. This is done in Sec. 4.2.4 based on an automated image processing of micro-scale markers.

4.2.2 Mask-based UV lithography of chip-scale substrates from LCE

Parts of the fabrication process of chip-scale LCE substrates have been adapted from [188, 198, 206] and have been advanced in close cooperation with Jannis Hessenauer, Lukas Mall, Osman Karayel and Pascal Rietz within their respective Master's theses [62, 142, 158, 159]. A listing of all process steps is given in App. A.4, a more detailed illustration of these steps can be found in [142].

To realize a mask-based UV lithography of chip-scale substrates from LCE, the resist (also see Sec. 4.1.1) is sandwiched into a cell between two cover slips. The cover slips are coated with polymeric orientation layers. The distance between these cover slips defines the later thickness of the substrates and is ensured by self-adhesive spacer foils at the outer edges of the cell. The cell is covered by a mask and il-

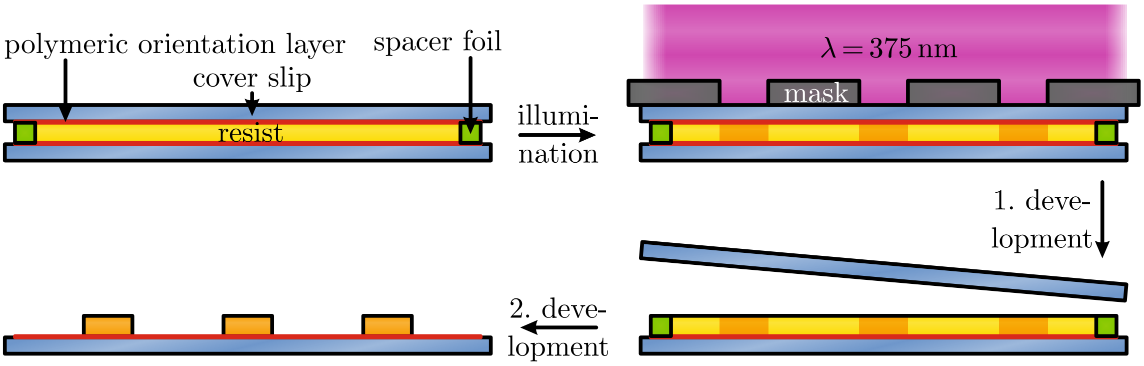

Figure 4.3: Illustration of the fabrication of micro-scale LCE substrates. The resist (yellow) is sandwiched between two cover slips (blue) with polymeric orientation layers (red). Via these layers, a surface-mediated alignment of the mesogens along a common director in plane of the cell is realized. The distance between the cover slips is defined by self-adhesive spacer foil (green) at the outer edges of the cell. The cell is illuminated at 375 nm using a custom-built UV lamp. Due to a custom-built mask, only small parts of the resist are polymerized into LCE substrates (orange). After illumination, the cell is opened in a first development step in deionized water. Via a second development in an organic solvent, the unpolymerized LCE resist is dissolved. The spacers are mechanically removed.

luminated at 375 nm wavelength using a custom-built UV lamp. Due to the used mask, substrates with radii of 150 µm or 250 µm and distances of several millimeter arranged in a two-dimensional grid are polymerized. (Without mask, macroscopic LCE substrates can be fabricated [159].) After polymerization, the cell is opened in a first development step in deionized water which is dissolving one of the polymeric alignment layers. The unpolymerized LCE resist is removed via a second development in an organic solvent. The fabrication process is illustrated in Fig. 4.3.

4.2.3 Verification of the molecular alignment using polarizing optical microscopy

The most important property for a strong actuation behavior of the LCE substrates is a sufficient mesogen alignment. However, various factors within the fabrication of these substrates can potentially diminish the degree of alignment. Especially surface-mediated alignment mechanisms as the polymeric orientation layers used here are susceptible to external influences like shear forces due to incautious handling. Thus, a qualitative check of the general degree of alignment is performed prior to the elaborate analysis of the actuation behavior of the LCE substrates presented in Sec. 4.2.4. This is done using polarizing optical microscopy (POM).

Within polarizing optical microscopy, a transparent sample of interest is investigated between two orthogonal polarizers using a transmitting-light microscope. If the polarization of the light is not altered while passing the sample, it is blocked by the second polarizer and the sample appears dark. If an LCE substrate with an intended mesogen alignment in the substrate's plane is investigated via POM, the expected image depends on the relative angle α between the first polarizer and the LCE's director: If the director is parallel/vertical ($\alpha = 0°/\alpha = 90°$) to the first polarizer, the light passing the substrate is only affected by the extraordinary/ordinary refractive index. Hence, the linear polarization of the light is not altered and the sample appears dark. If the director orientation differs from a parallel/vertical direction, the polarization of the transmitted light is rotated due to the birefringence of the LCE and the sample appears bright. The transmitted intensity changes according to $\sin^2(2\alpha)$ and is therefore maximal for a $\alpha = 45°$. [201, 208].
As a simple check of the LCE substrates' mesogen alignment, their transmitted intensity in POM images is compared for the cases $\alpha = 0°$ and $\alpha = 45°$. The larger the difference of the detected intensities is, the better the LCE substrates are aligned. To perform such investigations, two different approaches have been chosen: On the one hand, a commercial polarizing optical microscope owned by the research group of Prof. Dr. Martin Wegener at the Institute of Applied Physics has been used for a spatially resolved detection of the intensity transmitted through single LCE substrates. On the other hand, a custom-built POM setup has been used to investigate several substrates at once and thereby evaluate the reliability of the applied alignment method. This setup has been built in close cooperation with Pascal Rietz within his Master's thesis and is described therein in further detail [142].

To evaluate the mesogen alignment of fabricated LCE substrates as well as the reliability of the applied production process, an investigation of three different batches of LCE substrates based on POM images has been performed. In Fig. 4.4, respective POM images of these substrate are depicted. The substrates in Fig. 4.4(a) have been fabricated between unrubbed polymeric orientation layers and can therefore be understood as reference samples. At first glance, no intensity difference between the images for $\alpha = 0°$ (left) and $\alpha = 45°$ (right) is visible for these substrates. This also applies to the high-resolution image of a single substrate (inset). Therein, the expected formation of domains with independent director orientation on the scale of 10 µm [167] is evident from typical nematic schlieren textures [197]. These textures get approximately inverted under the polarizer rotation of 45°. These findings confirm the expected lack of an overall preferential mesogen orientation in the case of unrubbed polymeric layers.
Figure 4.4(b) depicts respective POM images of substrates fabricated with rubbed polymeric orientation layers. The rubbing direction is indicated by red arrows. Although the images in case of $\alpha = 45°$ have been detected with a relative exposure

(a) polymeric orientation layers **not rubbed**

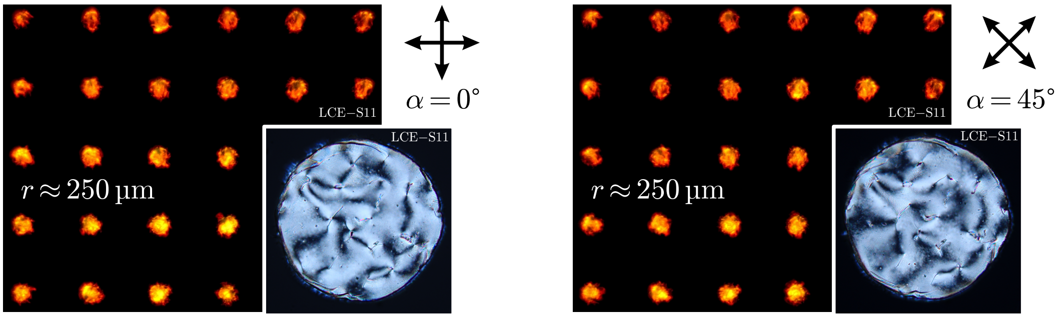

(b) polymeric orientation layers **rubbed at 0°**

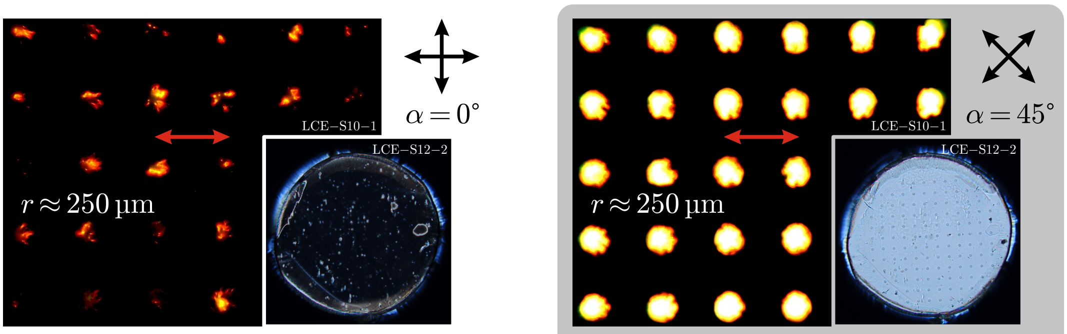

(c) polymeric orientation layer **rubbed at 0° but partly missing**

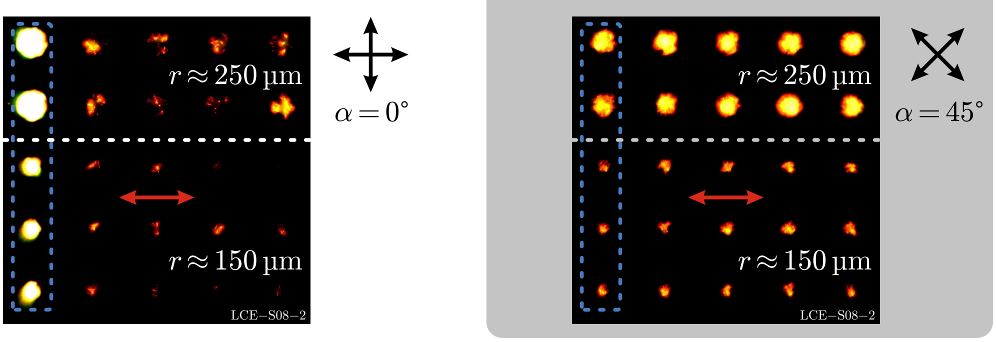

Figure 4.4: Verification of the mesogen alignment using POM. For three different samples, POM images of arrays of micro-scale substrates of radius r with polarizers (black arrows) at 0°/90° (left) and −45°/45° (right) relative to the intended director orientation (red arrow) are depicted. In (a) and (b), also single substrates with larger magnification are depicted as inset. Images with gray background have been detected with a relative exposure time of 33 %. The difference in brightness of the substrates is an indicator for the degree of mesogen alignment. In (a), substrates fabricated with unrubbed orientation layers are depicted. No difference in brightness is apparent. In (b), aligned substrates are shown: The brightness of all substrates is significantly larger between diagonal polarizers. The sample in (c) is comparable to that in (b), except that the substrates come in different sizes. For some (blue rectangles), a polymeric orientation layer is missing due to fabrication difficulties. These substrates appear brighter on the left-hand side. Adapted from [142].

time of only 33 % (indicated by the gray background), a significant higher intensity has been found. Except for small deviations due to surface imperfections, this also holds for the substrate in the high-resolution image. These results proofs the generation of preferential mesogen orientation over the whole batch of substrates induced by rubbing of the polymeric orientation layers. (The two-dimensional grid of structures visible in the high-resolution POM image in Fig. 4.4(b) is formed by micro-scale markers, also see Sec. 4.2.4.)
For the substrates depicted in Fig. 4.4(c), the same rubbing treatment as in (b) has been applied. These substrates again show significant differences in their intensities between $\alpha = 0°$ and $\alpha = 45°$ independent of their differing radii. This does however not hold for the most left-hand column of substrates (blue rectangles). For these substrates, one of the polymeric orientation layers has been missing due to fabrication difficulties. This finding demonstrates both the importance of both orientation layers as well as the utility of POM images for an easy and quick identification of insufficiently aligned LCE substrates.

In summary, most LCE substrates sandwiched between two intact and rubbed polymeric orientation layers show POM images with strong intensity differences as presented in Fig. 4.4(b). This proofs a successful and reliable mesogen alignment of the LCE along a common director. To be able to fully assess the potential of these substrates as micro actuators in photonic building blocks, their actuation behavior is precisely evaluated in the following section.

4.2.4 Evaluation of the actuation of LCE substrates using automated image processing of micro-scale markers

The temperature-induced actuation behavior of LCE substrates is evaluated using an automated processing of bright-field light microscopy images of two-dimensional arrays of cylindrical micro-scale markers on these substrates. This method has been developed in close cooperation with Pascal Rietz within his Master's thesis and is explained in detail therein [142]. It is published in [37].

The evaluation method introduced here bases on a comparison of optical micrographs of an LCE substrate at different temperatures. Herein, the contraction of the substrate along its director and the expansion in the perpendicular direction is determined simultaneously. A spatial resolution of contraction and expansion within a single substrate is of interest to estimate the homogeneity of the substrate's actuation behavior. To meet this requirement, a two-dimensional array of polymeric markers parallel/perpendicular to the alignment director is fabricated onto the respective substrate. (The fabrication of these markers is done using 3D laser printing,

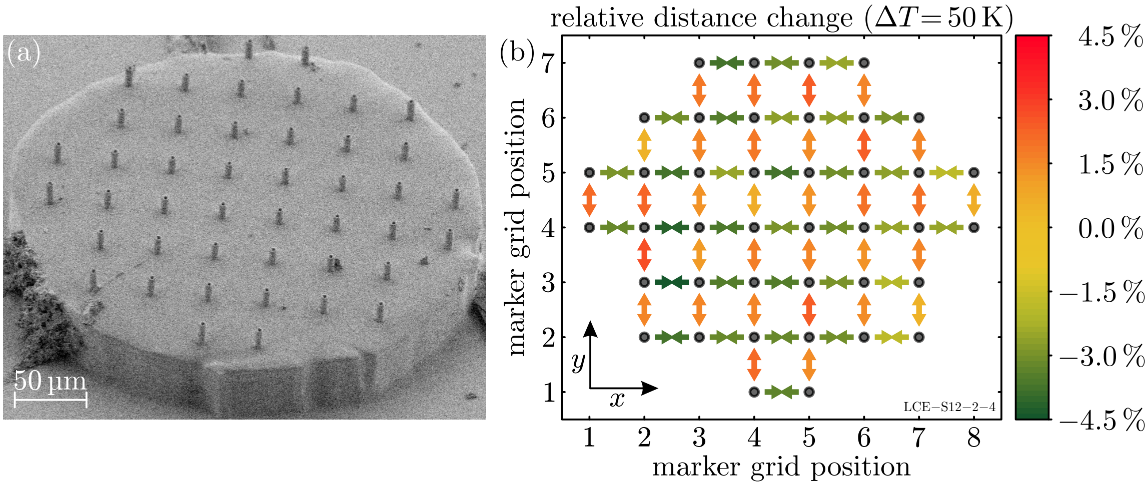

Figure 4.5: Evaluation of the actuation of LCE substrates based on micro-scale markers. In (a), an SEM micrograph of an LCE substrate is depicted. The two-dimensional grid of cylindrical markers with a next-neighbor distance of 40 µm has been fabricated using 3D laser printing. The relative distance change between the single markers (dark circles) on an LCE substrate with a mesogen alignment along the x-axis under a temperature change of $\Delta T = 50\,\mathrm{K}$ has been determined via an automated processing of microscopic images and is depicted in (b) by color-coded arrows. Despite a slightly inhomogeneous actuation behavior, the entire substrate contracts along its director and expands in the perpendicular direction. Local contractions larger than 4 % and expansions of around 3 % are evident. Reprinted with permission from [37] © Optica Publishing Group.

for more information see Sec. 4.3.) In the example depicted in the SEM micrograph in Fig. 4.5(a), cylindrical markers with an outer radius of 3 µm and a next-neighbor distance of 40 µm are used. This choice of the next-neighbor distance is adapted to the use case of tunably coupled WGM resonators with center-to-center distances in the same order. By using smaller markers with shorter distances, the homogeneity of the actuation behavior can be investigated in further detail. Using state-of-the-art cross-correlation methods, these distance changes should be resolvable down to the order of 1 nm [209]. Under a thermal actuation of the LCE, this is however not feasible due to the general change of the investigation configuration.

To evaluate the actuation behavior of LCE substrates fabricated in this work, a *MATLAB* routine using Hough transformations [210] has been used to detect the position of each marker and calculate the distance between all next-neighbor marker pairs for each temperature step. Based thereon, the temperature-dependent contraction and expansion has been derived. Figure 4.5(b) depicts an exemplary evaluation of the actuation of an LCE substrate with mesogen alignment along the x-axis under heating from room temperature by $\Delta T = 50\,\mathrm{K}$. The relative distance changes of next-neighbor pairs of markers (dark circles) are represented by color-coded arrows.

Considering the whole substrate, a contraction of a few percent along the x-axis as well as a sightly smaller expansion in the y-direction are obvious. These findings confirm an anisotropic actuation behavior due to the LCE's preferential mesogen alignment. Regarding the single next-neighbor distances, a slight inhomogeneity of the actuation is evident. Nevertheless, all distances along the x-direction decrease under heating while all distances along the y-axis increase. The maximum relative local contraction is larger than 4.0(5) % and the maximum local expansion is around 3.0(5) %. Although other substrates show slightly different actuations, a contraction along the director orientation and a perpendicular expansion on a scale comparable to the one presented here is found for most substrates with a preferential mesogen orientation. For substrates fabricated using unrubbed orientation layers (see Fig. 4.4(a)), an arbitrary actuation behavior is found [142].

The presented method is a useful approach to evaluate the actuation behavior of chip-scale LCE substrates. While in the present work only large distances in the order of 10 µm have been investigated, the scale on which an actuation is resolved can be controlled via the next-neighbor distance of the markers. In the more general context of configuration modulation in tunable photonic building blocks, this method could be applied to any kind of micro-scale actuator to estimate the feasibility of potential applications.

To assess the potential of chip-scale LCE substrates as actuators in photonic building blocks, the achieved contraction of more than 4 % is compared to the requirements derived in Sec. 4.2.1. Therein, a necessary actuation in the order of 1 % to 10 % has been found. Hence, the LCE substrates presented in this section are not generally suited for all applications of tunable photonic elements. In the case of tunably coupled WGM cavities as presented in Ch. 6, this issue is bypassed by optimizing the fabrication process of the cavities themselves (see Sec. 4.3.3). By minimizing the initial inter-cavity gap, the required contraction of the substrates is lowered to around 2 %. Hence, a large share of fabricated cavity pairs on LCE substrates can successfully be coupled due to a decrease of their inter-cavity distance.
Regarding the entirety of possible applications in tunable photonics, the actuation of the substrates needs to be further enhanced. This could on one hand be achieved by optimizing the mesogen alignment by either an improvement of the used alignment method based on polymeric orientation layers, or via the application of an alternative alignment approach [194,196]. On the other hand, a change of the share of crosslinker molecules in the LCE resist might induce an enhanced actuation behavior [189]. Furthermore, an increase of the substrate height should lead to an enhanced actuation (see Fig. 4.2), if the degree of mesogen alignment is preserved. This might be feasible using not surface-mediated alignment mechanisms, but others as static electric [196] or magnetic fields [211–213].

4.3 3D laser printing of rigid elements on chip-scale LCE substrates

The results presented in Ch. 5 and Ch. 6 of this work have been achieved using samples fabricated by so-called 3D laser printing (3DLP). 3DLP is a well-established method for the fabrication of three-dimensional polymeric structures on micro and nano scale. In the following, the advantages of 3DLP over conventional 2D lithographic methods, especially in the context of tunable photonic building blocks, is shortly summarized. Afterwards, the 3DLP working principle is introduced using the example of printing rigid polymeric structures on LCE substrates. Finally, the quality of these structures is evaluated in the context of photonic applications.

4.3.1 Advantages of 3D laser printing over 2D lithographic methods

Most modern photonic systems are fabricated from rigid materials using electron-beam lithography [10, 29, 30, 137]. This method offers a high resolution (especially compared to optical methods) as well as a high flexibility due to its mask-less approach. Nevertheless, a high conductivity of the used substrate is indispensable to facilitate an efficient acceleration of the electrons. This requirement strongly limits the applicable configurations and materials, especially in the context of photonic building blocks based on flexible materials. For instance the fabrication of rigid structures on flexible elastomer substrates is not feasible.
An alternative approach to overcome some of these issues is given by deep-UV lithography, which is also established in the production of photonic building blocks [33]. While deep-UV lithography does not require a conducting substrate and is therefore applicable to a wider range of materials, it is also mask-based and therefore less flexible than electron-beam lithography. Although the fabrication of rigid structures on flexible substrates is possible using deep-UV lithography, such approaches typically deliver insufficient results due to the flexibility of the substrate leading to a weak mechanical contact between mask and sample [159].
Furthermore, both these established processes are only two-dimensional. Hence, free-standing structures as disk-shaped WGM cavities on pedestals have to be fabricated employing complex and time-consuming multi-step processes [10,29,30,33,137]. Furthermore, three-dimensional structures from a single material are typically not feasible using these approaches.

To meet all the requirements mentioned above, 3D laser printing comes into play. This method enables the 3D printing of quasi-arbitrary geometries from various polymeric materials with a resolution on nano scale [214]. Therefore, also com-

plex structures can be produced from single material in just one fabrication step. Furthermore, there are close to no requirements regarding the used substrate material [17, 35, 37, 170, 214]. Additionally, 3DLP inherits a high flexibility, as the shape of the printed structure only depends on the trajectory of the used laser focus and can therefore be altered in situ. In consequence, 3DLP is the ideal method for applications in the sense of rapid prototyping. In earlier years, the printing speed of this serial method was its major drawback. However, this issue has been strongly tackled within recent years, leading to significantly enhanced printing speeds [215, 216].
In summary, 3DLP is a well-suited fabrication approach to realize complex, three-dimensional photonic structures including different and exotic material types in a rapid-prototyping approach. Therefore, this method is applied to fabricate rigid photonic structures on LCE substrates, as well as photonic elements made from LCE themselves. In the following, a short overview of the application of 3DLP on these configurations is presented.

4.3.2 3D laser printing on LCE substrates

3DLP is a well established method that has been used in recent years to fabricate WGM cavities [17, 35, 37, 170] as well as various other micro-scale photonic elements [217–222]. Therefore, a comprehensive discussion of the working principle of this fabrication process is spared here but can be found elsewhere [214, 223]. In the following, only the use case of printing rigid structures onto chip-scale LCE substrates is covered in detail.
Parts of the presented modifications of the 3DLP process have been partly adapted from [39, 198] and have been advanced in close cooperation with Jannis Hessenauer, Roman Oberle, Osman Karayel and Pascal Rietz within their respective theses [41, 62, 142, 158].

3DLP is based on the principle of polymerization of a transparent resist due to multi-photon absorption. Within this absorption process, a radical chain polymerization of the resist's monomers into a crosslinked polymer network is initiated. The probability of a multi-photon absorption depends on the light's intensity to the power of the number of simultaneously contributing photons. Hence, very high photon densities need to be generated. This is done by using an fs-pulsed laser source and tightly focusing its light into the resist via a microscope objective. Within the focal spot, a spheroidical volume element, the so-called voxel, is polymerized. By a relative displacement of sample and laser beam, this voxel can follow a pre-defined trajectory through the resist and thereby create nearly arbitrary three-dimensional structures in a serial manner. The leftover unpolymerized resist is then removed using an organic solvent. Due to the dependency of the polymerization probability

on at least the square of the intensity in case of a two-photon absorption, the resolution is significantly increased compared to a single-photon polymerization process, especially along the optical axis of the objective. [214, 223]
To fabricate the samples in this work, a commercially available 3DLP system (*Photonic Professional GT*, Nanoscribe GmbH & Co. KG) is used. Therein, an fs-pulsed, frequency-doubled fiber laser (*FemtoFiber pro*, TOPTICA Photonics AG) with a center wavelength of 780 nm, a pulse width < 100 fs and a repetition rate of 80 MHz is integrated. The laser's light is focused into the resist using a 63× microscope objective with a numerical aperture of 1.4. The relative displacement between sample and microscope objective perpendicular to the optical axis is realized by two galvanometer-driven mirrors which deflect the beam before entering the objective. Furthermore, the sample can be moved along the optical axis using a piezo stage. Using this system, typical voxel sizes are in the order of 400 nm in lateral and 1 µm in axial direction.

To print rigid polymeric elements onto an LCE substrate, the conventional 3DLP configuration is inverted [17, 39, 170]. The rigid structures are printed upside down to prevent the laser beam from passing the LCE substrate. This is necessary as the laser beam would get distorted due to the birefringence as well as possible surface imperfections of the substrate. As a resist, the commercially available *IP-S* (Nanoscribe GmbH & Co. KG) is used. This resist is sandwiched between the cover slip to which the LCE substrate is attached and a second cover slip. Additionally, immersion oil is used to ensure an index matching of objective, oil and lower cover slip. Following this approach, again nearly arbitrary structures can be structured onto LCE substrates by inverting their pre-defined trajectory. This inverted configuration is illustrated in Fig. 4.6 using the example of printing WGM cavities.
When printing rigid structures onto an LCE substrate, several new challenges arise. Compared to a conventional cover slip, the LCE substrates are expected to have a less planar surface. This is also apparent from the SEM micrograph in Fig. 4.5(a) under close inspection. Furthermore, an overall tilt of the LCE substrate with respect to the 3DLP system is possible. These issues can cause the automated interface finder of the 3DLP system that bases on a refraction at the index discontinuity between resist and substrate to generate erroneous results. This might lead to the printed structures to be insufficiently connected to the substrate. To counteract this issue, the interface finder can be deactivated and the pre-defined trajectory of the printed structures chosen to reach sufficiently deep into the LCE substrate and therefore compensate for any possible surface imperfections or overall substrate tilts. The necessary depth of these trajectories into the substrate mainly depends on the overall size of the structure that is to be printed at once. While for a WGM resonator pair with a center-to-center distance of around 50 µm (also see Fig. 4.7) a depth of 1 µm to 2 µm is sufficient, a depth in the order of 10 µm is necessary for a

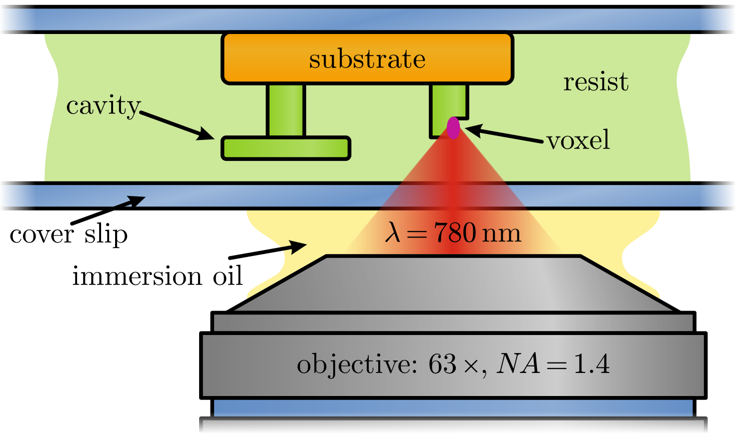

Figure 4.6: Illustration of the inverted 3DLP printing of rigid elements on LCE substrates. Light (red) from a pulsed laser centered at 780 nm is focused into the resist (light green) using a 63× microscope objective (gray) with a numerical aperture of 1.4. In the focal point, a small spheroidical volume element (the voxel, violet) is polymerized via multi-photon absorption. By continuously moving the focal spot through the resist, the rigid elements as WGM cavities (green) are printed onto the substrate (orange) that is attached to the upper cover slip (blue). To prevent the laser light from passing the substrate, the conventional printing configuration is inverted and the cavities are printed upside down. A second cover slip is used to sandwich the resist. Immersion oil (yellow) is used for index matching.

marker array as depicted in Fig. 4.5(a). This of course increases the overall printing time of the structure. Nevertheless, both a pair of WGM cavities and a marker array can be printed in well under one hour.
When the laser spot is focused into the substrate to ensure a sufficient adhesion of the later structure, heat is dissipated due to the LCE's material-intrinsic absorption. This can lead to micro-scale explosion and thus unintended deformations of the substrate as well as the rigid elements. To prevent this, printing parameters of such structures have to be thoroughly engineered.

Regarding the printing of tunably coupled WGM cavities, the inter-cavity distance of the resonators has to be optimized. This is due to the limited contraction behavior of the LCE substrates, also see Sec. 4.2.4.
The minimum achievable inter-cavity distance is limited by the resolution of the 3DLP process. If two structures are printed with a distance below a certain threshold, the so-called proximity effect causes an unintended polymerization of material in between the two structures [214, 223]. If furthermore printed structures still contain insufficiently crosslinked monomers after polymerization, these monomers are washed out during the development process leading to an overall shrinkage of the

printed structures and therefore an increase of their distance. This shrinkage can however be minimized via an adjustment of the 3DLP parameters and is distinctively small for the used resist IP-S [224]. Using cover slips as substrates, a minimum inter-cavity distance of around 1 µm has been achieved [41].
Another possible issue of reversed nature is based on the swelling of the structures within the development process due to a temporary absorption of organic solvent. This swelling increases the disks' radii and can therefore lead to a mechanical contact of formerly unconnected disks. After the development process, the structures are dried and the radii decrease. But the adhesive forces between the disks can lead to the overall cavities to get tilted and remain in mechanical contact. This effect is especially common on LCE substrates, as the flexibility of the elastomer eases a tilting of the overall cavities. Under consideration of all these influences, the resolution of 3DLP of free-standing structures is typically limited at around 2 µm [62, 142].

In App. A.3 and App. A.4, additional information regarding the fabrication of chip-scale LCE substrates and the 3D laser printing onto such substrates is given. More details on these fabrication processes can also be found in [37, 62, 142].

4.3.3 Evaluation of the obtained quality of structures in the context of photonic applications

In the following, the quality of rigid structures fabricated by 3D laser printing on LCE substrates as introduced in the previous section is shortly evaluated in the context of photonic applications. Herein, two different aspects are of major interest: the accordance of the printed structures with their intended geometrical shape as well as the surface roughness as this could potentially introduce optical losses.

A deviation of the shape of the printed structures can be induced by several different influences. Some of these influences, namely closed gaps between structures in close proximity as well as shrinkage and swelling behaviors have already been discussed. Furthermore, an insufficient adhesion to the substrate can lead to single parts of the printed structures to be missing after the development process. If the amount of energy deposited in the resist is too small, it can induce additional issues as mechanical instabilities and therefore unintended deformations. If the amount of deposited energy is too high, micro-scale explosions of the resist can again introduce deformations. This is especially crucial in close proximity of the substrate, since the LCE has a higher material-intrinsic absorption than the resist.
Nevertheless, all critical influences on the geometrical shape of a printed photonic building block can be brought under control via a thorough engineering of the printing parameters of the 3DLP process. Figure 4.7 exemplarily depicts such a photonic

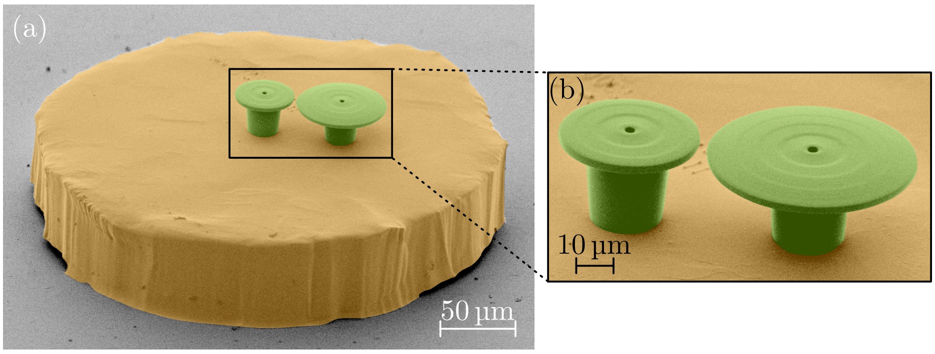

Figure 4.7: SEM micrograph of an LCE substrate with a radius of 150 µm and two WGM cavities. The size-mismatched cavities with radii of 20 µm and 30 µm have been structured using 3DLP. The cavities do not show any obvious deviation from their intended geometrical shape. The inter-cavity distance is in the order of 2 µm. The magnitude of the cavities' surface roughness is below the resolution of the depicted micrographs. Reprinted with permission from [225] © Optica Publishing Group.

system consisting of two disk-shaped WGM cavities. For both cavities, no deviation from their intended rotationally symmetric disk shape is visible. Furthermore, both cavities are tightly connected to the substrate, show no overall tilt and an inter-cavity distance of around 2 µm. Structures with such quality can be reliably fabricated using the approach presented in Sec. 4.3.2 as well as suitable printing parameters. The reliability of this process is also evident from the SEM micrograph in Fig. 4.5(a), where none of the 44 markers that have been produced in a serial manner is missing or shows any obvious deviation from its intended geometrical shape.

The second crucial quality aspect of the fabricated structures is their surface roughness, that could introduce optical losses to light guided inside the structures. This surface roughness is estimated from the quality factor of WGM cavities structured on LCE substrates. This is reasonable, as a potential surface roughness leads to a scattering of light guided within the cavity and therefore a reduction of its quality factor (see Sec. 2.1). In [142], quality factors of WGM cavities printed on LCE substrates of up to 7×10^4 have been demonstrated. These quality factors are in the order of other 3D laser printed WGM cavities [39, 41, 158] as well as other polymeric WGM resonators in general [33, 137, 170] and indicate a strong temporal confinement of light within the regarding cavities. Furthermore, this quality factor is in the order of the absorption limit of the regarding cavities (see Sec. 2.1) estimated from the absorption coefficient of IP-S determined in [52, 53]. Hence, the optical losses introduced by surface roughness are comparable to or smaller than those due to material-intrinsic absorption and are therefore not a limiting factor. This indicates that the surfaces of the printed structures are sufficiently smooth to realize high-quality photonic elements.

In summary, the shape quality as well as the surface roughness of the structures 3D laser printed onto LCE substrates following the approach presented in this section is sufficient for a wide field of photonic applications. These applications include the realization of tunably coupled WGM cavities as presented in Ch. 6 of this work.

4.4 3D laser printing of micro-scale photonic elements from LCE

In the following section, the 3D laser printing of micro-scale photonic structures entirely made from liquid crystal elastomer is introduced. At first, the challenges of printing from an LCE resist are addressed. Thereafter, a route to bypass these issues and thus optimize the quality of printed LCE structures is presented. Finally, the quality of the fabricated LCE structures is evaluated in the context of tunable photonic building blocks through the example of spectrally tunable whispering gallery resonators (compare Ch. 5). As such WGM cavities require a strong mesogen alignment as well as a good overall shape and surface quality, the insights taken from this use case can be transferred to the general fabrication of photonic elements from LCE.

Parts of the advancements of the fabrication methods presented in this section base on [16, 38] and have been developed in close cooperation with Jannis Hessenauer and Stefan Pfleging within their respective theses [151, 158] as well as Alexander Münchinger at the Institute of Applied Physics and are published in [37].

4.4.1 Optimization of the printing quality in birefringent photoresists

The requirements for high-quality 3D laser printed photonic elements from LCE can be divided into three main aspects: a good accordance of the printed structure with its intended geometrical shape, smooth surfaces and a sufficiently strong mesogen alignment along the intended director orientation. Within this section, the intended mesogen orientation is chosen to be perpendicular to the substrate on which the LCE structures are printed. (Choosing a different orientation direction would however not change the key aspects and conclusions of the following discussion.) Such an alignment of the LCE resist is initiated by silanized glass surfaces, as introduced in Sec. 4.1.3. To enhance this surface-mediated alignment mechanism, the resist is again sandwiched in a cell between two silanized cover slips (compare Fig. 4.3).

However, a conventional 3D laser printing of LCE structures within such a cell leads to unsatisfactory results. Both the quality of the geometrical shape of such structures as well as their degree of mesogen alignment is insufficient for any photonic application. This has been shown in [158] using bright-field light as well as POM images and is mainly attributed to the low resolution of the 3DLP process due to the solid phase of the LCE resist at room temperature. Therefore, the melting point of the LCE resist has been lowered below room temperature by adding a eutectic nematic liquid crystal host material (*E7*, SYNTHON Chemicals GmbH & Co. KG) in line with [195, 226]. This adjustment of the resist's composition also promotes its mesogen alignment, as the mesogens of the eutectic host material are easily aligned by the silanized glass surfaces. Therefore, both requirements stated above can be met using this alternative composition of the LCE resist.

The mesogens of the eutectic nematic host are not crosslinked into the network while polymerization due to their missing reactive group. Hence, they are washed out in the wet-chemical development process and the printed structures undergo a significant shrinkage that needs to be taken into account.
The nematic host material increases the birefringence of the resist from an maximum possible index difference of $\Delta n = 0.15$ to around $\Delta n = 0.18$ [37, 188, 227–229]. In combination with the promoted mesogen alignment, this enhanced birefringence introduces a new problem into the process of 3DLP. Due to the high numerical aperture of the used microscope objective, a significant part of the fs-pulsed laser light travels along a direction notably tilted with respect to the optical axis of the objective. As this axis corresponds to the extraordinary axis of the resist, its birefringence splits the laser light into two separate foci and therefore induces a simultaneous polymerization of two voxels. This is clearly unwanted in the context of printing high-quality polymeric structures.

To further understand the impact of this issue, numerical calculations have been performed by Dominik Beutel at the Institute of Theoretical Solid State Physics. Within these calculations, the objective lens, the immersion oil, the glass cover slip, and the birefringent resist in form of an infinite half space have been considered. The extraordinary axis of the resist has been supposed to be aligned with that of the objective which has been chosen to be the z-axis. The laser light entering the objective lens has been assumed to be a Gaussian beam with a width of 5 mm and circular polarization. The field distribution behind the objective lens has been calculated using the Richards-Wolf method [230]. Afterwards, the field propagation through the layer stack has been modeled using the 4-by-4 matrix method [231]. These calculations including details on the computational methods as well as robustness tests are published in [37].

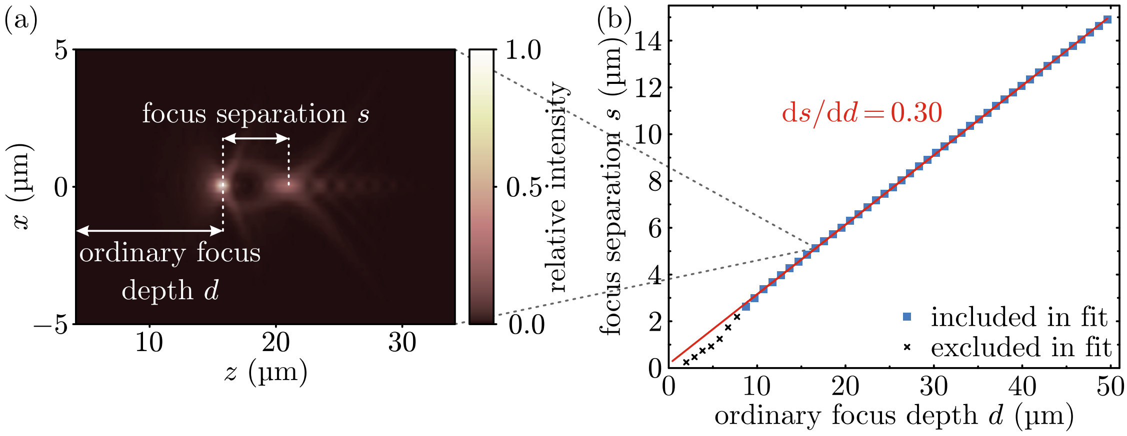

Figure 4.8: Calculated separation of the 3DLP focus in a birefringent resist using rotational polarization. (a) The intensity distribution in the xz-plane of the birefringent resist in case of an ordinary focus depth of $d = 17\,\mu\text{m}$ is depicted. A separation into two foci with a distance $s \approx 5\,\mu\text{m}$ of several micrometer along the z-direction is found. (b) The focus separation s is computed by simultaneously applying two 2D-Gaussian fits and depicted versus the ordinary focus depth d. A linear dependency over the whole investigated range is evident. The small deviations from this linear trend for $d < 9\,\mu\text{m}$ are due to a significant spatial overlap of the two foci, which hinders a reliable application of the Gaussian fits. For $d \geq 9\,\mu\text{m}$, the linear fit yields a slope of 0.30. Reprinted with permission from [37] © Optica Publishing Group.

To estimate the extent of the focus separation, the intensity distribution in the xz-plane of the birefringent resist has been calculated for 50 different depths of the ordinary focus d reaching from 1 µm to 50 µm. Due to the rotational symmetry of the system, the xz-plane contains full information of the position of the focal spots. In Fig. 4.8(a), the intensity distribution with an ordinary focus depth of $d = 17\,\mu\text{m}$ is exemplarily depicted. A clear separation of the two foci by several micrometer along the z-direction is found.

The separation s of the ordinary and extraordinary foci is computed by simultaneously applying two 2D-Gaussian fits to the intensity distribution. This separation is depicted in Fig. 4.8(b) versus the ordinary focus depth d. A linear dependency is clearly evident. For $d < 9\,\mu\text{m}$, the data slightly deviates from this linear trend. This deviation is attributed to a significant spatial overlap of the two foci, which hinders the reliable application of the two separate Gaussian fits. For $d \geq 9\,\mu\text{m}$, a slope of the linear dependency of the focus separation of 0.30 is found. Comparing this slope to the typical voxel size in z-direction in the order of 1 µm, a significant shape distortion of the voxel/separation into two independent voxels is expected for an ordinary focus depth larger than very few micrometers.

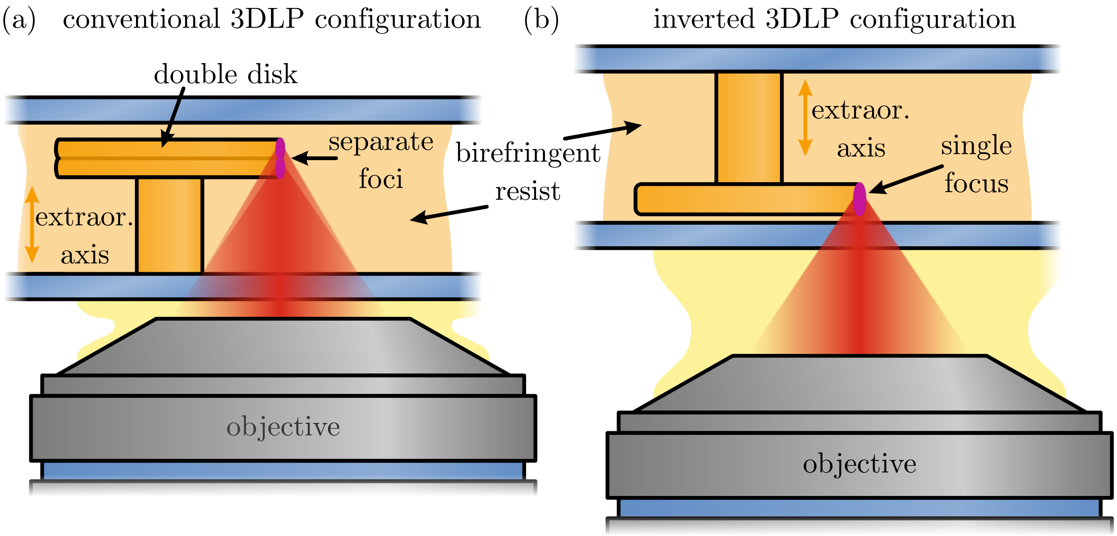

Figure 4.9: Illustration of 3D laser printing in birefringent resists between two silanized cover slips (also compare Fig. 4.6). The extraordinary axis of the resist is indicated by an orange arrow. (a) Due to the high numerical aperture of the used objective, the birefringence of the resist splits the light of the fs-pulsed laser into two separate foci, leading to a simultaneous polymerization of two voxels. In case of disk-shaped WGM cavities, this induces an unintended double-disk shape. (b) By inverting the printing configuration, the resonator disk is structured under a small ordinary focus depth and thus with an unseparated voxel. The printing of the pedestal with two separated voxels is not critical, as the pedestal only requires a sufficient mechanical stability.

The implications of the focus separation on 3DLP photonic elements from LCE is demonstrated for the case of disk-shaped WGM resonators. The birefringence of the resist leads to a significant unintended double-disk shape, as illustrated in Fig. 4.9(a). Based on a typical pedestal height of 20 µm to 30 µm, a focus separation (and thus distance between the two disks) in the order of 5 µm to 10 µm is expected. This double-disk shape is clearly unwanted, as it is expected to affect both the field distribution of the modes inside the cavity as well as the overall confinement of these modes. Regarding disk-shaped WGM cavities on pedestals, a simple solution to this issue has been found: By inverting the printing configuration, the cavity disk can be structured using a small ordinary focus depth, preventing the separation into two voxels. This inverted configuration is illustrated in Fig. 4.9(b).
Using this inverted 3DLP configuration, the pedestals of the disk-shaped resonators are mainly structured with two separated foci. This however is not a critical issue, as these pedestals only require a sufficient mechanical stability. Nevertheless, as the used laser power is split into two foci, a higher overall power is needed to overcome the resist's polymerization threshold. As the focus separation changes with

the ordinary focus depth, the used laser power has to be continuously adjusted while printing these resonator pedestals. Therefore, the printing parameters of such structures from birefringent resists in the inverted configuration need to be thoroughly engineered. Detailed information on the printing process can be found in [151] as well as in App. A.2.

Regarding photonic structures made from LCE in general, the issue of separated foci can be overcome if the structures can be designed in a way that all optically relevant parts are printed with a small ordinary focus depth. Depending on the intended structure, this might require additional adaptions to the 3DLP process, as for example a cell with an in-situ controllable thickness. Despite these limitations, combining the integration of a eutectic nematic host material into the LCE resist with the inverted 3DLP printing configuration facilitates the fabrication of high-quality photonic structures entirely made from highly aligned liquid crystal elastomer.

4.4.2 Evaluation of the shape quality and molecular alignment of fabricated structures

In the following section, the shape quality and molecular alignment of photonic LCE structures fabricated using the approach presented in Sec. 4.4.1 are evaluated. Again, this is done using the example of disk-shaped whispering gallery resonators.

The shape quality of the printed WGM resonators is evaluated using SEM micrographs as depicted in Fig. 4.10(a) and (b). Comparing these cavities to those structured from a resist without eutectic nematic host material (see [158]), a significant improvement of their shape is evident.
Both cavities in Fig. 4.10(a) and (b) show a high rotational symmetry. Nevertheless, the cavity in (a) printed in the conventional 3DLP configuration consists of two connected but distinct disks. This fits the expectations based on the existence of two focal spots due to the resist's birefringence. The slightly different radii and thicknesses of these disks is expected to be induced by the differing shapes of the ordinary and extraordinary foci: As it is apparent from Fig. 4.8(a), the extraordinary focus (which is at higher z-values) shows a larger spatial extent than the ordinary one. As the extraordinary voxel prints the upper of the two disks of the resonator in the conventional printing configuration, this causes the upper disk to be slightly thicker. Additionally, the deposited energy per volume of this upper disk is lower, leading to a smaller degree of crosslinking. Therefore, the upper disk undergoes a stronger shrinkage within the development process and hence has a smaller radius. For the cavity printed in the inverted 3DLP configuration in Fig. 4.10(b), this double-disk shape is significantly reduced. This is especially evident from the inset, which shows

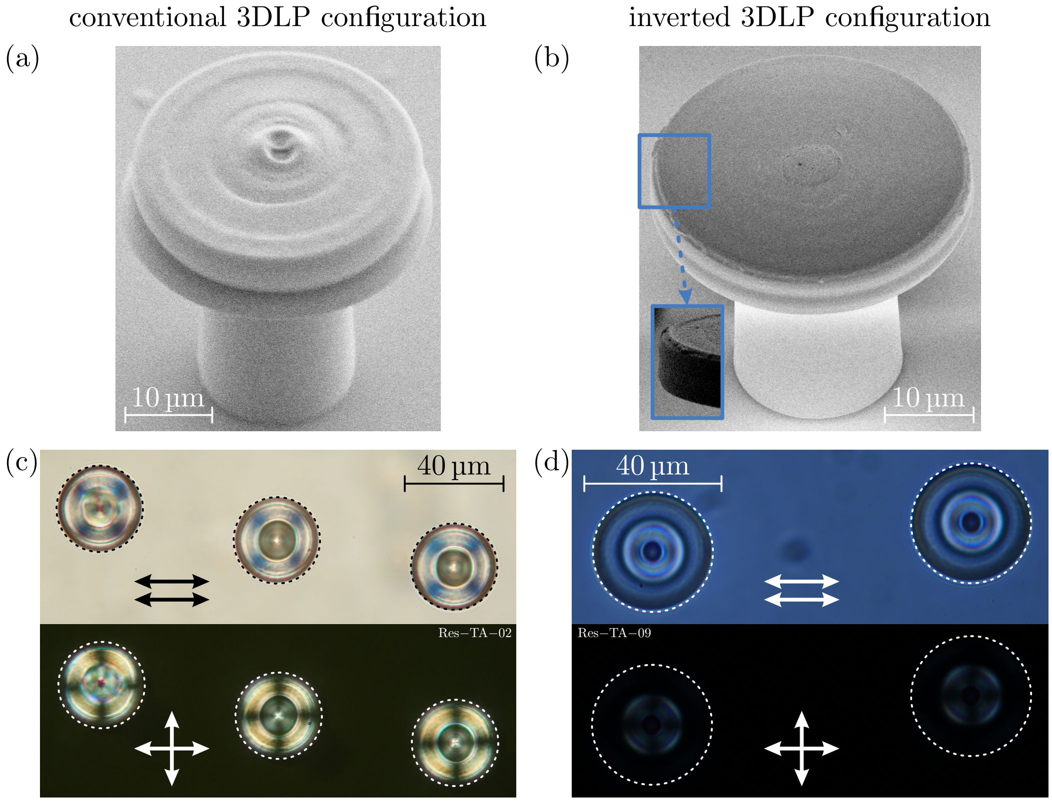

Figure 4.10: SEM, bright-field light and POM micrographs of disk-shaped WGM resonators from an LCE resist including a eutectic nematic host structured in conventional ((a),(c)) as well as inverted ((b),(d)) 3DLP configuration. (a) The cavity shows a high rotational symmetry compared to structures printed from resists without eutectic host material (see [158]). Nevertheless, a severe unintended double-disk shape is apparent. (b) The cavity printed in inverted configuration again shows a high rotational symmetry and smooth surface as well as a significantly decreased double-disk shape (also see inset). This structure is very close to its intended shape. (c) Comparing the resonator disks in bright-field light (top) and POM micrographs (bottom), no clear difference of brightness is evident. This reveals a poor mesogen alignment. The dark crosses on the resonator disks however indicate a rotationally symmetric tilting of the mesogen director (see main text). (d) For cavities printed in inverted configuration, a reduced brightness in POM micrographs is found. While still some intensity is detected from the cavities' pedestals, the disks appear completely dark. This indicates a strong mesogen alignment along its intended direction. Black/white arrows indicate polarizer orientations. Reprinted with permission from [37] © Optica Publishing Group.

the same cavity. All in all, this cavity nicely matches its intended shape and therefore demonstrates the successful prevention of an unwanted second voxel using the inverted 3DLP configuration.

The mesogen alignment of the printed cavities is investigated by comparing POM micrographs between crossed polarizers to bright-field micrographs between parallel polarizers. As the mesogens are intended to be aligned along the optical axis of the microscope, sufficiently aligned cavities are expected to appear dark in POM micrographs independent of the absolute orientation of the crossed polarizers. In Fig. 4.10(c), cavities printed in the conventional 3DLP configuration are depicted. Comparing the bright-field light (top) to the POM micrograph (bottom), the brightness of the cavities does not seem to depend on the relative orientation of the two polarizers. This indicates an insufficient mesogen alignment along the resonators' rotational axis. However, a dark cross corresponding to the orientation of the polarizers is visible on each of the resonator disks. By turning the crossed polarizers, the dark crosses follow accordingly [151]. This observation can be explained by a rotationally symmetric tilt of the mesogens within the resonator disk. Such a rotationally symmetric tilt could be induced by the differing shrinkage behavior of the two stapled disks and is therefore in line with the explanation of the resonator's geometrical shape given earlier.
In case of resonators printed in inverted configuration in Fig. 4.10(d), the pedestals look comparable to the overall cavities in (c) between crossed polarizers, which matches the fact that these pedestals are predominantly printed with separated voxels. The resonator disks however appear completely dark, indicating a strong mesogen alignment along the intended director orientation.

The surface roughness of such 3D laser printed photonic structures from LCE is again evaluated based on the quality factor of WGMs (compare Sec. 4.3.3). Tunable LCE resonators with quality factors of up to 6×10^4 have been fabricated [37]. These quality factors are more than one order of magnitude larger than those of LCE resonators printed from resist without a eutectic nematic host [158] and comparable to non-tunable 3D laser printed cavities in general as well as on LCE substrates, which are expected to be close to their absorption limit (see Sec. 4.3.3). As the LCE cavities are printed from a custom-mixed resist, no data on their material-intrinsic absorption is available. Hence, it can not be estimated whether their quality factor is limited by scattering or absorption. Nevertheless, their high quality factor indicates a surface roughness comparable to that of non-tunable WGM cavities printed from commercial resists as well as a strong temporal confinement of the guided WGMs.

In summary, the geometrical shape, the degree of mesogen alignment and the quality factor of spectrally tunable LCE resonators has been significantly improved by introducing the eutectic nematic host material to the resist and printing in an inverted 3DLP configuration. Therefore, the fabrication process presented here yields high potential for tunable photonic applications based on actuating three-dimensional micro-scale structures.

4.5 Assessment of the developed fabrication processes

In the following, the advanced fabrication processes that have been established within the scope of this work are summarized and assessed in the context of the future fabrication of tunable photonic elements based on actuating liquid crystal elastomers.

As presented in Sec. 4.2, a fabrication scheme of chip-scale LCE substrates with an in-plane director orientation has been successfully developed. The initiation of mesogen alignment via rubbed polymeric layers has been adapted from earlier works [177,178,188,206] and transformed into a semi-automated and therefore more reliable process by applying methods from the liquid crystal display technology [207]. The chip scale of the substrates has been realized by introducing a simple but effective mask-based illumination. Although the fabricated substrates are still in the order of 100 µm, this technique should also be applicable to further reduce the substrate size by up to two orders of magnitude. It should therefore facilitate a wide range of photonic applications based on actuating micro-scale substrates. An in-plane actuation of these substrates of more than 4 % under a temperature change of 50 K has been demonstrated. Although this actuation is sufficient for the tunable coupling of WGM cavities in Ch. 6, an enhancement of this actuation is desirable in the general context of tunable photonics. This could probably be achieved by an adjustment of the dimensions of the substrates as well as the composition of the underlying LCE. Also, a novel approach to characterize the substrates' actuation behavior using image processing of chip-scale substrates has been presented. This method should be applicable to all kinds of future flexible photonic elements and offer a possible resolution down to the regime of single nanometers [209].

The successful 3D laser printing of rigid structures onto chip-scale LCE substrates has been demonstrated. The general approach of an inverted printing configuration has been adapted from [17,39,170], and adjusted to the use case of LCE substrates. Herein, mainly the printing parameters of the 3DLP process have been thoroughly engineered to account for novel challenges introduced by the LCE substrates' mechanical flexibility, birefringence, chip scale, and surface imperfections. Doing so, a reliable fabrication scheme of rigid structures on actuating chip-scale substrates has been developed. A high optical quality of these structures has been demonstrated. The presented fabrication approach is of high interest for any kind of future application that requires a precise distance control between rigid photonic elements on an overall chip scale via an external stimulus.

Finally, a fabrication process towards the realization of actuating micro-scale LCE structures of arbitrary shape has been demonstrated. The general idea of 3D laser printing micro-scale structures from liquid crystal elastomer has been adapted from earlier works [16, 38]. However, by introducing a eutectic nematic LC host material to the used resist [195, 226], both the shape quality as well as the mesogen alignment have been significantly improved. Furthermore, the impact of the resists birefringence on the printing process has been understood from numerical simulations and an adaption of the process has been performed to facilitate the fabrication of high quality disk-shaped WGM cavities. To enable the fabrication of really arbitrary high-quality LCE structures, an additional modification as, e.g., an in-situ controllable cell thickness is indispensable. Alternatively, this issue could be overcome by performing an elaborate adjustment of the polarization of the used laser light [196]. Under the assumption of such a successful modification, the fabrication methods presented here are of high interest for any future photonic application in which the optical or mechanical properties of a micro-scale element need to be precisely controlled via an external stimulus.

The major limitation to all fabrication processes of micro-scale LCE actuators presented in this work is the homogeneity of the LCE's director orientation over the whole structures. This homogeneity leads to only one common actuation behavior of the overall structures and therefore limit their possible applications. To overcome this issue, several approaches are conceivable: By replacing the homogeneously rubbed polymeric alignment layers with 3D laser printed structures of changing preferential orientations, micro-scale structures with domains of varying director in the order of 10 µm are feasible [194]. By completely substituting the concept of surface-mediated mesogen alignment with an alignment induced by an in-situ controllable quasi-static electric field, the size of the domains of changing director orientation within the micro-scale structure is only limited by the dimension of the voxel of around 1 µm [196]. Combining one of these promising approaches with the fabrication methods presented in this work would enlarge the area of possible applications of such tunable photonic structures even further.

Chapter 5

Full spectral tunability of modes in actuating resonators

Within the present chapter, the full and precise spectral tunability of WGMs in resonators entirely made from LCE is demonstrated. In Sec. 5.1, the basics of the spectral tuning of WGM cavities are shortly addressed. Herein, an overview of different possible factors influencing the spectral position of WGMs is given. Also, established approaches to tune various kinds of WGM cavities are shortly introduced. The potential of the spectral tuning of WGMs in resonators made from LCE is discussed based on recent results in literature in Sec. 5.2. Afterwards, the full and precise spectral tunability under thermal actuation of these LCE cavities is demonstrated in Sec. 5.3. This includes an investigation of the reversibility of the spectral position of the WGMs as well as a possible control of the extent of tunability by an adjustment of the degree of polymeric crosslinking of the material. In Sec. 5.4, the achieved full tunability of WGMs in resonators made from LCE is shortly assessed.

5.1 Basics of spectral tuning of WGMs

The possibility of a spectral tuning of WGMs largely widens the field of potential photonic applications of such cavities. An overview over these possible applications including the implications of a potential spectral tunability is given in Sec. 2.3. In addition to these applications, such a tunability of the resonance wavelength is often also required due to a fabrication-related issue: As evident from their resonance condition given in Eq. (2.1), the resonance wavelength of a WGM is very sensitive to changes of the cavity's radius. Therefore, small fabrication imperfections in the order of only 10 nm can already induce critical deviations between the designed and real resonance wavelengths in the order of 1 nm. To compensate for such unwanted mismatches, a post-fabrication tunability of the spectral position of WGMs is of great interest.

To fully understand the spectral tunability of WGMs, the different possible factors of influence of their spectral position are introduced. These different factors can be derived from the WGMs' fundamental resonance condition given in Eq. (2.1):

$$2\pi R \times n_{\text{eff}} = N_\phi \lambda_0 \text{ with } N_\phi \in \mathbb{N}.$$

Under consideration of a mode with a fixed form of the field distribution (implying a constant N_ϕ), the resonant wavelength λ_0 can be tuned by either changing the cavity's radius R or the effective refractive index n_{eff}. As obvious from Eq. (2.1), a relative change of the cavity's radius directly leads to an equal relative change of its resonance wavelength. This also holds for changes of the material-intrinsic refractive index n_{r} under the assumption that it is approximately equal to the cavity's effective refractive index. A third possible tuning mechanism is given by a change of the cavity's thickness d, as it influences the confinement of the mode in axial direction and thus the effective refractive index. This effect is only explicitly included in Eq. (2.1) and the exact dependency of the resonance wavelength on the cavity's thickness is not obvious. Based on FEM simulations depicted in Fig. 2.4, this dependency is expected to strongly depend on the absolute value of the resonator thickness. Finally, also a resonance tuning due to a change of the refractive index of the surrounding medium is in principle possible. This effect is largely utilised within WGM-based sensing applications [33,70] but ignored here, as photonic building blocks are usually operated under ambient conditions.
Regarding all of these conceivable tuning mechanisms, the requirements are the same: The resonance wavelength of a WGM is aimed to be tuned post fabrication over a large spectral range by applying a small external stimulus. A so-called full tunability of a WGM cavity is achieved, if the spectral positions of the modes can be tuned over more than its free spectral range $\Delta\lambda_{\text{FSR}}$ (see Eq. (2.13)). Furthermore, the tuning mechanism should offer a high tuning speed and precision. Finally, also a reversibility of the spectral position of the modes after application of an external stimulus is required to enable a reliable tuning over a large number of cycles.

The most common approach to realize a spectral tunability of WGM resonances is via so-called index modulation: a change of the cavity's material-intrinsic refractive index n_{r}. While there is a large number of stimuli that alter the refractive index of such cavities [77,82,232–235], usually either temperature or electric fields are used. Herein, the wavelength range over which such WGMs can be tuned strongly depends on the thermo-optic coefficient or Pockels and Kerr coefficients, respectively. While a thermo-optic tuning typically offers a significantly larger tuning range, the electro-optic effect facilitates higher switching frequencies. Most rigid polymers, including those used in the present work, do not show a distinct electro-optic behavior. Hence, a thermal tuning of the refractive index due to the most often negative thermo-optic coefficient $\mathrm{d}n_\mathrm{r}/\mathrm{d}T$ is typically conducted in case of polymeric cavities (see App. C.2).

A reversible post-fabrication change of a WGM cavity's radius is usually not feasible using widely established rigid resonator materials as inelastic polymers, silica or semiconductors. However, tuning induced by an irreversible reduction of the radius of cavities based on wet-chemical [236, 237] or photo-electrochemical etching [238] as well as illumination-induced material desorption [239] has been reported.
In more general, this approach towards a spectral tunability is called a configuration modulation: a reversible change of the cavity's geometrical configuration, including, e.g., its radius, thickness or general shape. While such a configuration modulation is again only possible via the application of flexible materials, it is more easy to realize than an isolated radius change. Ta *et al.* have tuned the spectral position of WGMs in rigid self-assembled polymer droplets embedded in a macroscopic flexible PDMS substrate. Under the application of direct mechanical stress to the substrate, the spherical shape of the cavities has been reversibly distorted [31]. An alternative approach towards a full tunability of WGMs based on so-called split-disk cavities mounted onto an elastomer substrate has been reported by Siegle *et al.* Although these cavities including an air-filled gap of adjustable size have been demonstrated to be widely tunable, their quality factors have been significantly reduced compared to gap-free resonators [17].
A tuning of WGM resonances based on a direct and reversible post-fabrication change of the cavity's radius has only been achieved in very few cases up to now. Flatae *et al.* have demonstrated a full spectral tuning of WGMs in goblet-shaped cavities from a rigid polymer that have been reversibly deformed using a micro-scale LCE actuator inside the goblet. This approach however includes a time-consuming pick-and-place positioning of the single LCE actuators [16]. Spectral tuning via the reversible change of the radius of a WGM cavity entirely made from LCE has been realized by Nocentini *et al.* [38]. This approach is also adopted in the present work and therefore covered in detail in the following section.

5.2 Tuning potential of WGMs in LCE resonators

Before the full spectral tunability of WGM resonators which are 3D laser printed from LCE is demonstrated in Sec. 5.3, the general potential of this approach is estimated. This is done based on the LCE's material parameters (see Sec. 4.1.2), the geometrical and alignment properties of the printed cavities (see Sec. 4.4.2) as well as results of a similar system recently reported by Nocentini *et al.* [38].

Within the proof-of-principle measurements presented in this chapter, the actuation of the LCE is initiated using local heating as external stimulus. Hence, the tuning of these cavities due to a change of the actuation temperature T_{act} is exemplarily discussed in the following.

Within the concept of spectrally tunable WGM cavities made from LCE, the temperature-induced actuation is used to reversibly change the cavity's radius and thereby tune its resonant wavelengths. Thus, such cavities are fabricated with a mesogen alignment along their axis of rotational symmetry. This configuration leads to a rotationally symmetric increase of the cavity radius under external stimuli.
Within their spectral tuning, the thermo-optic effect of LCE cavities has to be considered. As introduced in Sec. 4.1.2, LCEs are birefringent in their nematic phase. When heated, the two refractive indices both decrease and slightly approach each other towards an isotropic state. This leads to the thermo-optic coefficients of the ordinary and extraordinary index to be both negative but differ in their absolute value by about 10 %. Herein, the larger absolute value of the thermo-optic coefficient corresponds to the extraordinary index n_{e} [190]. These thermo-optic coefficients influence the spectral tunability of the WGM cavities. As introduced earlier, the thickness of the cavity disk impacts the resonance wavelength of WGMs. For tunable LCE resonators, this thickness decreases under thermal actuation due to the contraction of the LCE along the director of its mesogen alignment. But as the investigated LCE cavities are thick compared to the resonance wavelengths near the IR c-band (compare Fig. 4.10), this influence of the disk thickness is assumed to be neglectable in the following. Nevertheless, all potential factors influencing the resonance wavelength λ_0 of WGMs in an LCE resonator are summed up in Fig. 5.1.

Neglecting the influence of the cavity thickness d, the overall change of the spectral position of a WGM in an LCE cavity with the actuation temperature T_{act} is depending on its positive expansion coefficient α perpendicular to its director as well as the negative thermo-optic coefficients $\mathrm{d}n_{\mathrm{o,e}}/\mathrm{d}T_{\mathrm{act}}$ [232, 233]:

$$\frac{\mathrm{d}}{\mathrm{d}T_{\mathrm{act}}}\lambda_0 = \lambda_0 \left(\frac{1}{n_{\mathrm{o,e}}} \frac{\mathrm{d}n_{\mathrm{o,e}}}{\mathrm{d}T_{\mathrm{act}}} + \alpha \right). \tag{5.1}$$

The two theoretically expected kinds of WGMs with differing preferential field orientations of TE- and TM-like polarization (compare Sec. 2.2) are primarily effected by the ordinary and extraordinary refractive index, respectively. This leads to the following conclusions: For both kinds of modes, the negative thermo-optic coefficient is expected to counteract the spectral tuning under thermal actuation due to the positive expansion coefficient α. The sign of the overall spectral shift hereby depends on which of these two effects is stronger. Nevertheless, a slightly larger red-shift/smaller blue-shift is expected for modes with a TE-like polarization due to the slightly smaller thermo-optic coefficient of the ordinary refractive index n_{o}.

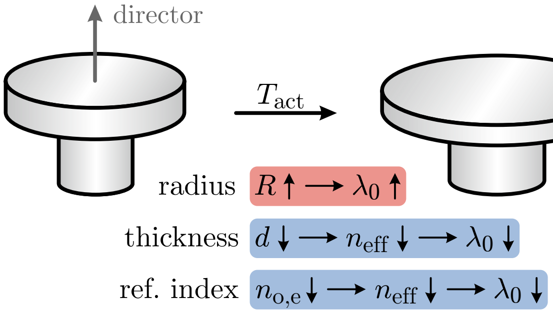

Figure 5.1: Illustration of the tuning mechanism of WGMs in cavities from LCE. The cavities are fabricated with a mesogen director orientation along their axis of rotational symmetry. Under thermal actuation, the radius R of the cavity disk increases due to the LCE's expansion perpendicular to its director. This induces a red-shift of the resonance wavelength λ_0. The LCE's contraction along its director leads to a reduction of the thickness d of the cavity disk and therefore also of the effective refractive index n_{eff}. This change of n_{eff} leads to a blue-shift of λ_0. This effect is however neglected here, as the cavity disks are thick compared to the resonance wavelengths. Due to their negative thermo-optic coefficients, both the ordinary and extraordinary refractive index $n_{\mathrm{o,e}}$ decrease with elevating actuation temperature T_{act}. This decreases the effective refractive index n_{eff} and therefore again leads to a blue-shift of λ_0. The sign and absolute value of the overall wavelength shift depends on the relative strengths of these different effects.

Nocentini *et al.* have demonstrated the spectral tuning of two different WGMs in a ring-shaped cavity 3D laser printed entirely from LCE. The cavity has been doped with an absorber dye and its reversible actuation has been initiated using laser illumination. For the two investigated modes, maximum blue shifts of 1.0 nm and 3.7 nm have been found, respectively. Both these modes have been assumed to carry a TM-like polarization and therefore mainly be effected by the extraordinary refractive index of the LCE n_{e}. Based on [190], a change of the extraordinary index of $\Delta n_{\mathrm{e}} = 0.02$ has been expected. This index change should theoretically induce a spectral blue-shift of around 20 nm. Based on these estimations, compensating red-shifts induced by radius expansion of 19.0 nm and 16.3 nm, respectively, have been assumed. [38]
Based on these results, the concept of tunable cavities made from LCE does not seem to be promising, as the achieved spectral shifts are comparable to the thermal tuning of WGMs in resonators made from conventional polymers [64,65,159]. This fact can also be understood from the intrinsic material parameters of a macroscopic thin film of LCE as investigated by Liu *et al.* [190]: The absolute values of the expansion coefficient α as well as both relative thermo-optic coefficients $n_{\mathrm{o}}^{-1} \times \mathrm{d}n_{\mathrm{o}}/\mathrm{d}T$ and $n_{\mathrm{e}}^{-1} \times \mathrm{d}n_{\mathrm{e}}/\mathrm{d}T$ are roughly around $2 \times 10^{-4}\,\mathrm{K}^{-1}$. As the relative wavelength change is proportional to the difference of the expansion and the respective thermo-optical

coefficient, a change in the order of $\lambda_0^{-1} \times \mathrm{d}\lambda_0/\mathrm{d}T_{\mathrm{act}} = 1 \times 10^{-5}\,\mathrm{K}^{-1}$ is expected. This also matches the results presented by Nocentini *et al.* [38].

Within the scope of the present work, disk-shaped WGM cavities similar to the ones by Nocentini *et al.* have been 3D laser printed from LCE and investigated. However, due to the presented advances of the process of 3D laser printing structures from LCE (see Sec. 4.4), a significantly enhanced overall quality of these LCE cavities is presumed. As an improved degree of mesogen alignment should also enhance the general actuation behavior of such resonators, they could potentially show a notably increased spectral tuning under thermal actuation.
In the following, the full spectral tunability of two different kinds of LCE cavities is demonstrated. While the first of these cavities has been fabricated adopting the process employed by Nocentini *et al.*, the second one has been printed by applying all fabrication enhancements introduced in Sec. 4.4. The tunability of both these cavities is compared to the results presented by Nocentini *et al.* [38] and possible reasons for their significantly enhanced tunability are discussed.

5.3 Full spectral tunability of modes in LCE resonators

In this section, the spectral tunability of two kinds of 3D laser printed WGM cavities entirely made from LCE is investigated in detail. The two investigated kinds of cavities are both disk-shaped with a mesogen alignment along their axis of rotational symmetry. The first kind of cavity (type 1) has been fabricated following the approach used by Nocentini *et al.* [38]. For such cavities, quality factors of only around $Q = 4 \times 10^3$ have been achieved within the scope of the present work [158]. (For comparison: $Q = 1.5 \times 10^4$ in [38].) The second kind of cavity (type 2) has been printed using the advanced fabrication process introduced in Sec. 4.4. Regarding these cavities, quality factors of up to 6×10^4 have been demonstrated [37]. The tunability of both kinds of cavities is compared to the results of the ring-shaped LCE cavity by Nocentini *et al.* [38]. For cavities of type 2, the reversibility of the tuning is investigated. Finally, an adjustment of the spectral tunability via a change of the degree of polymeric crosslinking of the LCE is demonstrated.
Parts of the results presented in this section have been achieved in close cooperation with Jannis Hessenauer, Evelyn Kaiser and Stefan Pfleging within their respective theses [145, 151, 158] and are published in [37, 240].

Before the spectral tunability under thermal actuation is investigated using fiber-transmission spectroscopy, the radius change due to the expansion coefficient α of an LCE cavity is exemplarily examined. However, the real-time determination of the change of this radius under thermal actuation is experimentally challenging,

as it is in the order of the diffraction limit. Furthermore, due to the overall thermal expansion of the measurement setup, the focal plane of any optical microscope needs to be continuously readjusted. To still get a coarse estimate of the cavity's relative radius change, the circle of the cavity disk is identified in microscope images at different actuation temperatures using a *MATLAB* routine based on Hough transformations [210]. The distance between two arbitrary scatterers on the glass substrate is used as an approximately temperature-independent measure. Based on this approach, a roughly constant expansion coefficient of $\alpha \approx 2 \times 10^{-3}\,\mathrm{K}^{-1}$ is found for an exemplary cavity of type 1. The respective data is presented in App. B.1.
The experimentally estimated expansion coefficient is one order of magnitude larger than that found as intrinsic material parameter by Liu *et al.* [190] as well as that estimated from the spectral tunability of ring-shaped LCE cavities reported by Nocentini *et al.* [38]. Nevertheless, the estimated value is assumed to be in the correct order of magnitude, as comparable values have also been found in other investigations of disk-shaped LCE cavities [158]. The origin of this deviation is not finally resolved. Compared to macroscopic thin films as investigated by Liu *et al.* [190], the shape of a free-standing micro-disk could strongly promote the in-plane expansion of the LCE cavity disk. (Also compare the limited actuation of LCE substrates on a macro-scale glass surface in Sec. 4.2.) Regarding the ring-shaped LCE cavities demonstrated by Nocentini *et al.* [38], the significantly enhanced expansion coefficient of the cavities presented in this work could possibly be a consequence of a notably higher degree of mesogen alignment. Alternatively, it could be induced by the slightly differing cavity architectures: While the cavity presented by Nocentini *et al.* [38] consists of an LCE ring mounted onto a rigid pedestal, the cavity introduced here is printed as a solid LCE disk on an LCE pedestal. These differences could lead to a strongly enhanced expansion coefficient in the case demonstrated here.

The second major factor influencing the resonance wavelengths is the change of the LCE's refractive indices. Unfortunately, an experimental determination of these indices as well as their change under thermal actuation is not feasible due to the small size of the investigated LCE cavities. Nevertheless, both the expansion coefficient as well as the relative thermo-optic coefficients base on the same physical effect of a decrease of the degree of molecular order. Hence, the fact of these three coefficients being of comparable size (as shown by Liu *et al.* [190]) is assumed to still hold for the cavities presented here. If furthermore the thermal expansion and the accompanying decrease of the refractive indices are again approximately counteracting each other, a relative spectral tuning in the order of $\lambda_0^{-1} \times \mathrm{d}\lambda_0/\mathrm{d}T_{\mathrm{act}} \approx 1 \times 10^{-4}\,\mathrm{K}^{-1}$ is expected. This expectation of the spectral tuning based on the real-time estimation of the cavity's radius is approximately one order of magnitude larger than that demonstrated by Nocentini *et al.* [38]. In the following, this spectral tuning is experimentally investigated using fiber-transmission spectroscopy.

5.3.1 Full tunability under thermal actuation

To demonstrate the full tunability of a WGM resonance, its wavelength has to be tuned over more than one free spectral range $\Delta\lambda_{\mathrm{FSR}}$. This free spectral range is inversely proportional to the cavity radius (see Eq. (2.13)). Cavities of type 2 show a significant shrinkage behavior post printing due to the used liquid crystal host material (compare Sec. 4.4). Hence, these cavities have a distinctly smaller radius and therefore larger free spectral range. Consequently, cavities of type 2 need to be tuned over a larger spectral range to demonstrate a full tunability. As an independent measure for the general tunability of such LCE cavities, the temperature change under which a full tuning is achieved is used.
The full spectral tunability of disk-shaped resonators under thermal actuation is demonstrated using fiber-transmission spectroscopy near the IR c-band (compare Sec. 3.1). The resonance wavelengths have been determined by the application of Lorentz-shaped fits to resonance dips in FTS spectra. The thermal actuation has been initiated using a macroscopic Peltier element.

At first, the full tunability of a cavity of type 1 is demonstrated. In Fig. 5.2(a), the wavelength detuning of a WGM with respect to its wavelength at room temperature in a type 1 cavity is plotted versus the actuation temperature T_{act}. The respective LCE resonator has been heated from room temperature to an actuation temperature of $T_{\mathrm{act}} = 80\,^{\circ}\mathrm{C}$ and cooled back to room temperature afterwards. At first, only the spectral behavior under heating is considered. For $T_{\mathrm{act}} < 36\,^{\circ}\mathrm{C}$, the resonance wavelength is approximately constant. For actuation temperatures $T_{\mathrm{act}} > 36\,^{\circ}\mathrm{C}$, an approximately linear increase of the resonance wavelength is evident. This temperature at which the wavelength starts to shift with the actuation temperature matches the temperature T_{tr} at which the LCE's transition from its nematic into a paranematic phase is expected to set in [188]. The investigated resonator has been shown to have a free spectral range of $\Delta\lambda_{\mathrm{FSR}} = 8.3\,\mathrm{nm}$ [158]. Hence, a full spectral tuning of the resonator has been achieved under a temperature change of around 32 K.
While cooling the cavity back to room temperature, the resonance wavelength of the investigated mode shifts back in a similar manner. Nevertheless, the overall slope of this spectral shift is slightly smaller compared to that under heating, leading to a hysteresis of the room-temperature wavelengths prior to and after thermal actuation of $\Delta\lambda_{\mathrm{hys}} = 2.6\,\mathrm{nm}$. This hysteresis has been shown to exponentially decay over time after a heating cycle [151]. It therefore is attributed to the visco-elastic material properties of the LCE. Nevertheless, such a hysteresis of the resonance wavelength of a tunable cavity is unwanted regarding future photonic applications. The requirement of reversibility is addressed in detail in Sec. 5.3.2.

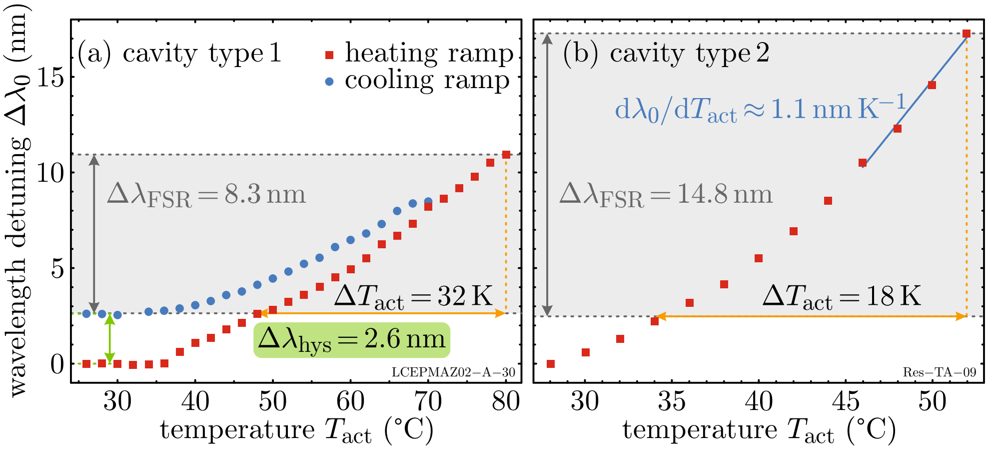

Figure 5.2: Demonstration of the full spectral tunability under thermal actuation. (a) An LCE cavity of type 1 has been heated from room temperature to $T_{\mathrm{act}} = 80\,°\mathrm{C}$ and cooled back to room temperature. The resonance wavelength λ_0 of a WGM has been determined by applying Lorentzian fits to resonance dips in FTS spectra near the IR c-band. The detuning of this resonance wavelength $\Delta\lambda_0$ with respect to the first measurement at room temperature is plotted versus T_{act}. From the heating ramp, an approximately linear increase of λ_0 for $T_{\mathrm{act}} > 36\,°\mathrm{C}$ is evident. Compared to the free spectral range $\Delta\lambda_{\mathrm{FSR}} = 8.3\,\mathrm{nm}$ of the cavity (gray box), a full tuning has been achieved under a change of T_{act} of around 32 K. The cooling ramp shows a similar decrease of λ_0 with a slightly smaller slope. This leads to a hysteresis of the room-temperature wavelengths prior to and after the actuation of $\Delta\lambda_{\mathrm{hys}} = 2.6\,\mathrm{nm}$. (b) The detuning of a WGM in a cavity of type 2 under thermal actuation from room temperature to $T_{\mathrm{act}} = 52\,°\mathrm{C}$ is depicted. Over the whole range of T_{act}, a super-linear increase of λ_0 is found. In the regime of high T_{act}, a tuning response around $1\,\mathrm{nm\,K^{-1}}$ is found. Compared to $\Delta\lambda_{\mathrm{FSR}} = 14.8\,\mathrm{nm}$ (gray box), a full tuning has been achieved changing T_{act} by around 18 K. (a)/(b) adapted/reprinted with permission from [241]/[37] © Optica Publishing Group.

The results presented in Fig. 5.2(a) strongly differ from the small blue-shift of modes in LCE ring resonators demonstrated by Nocentini *et al.* [38]. As expected based on real-time estimations of its radius, the cavity presented here is tuned over a significantly larger spectral range. Furthermore, the cavity is tuned to higher wavelengths. These differing signs of the spectral tuning are unexpected, as both samples have been fabricated using similar processes. The origin of these differences is not finally resolved, however there are several potential explanations: The most obvious possible reason are the different geometrical shapes of the cavities. The solid disk of the resonator presented here might lead to a comparably larger radius increase under actuation and therefore induce a stronger red-shift. Another possible influence is the thickness of the cavities. The comparably large red-shift of WGMs in the cavities presented here could be attributed to resonator disks with a large thickness compared to the LCE ring presented by Nocentini *et al.* [38].

The preferential field orientation of the investigated WGMs is however not considered as possible cause for the observed deviations. On the one hand, this is based on the fact that despite the conduct of comprehensive polarization-sensitive investigations of WGMs in cavities of type 1, no correlation between the alleged preferential field orientation of modes and their spectral tuning under thermal actuation has been found [145]. A direct investigation of the preferential field orientation of WGMs in a type 2 LCE cavity employing the modes' directional radiation on the other hand even suggests, that primarily modes without distinct preferential field orientation propagate in such resonators (see App. B.2).
Based on the experimentally estimated expansion coefficient of $\alpha \approx 2 \times 10^{-3}\,\mathrm{K}^{-1}$ of a cavity of type 1, a spectral tuning in the order of $1 \times 10^{-4}\,\mathrm{K}^{-1}$ has been predicted. In the linear regime for actuation temperatures above 36 °C, a spectral tuning of $\lambda_0^{-1} \times \mathrm{d}\lambda_0/\mathrm{d}T_{\mathrm{act}} = 1.8 \times 10^{-4}\,\mathrm{K}^{-1}$ has been found. These matching values nicely demonstrate the accordance of the measured spectral tuning with the in-plane expansion of the resonator disk and the presumed change of its refractive indices.

As a next step, the full spectral tunability of a cavity of type 2 is demonstrated. To that end, the resonance wavelength of a WGM under thermal actuation is determined as described earlier and plotted versus T_{act} in Fig. 5.2(b). The WGM resonator under investigation has been heated from room temperature to 52 °C. Over the whole temperature range, a super-linear increase of the resonance wavelength is apparent. Hence, the starting temperature at which the LCE's transition from its nematic into a paranematic phase sets in is not apparent. The free spectral range of the investigated cavity has been shown to be $\Delta\lambda_{\mathrm{FSR}} = 14.8\,\mathrm{nm}$ [151]. Consequently, a full spectral tuning of this cavity has been achieved under a temperature change of only 18 K. In the regime of high T_{act}, an absolute tuning response of $\mathrm{d}\lambda_0/\mathrm{d}T_{\mathrm{act}} \approx 1.1\,\mathrm{nm}\,\mathrm{K}^{-1}$ has been found.
Compared to the results of a cavity of type 1 presented in Fig. 5.2(a), the cavity of type 2 yields an even higher tunability. While a temperature change of 32 K is necessary to fully tune a type 1 cavity, 18 K are sufficient in the case of the type 2 cavity. This enhanced tunability matches the expectations based on an improved mesogen alignment as well as overall structure quality due to the advanced fabrication process (compare Fig. 4.10). As already discussed regarding the cavity of type 1, also the demonstrated type 2 cavity shows an inverted and significantly higher tunability than the LCE ring resonator demonstrated by Nocentini *et al.* [38].

In summary, both presented cavities show a full spectral tunability of their WGM resonances under thermal actuation to moderate temperatures. Furthermore, the advanced fabrication process developed within the scope of this work is not only reflected in a notably larger quality factor, but also a significantly enhanced tunability of the regarding cavities.

5.3.2 Reversibility and precision of the spectral tuning of WGMs

After the full spectral tunability has been demonstrated in the previous section, the reversibility and precision of this tuning is addressed in detail using the example of a disk-shaped LCE cavity of type 2. As introduced in Fig. 5.2(a) in case of a type 1 cavity, thermally tuned WGMs in LCE resonators typically show a hysteresis of their resonance wavelength. This also holds for cavities of type 2. The hysteresis has been shown to depend on the degree of polymeric crosslinking of the LCE as well as the overall range of T_{act} and has been attributed to the visco-elasticity of the LCE [151]. Nevertheless, such a spectral hysteresis is obviously unwanted in the context of photonic applications. In the following, the impact of this hysteresis on the usefulness of such tunable cavities under operation conditions is estimated.

As introduced earlier, one of the leading motivations to realize a post-fabrication spectral tunability of WGMs is the mismatch between the resonance wavelength after production and their designed value. Therefore, a frequent full spectral tuning is not expected to be the typical use case for lot of photonic applications of tunable WGM cavities. Instead, the cavities are expected to be operated in an approximately constant actuated state. The WGM's tunability should then be used to keep the resonance wavelength constant despite any environmental impacts. Under these operation conditions, the spectral hysteresis after a full spectral tuning cycle as in Fig. 5.2(a) is not of particular importance. Instead, the reversibility of the spectral tuning of an LCE cavity in an already actuated state under small changes of the applied external stimulus is mostly relevant. Therefore, this spectral reversibility of a WGM under small temperature changes is investigated in the following.

To evaluate the reversibility of the spectral position of a mode in an LCE cavity under small tuning cycles, the resonance wavelength of the WGM has again be determined using FTS. In Fig. 5.3, the spectral position of the WGM in a cavity at around $T_{\text{act}} = 40\,^{\circ}\text{C}$ under three small consecutive heating and cooling cycles of $\Delta T_{\text{act}} = 5\,\text{K}$ is plotted versus the actuation temperature T_{act}. The different heating and cooling ramps are separated by dotted lines.
Considering an isolated heating/cooling ramp, a large and approximately linear absolute tuning response of around $0.6\,\text{nm}\,\text{K}^{-1}$ is found. This finding is in accordance with the general tunability of a type 2 LCE cavity demonstrated in Fig. 5.2(b).
To evaluate the reversibility of this spectral tuning, the resonance wavelengths at each fixed actuation temperature within the different heating and cooling cycles are compared (indicated by color-coded bars). For each value of T_{act}, the resonance wavelengths λ_0 slightly scatter around a common mean value (dark-colored lines). The standard deviations are in the order of 100 pm (light-colored bars). Furthermore, the deviation from their common mean value is within the uncertainty due to

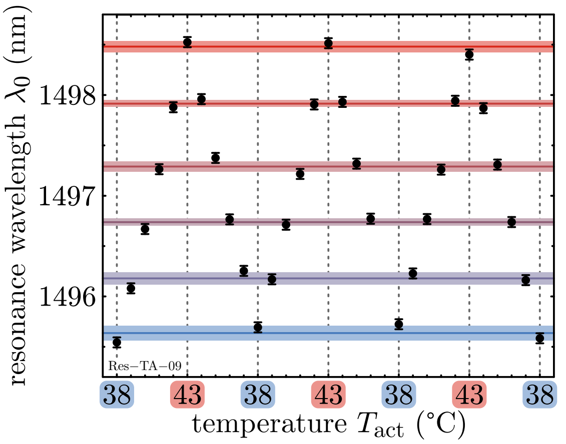

Figure 5.3: Demonstration of the tuning reversibility under operation conditions. A type 2 cavity has been thermally tuned over a range of 5 K. The resonance wavelength λ_0 of a WGM has been determined from FTS near the IR c-band and is plotted versus the actuation temperature T_{act}. Three consecutive heating and cooling cycles have been conducted. The different ramps are separated by dotted lines. Within each ramp, an absolute tuning response of around 0.6 nm K^{-1} is found. Comparing the different values of λ_0 for one fixed actuation temperature (indicated by colored stripes), the reversibility of the spectral tuning is evident: The values of λ_0 slightly scatter around a common mean value (dark-colored lines) with a standard deviation in the order of 100 pm (light-colored stripes). For most measurements, the mean value is within the uncertainty induced by the wavelength precision of the laser source. As no trend of the larger deviations is obvious, they are mainly attributed to the limited precision of the temperature control. Adapted from [151].

the absolute wavelength precision of the used laser source for most of the investigated modes. These findings demonstrate the high reversibility as well as precision of the spectral position of slightly tuned WGM resonances within the precision limit of the applied investigation approach. Hence, the demonstrated LCE cavities yield high potential for all kinds of photonic applications, where a mainly constant but precise compensation of a fabrication-induced spectral mismatch is wanted.
Regarding the small deviations from the mean value at one specific actuation temperature in Fig. 5.3, no clear trend is found. Therefore, this data scattering is not attributed to a spectral hysteresis of the investigated modes, but to the precision of the applied temperature control [151]. Therefore, these deviations are expected to be reducible under the application of a more sophisticated external stimulus.

Regarding photonic applications where a frequent large spectral tuning of WGMs is of interest, the spectral hysteresis of the WGMs is still a critical issue. Therefore, additional effort to overcome this problem is indispensable. First investigations to gain deeper insight into the nature of this irreversible spectral tunability have been conducted in [151].

5.3.3 Adjusted spectral tunability under varying degrees of polymeric crosslinking

As obvious from the tuning mechanism of thermal actuation (see Fig. 5.3), the precision of the spectral tuning of a WGM depends on the precision of used temperature control. While the overall tuning range increases with a larger absolute tuning response $\mathrm{d}\lambda_0/\mathrm{d}T_{\mathrm{act}}$, the feasible wavelength precision of this tuning decreases. This fact generally holds for all kinds of conceivable external stimuli. Some of these stimuli should be applicable with a significantly higher precision than the temperature control demonstrated in this work. Nevertheless, the possibility of a deliberate adjustment of the tuning response enables to tailor the overall tuning range and tuning precision to all different combinations of stimuli and photonic applications. Therefore, such a potential adjustability should further increase the area of possible applications of such tunable WGM resonators made from LCE.

Within the scope of the present work, the absolute tuning response of LCE cavities is adjusted via the degree of crosslinking of the LCE's polymeric network. To control this degree of crosslinking, the share of crosslinker molecules of the liquid crystal resist from which the resonators are printed (compare Sec. 4.1.1) is altered. As the degree of crosslinking changes the overall actuation of the LCE under the application of an external stimulus (compare Sec. 4.1.2), it is expected to also impact the spectral tuning of the introduced LCE resonators. To exemplarily demonstrate the impact of this degree of crosslinking onto the tuning response, three different samples of type 2 have been fabricated and investigated: An LCE resonator with a maximum degree of crosslinking due to a crosslinker share of 100 wt%, a resonator with a medium share of crosslinker of 50 wt% and one resonator with a small degree of crosslinking due to a crosslinker share of 10 wt%. (A share of 0 wt% is not feasible as polymeric structures cannot be printed from a resist without crosslinker.)

To determine the absolute tuning response of WGMs in these LCE resonators, the spectral detuning under thermal actuation has again been investigated using FTS near the IR c-band. This spectral tuning has been plotted versus the actuation temperature and a linear fit has been applied in the regime of high actuation temperature (compare Fig. 5.2(b)). The slope of the applied fit is taken as tuning response $\mathrm{d}\lambda_0/\mathrm{d}T_{\mathrm{act}}$. In Fig. 5.4, the tuning response of the three introduced samples is plotted on a semi-logarithmic scale versus their molecular share of crosslinker in weight percent.

The presented data shows a decrease of the absolute tuning response of LCE cavities by more than two orders of magnitude with an increasing degree of crosslinking. As an LCE polymer with a higher degree of crosslinking yields a weaker actuation behavior, the general trend of the tuning response fits the expectations.

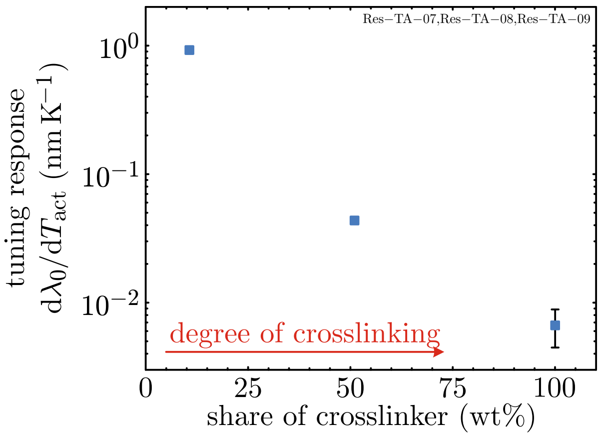

Figure 5.4: Adjustment of the absolute spectral tuning response $\mathrm{d}\lambda_0/\mathrm{d}T_\mathrm{act}$ of WGMs in thermally actuated LCE resonators. The tuning response of WGMs in different LCE cavities is compared. The tuning response is hereby determined from a linear fit to the change of the resonance wavelength λ_0 with the actuation temperature T_act as demonstrated in Fig. 5.2(b). The tuning response is controlled via the degree of polymeric crosslinking in cavities with a differing share of crosslinker molecules in their resist. The tuning response is plotted versus the molecular share of crosslinker in weight percent for three different samples on a semi-logarithmic scale. The presented data shows a significant decrease of the tuning response over more than two orders of magnitude with increasing share of crosslinker. Furthermore, the data indicates an approximately exponential nature of this dependency. Reprinted with permission from [37] © Optica Publishing Group.

Furthermore, the presented data indicates an approximately exponential change of the tuning response with the share of crosslinker molecules. Nevertheless, no theoretical basis to expect such an exponential behavior is given. Furthermore, only three data points are presented. Hence, this exponential nature should not be taken as more than a coarse first estimate.

Nevertheless, a significant dependency of the tuning response on the degree of polymeric crosslinking of the LCE has been successfully demonstrated. These findings should enable to tailor the spectral tuning range of WGMs in LCE resonators as well as the precision of this tuning to various potential combinations of applied external stimuli and photonic applications.

5.4 Assessment of the spectral tunability of WGMs

In this section, the achieved spectral tunability of WGMs in cavities entirely made from LCE under thermal actuation is assessed. This tunability is compared to that of other cavities made from LCE as well as inelastic resonators made from conventional polymers or silica. Furthermore, the potential usability of these resonators within more complex photonic building blocks is shortly addressed.

Within the context of spectrally tunable LCE cavities, the cavities' increasing radius under an external stimulus is used to tune their resonance wavelengths. Nevertheless, the large expected red-shifts induced by this radius change have been shown to be counteracted by blue-shifts of comparable size due to the negative thermo-optic coefficients of the ordinary and extraordinary refractive indices of the LCE. This fact reduces the potential tunability of such LCE cavities by around one order of magnitude.
Using FTS measurements of WGM resonances in LCE cavities at different actuation temperatures, their tunability under thermal actuation has been studied. For all investigated modes, a significant red-shift under thermal actuation has been demonstrated. For the cavity with highest tunability, a full spectral tuning under a change of the actuation temperature of only 18 K has been shown. Also, an absolute tuning response of more than $1\,\mathrm{nm\,K^{-1}}$ for WGMs near the IR c-band has been found. This spectral tunability nicely matches expectations based on real-time investigations of the cavity radius under thermal actuation in combination with material properties of the LCE reported in literature. It furthermore demonstrates the high potential of spectrally tunable LCE cavities despite their counteraction of expansion and thermo-optic effect.
Next, the reversibility and precision of the demonstrated spectral tuning has been studied. Under repeated small changes of the actuation temperature, a full reversibility and high precision of the modes' spectral positions has been found. The standard deviation of the resonance wavelength of a WGM at a fixed actuation temperature is in the order of the precision of the used laser source. Nevertheless, this deviation is expected to be even smaller under an external stimulus with higher precision.
Finally, a possible route towards a deliberate adjustment of the tuning response of LCE cavities has been introduced. Such an adjustment has been realized via a change of the polymeric degree of crosslinking of the LCE. Doing so, the tuning response has been changed by more than two orders of magnitude.

Compared to tunable LCE ring resonators reported by Nocentini *et al.* [38], a significantly improved tunability of the disk-shaped cavities presented here has been shown. This improvement includes not only a notably larger overall tuning range, but also an enhanced precision of this tuning. Additionally, increased quality fac-

tors compatible with those of inelastic polymeric cavities of up to 6×10^4 have been found. These improvements are mainly attributed to the advancements of the cavities' fabrication process as presented in Sec. 4.4.
Due to the significant improvements in fabrication, the LCE cavities presented in this work also provide a notably higher tunability than resonators made from conventional polymers as poly(methylmethacrylate) (PMMA) or silica. For such inelastic cavities, typical tuning responses under thermal actuation of less than $0.1\,\mathrm{nm\,K^{-1}}$ are found [64, 159, 233].

To fully deploy the potential usage of such tunable LCE resonators in photonic systems, their spectral hysteresis under large actuation cycles needs to be eliminated. As this hysteresis effect is mainly attributed to the visco-elasticity of the polymeric LCE network [151], a reduction of this effect should be feasible based on a change of the composition of the LCE resist.
To enable an integration of the LCE resonators into larger photonic systems, two additional measures are necessary: Firstly, a simplification of the cavities' fabrication process is required. This should be possible using recent advances in the 3D laser printing of LCE structures [196]. As large temperature changes are expected to generally deteriorate the functionality of complex photonic systems, the actuation of LCE cavities should not be realized using a macroscopic heating resistor. Instead, the integration of an organic absorber dye should enable a free-space optical actuation of the resonators [16, 38].

In summary, the here presented LCE resonators offer a very large and precise spectral tunability compared to other polymeric WGM cavities with comparable quality factors. Furthermore, this tunability has been achieved fully on chip scale and can be initiated under the application of various external stimuli. Hence, these cavities yield a high potential as tunable elements in future all-polymeric photonic platforms.

Chapter 6

Tunable coupling of modes in chip-scale photonic molecules

In the following chapter, the variable coupling of photonic molecules (PMs) consisting of disk-shaped WGM resonators on actuating chip-scale LCE substrates is exemplarily demonstrated for two cavities.
In Sec. 6.1, the basic principle of tunable evanescent coupling of WGM cavities with a variable inter-cavity distance is introduced. Herein, a short overview of tunably coupled PMs based on WGM cavities reported in literature within recent years is given and the controllability of the inter-cavity distance of a PM under thermal actuation of an LCE substrate is demonstrated. Afterwards, the system of two tunably coupled WGM cavities is analytically solved using coupled-mode theory in Sec. 6.2: Delocalized supermodes are presented as the solution of the coupled system. The single-fiber transmission spectra of a tunably coupled LCE-PM as well as the intensity transfer through the PM in add-drop configuration are calculated from the driven solutions of the system. In Sec. 6.3, the precisely and widely tunable coupling of the PM is revealed based on experimental data and its coupling strength is computed from mode splittings in FTS measurements. Afterwards, the PM's potential as tunable add-drop filter is demonstrated in Sec. 6.4. The controllability of the intensity transfer through the PM in add-drop configuration is presented by means of 2FTS measurements. Herein, the enhancement of this transferred intensity with the actuation temperature of the substrate is compared to expectations based on coupled-mode theory. Finally, the demonstrated tunable coupling of photonic molecules is shortly assessed with respect to a future upscaling to larger ensembles of coupled cavities as well as an integration of such PMs into more complex photonic systems in Sec. 6.5.

Large parts of the calculations and experimental results presented within this chapter have been obtained in close cooperation with Osman Karayel and Pascal Rietz within their Master's theses [62, 142] and are published in [225].

6.1 Basics of variable evanescent coupling of WGMs

The discrete eigenstates of optical micro cavities in general are comparable to the electronic states of an atom. This is especially true for spherical WGM resonators for which the field distributions of the optical modes are given by a set of spherical harmonics. Although the modes in other micro cavities are given by different sets of solutions (for disk-shaped WGM cavities see Sec. 2.2), the similarity to the electronic states of atoms still holds. Therefore, optical micro cavities are referred to as photonic atoms [242, 243].

In analogy to the formation of molecules from single atoms, ensembles of coupled optical micro cavities are also called photonic molecules [20, 21]. Similarly to the modified electronic states in molecules, the optical eigenstates of photonic molecules are given by so-called supermodes which are spatially delocalized over the whole ensemble of coupled cavities and are spectrally split and shifted in comparison to the single-cavity resonances (see Fig. 6.2(b)). The resonance frequencies of these supermodes as well as additional key characteristics of PMs are computed in Sec. 6.2 for the case of coupled WGMs using CMT.

Within recent years, photonic molecules have been realized from various kinds of optical micro cavities, including photonic crystals [244, 245], plasmonic nano cavities [246], and micro pillars [20]. Herein, the coupling of the single cavities is typically enabled using connective photonic elements as structured waveguides. In comparison therewith, photonic molecules from WGMs are of special interest for future photonic applications (see Sec. 2.3), as their evanescent coupling facilitates a PM formation of nearly arbitrary ensembles of large numbers of cavities as long as all inter-cavity distances are sufficiently small [247].

The possibility of an evanescent coupling of two WGM cavities is inherent to their fundamental physical working principle. Due to the total internal reflection of a WGM at the outer rim of its cavity, a small fraction of the mode is evanescently guided in the cavity's close surrounding (as introduced in Sec. 2.1 and Fig. 2.1). These evanescent fields decay on the length scale of the wavelength and do not carry energy [42]. This however changes, if the evanescent fields penetrate into a dielectric medium in which they can propagate. In this case, a propagating wave is excited inside the penetrated dielectric medium and an energy transfer takes place (compare Fig. 6.2(a)). This process can also be understood in a quantum mechanical picture as tunneling. Within the scope of fiber-transmission spectroscopy, this effect is deployed to realize an efficient coupling between waveguide and resonator mode (see Sec. 3.1.2). Within ensembles of WGM cavities in close spatial proximity, it induces an evanescent but efficient coupling between all single-cavity resonances [20].

A key requirement of various applications of PMs in general is a tunability of the coupling between the single cavities. This can be achieved in real-time via a spectral detuning of the contributing single-cavity resonances using, e.g., optical [248], acousto-optical [249] or electro-optical stimuli [250]. In WGM-based photonic molecules, the coupling strength itself depends on the spatial overlap of the evanescent parts of the single-cavity WGMs [97]. Hence, a more convenient tuning of the PMs' coupling strength regarding future photonic applications is feasible based on an adjustment of their inter-cavity gaps. This is usually achieved by mounting all cavities onto independent piezo actuators [28, 117, 135, 137]. Although this approach offers a very high resolution of the coupling strength, it strongly limits the number of simultaneously coupled resonators. Usually, only two cavities are tunably coupled this way. Furthermore, the overall size of this setup is on the macro scale, which hinders the on-chip integration of such tunably coupled PMs into complex photonic systems.

A first step towards overcoming this issue has been demonstrated by Siegle *et al.* [170]: By mounting several WGM cavities to a macro-scale PDMS elastomer substrate, the flexibility of the substrate under mechanical stress has been used to reversibly change the inter-cavity distances and therefore control the coupling strength. The tunable coupling has been revealed from photoluminescence spectra of delocalized lasing supermodes. Despite the advances of this approach, the application of direct mechanical stress still requires macroscopic mechanical tools.
Within the scope of the present work, a tunably coupled photonic molecule fully on chip scale has been developed via an adaption of the formerly mentioned system. This has been achieved by using chip-scale substrates from liquid crystal elastomers as introduced in Sec. 4.2. These substrates offer a reversible contraction along their pre-defined director under various external stimuli. This contraction can be applied to reversibly adjust the inter-cavity distance and thus the coupling strength of WGM cavities fabricated onto such substrates. As introduced in Sec. 4.5, LCE substrates with domains of independent pre-defined director orientation on the scale of a few micrometer are conceivable due to recent advances in 3D laser printing of LCE [194, 196]. Such substrates are expected to enable a tunable coupling of nearly arbitrary two-dimensional ensembles of WGM cavities on these substrates. Furthermore, this coupling should be controllable under various external stimuli as electric/magnetic fields or illumination.

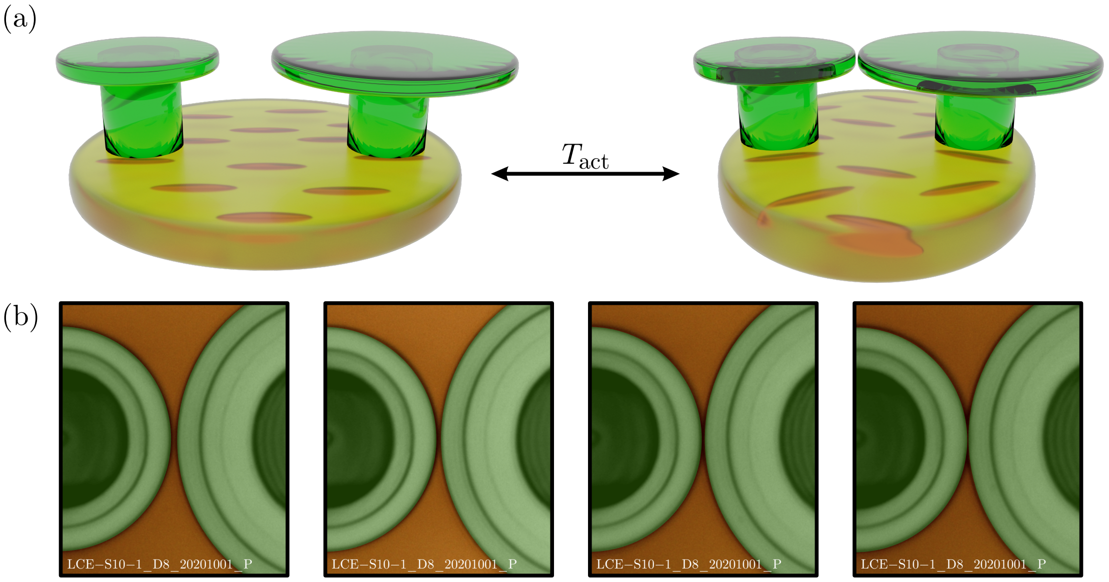

$T_{\mathrm{act}} = 23\,^{\circ}\mathrm{C}$ $T_{\mathrm{act}} = 53\,^{\circ}\mathrm{C}$ $T_{\mathrm{act}} = 61\,^{\circ}\mathrm{C}$ $T_{\mathrm{act}} = 72\,^{\circ}\mathrm{C}$

Figure 6.1: The photonic molecule consisting of two rigid disk-shaped WGM cavities with different radii on an LCE substrate. (a) Illustration of the working principle of the LCE-PM. Due to a decrease of the degree of molecular order, the LCE substrate reversibly contracts along the axis of the PM under local heating. This induces a reduction of the inter-cavity distance with elevating actuation temperature of the substrate T_{act}, leading to an increase of the degree of evanescent coupling. (b) Colored optical micrographs of the inter-cavity gap of an LCE-PM with radii of $R_1 = 20\,\mu\mathrm{m}$ and $R_2 = 30\,\mu\mathrm{m}$ at different actuation temperatures. The inter-cavity distance is reduced from around $2\,\mu\mathrm{m}$ at room temperature below the diffraction limit of the used optical microscope at $72\,^{\circ}\mathrm{C}$. Adapted with permission from [225] © Optica Publishing Group.

To demonstrate the great potential of this approach, a proof-of-principle system is introduced here: Two disk-shaped WGM cavities on a chip-scale LCE substrate with homogeneous director orientation are tunably coupled using the contraction of the LCE under local substrate heating via a macroscopic heating resistor as external stimulus. The fabrication of this LCE-PM has been carried out as described in Sec. 4.2 and Sec. 4.3. An illustration of its working principle as well as exemplary optical micrographs of the gap between two WGM resonators shrinking under elevating actuation temperature T_{act} are shown in Fig. 6.1. (A more detailed investigation of the inter-cavity distance changing with T_{act} is exemplarily given in App. C.1.) An SEM micrograph of an LCE-PM is depicted in Fig. 4.7.
All experimental data presented in this section has been achieved by coupling two size-mismatched WGM cavities with radii of $R_1 = 20\,\mu\mathrm{m}$ and $R_2 = 30\,\mu\mathrm{m}$. These radii have been chosen solely due to experimental convenience. In general, these radii as well as their ratio are only limited by the applied fabrication technique.

Within the proof-of-principle measurements in this work, the coupling of the LCE-PM has always been controlled via thermal actuation of the LCE substrate. The inter-cavity distance at room temperature fluctuates between the different investigated LCE-PMs due to the limitations of the 3DLP fabrication process (see Sec. 4.3). Hence, the absolute actuation temperatures of the different performed measurements are not directly comparable.

6.2 Analytical description using coupled-mode theory

Before the tunability of the LCE-PM's coupling under substrate heating is investigated using FTS measurements in Sec. 6.3 and 2FTS measurements in Sec. 6.4, the system of two tunably coupled WGM cavities is analytically described using coupled-mode theory. First, delocalized supermodes are presented as the eigenstates of the system of coupled harmonic oscillators. Afterwards, the photonic molecule is investigated coupled to one and two optical waveguides. Parts of this analytical description are based on [59, 97, 133, 135], can also be found in Osman Karayel's Master's thesis [62] and are published in [225].

6.2.1 Delocalized supermodes as eigenstates of coupled resonators

The analytical calculation given here models the two tunably coupled WGM resonators as lossy harmonic oscillators with a mutual perturbation η. This setup is also illustrated in Fig. 6.2(a): The overlap of the evanescent fields of the two WGM resonances leads to a mutual perturbation within their coupling region. η depends on the integral over the spatial overlap of the evanescent fields of the two coupled WGMs [97]. Its absolute $|\eta|$ is a coupling strength with the dimension of a frequency. In analogy to Eq. (2.3), the following system of coupled linear differential equations is assumed:

$$\begin{aligned} \frac{\mathrm{d}}{\mathrm{d}t}a_1(t) &= \left(\mathrm{i}\omega_1 - \frac{1}{2\tau_1}\right) a_1(t) - \mathrm{i}\eta^* a_2(t) \\ \frac{\mathrm{d}}{\mathrm{d}t}a_2(t) &= \left(\mathrm{i}\omega_2 - \frac{1}{2\tau_2}\right) a_2(t) - \mathrm{i}\eta a_1(t). \end{aligned} \tag{6.1}$$

Herein, $a_j(t)$ with $j = 1, 2$ are the field amplitudes within the two coupled cavities with resonance frequencies ω_j and intrinsic photon lifetimes τ_j. Using an exponential ansatz, the complex eigenfrequencies

$$\Omega_\pm = -\frac{\mathrm{i}\left(\alpha_1 + \alpha_2\right)}{2} \pm \sqrt{|\eta|^2 - \frac{\left(\alpha_1 - \alpha_2\right)^2}{4}} \tag{6.2}$$

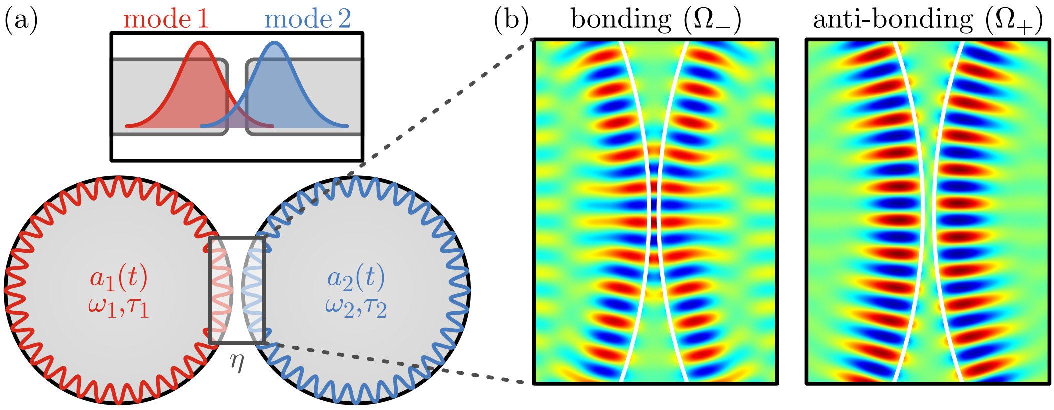

Figure 6.2: Supermodes in evanescently coupled WGM cavities. (a) If two WGM cavities ($j = 1, 2$) with field amplitudes $a_j(t)$, resonance frequencies ω_j and intrinsic photon lifetimes τ_j are in close spatial proximity, their evanescent fields overlap and the modes are coupled. The inset illustrates a cross-section of the coupling region with overlapping evanescent fields. (b) depicts field amplitudes of such coupled WGMs in the (ρ, ϕ)-plane of the cavities calculated using finite-element method. As evident from these simulations, bonding and anti-bonding supermodes form. In case of the bonding modes, field extrema of the same sign face each other in the two disks, inducing a strong field enhancement within the inter-cavity gap. For anti-bonding modes, the opposing field extrema of opposite sign lead to a zero-crossing of the field strength within the gap. The resonance frequency of the bonding/anti-bonding supermode is shifted to lower/higher frequencies in comparison to the uncoupled modes, respectively. (b) adapted from [142].

with $\alpha_j = \mathrm{i}\omega_j - 1/(2\tau_j)$ are found. These eigenvalues correspond to the resonant supermodes of the system of coupled cavities. The real part of $\Omega_\pm$ represents the resonance frequencies of these modes. As commonly known, the coupling of formerly independent modes usually leads to an avoided-crossing behavior. In the calculations presented here, this behavior is apparent in the spectral splitting of the supermodes. Under the assumption of similar intrinsic photon lifetimes $\tau_1 \approx \tau_2$, this splitting is given by

$$\Delta\Omega = \Omega_+ - \Omega_- \approx \sqrt{4\,|\eta|^2 + \Delta\omega^2}. \tag{6.3}$$

If the spectral distance of the uncoupled modes $\Delta\omega = \omega_1 - \omega_2$ is small compared to the coupling strength $|\eta|$, the spectral splitting of the supermodes is approximately equal to the coupling strength (Herein, $\omega_1 \geq \omega_2$ has been chosen without loss of generality.). For small spectral splittings compared to the resonance frequencies themselves (meaning $\Delta\omega \ll \omega_1, \omega_2$ and $\Delta\Omega \ll \Omega_+, \Omega_-$), the coupling strength can also be calculated from the uncoupled ($\Delta\lambda = \lambda_2 - \lambda_1$) and coupled ($\Delta\Lambda = \Lambda_- - \Lambda_+$) spectral splittings in the wavelength regime:

$$|\eta| \approx \frac{c\pi}{\lambda_\mathrm{c}^2}\sqrt{\Delta\Lambda^2 - \Delta\lambda^2} \tag{6.4}$$

with the speed of light c and a central wavelength $\lambda_\mathrm{c} = (\lambda_2 - \lambda_1)/2$. Equation (6.4) is used in Sec. 6.3 to calculate the coupling strength of a tunably coupled LCE-PM from mode splittings in single-fiber transmission spectra.
Physically, the two solutions to the set of differential equations in Eq. (6.1) can be understood as a so-called bonding and an anti-bonding supermode (labeled in analogy with electronic states in atoms). These modes differ by their relative orientation of the field distributions within the coupling region of the two cavities under consideration. In case of the bonding supermode $(-)$, extrema of the same sign oppose each other in both resonator disks. The constructive superposition of the amplitudes of the single modes leads to a field enhancement within the air-filled gap and a smaller resonance frequency. For anti-bonding supermodes $(+)$, the opposing field extrema of opposite sign induce a zero crossing of the field amplitude within the gap and shift the resonance frequency to higher values. These different kinds of supermodes are also illustrated by results from finite-element method simulations in Fig. 6.2(b).

The localization of these supermodes is investigated based on the eigenvectors to the eigenvalues given in Eq. (6.2). These eigenvectors are given by

$$\begin{pmatrix} a_1(t) \\ a_2(t) \end{pmatrix} = C_+ \begin{pmatrix} -\Delta\omega_\mathrm{mean} \\ \eta \end{pmatrix} \exp\left(\mathrm{i}\Omega_+ t\right) + C_- \begin{pmatrix} \eta^* \\ \Delta\omega_\mathrm{mean} \end{pmatrix} \exp\left(\mathrm{i}\Omega_- t\right). \tag{6.5}$$

with unknown normalization factors $C_\pm$ and $\Delta\omega_\mathrm{mean}$ being the mean of the spectral splittings with and without coupling:

$$\Delta\omega_\mathrm{mean} = \frac{\Delta\omega + \Delta\Omega}{2}. \tag{6.6}$$

By inverting Eq. (6.5), the field amplitudes $C_\pm \exp\left(\mathrm{i}\Omega_\pm t\right)$ of the two supermodes are found:

$$\begin{pmatrix} C_+ \exp\left(\mathrm{i}\Omega_+ t\right) \\ C_- \exp\left(\mathrm{i}\Omega_- t\right) \end{pmatrix} = \frac{1}{\Delta\omega_\mathrm{mean}^2 + |\eta|^2} \left[\begin{pmatrix} -\Delta\omega_\mathrm{mean} \\ \eta \end{pmatrix} a_1(t) + \begin{pmatrix} \eta^* \\ \Delta\omega_\mathrm{mean} \end{pmatrix} a_2(t) \right]. \tag{6.7}$$

Equation (6.7) describes the composition of the field amplitude of each supermode from the field amplitudes $a_j(t)$ localized within the single cavities $(j = 1, 2)$.
In the absence of coupling $(\eta = 0)$, $\Delta\omega_\mathrm{mean}$ is equal to $\Delta\omega$ and Eq. (6.7) describes two uncoupled WGMs each propagating in its own cavity. For an increasing coupling $(\eta > 0)$, the field amplitude of each supermode is non-zero in both cavities. In the theoretical limit of an infinite coupling $(\eta \to \infty)$, both η and $\Delta\omega_\mathrm{mean}$ are equal. In this case, also the absolute value of the field amplitude of each supermode is equal in both cavities, indicating a perfect delocalization of the supermodes. In general, the ratio of $|\eta|^2$ and $\Delta\omega_\mathrm{mean}^2$ can be used as a measure for the delocalization of the intensity of supermodes. This ratio ranges from 0 in the case of no coupling to 1 in the case of an infinitely strong coupling.

6.2.2 Fiber-transmission spectra under waveguide excitation

In Sec. 6.3, the tunable coupling of an LCE-PM is investigated using fiber-transmission spectroscopy with one tapered optical fiber. Therefore, this waveguide is now included into the analytical calculations.

In the following, a measurement configuration as introduced in Sec. 3.1 and Fig. 3.1(b) with two coupled WGM cavities instead of a single one is considered. In analogy to the analytical description of FTS of a single cavity (see Sec. 3.1.1), the waveguide is assumed to be coupled to WGM cavity 1 by a coupling coefficient of μ_{in}, therefore introducing an additional loss accommodated for by the photon lifetime $\tau_{\mathrm{in}} = |\mu_{\mathrm{in}}|^{-2}$ and carrying a waveguide mode $s_{\mathrm{i}}(t) = S_0 \exp \mathrm{i}\omega t$ propagating from the input port towards the LCE-PM. This leads to a modification of the system of coupled differential equations in Eq. (6.1):

$$\begin{aligned}\frac{\mathrm{d}}{\mathrm{d}t}a_1(t) &= \left(\mathrm{i}\omega_1 - \frac{1}{2\tau_1} - \frac{1}{2\tau_{\mathrm{in}}}\right) a_1(t) - \mathrm{i}\eta^* a_2(t) - \mathrm{i}\mu_{\mathrm{in}} S_0 \exp \mathrm{i}\omega t \\ \frac{\mathrm{d}}{\mathrm{d}t}a_2(t) &= \left(\mathrm{i}\omega_2 - \frac{1}{2\tau_2}\right) a_2(t) - \mathrm{i}\eta a_1(t).\end{aligned} \tag{6.8}$$

Since the LCE-PM is driven by the external frequency ω, only the particulate solution of these equations is of interest. The expected transmission dip of a tunably coupled LCE-PM within FTS measurements can be estimated from the transmission at the through port of the incoupling fiber. This transmission is computed following Eq. (3.5) and (3.6):

$$T_{\mathrm{t}}(\omega) = \left|\frac{s_{\mathrm{t}}(t)}{s_{\mathrm{i}}(t)}\right|^2 = \left|1 - \frac{|\mu_{\mathrm{in}}|^2}{\mathrm{i}\left(\omega - \omega_1\right) + \frac{1}{2}\tau_1^{-1} + \frac{1}{2}\tau_{\mathrm{in}}^{-1} + \frac{|\eta|^2}{\mathrm{i}(\omega-\omega_2)+\frac{1}{2}\tau_2^{-1}}}\right|^2 . \tag{6.9}$$

This equation is significantly more complex than in the case of a single cavity (see Eq. (3.6)) and can not be analytically evaluated without additional effort. Nevertheless, in the limit of a vanishing inter-cavity coupling ($\eta \rightarrow 0$), Eq. (3.6) of the FTS transmission dip of a single WGM cavity is reproduced. In Sec. 6.3, Eq. (6.9) is plotted for different values of $|\eta|$ and compared to experimental FTS spectra of a tunably coupled LCE-PM in Fig. 6.3(b).

6.2.3 Intensity transfer through a PM in add-drop configuration

As a next step, an additional outcoupling fiber is assumed to be evanescently coupled by μ_{out} to cavity 2. The possible energy transfer from cavity 2 into the outcoupling fiber is accommodated for by an additional photon lifetime $\tau_{\mathrm{out}} = |\mu_{\mathrm{out}}|^{-2}$ of that cavity. As this waveguide does not carry a mode (except of what is coupled from the LCE-PM itself), it is included into the system of differential equations in Eq. (6.8) as it follows:

$$\begin{aligned}\frac{\mathrm{d}}{\mathrm{d}t}a_1(t) &= \left(\mathrm{i}\omega_1 - \frac{1}{2\tau_1} - \frac{1}{2\tau_{\mathrm{in}}}\right) a_1(t) - \mathrm{i}\eta^* a_2(t) - \mathrm{i}\mu_{\mathrm{in}} S_0 \exp \mathrm{i}\omega t \\ \frac{\mathrm{d}}{\mathrm{d}t}a_2(t) &= \left(\mathrm{i}\omega_2 - \frac{1}{2\tau_2} - \frac{1}{2\tau_{\mathrm{out}}}\right) a_2(t) - \mathrm{i}\eta a_1(t).\end{aligned} \tag{6.10}$$

Within the context of 2FTS measurements, the coupled system again follows the external driving frequency, hence only the particulate solution is of interest. For the transmission to the through port at the end of the incoupling fiber, Eq. (6.9) with the substitution $1/(2\tau_2) \rightarrow 1/(2\tau_2) + 1/(2\tau_{\mathrm{out}})$ is reproduced. As also demonstrated in Sec. 3.2 and Fig. 3.5 for the case of 2FTS measurements on single WGM cavities, this mainly increases the FWHM of the transmission dips.

To investigate the intensity transfer through a tunably coupled LCE-PM in add-drop configuration, the waveguide mode to the drop port at the end of the outcoupling fiber is of interest. In analogy to the analytical description of 2FTS measurements of a single cavity, the amplitude of this mode can be computed using Eq. (3.10). The relative intensity at the drop port is given by:

$$\begin{aligned} I_{\mathrm{d}}(\omega) &= \left|\frac{s_{\mathrm{d}}(t)}{s_{\mathrm{i}}(t)}\right|^2 \\ &= \left|\frac{\mathrm{i}\mu_{\mathrm{in}}\mu_{\mathrm{out}}^*\eta}{\left[\mathrm{i}\left(\omega-\omega_1\right) + \frac{1}{2}\tau_1^{-1} + \frac{1}{2}\tau_{\mathrm{in}}^{-1}\right] \times \left[\mathrm{i}\left(\omega-\omega_2\right) + \frac{1}{2}\tau_2^{-1} + \frac{1}{2}\tau_{\mathrm{out}}^{-1}\right] + |\eta|^2}\right|^2 .\end{aligned} \tag{6.11}$$

(**Note:** The same result can be obtained using energy conservation: To compute the mode amplitude at the drop port, the amplitude at the through port as well as the intrinsic losses of both cavities are subtracted from the amplitude of the input mode. The intensity at the through port has been calculated earlier, the intrinsic losses can be directly calculated from the particulate solutions of the amplitudes of both cavity modes. [225])

The relative amplitude at the drop port given in Eq. (6.11) can again not be analytically evaluated in an easy manner. To still get a feeling of the dependency of the relative transferred intensity on the various physical parameters, Eq. (6.11) is plotted for different sets of these parameters in App. C.3. In Sec. 6.4.2, Eq. (6.11) is simplified based on several assumptions and compared to experimental data of the intensity transfer through a tunable coupled LCE-PM.

6.3 Tunable coupling determined from resonance splittings of supermodes

The tunable coupling of an LCE-PM is now demonstrated experimentally and compared to its analytical description. The investigated LCE-PM consists of two size-mismatched cavities with radii of $R_1 = 20\,\mu\text{m}$ and $R_2 = 30\,\mu\text{m}$, similar to that shown in the SEM micrograph in Fig. 4.7. The working principle is demonstrated in Fig. 6.1(a).
The reversible coupling of the WGMs under thermal actuation of the LCE substrate is revealed based on the evidence of the generation of delocalized supermodes in FTS spectra. Afterwards, the coupling strength $|\eta|$ as well as its change with increasing actuation temperature T_{act} is derived from the spectral splitting of these supermodes.

Parts of the results presented here have been achieved in close cooperation with Osman Karayel and Pascal Rietz within the scope of their Master's theses [62, 142] and are published in [225, 251, 252].

6.3.1 Spectral splitting of resonant supermodes induced by thermal substrate actuation

The tunable evanescent coupling of an LCE-PM is experimentally demonstrated via the generation of delocalized supermodes. Single-fiber transmission spectra of such an LCE-PM are compared to analytical calculations based on CMT.

As the actuation temperature of the LCE substrate and therefore the coupling strength $|\eta|$ are gradually increased, a continuous transition from independent single-cavity resonances into delocalized supermodes of the coupled PM is expected. This transition should be accompanied by an increasing spectral splitting of the bonding and anti-bonding supermode $\Delta\Lambda$ (see Eq. (6.4)) as well as a decreasing asymmetry of the field amplitudes of each supermode within the two cavities (see Eq. (6.7)). The asymmetry of the depth of detected transmission dips is however only indirectly connected to the asymmetry of the field amplitudes given in Eq. (6.7). Nevertheless, the dips' asymmetry is expected to vanish in case of strong coupling ($|\eta| \to \infty$) and can thus be used as a qualitative indicator for the degree of delocalization of the supermodes. Furthermore, single-cavity resonances should be detectable in only one of the two cavities, while delocalized supermodes are expected to appear in the fiber-transmission spectra of both resonators.

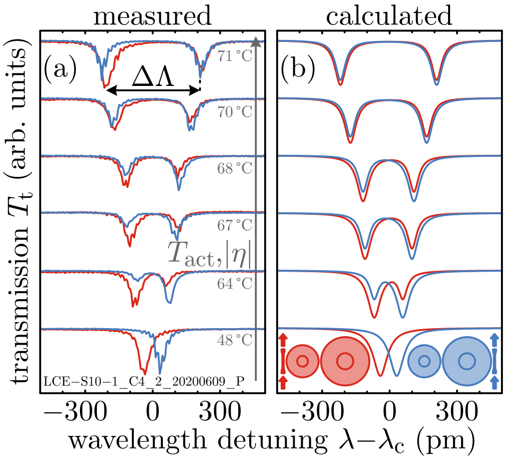

Figure 6.3: Demonstration of the generation of delocalized supermodes due to evanescent coupling. With elevating actuation temperature T_{act}, the inter-cavity distance is reduced and the coupling strength $|\eta|$ is increased. (a) depicts FTS spectra of an LCE-PM at different exemplary T_{act} between 48 °C and 71 °C. The two spectra at each temperature step represent measurements with the fiber coupled to either one of the two cavities consecutively. (red/blue: fiber coupled to small/large cavity, respectively. See pictograms in (b).) While for weak coupling two spectrally close but independent WGMs are detected in the cavities, two resonances are found in each cavity for high $|\eta|$. The asymmetry of the depth of the two dips within one spectrum decreases with increasing $|\eta|$. A spectral splitting $\Delta\Lambda$ of the supermodes is evident. In (b), corresponding fiber-transmission spectra are calculated using Eq. (6.9). Required fitting parameters are derived from the experimental data in (a) and critical fiber-resonator coupling has been assumed. A strong similarity of the measured and calculated spectra is apparent, including the asymmetry of the resonance dips. The slight deviations of the absolute depth of the dips are caused by a changing fiber-resonator coupling. (a) sample fabrication and measurement performed by Pascal Rietz [142] and data partly published in [225], (b) adapted from [62].

The mode structure of an LCE-PM under elevating substrate temperature is investigated using single-fiber transmission spectroscopy. To gain a more thorough understanding of the mode structure, two spectra with the fiber coupled to each of the two WGM cavities have been detected consecutively and are compared. Figure 6.3(a) depicts fiber-transmission spectra of a tunably coupled LCE-PM at six exemplary actuation temperatures ranging from $T_{act} = 48\,°C$ to $71\,°C$. An allocation of the two spectra at each temperature step to their measurement configuration (red/blue: fiber coupled to small/large cavity, respectively) is given by the color-coded pictograms in Fig. 6.3(b).

In the case of a low substrate actuation temperature, two nearly degenerate but independent single-cavity resonances are found in the two cavities. As T_{act} (and therefore also $|\eta|$) is increased, two resonance dips appear in each spectrum, indi-

cating the beginning of a gradual delocalization of the now coupling modes. Also, a slightly larger spectral distance of the two dips is found. The depth of the dips of each spectrum is still strongly asymmetric.
Increasing the coupling strength even further, both effects get more pronounced. In case of the highest actuation temperature of 71 °C, the two transmission dips are nearly symmetric in both spectra. The spectral distance is more than 5 times larger than that of the uncoupled modes. This spectral distance of the two dips in the spectra directly corresponds to the resonance splitting $\Delta\Lambda$ of the bonding and anti-bonding supermode given in Eq. (6.4).
Furthermore, a maximum delocalization ratio of $|\eta|^2 / \Delta\omega_{\text{mean}}^2 = 0.69$ is calculated from the spectral splitting of the supermodes using Eq. (6.6). This value gives the ratio of the intensities of a supermode localized within either of the two cavities and thus further supports the hypothesis of strongly delocalized supermodes.
In summary, the increasing spectral distance of the transmission dips in combination with their approximately symmetric depths and the high calculated delocalization ratio clearly proofs the gradual generation of delocalized supermodes under thermal actuation of the LCE substrate.

To get a better understanding whether the detected asymmetry matches its analytical description given in Sec. 6.2.1, the measured spectra are compared to the analytically calculated transmission at the through port given in Eq. (6.9). Respective calculated spectra are depicted in Fig. 6.3(b).
To calculate these spectra, the uncoupled resonance wavelengths of the two contributing WGMs as well as their intrinsic photon lifetimes have been estimated from Lorentzian fits to the transmission dips of the measured spectra in the uncoupled case. Furthermore, a critical fiber-resonator coupling $|\mu_{\text{in}}|$ has been assumed. The inter-cavity coupling strength $|\eta|$ has been computed from the experimental spectral splittings following Eq. (6.4). (Hence, a perfect matching of the spectral splittings of the two data sets is pre-defined.)
Comparing the calculated spectra in Fig. 6.3(b) to the experimentally detected ones in Fig. 6.3(a), the general shape of the spectra as well as the asymmetry of the two resonance dips within one spectrum show a strong similarity between the two data sets. This resemblance again confirms the formation of delocalized supermodes due to a tunable evanescent coupling of the WGM cavities. It furthermore also confirms the utility of the analytical description based on coupled-mode theory given in Sec. 6.2.

6.3.2 Exponential behavior of the coupling strength

After the tunable evanescent coupling of the LCE-PM has been revealed via the formation of delocalized bonding and anti-bonding supermodes in the previous section, the change of the coupling strength $|\eta|$ with increasing actuation temperature is now investigated in detail. This is done using the spectral splitting of the already discussed delocalized supermodes in FTS spectra.
Based on common properties of the LCE, an approximately linear contraction of the substrate in the investigated temperature regime is expected [189]. (This assumption is further supported by the linear change of the resonance wavelength under thermal tuning of WGM cavities entirely made from the same LCE material demonstrated in Fig 5.2.) As the coupling strength is proportional to the spatial overlap of the exponentially decaying evanescent fields of the WGMs [97, 133], the expected linear decrease of the inter-cavity distance with elevating substrate actuation temperature should lead to an exponential increase of the LCE-PM's coupling strength $|\eta|$.

To investigate the coupling strength $|\eta|$, the resonance splitting of the bonding and anti-bonding supermode is determined from single-fiber transmission spectra as already introduced in Fig. 6.3(a). In the coupled regime at high actuation temperature, this spectral splitting $\Delta\Lambda$ is deduced from each of the FTS spectra with the fiber coupled to one of the two WGM cavities. In the uncoupled regime, the spectral distance of the independent single-cavity WGMs $\Delta\lambda$ is determined by comparing the two spectra measured at one value of T_{act}. This is also illustrated in Fig. 6.4(a), where FTS spectra detected in the uncoupled (48 °C, bottom) and coupled (72 °C, top) regime are depicted including applied Lorentzian fits. An allocation of the spectra to their respective measurement configuration is given by the color-coded pictograms. Again, the appearance of two resonance dips in each of the spectra in the coupled regime is visible. For the spectra in the uncoupled/coupled regime, the spectral distance of the single-cavity WGMs/spectral splitting of the bonding and anti-bonding supermode is indicated, respectively.
The change of the resonance splitting with elevating T_{act} is investigated for several temperature steps between $T_{\mathrm{act}} = 48\,^{\circ}\mathrm{C}$ and $72\,^{\circ}\mathrm{C}$, as depicted in Fig. 6.4(b). Herein, the very first and last data points correspond to the spectra shown in Fig. 6.4(a). In the uncoupled regime (gray area), the spectral distance of the independent single-cavity WGMs is plotted (As this spectral distance has been computed by comparing two consecutively detected spectra, the precision of these data points is given by the absolute wavelength precision of the used laser source.). In the coupling regime, an significant increase of the resonance splitting $\Delta\Lambda$ is evident. By elevating the actuation temperature, the resonance splitting of the supermodes is increased in a continuous and super-linear manner to more than 5 times the spectral distance of the single-cavity WGMs.

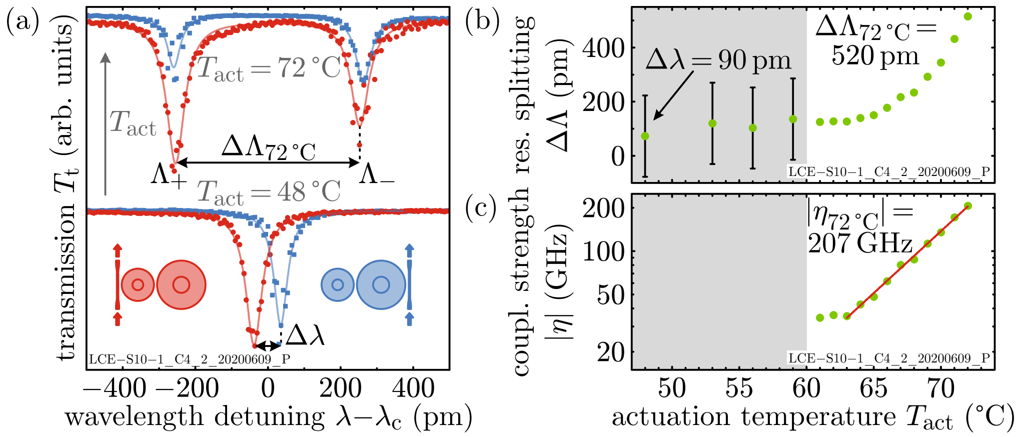

Figure 6.4: Exponential change of the coupling strength with elevating actuation temperature. (a) FTS spectra around a (temperature-dependent) center wavelength λ_c at two exemplary T_{act} of 48 °C and 72 °C (compare Fig. 6.3(a)). At each T_{act}, two spectra with the fiber coupled to either one of the two cavities have been detected consecutively (see color-coded pictograms) and Lorentzian fits have been applied. At low T_{act}, the spectral distance $\Delta\lambda$ of the uncoupled single-cavity WGMs is determined from the two independent spectra. At high T_{act}, the spectral splitting $\Delta\Lambda$ of the delocalized bonding (Λ_-) and anti-bonding (Λ_+) supermode can be computed from each single spectrum separately. (b) In the uncoupled regime (gray area), $\Delta\lambda$ does not depend on the actuation temperature of the substrate. In the coupled regime above 60 °C, the resonance splitting $\Delta\Lambda$ shows a super-linear increase with T_{act}. The maximum of $\Delta\Lambda$ is more than 5 times $\Delta\lambda$. (c) The coupling strength $|\eta|$ is computed from the resonance splitting in the coupled regime in (b) using Eq. (6.4) and depicted versus T_{act} on a semi-logarithmic scale. For substrate temperatures above 63 °C, a nearly perfect exponential behavior up to more than 200 GHz is found, as indicated by the applied linear fit. This exponential increase meets the expectations based on the exponential nature of the evanescent fields of the WGMs. Reprinted with permission from [225] © Optica Publishing Group.

Finally, the coupling strength $|\eta|$ is computed for each actuation temperature using Eq. (6.4) and depicted versus T_{act} on a semi-logarithmic scale in Fig. 6.4(c). Herein, the spectral distance at an actuation temperature of 48 °C is used as $\Delta\lambda$ of the uncoupled case for all T_{act}. In general, this choice is critical due to a possible temperature dependency of the single-cavity resonance wavelengths. In the presented case however, this temperature dependency is negligible, as shown in App. C.2. As the calculation of a coupling strength is not reasonable in the uncoupled regime for $T_{act} < 60\,°C$, no data is presented in the gray area.

For $61\,°C < T_{act} < 63\,°C$, the coupling strength seems to be approximately constant. This is attributed to the fact that the change of $\Delta\Lambda$ due to an increasing coupling strength $|\eta|$ is still on the same scale as the inaccuracy of $\Delta\lambda$. For larger actuation temperatures however, a nearly perfect exponential increase of $|\eta|$ with the the sub-

strate actuation temperature is found. This is also illustrated by the applied linear fit. The exponential behavior of $|\eta|$ perfectly matches the expectations based on the exponential nature of the WGMs' evanescent fields.
As apparent from the fit applied in the coupling regime, the coupling strength $|\eta|$ of the presented LCE-PM can be changed by a factor of 2 under a temperature change of only 3.5 K. Furthermore, a maximum coupling strength of more than 200 GHz has been realized.
A quantitative comparison of the achieved coupling to that of other (tunably) coupled WGM-based photonic molecules is given in Sec. 6.5. Based on the inter-cavity distance of such LCE-PMs at room temperature (see Fig. 6.1(a)) and the change of this distance with the actuation temperature (see App. C.1), the achieved coupling strength is expected to be close to the maximum achievable coupling of the investigated modes in the case of touching cavities. This maximum coupling strength could however be increased by, e.g., a decrease of the radii of the WGM cavities.

The coupling strength of 207 GHz has been achieved fully on chip scale in a tunable and reversible manner by heating the substrate of the uncoupled LCE-PM from room temperature by around 50 K. This clearly demonstrates the great potential of the presented LCE-PM as a precisely and widely tunable PM in future photonic applications.

6.4 Chip-scale photonic molecules as tunable add-drop filters

After the widely and precisely tunable coupling of the presented chip-scale LCE-PM has been demonstrated in the previous section, here a route towards a possible application of this tunability is presented. To that end, the controllable intensity transfer through an add-drop filter based on an LCE-PM is revealed using 2FTS spectra. At first, the generation of delocalized supermodes is shown to be a fundamental requirement of any intensity transfer through the LCE-PM. Afterwards, the controllability of the amount of transferred intensity using the actuation temperature of the substrate as stimulus is demonstrated. The dependency of this transferred intensity on T_{act} is compared to expectations based on the analytical calculations introduced in Sec. 6.2.3.

The results presented in this section have again been achieved using a pair of size-mismatched WGM cavities with radii of $R_1 = 20\,\mu\mathrm{m}$ and $R_2 = 30\,\mu\mathrm{m}$. This PM has been investigated using 2FTS measurements as introduced in Sec. 3.2. Within such 2FTS spectra, both fiber-resonator couplings $|\mu_{\mathrm{in}}|$ and $|\mu_{\mathrm{out}}|$ strongly influence the transferred intensity. To compare the amount of transferred intensity in different measurements, this influence needs to be taken into account. This is however only feasible in an averaging manner as explained in detail in App. C.5. All measurements presented in this section have been normalized following this approach. Unfortunately, this averaged normalization causes a significant scattering of the experimental data. Nevertheless, this scattering is mainly attributed to the applied measurement approach of 2FTS and is therefore not an issue inherent to the performance of an LCE-PM itself.

Parts of the results in this section have been achieved in close cooperation with Pascal Rietz within his Master's thesis [142] and are published in [225].

6.4.1 Reversible generation of resonant supermodes as requirement for intensity transfer

To demonstrate the generation of delocalized supermodes to be the fundamental requirement causing the intensity transfer through a tunably coupled LCE-PM, the transferred intensity I_d in the coupled regime at high temperature is compared to the single-fiber transmission spectra of the two WGM cavities. An exemplary measurement is depicted in Fig. 6.5(a). The configuration of the performed measurement is illustrated by the color-coded pictogram. The choice of incoupling and outcoupling waveguide is arbitrary and not expected to influence the following results.

For both single-fiber transmission spectra, a large number of Lorentz-shaped resonance dips within the expected free spectral ranges of $\Delta\lambda_{\mathrm{FSR},1} \approx 12\,\mathrm{nm}$ and $\Delta\lambda_{\mathrm{FSR},2} \approx 8\,\mathrm{nm}$ are apparent. Regarding the transferred intensity, fewer but also Lorentz-shaped peaks appear. These peaks only exist at spectral positions of pronounced resonance dips in both single-fiber transmission spectra.
A magnified depiction of the peaks and dips highlighted by a green background is given in the center plot of Fig. 6.5(b). Herein, the supermode character of the regarding resonances becomes apparent: Both single-fiber transmission spectra show two spectrally close resonance dips with an approximately inverted asymmetry of their amplitudes. This perfectly matches the appearance of delocalized supermodes as calculated in Eq. (6.9) and demonstrated in Fig. 6.3 and Fig. 6.4(a).
The transferred intensity shows two Lorentzian peaks of approximately similar height at the same two spectral positions. This observation generally matches the expectations based on Eq. (6.11) (compare App. C.3) and therefore again demonstrates the experimentally found intensity transfer to be induced by the generation of delocalized supermodes.

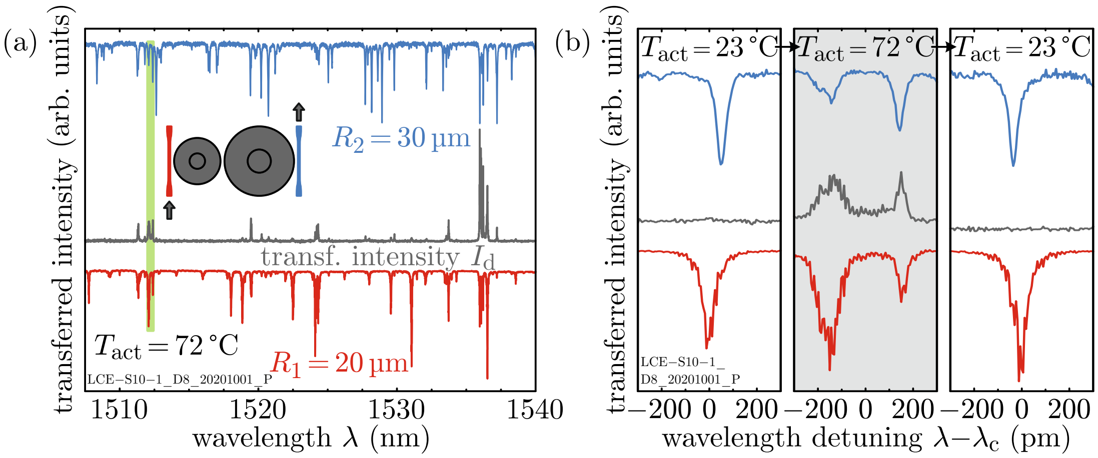

Figure 6.5: Delocalized supermodes as fundamental requirement for an intensity transfer through an LCE-PM in 2FTS measurements. (a) Single-fiber transmission spectra of both cavities (blue/red) and the 2FTS intensity transfer through the LCE-PM (gray) at an elevated T_{act} of 72 °C are plotted. (Measurement configuration given by color-coded pictogram.) In both single-fiber transmission spectra, several resonance dips are present. In the transferred intensity, a comparably small number of peaks appears. These peaks only exist at spectral positions, for which dips are found in both single-fiber spectra. This indicates the generation of delocalized supermodes to induce the energy transfer (compare Sec. 6.3). In (b), a detailed investigation of peaks and dips in (a) (highlighted by green background) is performed. For this spectral region around a (temperature dependent) central wavelength λ_c, all three spectra are depicted at high T_{act} (middle), as well as at room temperature prior to (left) and after (right) substrate heating. Prior to heating, spectrally close but independent single-cavity WGMs (compare Fig. 6.3(a) and Fig. 6.4(a)) and no intensity transfer are found. At increased T_{act}, delocalized supermodes with asymmetric resonance dips are found in the single-fiber spectra. The 2FTS spectrum shows two peaks of comparable height at the same spectral positions. The slightly smaller amplitude of the left peak can be attributed to its smaller quality factor (see Eq. (6.11)). Comparing the spectra after and prior to heating, the reversibility of the tunable coupling is obvious. (a) data partly published in [225] © Optica Publishing Group, (b) reprinted from [251, 252].

As the absolute values of the fiber-resonator couplings $|\mu_{\text{in,out}}|$ do significantly influence the curve shape of the transferred intensity and are not known, a direct comparison of the experimental data in Fig. 6.5 with Eq. (6.11) is spared here. Nevertheless, the small height difference of the two intensity peaks can be attributed to the also differing quality factors that are evident from their FWHMs. The existence of what seems to be single peaks of transferred intensity in Fig. 6.5(a) is attributed to a small coupling strength compared to the respective intrinsic losses inducing a resonance splitting smaller than the modes' FWHM.

Comparing the spectra at elevated temperature in Fig. 6.5(b) with those prior to (left) and after (right) substrate heating, the intensity transfer due to the reversible generation of delocalized supermodes is further validated: As in the case of the FTS spectra in Fig. 6.4(a), spectrally close but independent single-cavity WGM resonances are found at low actuation temperatures. As these modes are not coupled, no intensity transfer through the LCE-PM is detected. This holds for the entire spectral range investigated in Fig. 6.5(a), compare Fig. 6.6.
Comparing only the spectra prior to and after heating, also the high reversibility of the tunable coupling of the cavities is obvious.

In combination, all these findings clearly demonstrate the controllable intensity transfer through the presented LCE-PM via the generation of supermodes delocalized over both tunably coupled WGM cavities.

While the presented 2FTS spectra have already been used to demonstrate the controllable intensity transfer through the LCE-PM, they are also expedient for a reliable identification of delocalized supermodes. This is directly evident from the fact that in Fig. 6.5(a) there are spectral positions where at least one single-fiber transmission spectrum shows a resonance dip but no transferred intensity is detected. In these cases, single-cavity WGMs that are not part of a delocalized supermode due to a lack of a coupling partner are detected in the single-fiber transmission spectra. Using solely these single-fiber transmission spectra, such modes can only be distinguished from delocalized supermodes by performing an elaborated analysis of their behavior under an increasing coupling strength $|\eta|$ as done in Sec. 6.3. Using an additional 2FTS spectrum on the other hand, delocalized supermodes can be easily and reliably identified as only such supermodes induce an intensity transfer. Therefore, 2FTS spectra are a very useful approach for the general characterization of WGM-based photonic molecules.

6.4.2 Enhancement of the transferred intensity with increasing coupling strength

After demonstrating the reversible generation of delocalized supermodes to induce the intensity transfer through a tunably coupled LCE-PM, the dependency of this intensity I_d on the actuation temperature T_act is investigated in detail. This is done by comparing the intensity transfer in 2FTS spectra of an LCE-PM at different actuation temperatures of the substrate. Such spectra are depicted in Fig. 6.6. The measurement configuration is illustrated by the pictogram. As the data has been normalized for the fiber-resonator couplings in an averaging manner (also see App. C.5),

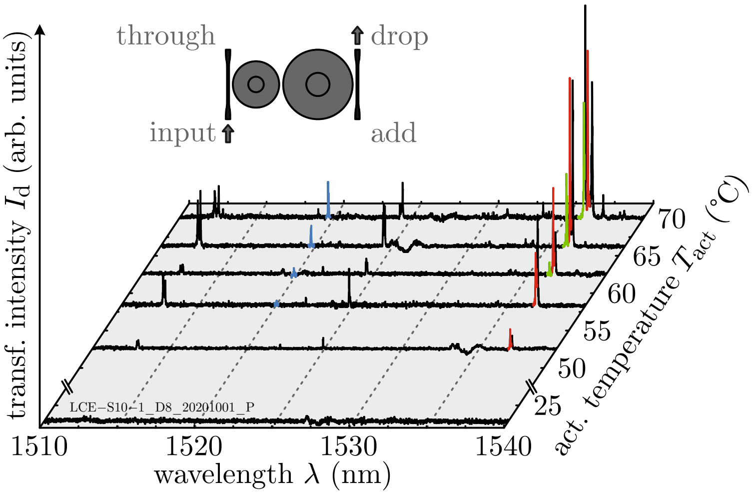

Figure 6.6: 2FTS spectra demonstrating the enhancement of intensity transferred through an LCE-PM under substrate heating. The intensity I_d transferred from the input port to the drop port (see pictogram) is depicted for different actuation temperatures T_act. These intensities have been corrected for the fiber-resonator couplings in an averaging manner as described in App. C.5. At room temperature, no intensity transfer is detected. Elevating T_act above around 50 °C, several peaks arise. Going to even higher T_act, both the number as well as the height of the peaks generally increase. For some peaks, e.g. at $\lambda \approx 1512\,\mathrm{nm}$, also the spectral splitting into two peaks of bonding and anti-bonding supermodes is visible. From room temperature to $T_\mathrm{act} = 72\,°\mathrm{C}$, an enhancement of transferred intensity by a factor of more than 50 has been achieved. For the three highlighted peaks, the change of the maximum intensity transfer with increasing T_act is investigated in detail in Fig. 6.7. Reprinted with permission from [225] © Optica Publishing Group.

not the absolute peak heights of different supermodes but only the relative changes of each single supermode with the actuation temperature are of interest.

At an actuation temperature close to room temperature, no intensity transfer is found. This matches the fact that due to the room-temperature inter-cavity distance of around 2 µm, no evanescent coupling of the WGM cavities is expected.
Heating the substrate above around 50 °C, few small intensity peaks arise. Elevating T_act even further, both the height of these peaks as well as the overall number of peaks generally increases. This is reasonable due to the general increase of I_d with the coupling strength $|\eta|$ (see Eq. (6.11) and (6.12) as well as App. C.3). For some intensity peaks (e.g. at $\lambda \approx 1512\,\mathrm{nm}$), the spectral splitting into a bonding and anti-bonding supermode is large enough to be visible. Comparing the maximum intensity transfer at $T_\mathrm{act} = 72\,°\mathrm{C}$ with the detected noise at room temperature, an enhancement of I_d by a factor of more than 50 has been achieved. This enhancement factor demonstrates the great potential of these LCE-PMs in applications such as tunable filters.

Regarding the three supermodes highlighted in Fig. 6.6, also strong differences are apparent: The red supermode already shows a significant intensity transfer at comparably low actuation temperatures, while both the blue and green mode only become apparent at higher values of T_{act}. These differences are mainly attributed to the differing amplitudes and extents of the evanescent fields of different WGMs. Comparing the peak heights at the two highest actuation temperatures for each mode, also certain differences are visible. While both the blue and the green mode still show a large increase of intensity transfer between these two measurements, the red supermode seems to a approach a threshold value. To further understand this issue, the presented experimental data is compared to the analytical calculations in Sec. 6.2.3.

As derived from CMT in Sec. 6.2.3, the intensity transfer through an LCE-PM in add-drop configuration is given by Eq. (6.11). This equation can not be easily evaluated. To still get a feeling for the dependency of the transferred intensity on the actuation temperature, additional assumptions have to be made: Equation (6.11) is evaluated for the case of resonators with identical resonance frequencies ($\omega_1 = \omega_2 =: \omega_0$) and intrinsic losses ($\tau_1 = \tau_2 =: \tau$). Both fiber-resonator coupling coefficients are assumed to be equal ($\mu_{\mathrm{in}} = \mu_{\mathrm{out}} =: \mu$ and therefore $\tau_{\mathrm{in}} = \tau_{\mathrm{out}} =: \tau_{\mathrm{fiber}}$). As the maximum intensity transfer of each supermode is of interest, the relative transferred intensity is computed for the case of the external driving frequency matching the resonance frequency of one of the delocalized supermodes ($\omega = \omega_0 \pm |\eta|$). Under these assumptions, the relative transferred intensity is given as

$$I_{\mathrm{d}}(\omega = \omega_0 \pm |\eta|) = \frac{16\beta^2}{16\alpha^2\beta^2 + \alpha^4} \tag{6.12}$$

with

$$\alpha := \frac{\tau_{\mathrm{fiber}}}{\tau} + 1 \tag{6.13}$$

describing the rate between the intrinsic losses of the cavities and their external losses due to fiber coupling ($\alpha = 1$ represents the case without intrinsic losses) and

$$\beta := \frac{|\eta|}{|\mu|^2} \tag{6.14}$$

being the rate between the inter-cavity $|\eta|$ and the fiber-resonator coupling $|\mu|^2$. Obviously, both α and β strongly influence the intensity I_{d} transferred through a tunably coupled LCE-PM. A detailed evaluation of the influence of α on the curve shape of I_{d} is given in App. C.4. As the intrinsic losses do not crucially change the dependency of I_{d} on β, Eq. (6.12) in the limit of vanishing intrinsic losses (meaning $\alpha = 1$) is compared to the experimental data in the following.

Although the analytical expression describing the intensity transfer I_d is significantly simplified in Eq. (6.12), it still depends on β instead of the actuation temperature T_act. Thus, a dependency of β on T_act is found: Since the experimental data has been normalized with respect to the influence of the fiber-resonator coupling $|\mu|$ (see App. C.5), the change of β with T_act is expected to only depend on $|\eta|$. As demonstrated in Sec. 6.3.2, $|\eta|$ depends on T_act in a nearly perfect exponential fashion. Therefore, an exponential dependency of T_act is assumed for β:

$$\beta =: A \times \exp \frac{T_\mathrm{act}}{T_0} \tag{6.15}$$

with a constant pre-factor A and a temperature scale T_0. This finally leads to an intensity transfer of

$$I_\mathrm{d} = \frac{16A^2 \exp\left(2T_\mathrm{act}/T_0\right)}{16A^2 \exp\left(2T_\mathrm{act}/T_0\right) + 1} \tag{6.16}$$

with T_0 being the temperature scale on which $|\eta|$ and therefore I_d changes with T_act. The pre-factor A contains several unknown physical parameters and is therefore not discussed further.

To obtain a more thorough understanding of the maximum intensity transfer of a delocalized supermode through a tunably coupled LCE-PM, Eq. (6.16) is compared to the experimental data depicted in Fig. 6.6. To that end, the maximum intensity transfer of each of the three highlighted supermodes is plotted versus T_act on a semi-logarithmic scale in Fig. 6.7. For each of the modes, the intensity has been normalized to a maximum value of 1. A fit following Eq. (6.16) has been applied to the data of each of the modes.

Despite the significant scattering of the experimental data, the applied fit function approximately reproduces this data in case of all three modes. This demonstrates the CMT-based equations (6.11), (6.12) and (6.16) to describe the dependency of the relative intensity transfer through a tunable coupled LCE-PM on the actuation temperature of its substrate in good approximation.

All three depicted supermodes show a significant increase of their intensity transfer with T_act. For all three modes, the increase of the intensity transfer $I_\mathrm{d,norm}$ is approximately exponential in the regime of low T_act. This is apparent from the linearity of the applied fits on the left side of the plot. In this regime, the intensity transfer is limited by the still small inter-cavity coupling strength $|\eta|$. As $|\eta|$ exponentially increases with elevating T_act, so does $I_\mathrm{d,norm}$. This is also evident from Eq. (6.12), as the transferred intensity $I_\mathrm{d,norm}$ is approximately proportional to β^2 in case of small β (meaning $16\beta^2 \ll \alpha^2$).

Going to higher substrate temperatures and thus inter-cavity coupling strengths, the intensity transfer of all modes eventually starts to flatten towards a T_act-independent threshold value. This case is described by Eq. (6.12) in the case of large β (meaning

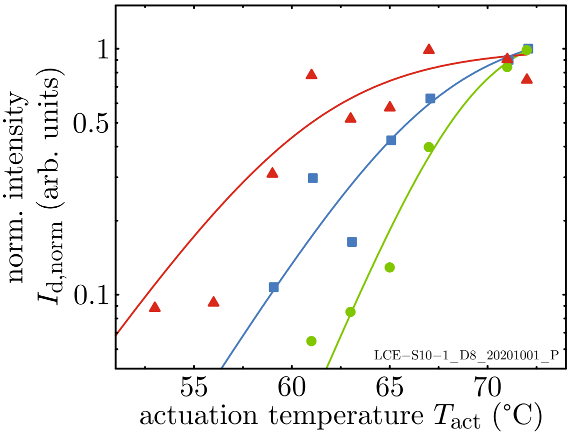

Figure 6.7: Change of the intensity transferred through a tunably coupled LCE-PM with elevating substrate actuation temperature. For three supermodes (highlighted in Fig. 6.6), the maximum intensity transfer is plotted on a semi-logarithmic scale versus T_{act}. The intensities have been corrected for the fiber-resonator couplings in an averaging manner as described in App. C.5. The intensity of each mode has been normalized to a maximum value of 1 to enable a comparison of the relative changes of intensity with T_{act}. The experimental data of the three modes has been fitted using Eq. (6.16). For all three investigated modes, a strong increase of the transferred intensity with T_{act} is evident. At low T_{act}, this surge is approximately exponential, as obvious from the linearity of the applied fits. Going to higher T_{act}, the intensity transfer of all investigated supermodes seems to flatten and approach a maximum value. Despite the strong scattering of the experimental data, the applied CMT-based fits nicely reproduce the general behavior of the transferred intensity. Reprinted with permission from [225] © Optica Publishing Group.

$16\beta^2 \gg \alpha^2$), in which $I_{\mathrm{d,norm}}$ does not depend on β anymore. Physically speaking, this maximum intensity transfer in the regime of large $|\eta|$ is mainly limited by the intrinsic losses of the WGM cavities.
As already observed from the data depicted in Fig. 6.6, the intensity of the different modes starts to flatten towards their threshold at different values of T_{act}. As α and hence the intrinsic losses are only slightly affecting the relative change of the transferred intensity (compare App. C.4), these differences are mainly attributed to the different extents and amplitudes of the evanescent fields of these modes and therefore different inter-cavity coupling strengths of the single supermodes.

In summary, all three supermodes of the investigated LCE-PM show a strong enhancement of their intensity transfer under thermal actuation of the LCE substrate. Furthermore, the transferred intensity of all modes shows a strong dependency on the actuation temperature as expected based on CMT calculations. The significant scattering of the experimental data is mainly attributed to the investigation approach of 2FTS and is therefore not an issue inherent to the presented LCE-PMs themselves. These findings further support the potential of such LCE-PMs in future photonic applications, e.g., where chip-scale optical filters with a strongly tunable and precisely predictable intensity transfer are required.

6.5 Assessment of the tunable coupling of photonic molecules

In the following, the achieved tunable coupling of a photonic molecule consisting of two WGM cavities is assessed. Herein, the tunability of the presented LCE-PM is compared to that of other WGM-based PMs. Furthermore, the requirements for a possible future integration of such tunable LCE-PMs as well as for the potential upscaling to larger coupled ensembles is discussed.

In tunably coupled photonic molecules on actuating LCE substrates, the substrate's contraction under an external stimulus is used to reversibly decrease the inter-cavity distance of WGM resonators and thereby increase the evanescent coupling of their optical modes. This change of the inter-cavity distance with the actuation temperature has been demonstrated using optical microscope images. The tunable coupling of two WGM cavities has been studied using FTS measurements at different actuation temperatures. A reversible generation of delocalized supermodes has been demonstrated based on a qualitative comparison of calculated and measured fiber-transmission spectra. From the resonance splitting of these experimentally detected supermodes, the coupling strength of the PM has been calculated. A nearly perfect exponential increase of the coupling strength with the actuation temperature from the uncoupled case to more than 200 GHz has been demonstrated. Furthermore, the intensity transfer through an LCE-PM in add-drop configuration has been studied using 2FTS measurements. By comparison of these spectra with single-fiber transmission spectra, the generation of delocalized supermodes has been shown to be the fundamental requirement for an intensity transfer through the LCE-PM. Finally, the change of the transferred intensity with the actuation temperature has been studied. This intensity shows a significant enhancement by a factor of more than 50 with elevating actuation temperature that is again in good agreement with calculations from coupled-mode theory.

Within recent years, various systems based on the tunable coupling of WGMs by manipulation of the inter-cavity distance have been demonstrated [28,117,135,137,170]. Therein, a tunable coupling exploiting the flexibility of an elastomer substrate has to the best of the author's knowledge only been reported by Siegle *et al.* [170]. A direct comparison of that system to the here presented LCE-PM is hardly feasible, as no quantitative characterization of the evanescent coupling has been performed by Siegle *et al.* Nevertheless, only the LCE-PM presented here has been shown to operate fully on chip scale. Furthermore, the variety of possible external stimuli of the LCE-PM is clearly advantageous compared to the application of mechanical stress in [170].

Generally speaking, state-of-the-art tuning ranges and precision of the coupling strength of two WGM cavities is usually achieved using piezo actuators [28,135,137]. To compare the achieved tunability of the LCE-PM with that of piezo-based PMs, the dimensionless coupling coefficient $\kappa = \Delta\Omega/2\omega_0$ is defined. In case of the LCE-PM presented here, this leads to $\kappa \approx 1.7 \times 10^{-4}$. A comparable coupling coefficient of 1.2×10^{-4} has been achieved by Beck *et al.* by mounting one of two WGM cavities onto a piezo actuator via a gold wire [137]. Due to strong mechanical vibration of the wire, this tuning mechanism has been shown to be significantly less precise. An more precise tuning has been achieved by Peng *et al.* using a similar approach [135]. However, herein a coupling coefficient of only 7.4×10^{-6} has been achieved. An alternative approach applied by the same authors is mounting both WGM cavities onto an individual piezo actuator via independent substrates. Following this route, a breaking of $\mathcal{PT}$-symmetry in such a coupled resonator pair has been demonstrated [28]. Nevertheless, a maximum coupling coefficient of only around 1.4×10^{-8} has been reported. As this coupling coefficient is changed by a factor of around 2 under three incremental changes of the inter-cavity distance, the precision of the tunability is comparable to that of the LCE-PM presented in Sec. 6.3. Nevertheless, the precision of the LCE-PM is currently only limited by the used temperature control and therefore leaves large space for improvement. In summary, both the range as well as the precision of the tunability of the LCE-PM's coupling strength are comparable to those of macro-scale, piezo-based systems.

In addition to the wide and precise tunability of the coupling strength by applying an external stimulus, the general working principle of the LCE-PM should enable a future upscaling to larger and nearly arbitrary ensembles of coupled cavities. This possibility is a significant advantage compared to PMs based on both macroscopic flexible substrates [170] as well as piezo actuators [28, 135, 137]. To realize such large ensembles of tunably coupled cavities, an improved reliability of the LCE-PM's fabrication process (see Sec. 4.2 and 4.3) is inevitable. This should however be feasible employing an elaborated automatization of all fabrication steps.

To realize a tunable coupling of arbitrary two-dimensional resonator arrays, LCE substrates with domains of independent director orientation on the scale of 10 µm are necessary. Nowadays, such substrates are conceivable due to recent advances in 3D laser printing of LCE [194,196]. To furthermore facilitate the independent actuation of these substrate domains, an alternative external stimulus is indispensable. To that

end, one possible approach is given by doping the independent domains with different absorber dyes and using monochromatic illumination at various center wavelengths as stimuli.
Resumed, several large adaptions of the LCE-PM are necessary to realize large and arbitrary two-dimensional ensembles of coupled cavities with independent tunability of the single inter-cavity coupling strengths. Nevertheless, the tunable coupling based on a contraction of an LCE substrate as demonstrated in the present work for the first time offers a possible route towards these large resonators arrays with tunable coupling. Such an upscaling is not conceivable based on established methods using piezo-based actuation.

To fully deploy the tunable coupling of the demonstrated LCE-PM, an integration into more complex photonic systems is essential. To facilitate such an integration, again a higher reliability of the LCE-PM's fabrication process is required.
As large temperature changes are expected to generally deteriorate the functionality of complex photonic systems, the actuation of LCE substrates should not be realized using a macroscopic heating resistor, but in a more sophisticated manner. For example, electrically-driven micro heaters [116,253] or the illumination of dye-doped substrates [16] are conceivable.
Furthermore, an alternative in- and outcoupling approach is necessary to prevent intensity fluctuations as evident in Sec. 6.4.2. This should be possible using structured waveguides with a fixed coupling distance to their regarding cavity. Such waveguides could for example be mounted onto the pedestals of the respective cavities. Alternatively, doping the WGM cavities with a suitable laser dye does enable a free-space excitation and readout of lasing modes [170].
Summed up, the integration of the LCE-PM into complex photonic systems also requires several adjustments of the presented system. Nevertheless, the comparably large effort linked to these necessary adaptions of such LCE-PMs might strongly pay off due to their unique potential of future upscaling to nearly arbitrary ensembles of coupled cavities.

The LCE-PM introduced in this chapter offers a platform for a reversible, wide and precise tunability of the coupling strength of photonic molecules under an external stimulus. The tunability, that is comparable to that of established, piezo-based systems has been achieved fully on chip scale. Due to the possibility of tuning the coupling strength fully on chip scale by an external stimulus, this platform yields a great and unique potential for future upscaling to large cavity arrays and integration into complex all-polymeric photonic circuits. The probability of a successful realization of such future applications is mainly linked to necessary advancements of the fabrication process and therefore not limited by the fundamental concept of the LCE-PM itself.

Chapter 7

Conclusion and outlook

The present thesis aimed at the realization of a chip-scale and all-polymeric platform for tunable photonic building blocks based on whispering gallery modes (WGMs). The intended tunability was achieved via the incorporation of the exotic material class of liquid crystal elastomers (LCEs). All samples in the scope of this thesis were fabricated using newly developed processes based on optical lithography like 3D laser printing. The potential of the all-polymeric chip-scale platform was demonstrated by tuning two exemplary key characteristics of WGM-based photonic building blocks: the spectral positions of the resonances of an individual WGM cavity made of LCE as well as the inter-cavity coupling of a photonic molecule consisting of two WGM resonators in close spatial proximity on an LCE substrate. Within these proof-of-principle experiments, the tuning of the photonic building blocks was initiated under thermal actuation of the LCE.

Summary and conclusion

In the general context of photonic building blocks, WGM resonators are mostly ring- or disk-shaped. The spatial field distribution of WGMs in disk-shaped cavities was computed using finite-element method simulations. Incongruous differences to the field distribution of such modes calculated using the established analytical effective-index method were found. These differences were attributed to the unjustified assumptions of a separable refractive index distribution as well as orthogonal TE and TM polarizations within the analytical calculations. These assumptions lead to a separability and orthogonality of the computed field distributions that does not coincide with reality. Instead, different WGMs in disk-shaped cavities can undergo a strong optical coupling if they are in close spectral proximity. Hence, the established classification scheme of WGMs based on their binary polarization state as well as independent azimuthal, radial and axial mode numbers is incomplete. Using the findings from thorough finite-element studies, an alternative classification scheme was proposed. Herein, the actually orthogonal modes are classified based on their azimuthal mode number, their parity under a mirror transformation along the axial direction and their spectral order. This novel classification scheme takes the observed inseparability of the spatial field distribution of WGMs in disk-shaped cavities into account.

Several novel processes for the fabrication of tunable photonic building blocks based on upscalable optical methods were developed. Actuating chip-scale LCE substrates were fabricated using a mask-based UV illumination. A strong molecular alignment was demonstrated via polarizing optical micrographs. To evaluate the substrates' actuation, a novel investigation scheme was introduced. Micro-scale markers were 3D laser printed onto the respective substrates and the actuation was derived from an automated processing of optical micrographs. An anisotropic and sufficiently strong actuation of the substrates was demonstrated. Also rigid photonic elements were 3D laser printed successfully onto such chip-scale LCE substrates. The general quality of these structures was evaluated and is in accordance with that of conventional 3D laser printed structures.
Also, the 3D laser printing of photonic structures entirely made from LCE was realized. Challenges induced by the birefringence of the LCE resist were overcome via an adaption of the printing configuration. A strong molecular alignment of these structures was also demonstrated using polarizing optical micrographs and their overall quality is again in accordance with that of structures 3D laser printed from conventional resists.

To demonstrate the potential of the developed platform of tunable photonic elements, the spectral tunability of WGMs in disk-shaped cavities entirely made from LCE was investigated under thermal actuation. The expected spectral tunability of such cavities was estimated based on a comparison of its different factors of influence. This potential tunability was found to be significantly reduced by a counteraction of the thermal expansion of the LCE material and its thermo-optic effect. Nevertheless, a distinct spectral tunability of the LCE cavities was experimentally demonstrated. The extent of this tuning is in accordance with the estimated expectations. The spectral position of WGM resonances was tuned over more than one free spectral range, showing these resonators to be fully tunable. An absolute tuning response of more than one nanometer per Kelvin under thermal actuation of the LCE was demonstrated. Under the performance of large tuning cycles, the spectral position of the WGMs was found to yield a significant hysteresis. This effect was attributed to the visco-elasticity of the LCE. Under small and repeated tuning cycles however, a high reversibility of the spectral positions within the accuracy of the applied investigation scheme was demonstrated. Via a change of the chemical composition of the LCE, the absolute tuning response of the cavities was adjusted over more than two orders of magnitude.

Furthermore, the tunable evanescent coupling of a photonic molecule consisting of two rigid disk-shaped WGM cavities on an LCE substrate (LCE-PM) was demonstrated under thermal actuation. The reversible decline of the inter-cavity distance was proven using optical micrographs. A resonance splitting of bonding and anti-bonding supermodes was successfully demonstrated. The overall appearance of the experimentally obtained single-fiber transmission spectra was shown to be in clear accordance with expectations based on coupled-mode theory (CMT) calculations. Using equations from CMT, the LCE-PM's coupling strength was computed from the resonance splitting of these supermodes. The coupling strength was shown to undergo an exponential increase with elevating actuation temperature of the LCE substrate. This behavior is in agreement with the expectations based on the exponential nature of the evanescent field of WGMs. The coupling strength was tuned from the uncoupled case close to the state of maximum achievable coupling under a mechanical contact of the cavity disks.
The usability of the tunably coupled LCE-PM as a tunable add-drop filter was demonstrated as its intensity transfer was investigated using two tapered optical fibers. The reversible generation of delocalized supermodes was proven to be the fundamental requirement for a non-vanishing transfer of intensity through the LCE-PM. Due to the increasing coupling strength under thermal actuation of the LCE substrate, the intensity transfer was enhanced by a factor of more than 50. The change of the intensity transfer with elevating substrate temperature was evaluated. For small substrate temperatures, an approximately exponential increase of transferred intensity was found, as it is mainly limited by the also exponentially increasing coupling strength. For large substrate temperatures, the intensity transfer is mainly limited by the intrinsic losses of the cavities. Hence, an asymptotic approach towards a threshold value was found. This change of the transferred intensity with the actuation temperature of the substrate is again in good agreement with expectations based on CMT calculations.

The presented results of tunable WGM resonators and photonic molecules give a first impression of the great potential of the successfully developed platform of all-polymeric and chip-scale tunable photonic building blocks.

Outlook

The observed inseparability and non-orthogonality of WGMs in disk-shaped cavities should be further investigated. Therein, both a correct analytical prediction as well as experimental evidence of the optical coupling of different WGMs is worthwhile. In the long term, a more thorough understanding of this issue could be made use of in applications like a WGM-based polarization-conversion device.

The exemplary photonic building blocks presented in this thesis only scratch the surface of possible designs of tunable photonic elements. Various and more complex systems also including other building blocks as, e.g., Fabry-Pérot cavities, photonic crystals or structured waveguides could be fabricated on the presented all-polymeric platform.

Recent advances in fabrication technology also facilitate LCE structures with domains of independent direction of actuation on the scale of down to single micrometers [194,196]. Via the integration of organic absorber dyes into the LCE's polymer matrix, also a separate optical actuation of different LCE elements is conceivable [16,38]. These fabrication advances enlarge the field of possible designs of such tunable photonic building blocks even further.

Regarding the exemplarily demonstrated photonic building blocks, especially the tunably coupled photonic molecules yield high potential for further investigations and improvements. The most obvious possible next step would be the tunable coupling of more than two WGM cavities. Using LCE substrates with a non-homogeneous direction of actuation based on [194, 196], such larger ensembles of cavities could even be arranged in a nearly arbitrary two-dimensional fashion.

The investigation of the intensity transfer in add-drop configuration resembles the working principle of coupled resonator optical waveguides (CROWs) which can act as an optical delay line [107]. This time delay is expected to change under a tuning of the inter-cavity coupling [27, 108]. To estimate the potential of the presented LCE-PM as a CROW with tunable delay, time-resolved transmission spectroscopy using two optical fibers needs to be performed.

Finally, also exceptional point lasing in such an LCE-PM could be realized [115]. To that end, a hybrid LCE-PM with one of the resonators being doped with a laser dye is required. First attempts to fabricate such hybrid LCE-PMs were already demonstrated [142]. Following this route, the LCE-PMs resonant supermodes could be driven in and out of their exceptional point of degenerate eigenfrequencies by an adjustment of the inter-cavity coupling strength [28,117].

Appendix A

Samples and fabrication process parameters

In the following, all samples used to generate the results presented in this work are listed. Additionally, summaries of the applied fabrication processes including important parameters are given. More comprehensive descriptions of these processes can be found is the respective Bachelor's and Master's theses. At first, an overview of all used chemicals is given.

A.1 List of chemicals

Table A.1: List of chemicals. The given *terms* are used in the following to refer to these chemicals. The manufacturers “SYNTHON”, “Sigma-Aldrich” and “LENS Florence” are short for “SYNTHON Chemicals GmbH & Co. KG, Bitterfeld-Wolfen, Germany”, “Sigma-Aldrich Chemie GmbH, Munich, Germany” and the “research group of Prof. Dr. Diederik Wiersma at the European Laboratory for Non-Linear Spectroscopy, Florence, Italy”, respectively. The polyimide has been synthesized by Dr. Eva Blasco at the Institute for Chemical Technology and Polymer Chemistry at KIT (now Centre for Advanced Materials at the University of Heidelberg). For chemicals that are not commercially available, a respective citation is given.

	term	**CAS number**	**mol. formula**	**manufacturer**
monomer	*monomer*	130953-14-9	$C_{23}H_{26}O_6$	SYNTHON
crosslinker	*crosslinker*	174063-87-7	$C_{33}H_{32}O_{10}$	SYNTHON
photo initiators	*Irgacure 369*	119313-12-1	$C_{23}H_{30}O_2N_2$	Sigma-Aldrich
	Irgacure 819	162881-26-7	$C_{26}H_{27}O_3P$	Sigma-Aldrich
dyes	*PM597*	137829-79-9	$C_{22}H_{33}BF_2N_2$	Sigma-Aldrich
	Azo-dye	?, see [177]	?, see [177]	LENS Florence
LC host	*E7*	40817-08-1 41122-71-8 52364-73-5 54211-46-0	$C_{18}H_{19}N$ $C_{20}H_{23}N$ $C_{21}H_{25}ON$ $C_{24}H_{23}N$	SYNTHON
silanes	*DMOAP*	27668-52-6	$C_{26}H_{58}ClNO_3Si$	Sigma-Aldrich
	A174	2530-85-0	$C_{10}H_{20}O_5Si$	Sigma-Aldrich
polyvinyl alcohol	*PVA*	9002-89-5	$[-CH_2CHOH-]_n$	Sigma-Aldrich
polyimide	*PI*	?, see [254]	?, see [254]	Eva Blasco

All rigid 3D laser printed structures have been fabricated from the commercially available resist *IP-S* [224](Nanoscribe GmbH, Eggenstein-Leopoldshafen, Germany).

A.2 Micro-scale LCE resonators for spectral tuning

A.2.1 Fabrication process

In this section, the fabrication process of tunable LCE cavities is given. The fabrication process has been developed and advanced within the scope of this work and is explained here in its final version. Hence, small deviations for some of the samples from the process steps described here are possible. A more comprehensive description of this process has been given by Stefan Pfleging [151] and is published in [37].

Tunable LCE cavities have been 3D laser printed in a glass cell filled with custom-mixed LCE resist. The surfaces of the glasses have been silanized to ensure the required mesogen alignment. Parts of the fabrication have been performed in an ISO6- or ISO7-clean room.

Silanization of glass surfaces

This process has been developed in close cooperation with Alexander Münchinger at the Institute of Applied Physics as well as Jannis Hessenauer [158] and Stefan Pfleging [151].

1. Thorough cleaning of two glass cover slips ($22 \times 22\,\mathrm{mm}^2$) with isopropanol, acetone and N_2.
2. Several cleaning steps in an ultrasonic bath at 70 °C using deionized water as well as the alkaline and acidic glass cleaners *deconex OP 146*, *OP 121* and *OP 171* (all Borer Chemie AG, Zuchwil, Switzerland).
3. Drying in a convection oven at 150 °C for 1 h.
4. Plasma activation of the glass surfaces by an oxygen treatment for 2 min at 30 W with a pressure of 0.3 mbar and an oxygen flow of 10 sccm.
5. Silanization in a solution of 0.025 vol% DMOAP and 0.157 vol% A174 in toluene for 20 min under nitrogen atmosphere.
6. Removal of leftover silanes in pure toluene for 5 min.
7. Drying in a convection oven at 150 °C for 1.5 h.

Fabrication of resist-filled glass cells

This process has been developed in close cooperation with Jannis Hessenauer [158] and Stefan Pfleging [151].

1. Mixing of monomer, crosslinker, Irgacure 819 (or Irgacure 369 in earlier cases) and E7 at room temperature and afterwards magnetic stirring at 80 °C for at least 24 h.

2. Attachment of a frame of adhesive spacer foil with a thickness of around 30 µm (CMC Klebetechnik GmbH, Frankenthal, Germany) to one of the two cover slips.
3. Stacking of the cover slips to create a cell with defined thickness.
4. Filling of the cell with the resist using capillary forces on a heat plate at 80 °C.
5. Cooling to room temperature over several hours.

3D laser printing

This process has been developed in close cooperation with Alexander Münchinger at the Institute of Applied Physics as well as Jannis Hessenauer [158] and Stefan Pfleging [151].

1. Mounting of the resist-filled cell into the 3D laser printer *Photonic Professional GT* (Nanoscribe GmbH, Eggenstein-Leopoldshafen, Germany).
2. Manual search for both resist-glass interfaces by observing the polymerization within the focal spot.
3. Calculation of the exact thickness of the resist at the position of interest.
4. Adjustment of the printing design of the resonator to be slightly less higher than the resist.
5. Printing of the pedestal as a stack of small spirals, beginning at the upper interface. The laser power needs to be adjusted with the height of the pedestal.
6. Printing of the resonator disk as a stack of larger spirals.
7. Mechanical opening of the cell.
8. Wet-chemical development in a 50:50 mixture of acetone and isopropanol for 15 min.

A.2.2 Samples

The samples are listed in the same order as they appear in this work. For all samples, the fabrication process given earlier has been applied. All samples include several resonators with identical fabrication parameters and a nominal radius of 25 µm.

Table A.2: List of all tunable LCE resonators in the same order as they appear in this work. Samples marked with * have been fabricated in cooperation with the author. Samples with the photo initiator Irgacure 369 are marked in blue. The sample LCEPMAZ02−A−30 also contains azo dye and PM597. Each sample includes several resonators with identical fabrication parameters.

	fabricated	**monomer**	**crosslinker**	**Ir. 819/369**	**E7**	**data in Fig.**
Res−TA−09	20.01.2020 Pfleging [151]	35.1 wt%	4.2 wt%	1.7 wt%	59.0 wt%	3.6(a),4.10(d), 5.2(b),5.3,5.4
Res−TA−02	16.10.2019 Karayel [62],*	34.1 wt%	12.6 wt%	1.6 wt%	51.7 wt%	4.10(c)
LCEPMAZ02 −A−30	??.??.2018 Hessenauer [158]	58.5 wt%	38.2 wt%	0.8 wt%	-	5.2(a)
Res−TA−07	20.12.2019 Pfleging [151],*	-	30.0 wt%	1.6 wt%	68.4 wt%	5.4
Res−TA−08	30.12.2019 Pfleging [151]	19.3 wt%	20.1 wt%	1.8 wt%	58.8 wt%	5.4
LCEPMAZ10	05.09.2019 Karayel [62],*	72.1 wt%	27.1 wt%	0.8 wt%	-	B.1
R13−L03− 0706−1	14.07.2020 Rebholz [40],*	19.3 wt%	20.1 wt%	1.8 wt%	58.8 wt%	B.2

A.3 Actuating chip-scale LCE substrates

A.3.1 Fabrication process

In this section, the fabrication process of actuating micro-scale LCE substrates is given. The fabrication process has been developed and advanced within the scope of this work and is explained here in its final version. Hence, small deviations for some of the samples from the process steps described here are possible. A more comprehensive description of this process has been given by Pascal Rietz [142] and is published in [37].

Actuating LCE substrates have been fabricated using the mask-based UV illumination of a glass cell filled with custom-mixed LCE resist. The surfaces of the glasses have been covered with polymeric alignment layers to ensure the required mesogen alignment. Therefore, the polymeric alignment layers have been mechanically rubbed.

Fabrication of the PVA alignment layer

This process has been developed in close cooperation with Lukas Mall [159], Osman Karayel [62] and Pascal Rietz [142].

1. Thorough cleaning of a glass cover slip ($22 \times 22\,\mathrm{mm}^2$) with isopropanol, acetone and N_2.
2. Application of 200 µL of a saturated solution of PVA in deionized water.
3. Spin-coating at $1200\,\mathrm{min}^{-1}$ for 1 min.
4. Baking on a heat plate at 80 °C for 2 min.
5. Mechanical rubbing using a custom-built tool. More information in [142].

Fabrication of the PI alignment layer

This process has been developed in close cooperation with Lukas Mall [159], Osman Karayel [62] and Pascal Rietz [142]. The used PI has been synthesized by Dr. Eva Blasco at the Institute for Chemical Technology and Polymer Chemistry at KIT (now Centre for Advanced Materials at the University of Heidelberg).

1. Thorough cleaning of a glass cover slip ($22 \times 22\,\mathrm{mm}^2$) with isopropanol, acetone and N_2.

2. Drying on a heat plate at 180 °C for 10 min.
3. Plasma activation of the glass surface by an oxygen treatment for 2 min at 30 W with a pressure of 0.3 mbar and an oxygen flow of 10 sccm.
4. Drying on a heat plate at 180 °C for 10 min.
5. Application of 200 µL of the synthesized initial solution.
6. Spin-coating at 1800 min^{-1} for 45 s.
7. Imidation of the initial solution on a heat plate at 80 °C for 1.5 min, 180 °C for 1.5 min, 80 °C for 30 min, 120 °C for 30 min, 180 °C for 30 min and 230 °C for 60 min.
8. Mechanical rubbing using a custom-built tool. More information in [142].

UV illumination of micro-scale substrates

This process has been developed in close cooperation with Lukas Mall [159], Osman Karayel [62] and Pascal Rietz [142].

1. Mixing of monomer, crosslinker and Irgacure 369 at room temperature and afterwards magnetic stirring at 80 °C for at least 24 h.
2. Attachment of a frame of adhesive spacer foil with a thickness of around 30 µm (CMC Klebetechnik GmbH, Frankenthal, Germany) to one of the two cover slips.
3. Stacking of the cover slips to create a cell with defined thickness.
4. Filling of the cell with custom-mixed resist using capillary forces on a heat plate at 80 °C.
5. Cooling to room temperature over several hours.
6. Polymerization via UV illumination under a custom-built mask at around 3 mW cm^{-2} for 15 s to 20 s.
7. Solving of the PVA layer in deionized water for at least 24 h.
8. Mechanical opening of the cell.
9. Wet-chemical development of the substrates in PGMEA for at least 15 min.

A.3.2 Samples

The samples are listed in the same order as they appear in this work. For all samples, the fabrication process given earlier has been applied. All samples include several LCE substrates with identical fabrication parameters and nominal radii of 150 µm and 250 µm.

Table A.3: List of all actuating LCE substrates in the same order as they appear in this work. Each sample includes several substrates with identical fabrication parameters and nominal radii of 150 µm and 250 µm. Within this work as well as in [142], substrates are partly labeled with additional numbers, e.g. *LCE−S10−1*. These additional numbers represent parts of the the overall samples which are still consisting of several substrates. The markers on sample LCE−S12 (see Fig. 4.5) have been printed from IP-S using the process described in Sec. A.4.

	fabricated	**monomer**	**crosslinker**	**Ir. 369**	**data in Fig.**	**comment**
LCE−S11	20.02.2020 Rietz [142]	69.7 wt%	29.5 wt%	0.8 wt%	4.4(a)	not rubbed as reference
LCE−S10	12.02.2020 Rietz [142]	69.7 wt%	29.5 wt%	0.8 wt%	4.4(b)	-
LCE−S12	20.02.2020 Rietz [142]	69.7 wt%	29.5 wt%	0.8 wt%	4.4(b), 4.5(b)	partly with markers
LCE−S08	11.02.2020 Rietz [142]	69.7 wt%	29.5 wt%	0.8 wt%	4.4(c)	PI partly missing

A.4 LCE-PMs for tunable coupling

A.4.1 Fabrication process

In this section, the fabrication process of tunable PMs on LCE substrates is given. The fabrication process has been developed and advanced within the scope of this work and is explained here in its final version. Hence, small deviations for some of the samples from the process steps described here are possible. A more comprehensive description of this process has been given by Pascal Rietz [142] and is published in [37].

The tunable LCE-PMs have been 3D laser printed onto LCE substrates fabricated following Sec. A.3. As described in Fig. 4.6, this has been done in an inverted configuration with the resist being sandwiched between the LCE substrate and an additional cover slip.

Fabrication of the resist-filled cell

This process has been developed in close cooperation with Osman Karayel [62] and Pascal Rietz [142].

1. Thorough cleaning of a glass cover slip ($22 \times 22\,\mathrm{mm}^2$) with isopropanol, acetone and N_2.
2. Attachment of a frame of adhesive spacer foil with a thickness of around 70 µm (CMC Klebetechnik GmbH, Frankenthal, Germany) to the cover slip.
3. Mounting of the cover slip with the spacer foil pointing upwards into the 3D laser printer *Photonic Professional GT* (Nanoscribe GmbH, Eggenstein-Leopoldshafen, Germany).
4. Application of at least 15 µL of IP-S in the center of the frame of adhesive foil.
5. Placing a cover slip with attached LCE substrates pointing downwards onto the resist.

3D laser printing onto LCE substrates

This process has been developed in close cooperation with Osman Karayel [62] and Pascal Rietz [142].

1. Manual search for an LCE substrate using the microscope camera.
2. Automated search for the resist-substrate interface.
3. Manual fine adjustment to account for possible surface imperfections or sample tilts.
4. Printing of the pedestals/disks as a stack of small/larger spirals, beginning at the LCE substrate.
5. Mechanical opening of the cell.
6. Wet-chemical development in PGMEA for about 45 min.

A.4.2 Samples

The samples are listed in the same order as they appear in this work. For all samples, the fabrication process given earlier has been applied. All samples include several substrates with nominal radii of 150 µm or 250 µm and resonator pairs printed with identical fabrication parameters with nominal radii of 20 µm and 30 µm.

Table A.4: List of all tunable LCE-PMs in the same order as they appear in this work. Each sample includes several LCE-PMs with identical fabrication parameters. All PMs have been printed as size-mismatched cavities with radii of $R_1 = 20\,\mu\text{m}$ and $R_2 = 30\,\mu\text{m}$.

	fabricated	**substrate**	**resist**	**data in Fig.**	**comment**
LCE−S10−1_ D8_20201001_P	28.05.2020 Rietz [142]	LCE−S10	IP-S	6.1(b),6.5(a+b), 6.6,6.7,C.5(a+b)	-
LCE−S10−1_ C4_2_20200609_P	28.05.2020 Rietz [142]	LCE−S10	IP-S	6.3(a),6.4(a-c), C.1,C.2(a-c)	-

A.5 Reference WGM resonators from PMMA

In Ch. 3, several exemplary measurements are used to demonstrate the functionality of FTS, 2FTS and polarization-sensitive FTS. These exemplary measurements have been performed using polymeric state-of-the-art cavities made from PMMA. Although these cavities have been partly fabricated within the scope of this work, the applied fabrication processes have only been reproduced from earlier works and are not suited for the realization of tunable photonic elements. Hence, a detailed description of these processes is spared here. Instead, sources of additional information regarding the fabrication of these cavities are given.

Table A.5: List of all PMMA cavities used for exemplary measurements in the same order as they appear in this work. Each sample includes several WGM resonators with identical fabrication parameters. The fabrication methods “deep-UV” and “e-beam” refer to a structuring of the PMMA cavity using “deep-UV lithography” and “electron-beam lithography”, respectively. For all samples, citations for additional information are given.

	shape	**method**	**pedestal**	**substrate**	**data in Fig.**	**comment**
10062018 −4e−60−3	goblet	deep-UV	PMGI	glass	3.3(a+b)	see [33, 159]
MG0200−1A	goblet	e-beam	Si	Si	3.5	see [39]
PMMA_02 −Res02	disk	e-beam	Si	Si	3.6(b)	see [39, 40]

Appendix B

Additional data on tunable LCE resonators

In Ch. 5, the spectral tuning of WGMs in disk-shaped LCE cavities under thermal actuation is demonstrated. In the following section, additional data supporting these results are presented.

B.1 Real-time investigation of the resonator radius

In Sec. 5.3, the expected tunability of an LCE cavity is estimated based on the expansion of the resonator disk under thermal actuation. This expansion is experimentally investigated from microscope images as presented here.

A *MATLAB* routine based on Hough transformations [210] is used to detect the circle of the resonator disk within these microscope images and calculate its radius. Due to thermal actuation using a macroscopic Peltier element, also the macroscopic sample mount is heated and hence thermally expanding. Therefore, the focal plane of the used optical microscope has to be readjusted for every actuation temperature step. This leads to the calculated radii at different actuation temperatures to not be directly comparable. To circumvent this issue, the distance of two microscopic dot-like scatterers on the surface of the glass substrate is used as an approximately temperature-independent measure. This assumption is reasonable as the thermal expansion of the glass substrate is expected to be several orders of magnitude smaller than that of the LCE. The calculated radii are expressed in parts of this distance.

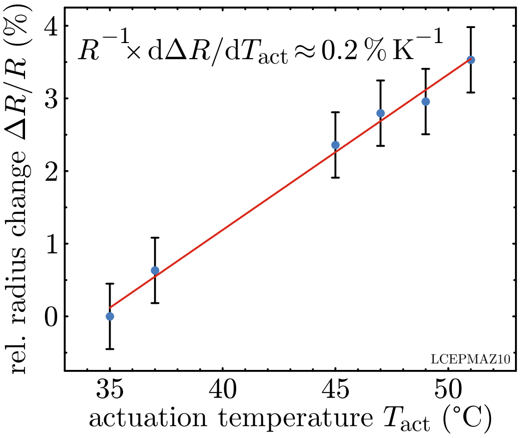

Figure B.1: Experimental investigation of the expansion coefficient of an LCE cavity. The relative change of the cavity's radius $\Delta R/R$ in percent is plotted versus the actuation temperature T_{act}. The relative radius change $\Delta R/R$ is estimated from microscope images. A *MATLAB* routine based on Hough transformations [210] is used to detect the circle of the cavity disk in these images and measure its radius. The cavity radius at the lowest investigated actuation temperature of $T_{\mathrm{act}} = 35\,°\mathrm{C}$ is used as reference value R. As the circle-detection routine is not working reliably for all microscope images, several data points are missing. The depicted data shows an approximately linear change of the radius with the actuation temperature. The applied linear fit reveals a slope of around $0.2\,\%\,\mathrm{K}^{-1}$. This corresponds to a linear expansion coefficient of $\alpha \approx 2 \times 10^{-3}\,\mathrm{K}^{-1}$. Sample fabricated in cooperation with Osman Karayel [62], measurement performed by Evelyn Kaiser [145].

Furthermore, also the room-temperature radius of the investigated cavity is unknown, as this radius deviates from its designed value within the 3D laser printing process due to polymeric shrinkage. To estimate the expansion coefficient α, the relative change of the radius $\Delta R/R$ at different actuation temperatures T_{act} is investigated. The radius at the lowest investigated actuation temperature is used as reference value R. In Fig. B.1, this relative radius change in the actuation temperature range of 35 °C to 51 °C is plotted versus T_{act}.
Based on the depicted data, an approximately linear relative change of the cavity radius with the actuation temperature is found. This linearity matches the expectations based on an approximately linear actuation behavior of the LCE in the investigated temperature regime [36, 190]. The applied linear fit reveals a slope of around $0.2\,\%\,\mathrm{K}^{-1}$. This change of the cavity's relative radius corresponds to a linear expansion coefficient of $\alpha \approx 2 \times 10^{-3}\,\mathrm{K}^{-1}$. This value is used in Sec. 5.3 to estimate the expected spectral shift of such disk-shaped LCE resonators under thermal actuation.

B.2 Preferential field orientations of WGMs in LCE resonators

In Sec. 5.3, potential reasons for the significant deviation of the tunability of modes in LCE resonators presented in this work from results reported by Nocentini *et al.* [38] are discussed. Within this evaluation, an influence of differing preferential field orientations of the investigated modes is ruled out. Here, experimental data supporting this assumption is presented.

The preferential field orientations of WGMs in an exemplary type 2 LCE resonator have been investigated using polarization-sensitive FTS. The directional radiation of the WGMs in the cavity under fiber excitation has been collected using a microscope objective and analyzed via a polarimeter. (For a detailed description of this measurement approach, see Sec. 3.3 and [40].) In case of a TE- or TM-like polarization of the WGMs, the azimuth of the polarization of the detected directional radiation corresponds to the preferential field orientation of the mode within the cavity.
In Fig. B.2, the fiber transmission spectrum (top) as well as the azimuth angles of the detected WGM resonances (bottom) of the exemplary LCE cavity are depicted (compare Fig. 3.6(b)). The investigated spectral region comprises approximately two free spectral ranges. A large number of dips in the fiber transmission corresponding to WGM resonances is found. The azimuth angles of the polarization of the radiation of these modes do not show a separation into orthogonal groups. Instead, a seemingly arbitrary scattering of the azimuth angles over the whole data range is evident. In addition, no periodicity of these azimuth angles with the free spectral range is apparent. These findings strongly suggest that the WGMs propagating in this type 2 LCE cavity do primarily not carry a preferential field orientation.

Despite the allegedly consistent disk shapes of the LCE cavity in Fig. B.2 and the PMMA resonator in Fig. 3.6(b), the experimental data of the azimuth angles of the radiation of WGMs presented here strongly differs from the expected behavior. This deviation is attributed to the non-perfect disk shape of the LCE cavity induced by the limitations of the 3DLP fabrication process. As demonstrated via FEM simulations in [40], already small deviations of the shape of a cavity disk lead to significant modifications of the field orientation of WGMs [40]. Thus, the fabrication-induced inaccuracy of the LCE resonator disk is assumed to distort the preferential field orientations of its different whispering gallery modes in an arbitrary manner. As the LCE ring resonators investigated by Nocentini *et al.* have been printed using a fabrication process without the advances presented in Sec. 4.4, these ring resonators are expected to yield a discrepancy from their intended shape at least comparable to that of the type 2 cavity investigated here. Hence, a propagation of modes with a TE- or TM-like polarization is also unlikely in these cavities.

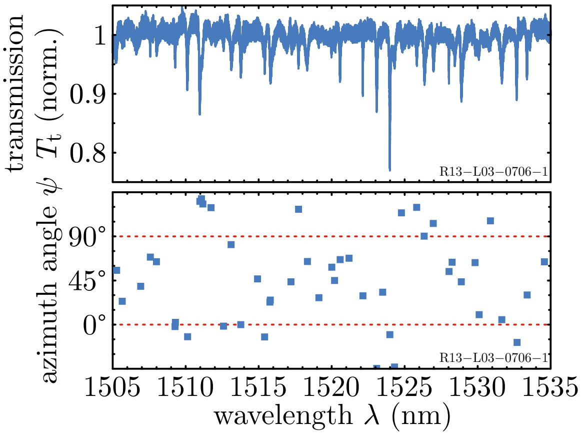

Figure B.2: Investigation of the preferential field orientation of WGMs in an LCE cavity using polarization-sensitive FTS. As introduced in Sec. 3.3 and Fig. 3.6(b), the directional radiation of the WGMs is collected and analyzed using a polarimeter. The depicted spectral region comprises approximately two free spectral ranges of the cavity of interest and contains a large number of dips in the fiber transmission corresponding to WGM resonances. The azimuth angles of the directional radiation of these modes seem to be arbitrarily scattered over the whole data range. No periodicity of the azimuth angles with the free spectral range is evident. These findings suggest that in such LCE resonators primarily modes without preferential field orientation propagate. Adapted from [40].

Based on the findings presented here, an attribution of different spectral tunabilities of WGMs in LCE cavities to either a TE- or TM-like polarization of these modes is not justified. Hence, an influence of the preferential field orientation of WGMs on their tunability is not considered in Sec. 5.3

Appendix C

Additional data and calculations on tunably coupled LCE-PMs

In Ch. 6, the tunable evanescent coupling of a photonic molecule consisting of two WGM resonators on an LCE substrate is demonstrated. The substrate's contraction under thermal actuation is used to reversibly decrease the inter-cavity distance. Here, additional data and calculations supporting these results are presented.

C.1 Real-time investigation of the inter-cavity distance

In Fig. 6.1, the decrease of the inter-cavity distance g with the actuation temperature is demonstrated using four microscope images at different values of T_{act}. Here, a quantitative study of this gap size is presented for an exemplary LCE-PM.

As for the estimation of the radius change of LCE resonators (see App. B.1), the cavity disks are detected as circles in microscope images at different actuation temperatures using a *MATLAB* routine based on Hough transformations [210]. The difficulties connected to the thermal expansion of the macroscopic sample mount described in App. B.1 also apply. Here nevertheless, the radii of the two cavity disks are assumed to approximately match their designed value and not change with T_{act}. Therefore, they are used as temperature-independent measures. The inter-cavity distance is calculated as the difference of the center-to-center distance of the two circles and the sum of their radii. Therefore, the inter-cavity distance can be expressed in terms of a length. The gap size at the lowest investigated actuation temperature is used as reference value. In Fig. C.1, the change of the inter-cavity distance in the actuation temperature range of 61 °C to 72 °C is plotted versus T_{act}.

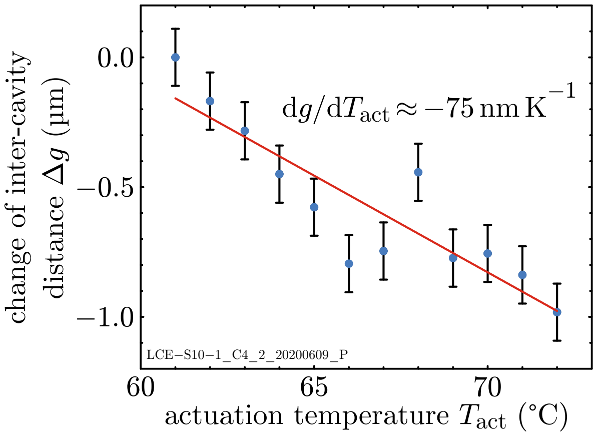

Figure C.1: Experimental investigation of the inter-cavity distance of an LCE-PM under thermal actuation. The change of the inter-cavity distance Δg is plotted versus the actuation temperature T_{act}. The distance change Δg is estimated from microscope images. A *MATLAB* routine based on Hough transformations [210] is used to detect the circles of the cavity disks in these images and measure their distance. The inter-cavity distance at the lowest investigated actuation temperature of $T_{\mathrm{act}} = 61\,°\mathrm{C}$ is used as reference value. The presented data shows a significant scattering. This scattering is attributed to the limited reliability of the circle-detection routine. Nevertheless, an approximately linear decrease of the inter-cavity distance with T_{act} is evident. The applied linear fit reveals a slope of $\mathrm{d}g/\mathrm{d}T_{\mathrm{act}} \approx -75\,\mathrm{nm\,K}^{-1}$. Reprinted with permission from [225] © Optica Publishing Group.

Based on the depicted data, an approximately linear change of the inter-cavity distance with the actuation temperature is found. This linearity matches the expectations based on an approximately linear actuation behavior of the LCE in the investigated temperature regime [36, 190]. The applied linear fit reveals a slope of $\mathrm{d}g/\mathrm{d}T_{\mathrm{act}} \approx -75\,\mathrm{nm\,K}^{-1}$. In combination with an estimated room-temperature gap size of around 2 µm (see Fig. 6.1) and a starting temperature of the LCE's phase transition of $T_{\mathrm{tr}} \approx 35\,°\mathrm{C}$ [188], this slope leads to an expected mechanical contact of the two investigated cavities at $T_{\mathrm{act}} \approx 63\,°\mathrm{C}$. As obvious from Fig. C.1 as well as Fig. 6.3 and 6.4, this is not true as the inter-cavity distance is still decreasing with T_{act} at $T_{\mathrm{act}} = 72\,°\mathrm{C}$. Nevertheless, the inter-cavity distance is expected to be close to 0 at that actuation temperature. Therefore, the respective coupling strength of $|\eta|_{72\,°\mathrm{C}} = 207\,\mathrm{GHz}$ (see Fig. 6.4) is assumed to be close to the maximum achievable coupling strength of the investigated LCE-PM in case of a mechanical contact of the WGM resonator disks.

C.2 Spectral shifts of WGMs in LCE-PMs under thermal actuation

In Sec. 6.3, the resonance splitting of bonding and anti-bonding supermodes in a tunably coupled LCE-PM under thermal actuation is investigated. The PM's coupling strength $|\eta|$ is calculated from this resonance splitting. As introduced in Sec. 5.1, most polymeric WGM cavities show a spectral shift of their resonance wavelength under elevating temperature due to the polymer's thermo-optic effect and thermal expansion. This also holds for the resonators of the presented LCE-PM. In the following, the implications of these spectral shifts on the determination of the coupling strength of the LCE-PM are discussed.

As the used resonator material IP-S has a small expansion coefficient and a larger but negative thermo-optic coefficient [224, 255], the resonance splitting of the delocalized supermodes is superimposed by a general blue-shift of the modes. For the reader's convenience, this general blue-shift of the modes has been neglected in Fig 6.4(a) via the definition of a temperature-dependent central wavelength λ_c.
The spectral blue-shift of WGMs under thermal actuation depends on the spatial field distribution and can therefore vary for different modes. Hence, an increasing spectral distance of two modes under thermal actuation of the LCE substrate can not be directly attributed to a resonance splitting of bonding and anti-bonding supermodes. Instead, additional investigations are required to ensure the resonance splitting of delocalized supermodes as leading effect of such spectral shifts. For the data presented in Fig. 6.4, such an investigation is exemplarily demonstrated here. To that end, the unedited FTS spectra of this resonance splitting are depicted in Fig. C.2(a). The spectral shifts of these modes are compared to those of other resonances of the same spectra: In Fig. C.2(b)/(c), spectra of a single-cavity resonance detected in the large/small cavity shifted from the modes in (a) by one/three times the free spectral range $\Delta\lambda_\mathrm{FSR}$ of the respective cavity are depicted.
As the single-cavity resonances in Fig. C.2(b) and (c) are shifted from the modes in (a) by integer numbers of the respective free spectral range of the cavities, they are expected to have the same spatial field distribution (expect their azimuthal mode number N_ϕ). Nevertheless, they don't show any coupling behavior as there is no suitable coupling partner due to the Vernier effect. Under equidistant changes of the actuation temperature of $\Delta T_\mathrm{act} = 1\,\mathrm{K}$ (white area), an approximately linear blue-shift is found for both single cavity resonances in (b) and (c). This observation matches the expectations based on a constant and negative thermo-optic coefficient of the resonator material IP-S [224]. The spectra in (a) on the other hand show a significantly differing behavior for high actuation temperatures: While the mode with smaller resonance wavelength yields a notably larger and non-linear blue-shift

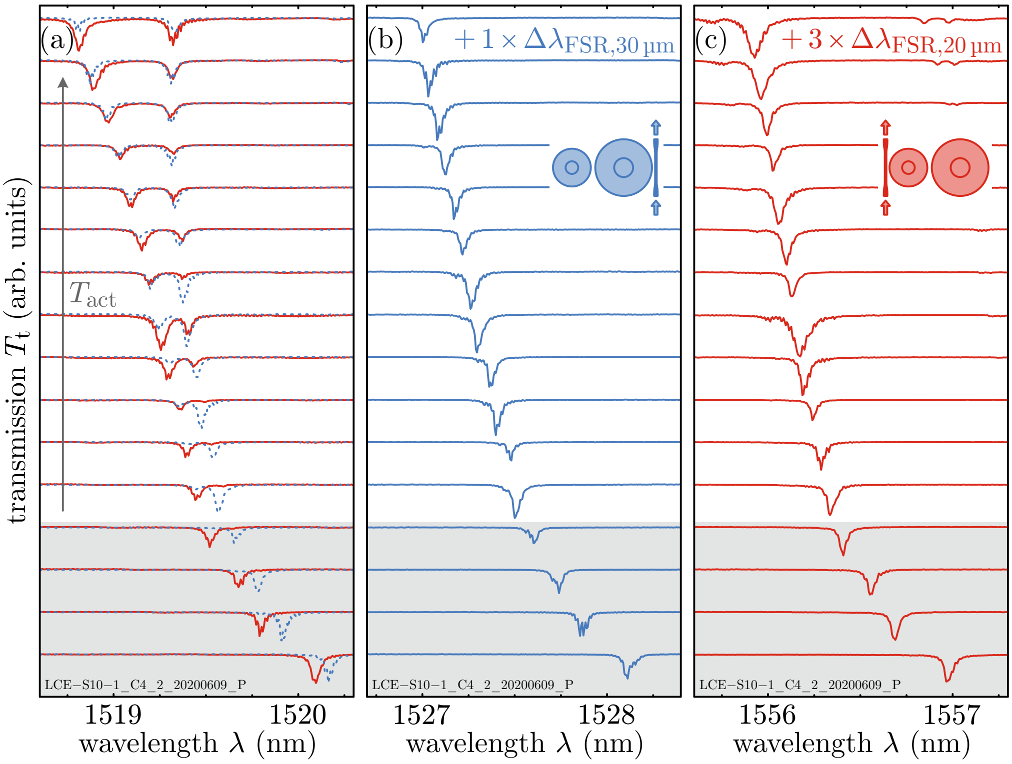

Figure C.2: Demonstration of negligibility of the thermal blue-shift of bonding and anti-bonding supermodes. In (a), the unedited FTS spectra at different actuation temperatures T_{act} of the resonance splitting presented in Fig. 6.4(a) are depicted. (An allocation to which resonator the fiber has been coupled for each measurement is given by the color-coded pictograms in (b) and (c).) An overall blue-shift with elevating actuation temperature is apparent. In the coupled regime at large actuation temperatures, both modes appear in each spectrum. Furthermore, the resonance splitting of the modes leads to an increased blue-shift and net red-shift of the left and right mode, respectively. In (b) and (c), other spectral regions of the same spectra are depicted: (b)/(c) shows the transmission dip of a single-cavity WGM in the large/small cavity that is shifted by one/three times the free spectral range $\Delta\lambda_{\mathrm{FSR}}$ of the respective cavity with respect to the signature depicted in (a). As these single-cavity resonances are shifted by integer numbers of $\Delta\lambda_{\mathrm{FSR}}$, they are expected to have the same spatial field distribution (expect their azimuthal mode number N_{ϕ}) and therefore an equal spectral tuning under increasing temperature as the respective modes in (a). Due to the Vernier effect, the modes in (b) and (c) do not show any coupling. For equidistant steps of $\Delta T_{\mathrm{act}} = 1\,\mathrm{K}$ (white area), approximately linear and equal blue-shifts are found for both single-cavity modes. Comparing the spectra in all three plots, these findings demonstrate the generation of bonding and anti-bonding supermodes to induce the the spectral splitting found in (a). Reprinted with permission from [225] © Optica Publishing Group.

with the actuation temperature, the mode with higher resonance wavelength even changes its direction of spectral shifting into a red-shift. In comparison with the linear blue-shifts in (b) and (c), this behavior can not be attributed to the thermal shift of the WGMs, but only to the resonance splitting of bonding and anti-bonding supermodes.

The blue-shifts of the single-cavity resonances in Fig. C.2(b) and (c) with T_{act} are not only linear, but also approximately equal. This finding justifies to assume that the increasing spectral distance of the bonding and anti-bonding supermode with elevating T_{act} in Fig. 6.4 is solely induced by the resonance splitting of these modes. In Sec. 6.3, this assumption has been applied by equating the modes' spectral distance at room temperature with their spectral distance $\Delta\lambda$ at elevated actuation temperature in the theoretical absence of coupling. However, also small deviations from this approximation would not be a critical issue, as they only lead to erroneous values of $|\eta|$ in the case of weak coupling ($\Delta\Lambda \approx \Delta\lambda$). For strong evanescent coupling ($\Delta\Lambda \gg \Delta\lambda$), small deviations in $\Delta\lambda$ should not induce relevant errors of the calculated coupling strength $|\eta|$.

C.3 Spectra of transferred intensity in add-drop configuration from CMT

In Sec. 6.2, the intensity transfer through a tunably coupled LCE-PM is calculated using coupled-mode theory. Based on the assumption of mutually coupled, lossy harmonic oscillators with an incoupling and an outcoupling waveguide, Eq. (6.11) is found to describe the intensity transfer via delocalized supermodes. This equation is compared with the change of the experimentally detected intensity transfer with increasing actuation temperature. However, Eq. (6.11) is rather complex and can not be analyzed without further effort. To get a more thorough understanding of this transferred intensity and its factors of influence, it is plotted in Fig. C.3 under different parameter variations.

As a starting situation, two coupled WGM resonators (cavity 1 and 2) with resonance wavelengths near the IR c-band, a small spectral distance in the uncoupled case of $\lambda_2 - \lambda_1 = 100\,\text{pm}$ and equal quality factors $Q_1 = Q_2 = 4 \times 10^4$ are assumed. This assumption leads to the intensity peak at larger wavelengths (right-hand side of the spectrum) to always correspond to the supermode generated from the single-cavity WGM of cavity 2. Cavity 1/2 are coupled to the incoupling/outcoupling waveguide by the respective critical coupling coefficient $|\mu_{\text{in}}|/|\mu_{\text{out}}|$ and are mutually coupled by the inter-cavity coupling strength $|\eta| = 200\,\text{GHz}$. (Here, critical fiber-resonator

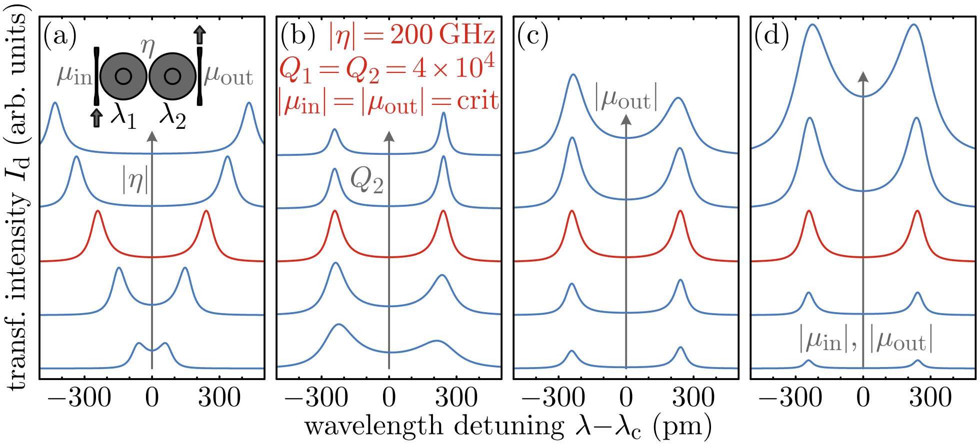

Figure C.3: To get a more thorough understanding of the intensity transfer through a tunably coupled LCE-PM, it has been calculated for delocalized supermodes near the IR c-band using Eq. (6.11) under different parameter variations. The assumed configuration is illustrated by the pictogram in (a). A spectral distance of the uncoupled WGMs of $\lambda_2 - \lambda_1 = 100\,\mathrm{pm}$ is assumed. Therefore, the left/right intensity peak always corresponds to the supermode generated from the uncoupled WGM of cavity 1/2. In all four plots, the same reference spectrum (red) with an inter-cavity coupling strength of $|\eta| = 200\,\mathrm{GHz}$, symmetric quality factors $Q_1 = Q_2$ and critical fiber-resonator couplings $|\mu_{\mathrm{in}}| \approx |\mu_{\mathrm{out}}|$ is depicted (parameters given in (b)). In (a), the inter-cavity coupling strength is increased by 80 GHz with each plot. An increasing spectral distance of the delocalized supermodes as well as enhanced maximum intensity transfer is evident. The intensity peaks for both supermodes are symmetric. In (b), the quality factor of cavity 2 is increased by a factor of 2 with each plot. The increasing quality factor leads to a decrease of the FWHM of both intensity peaks. The general amount of transferred intensity decreases. The decrease of the maximum intensity transfer is asymmetric and more pronounced for the left peak. In (c), the coupling between cavity 2 and the outcoupling fiber $|\mu_{\mathrm{out}}|$ is changed by a factor of $\sqrt{2}$ with each plot, $|\mu_{\mathrm{in}}|$ is assumed to still be critical. With increasing $|\mu_{\mathrm{out}}|$, the FWHM of both peaks increases due their increasing coupling losses. Furthermore, more light is coupled from the PM to the outcoupling waveguide and the maximum intensity transfer of both supermodes increases. This increase is however asymmetric and less pronounced for the right peak. In (d), both fiber-resonator couplings are simultaneously increased by a factor of $\sqrt{2}$ with each plot. This leads to a strong and symmetric enhancement of the maximum intensity transfer of both of the supermodes. Additionally, both intensity peaks are broadened due to their increased coupling losses.

coupling describes the coupling coefficient that would be critical in the absence of inter-cavity coupling.) The respective reference spectrum is depicted in each plot of Fig. C.3 in red and the corresponding parameters are given in (b). The pictogram in (a) illustrates the assumed configuration. Starting from this situation, different parameters of the calculated intensity transfer have been varied.

In Fig. C.3(a), the coupling strength is changed by 80 GHz with each plot. This leads to an increasing spectral distance of the delocalized supermodes and therefore also of their intensity peaks. Also, an increase of the maximum intensity transfer of each supermode is evident. This maximum intensity however asymptotically approaches a threshold value for large $|\eta|$ (compare Fig. C.4). All calculated spectra are symmetric due to the symmetry of the parameters and underlying Eq. (6.11).
In Fig. C.3(b), the quality factor of cavity 2 is changed by a factor of 2 with each plot. This increase of one of the quality factors leads to a decrease of the FWHM of both intensity peaks. This effect is however more pronounced for the right peak, as this supermode has a larger field amplitude in cavity 2 and is thereby more affected by the losses of this cavity. The general amount of transferred intensity decreases, as the assumption of critical fiber-resonator couplings leads to a declining $|\mu_{\text{out}}|$. As the intrinsic losses of cavity 1 are constant, the share of intensity being dissipated there increases. The decline of the maximum intensity transfer is more pronounced for the left peak as this supermode has a larger field amplitude in cavity 1.
In Fig. C.3(c), the fiber-resonator coupling $|\mu_{\text{out}}|$ is changed by a factor of $\sqrt{2}$ with each plot. $|\mu_{\text{in}}|$ is assumed to be constant and critical. With the increase of $|\mu_{\text{out}}|$, the FWHM of both intensity peaks increases due to the increasing coupling loss of both supermodes. This effect is again more pronounced for the right intensity peak due to the larger field amplitude in cavity 2 of this supermode. As expected, the general amount of transferred intensity increases with the coupling coefficient $|\mu_{\text{out}}|$ for both supermodes. However, the increase of the maximum intensity transfer is again asymmetric and less pronounced for the right peak, as the intensity transfer of this supermode is mainly limited by the coupling coefficient $|\mu_{\text{in}}|$.
In Fig. C.3(d), both fiber-resonator coupling coefficients are set equal $|\mu_{\text{in}}| = |\mu_{\text{out}}|$ and changed by a factor of $\sqrt{2}$ with each plot. As expected, the intensity transfer of both supermodes is significantly enhanced in a symmetric fashion. The FWHM of both intensity peaks is again increased due to the increasing coupling losses of both supermodes.

The spectra depicted in Fig. C.3(b) and (c) only show an asymmetric behavior due to the assumption of non-degenerate modes in the uncoupled case. In case of perfectly degenerate modes $\lambda_1 = \lambda_2$, all spectra are symmetric regardless their assumptions. All parameter variations and spectra in Fig. C.3 are symmetric under a swapping of the cavities.

C.4 Impact of intrinsic losses on the maximum intensity transfer in add-drop configuration

In Sec. 6.4, the intensity transfer through a tunably coupled LCE-PM in add-drop configuration is investigated and compared to calculations based on coupled-mode theory. These calculations are performed using Eq. (6.12) under the assumption of neglectable intrinsic losses, meaning $\alpha = 1$. Although this assumption is obviously not true, it is justified in the presented case as demonstrated in the following.

To get a more thorough understanding of the dependency of I_d on α and β, I_d is calculated using Eq. (6.12) and plotted versus the ratio β in Fig. C.4(a). $I_\mathrm{d}(\beta)$ is shown for α ranging from 1 to 2 in steps of 0.2. $\alpha = 2$ corresponds to a critical fiber-resonator coupling, significantly larger values of α are therefore not expected in the context of (2)FTS measurements. For all depicted values of α, I_d increases in an approximately exponential fashion for small values of β. For larger β, I_d is asymptotically approaching a threshold value. This threshold is strongly depending on on α. The scale of β on which this threshold value is approached is however only slightly changing with α.

In Sec. 6.4, not the absolute intensity transfer, but only its relative change with the actuation temperature is investigated. To evaluate the influence of α on the relative change of $I_\mathrm{d}(\beta)$ in detail, the graphs shown in Fig. C.4(a) are reproduced in Fig. C.4(b) is a normalized manner. The normalization is performed following

$$\lim_{\beta\to\infty} I_\mathrm{d} = \frac{1}{\alpha^2} \text{ and therefore } I_\mathrm{d,norm} = \left(\frac{1}{\alpha^2}\right)^{-1} I_\mathrm{d}. \tag{C.1}$$

As apparent from Fig. C.4(b), the normalized intensity transfer $I_\mathrm{d,norm}$ does only slightly change with α. All depicted plots show a comparable increase of of $I_\mathrm{d,norm}$ towards a threshold value of 1.

The ratio of the intrinsic losses and those due to fiber coupling (and therefore α) is not known for the measurements presented in Sec. 6.4. Nevertheless, α is expected to be approximately in the range of the plots depicted here. Hence, the influence of the exact value of α is not critical to I_d and the assumption of $\alpha = 1$ is reasonable for the investigations of the change of the relative intensity transfer through the LCE-PM in Sec. 6.4.

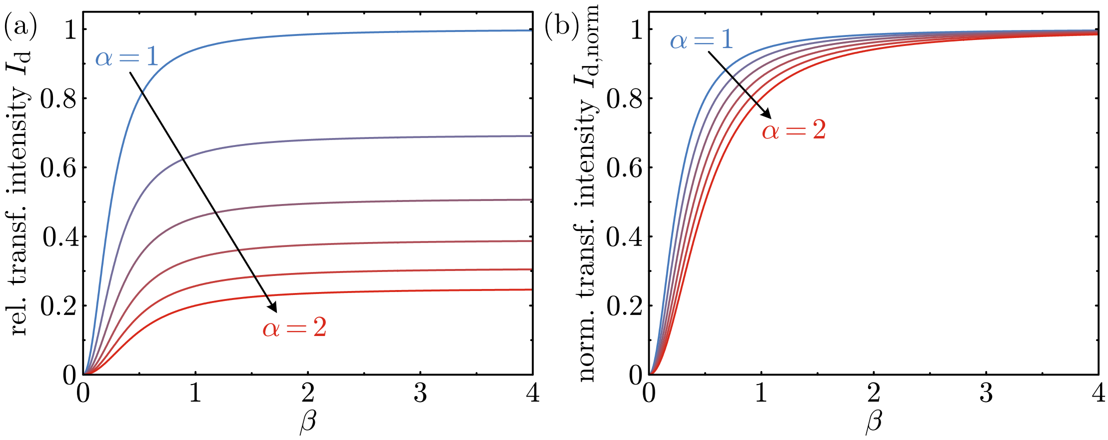

Figure C.4: Influence of α and β on the intensity transfer I_d. In (a), I_d is calculated using Eq. (6.12) and plotted versus β for different values of $\alpha = 1$ to $\alpha = 2$. All plots show an approximately exponential increase of I_d for small β. For larger β, I_d asymptotically approaches a threshold value. This threshold value strongly depends on α. In (b), the intensity transfer is calculated in a normalized manner using Eq. (C.1). All depicted plots show a comparable increase of the transferred intensity towards a threshold of 1. The shape of these curves is only slightly changing with α. This justifies the assumption of $\alpha = 1$ as used in Sec. 6.4. Reprinted with permission from [225] © Optica Publishing Group.

C.5 Normalization of the intensity transfer in add-drop configuration on fiber-resonator couplings

In Sec. 6.4, the intensity transfer through a tunably coupled LCE-PM in add-drop configuration is investigated using two tapered optical fibers. However, this intensity transfer does not only depend on the inter-cavity coupling strength $|\eta|$, but also on the fiber-resonator couplings $|\mu|$. These couplings are strongly influenced by the distance between the respective fiber and resonator, which has to be readjusted with every step of the actuation temperature. To account for the influence of the fiber-resonator couplings, they are estimated for each actuation temperature T_act.

The influence of both fiber-resonator couplings is estimated from the depth of resonance dips in single-fiber transmission spectra under the assumption of an undercritical coupling. As already mentioned in Sec. 3.2, a simultaneous detection of both FTS spectra with the 2FTS spectrum is not feasible. Hence, these measurements have to be performed in a consecutive manner. However, the tapered optical fibers

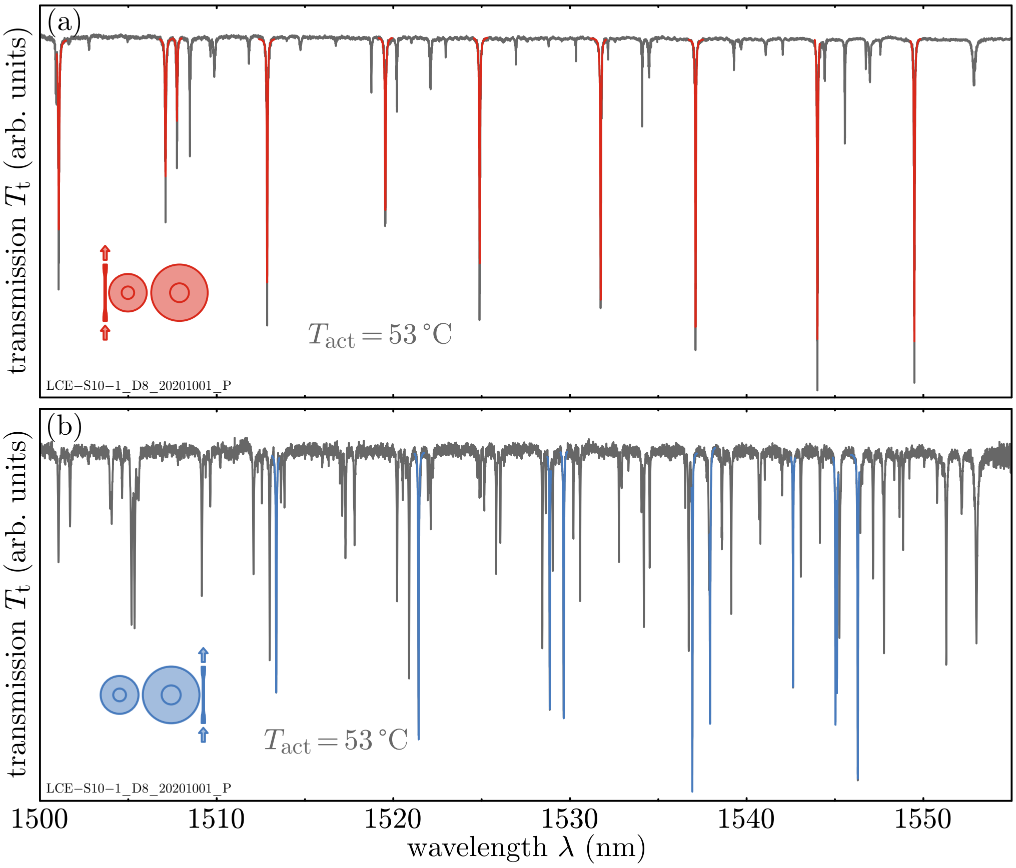

Figure C.5: Normalization of the fiber-resonator coupling using FTS spectra. Exemplary FTS spectra of a tunably coupled LCE-PM at $T_{\mathrm{act}} = 53\,^{\circ}\mathrm{C}$ with the respective fiber coupled to (a) the small or (b) the large resonator only are depicted (see color-coded pictograms). In each spectrum, Lorentz-shaped fits have been applied to the 10 deepest resonance dips. The average depth of these dips of one spectrum has been used as a normalization factor for the respective fiber-resonator coupling $|\mu|$. The intensity transfer of the LCE-PM at each actuation temperature (see Fig. 6.6 and 6.7) has been normalized using the two respective normalization factors. Reprinted with permission from [225] © Optica Publishing Group.

are known to undergo mechanical oscillations. Therefore, it is not reasonable to estimate the fiber-resonator coupling of a single supermode's intensity transfer from the resonance dip of a consecutively performed FTS measurement. Instead, the fiber is assumed to mechanically oscillate around a time-stable center position. This should lead to a change of the fiber-resonator couplings around an approximately time-stable value. Hence, the fiber-resonator couplings have been estimated in an averaging manner from the consecutively performed FTS measurements.

The number of resonance dips as well as their overall depth is expected to increase with the fiber-resonator coupling in the under-critical coupling regime. Therefore, the average depth of the 10 deepest resonance dips of an FTS spectrum is used as an averaging measure of the fiber-resonator coupling. Following this approach, two normalization factors are calculated for all supermodes at each actuation temperature: one for each fiber-resonator coupling using the respective single-fiber transmission spectrum. This approach is exemplarily depicted in Fig. C.5 for an actuation temperature of $T_{\mathrm{act}} = 53\,^{\circ}\mathrm{C}$. In Fig. C.5(a)/(b), the FTS spectrum of an LCE-PM with the respective fiber coupled to the small/large resonator only (see color-coded pictograms) is depicted. Lorentz-shaped fits are applied to the 10 deepest resonance dips. From the average depth of the 10 dips, the respective normalization factors are calculated.

The data of transferred intensity presented in Fig. 6.6 and 6.7 have been corrected following this approach. These corrections are however just coarse estimates due to their averaging nature. This leads to the significant scattering of the presented data.

Appendix D

Measurement data

All underlying measurements (including both raw as well as processed data) can be found in the respective directory of this thesis. This directory is structured in accordance to the thesis: the data is subdivided into chapters, sections, and single figures. For each figure, the complete set of used data is given despite potential overlaps with other figures.

List of publications

Regular articles

1. **Tunable photonic devices by 3D laser printing of liquid crystal elastomers**, S. Woska, A. Münchinger, D. Beutel, E. Blasco, J. Hessenauer, O. Karayel, P. Rietz, S. Pfleging, R. Oberle, C. Rockstuhl, M. Wegener, H. Kalt , *Optical Materials Express* **10**, 2928-2943 (2020)
2. **Tunable coupling of chip-scale photonic molecules via thermal actuation**, S. Woska, P. Rietz, O. Karayel, H. Kalt, *Optical Materials Express* **11**, 3194-3207 (2021)
3. **Multi-Photon 4D Printing of Complex Liquid Crystalline Microstructures by In Situ Alignment Using Electric Fields**, A. Münchinger, V. Hahn, D. Beutel, S. Woska, J. Monti, C. Rockstuhl, E. Blasco, M. Wegener, *Advanced Materials Technologies* **??**, 2100944 (2021)

Contributions to international conferences with proceedings

1. **Flexible Photonics Based on Whispering-Gallery-Mode Resonators and Liquid-Crystal-Elastomers**, S. Woska, O. Karayel, P. Rietz, J. Hessenauer, R. Oberle, E. Kaiser, S. Pfleging, C. Klusmann, T. Siegle, H. Kalt, *CLEO 2020: Laser Science to Photonics Applications, ~~San José, CA, USA~~ online (2020)*, talk

2. **3D two-photon printing of hetero-microstructures by in-situ alignment of liquid-crystal elastomers**,
   A. Münchinger, E. Blasco, V. Hahn, D. Beutel, S. Woska, J. Monti, C. Rockstuhl, M. Wegener, *SPIE Photonics West 2021, ~~San Francisco, CA, USA~~ online (2021)*, talk

3. **Transmission Switching of Coupled Whispering Gallery Mode Resonators on Flexible Substrates**,
   S. Woska, P. Rietz, O. Karayel, H. Kalt, *CLEO 2021: Laser Science to Photonics Applications, ~~San José, CA, USA~~ online (2021)*, poster presentation

4. **Transmission Switching of Coupled Whispering Gallery Mode Resonators on Flexible Substrates**,
   S. Woska, P. Rietz, O. Karayel, H. Kalt, *CLEO/EUROPE-EQEC 2021, ~~Munich~~ online (2021)*, talk

5. **Tunably coupled photonic molecules on a chip scale**,
   S. Woska, P. Rietz, O. Karayel, H. Kalt, *Frontiers in Optics & Laser Science Conference, ~~Washington DC, USA~~ online (2021)*, talk

Contributions to workshops and seminars

1. **Full Tunability of Whispering-Gallery-Modes in Resonators made from Liquid-Crystal Elastomers**,
   S. Woska, J. Hessenauer, C. Klusmann, M. Migeot, A. Münchinger, H. Kalt, *NATO Advanced Study Institute on Nanophotonics: Light-matter Interactions towards the Nanoscale, Erice, Italy (2019)*, poster presentation

Contributions to DPG spring meetings

1. **Widely tunable polymer-based photonic devices**,
   T. Siegle, S. Woska, S. Schierle, M. Remmel, M. Migeot, C. Klusmann, H. Kalt, *DPG spring meeting, Berlin (2018)*, talk

2. **Wide tunability of coupled WGM resonators using flexible elastomer substrates**,
   S. Woska, L. Mall, J. Hessenauer, C. Klusmann, T. Siegle, H. Kalt, *DPG spring meeting, Regensburg (2019)*, poster presentation

3. **Fabrication of polymeric Whispering-Gallery-Mode resonators on tunable liquid crystal elastomer substrates using deep-UV**,
   L. Mall, S. Woska, J. Hessenauer, C. Klusmann, T. Siegle, H. Kalt, *DPG spring meeting, Regensburg (2019)*, poster presentation

4. **Tunable Whispering-Gallery-Mode resonators made from liquid crystal elastomers**,
   J. Hessenauer, C. Klusmann, S. Woska, M. Migeot, H. Kalt, *DPG spring meeting, Regensburg (2019)*, poster presentation

Bibliography

[1] C. Yeh, *Applied Photonics* (Academic Press, San Diego, 1994).

[2] German Federal Ministry of Education and Research, "Research in Photonics," `https://www.bmbf.de/bmbf/en/research/hightech-and-innovation/research-in-photonics/research-in-photonics_node.html`. Accessed: 2021-10-06.

[3] VDI Technologiezentrum GmbH, "Industrie will bis zu 100 Mrd. Euro in neue Photonik-PPP investieren," `https://www.photonikforschung.de/service/nachrichten/detailansicht/industrie-will-bis-zu-100-mrd-euro-in-neue-photonik-ppp-investieren.html` (2019). Accessed: 2021-10-06.

[4] R. Kirchain and L. Kimerling, "A roadmap for nanophotonics," Nature Photonics **1**, 303–305 (2007).

[5] K. J. Vahala, "Optical microcavities," Nature **424**, 839–846 (2003).

[6] Y. N. Zhang, Y. Zhao, and R. Q. Lv, "A review for optical sensors based on photonic crystal cavities," Sensors and Actuators A: Physical **233**, 374–389 (2015).

[7] R. D. Richtmyer, "Dielectric resonators," Journal of Applied Physics **10**, 391–398 (1939).

[8] A. B. Matsko and V. S. Ilchenko, "Optical resonators with whispering-gallery modes - Part I: Basics," IEEE Journal on Selected Topics in Quantum Electronics **12**, 3–14 (2006).

[9] V. Sandoghdar, F. Treussart, J. Hare, V. Lefèvre-Seguin, J. M. Raimond, and S. Haroche, "Very low threshold whispering-gallery-mode microsphere laser," Physical Review A **54**, R1777 (1996).

[10] T. Grossmann, S. Schleede, M. Hauser, M. B. Christiansen, C. Vannahme, C. Eschenbaum, S. Klinkhammer, T. Beck, J. Fuchs, G. U. Nienhaus, U. Lemmer, A. Kristensen, T. Mappes, and H. Kalt, “Low-threshold conical microcavity dye lasers,” Applied Physics Letters **97**, 63304 (2010).

[11] P. Rabiei, W. H. Steier, C. Zhang, and L. R. Dalton, “Polymer Micro-Ring Filters and Modulators,” Journal of Lightwave Technology **20**, 1968–1975 (2002).

[12] A. Savchenkov, V. Ilchenko, A. Matsko, and L. Maleki, “Tunable filter based on whispering gallery modes,” Electronics Letters **39**, 389–341 (2003).

[13] Y. Louyer, D. Meschede, and A. Rauschenbeutel, “Tunable whispering-gallery-mode resonators for cavity quantum electrodynamics,” Physical Review A **72**, 031801 (2005).

[14] A. Kiraz, P. Michler, C. Becher, B. Gayral, A. Imamoğlu, L. Zhang, E. Hu, W. V. Schoenfeld, and P. M. Petroff, “Cavity-quantum electrodynamics using a single InAs quantum dot in a microdisk structure,” Applied Physics Letters **78**, 3932 (2001).

[15] S. M. Spillane, T. J. Kippenberg, K. J. Vahala, K. W. Goh, E. Wilcut, and H. J. Kimble, “Ultrahigh-Q toroidal microresonators for cavity quantum electrodynamics,” Physical Review A **71**, 013817 (2005).

[16] A. M. Flatae, M. Burresi, H. Zeng, S. Nocentini, S. Wiegele, C. Parmeggiani, H. Kalt, and D. Wiersma, “Optically controlled elastic microcavities,” Light: Science & Applications **4**, e282 (2015).

[17] T. Siegle, M. Remmel, S. Krämmer, and H. Kalt, “Split-disk micro-lasers: Tunable whispering gallery mode cavities,” APL Photonics **2**, 096103 (2017).

[18] M. Förtsch, G. Schunk, J. U. Fürst, D. Strekalov, T. Gerrits, M. J. Stevens, F. Sedlmeir, H. G. L. Schwefel, S. W. Nam, G. Leuchs, and C. Marquardt, “Highly efficient generation of single-mode photon pairs from a crystalline whispering-gallery-mode resonator source,” Physical Review A **91**, 023812 (2015).

[19] P. Munnelly, T. Heindel, A. Thoma, M. Kamp, S. Höfling, C. Schneider, and S. Reitzenstein, “Electrically Tunable Single-Photon Source Triggered by a Monolithically Integrated Quantum Dot Microlaser,” ACS Photonics **4**, 790–794 (2017).

[20] M. Bayer, T. Gutbrod, J. P. Reithmaier, A. Forchel, T. L. Reinecke, P. A. Knipp, A. A. Dremin, and V. D. Kulakovskii, “Optical modes in photonic molecules,” Physical Review Letters **81**, 2582–2585 (1998).

[21] Y. P. Rakovich and J. F. Donegan, “Photonic atoms and molecules,” Laser and Photonics Reviews **4**, 179–191 (2010).

[22] F. Morichetti, C. Ferrari, A. Canciamilla, and A. Melloni, “The first decade of coupled resonator optical waveguides: bringing slow light to applications,” Laser and Photonics Reviews **6**, 74–96 (2012).

[23] R. Katti and S. Prince, “Photonic Delay Lines Based on Silicon Coupled Resonator Optical Waveguide Structures,” Silicon **10**, 2793–2800 (2018).

[24] G. Harari, M. A. Bandres, Y. Lumer, M. C. Rechtsman, Y. D. Chong, M. Khajavikhan, D. N. Christodoulides, and M. Segev, “Topological insulator laser: Theory,” Science **359**, eaar4003 (2018).

[25] M. A. Bandres, S. Wittek, G. Harari, M. Parto, J. Ren, M. Segev, D. N. Christodoulides, and M. Khajavikhan, “Topological insulator laser: Experiments,” Science **359**, eaar4005 (2018).

[26] H. Hodaei, M. A. Miri, M. Heinrich, D. N. Christodoulides, and M. Khajavikhan, “Parity-time-symmetric microring lasers,” Science **346**, 975–978 (2014).

[27] J. K. S. Poon, L. Zhu, G. A. DeRose, and A. Yariv, “Polymer Microring Coupled-Resonator Optical Waveguides,” Journal of Lightwave Technology **24**, 1843–1849 (2006).

[28] B. Peng, Ş. K. Özdemir, F. Lei, F. Monifi, M. Gianfreda, G. L. Long, S. Fan, F. Nori, C. M. Bender, and L. Yang, “Parity-time-symmetric whispering-gallery microcavities,” Nature Physics **10**, 394–398 (2014).

[29] T. J. Kippenberg, S. M. Spillane, and K. J. Vahala, “Demonstration of ultra-high-Q small mode volume toroid microcavities on a chip,” Applied Physics Letters **85**, 6113–6115 (2004).

[30] V. R. Almeida, C. A. Barrios, R. R. Panepucci, and M. Lipson, “All-optical control of light on a silicon chip,” Nature **431**, 1081–1084 (2004).

[31] V. D. Ta, R. Chen, and H. D. Sun, “Tuning whispering gallery mode lasing from self-assembled polymer droplets,” Scientific Reports **3**, 1–5 (2013).

[32] K. S. Hsu, T. T. Chiu, P. T. Lee, and M. H. Shih, “Wavelength tuning by bending a flexible photonic crystal laser,” Journal of Lightwave Technology **31**, 1960–1964 (2013).

[33] T. Wienhold, S. Krämmer, S. F. Wondimu, T. Siegle, U. Bog, U. Weinzierl, S. Schmidt, H. Becker, H. Kalt, T. Mappes, S. Koeber, and C. Koos, "All-polymer photonic sensing platform based on whispering-gallery mode microgoblet lasers," Lab on a Chip **15**, 3800–3806 (2015).

[34] O. Bar-On, P. Brenner, T. Siegle, R. Gvishi, H. Kalt, U. Lemmer, and J. Scheuer, "High Quality 3D Photonics using Nano Imprint Lithography of Fast Sol-gel Materials," Scientific Reports **8**, 7833 (2018).

[35] T. Grossmann, S. Schleede, M. Hauser, T. Beck, M. Thiel, G. von Freymann, T. Mappes, and H. Kalt, "Direct laser writing for active and passive high-Q polymer microdisks on silicon," Optics Express **19**, 11451–11456 (2011).

[36] T. J. White and D. J. Broer, "Programmable and adaptive mechanics with liquid crystal polymer networks and elastomers," Nature Materials **14**, 1087–1098 (2015).

[37] S. Woska, A. Münchinger, D. Beutel, E. Blasco, J. Hessenauer, O. Karayel, P. Rietz, S. Pfleging, R. Oberle, C. Rockstuhl, M. Wegener, and H. Kalt, "Tunable photonic devices by 3D laser printing of liquid crystal elastomers," Optical Materials Express **10**, 2928–2943 (2020).

[38] S. Nocentini, F. Riboli, M. Burresi, D. Martella, C. Parmeggiani, and D. S. Wiersma, "Three-Dimensional Photonic Circuits in Rigid and Soft Polymers Tunable by Light," ACS Photonics **5**, 3222–3230 (2018).

[39] T. Siegle, "Durchstimmbare photonische Bauelemente aus polymeren Flüstergalerie-Resonatoren," Dissertation, Karlsruhe Institute of Technologie (KIT) (2017).

[40] L. Rebholz, "Modenhybridisierung in scheibenförmigen Flüstergalerieresonatoren," Master's thesis, Karlsruhe Institute of Technologie (KIT) (2021).

[41] R. Oberle, "Untersuchung von Lacken zur Strukturierung gekoppelter Flüstergalerieresonatoren mittels direkten Laserschreibens," Bachelor's thesis, Karlsruhe Institute of Technologie (KIT) (2019).

[42] I. Chremmos, O. Schwelb, and N. Uzunoglu, eds., *Photonic Microresonator Research and Applications* (Springer US, 2010), 1. edition.

[43] J. D. Jackson, C. Witte, and K. Müller, *Klassische Elektrodynamik* (De Gruyter, Berlin, Boston, 2011).

[44] A. H. W. Choi, ed., *Handbook of Optical Microcavities* (CRC Press, Boca Raton, 2015).

[45] I. S. Grudinin, V. S. Ilchenko, and L. Maleki, "Ultrahigh optical Q factors of crystalline resonators in the linear regime," Physical Review A **74**, 063806 (2006).

[46] S. L. McCall, A. F. Levi, R. E. Slusher, S. J. Pearton, and R. A. Logan, "Whispering-gallery mode microdisk lasers," Applied Physics Letters **60**, 289–291 (1992).

[47] G. C. Righini, Y. Dumeige, P. Féron, M. Ferrari, G. N. Conti, D. Ristic, and S. Soria, "Whispering Gallery Mode microresonators: Fundamentals and applications," Rivista del Nuovo Cimento **34**, 435–488 (2011).

[48] B. R. Johnson, "Theory of morphology-dependent resonances: shape resonances and width formulas," Journal of the Optical Society of America A **10**, 343–352 (1993).

[49] M. K. Chin and S. T. Ho, "Design and Modeling of Waveguide-Coupled Single-Mode Microring Resonators," Journal of Lightwave Technology **16**, 1433–1446 (1998).

[50] V. B. Braginsky, M. L. Gorodetsky, and V. S. Ilchenko, "Quality-factor and nonlinear properties of optical whispering-gallery modes," Physics Letters A **137**, 393–397 (1989).

[51] M. L. Gorodetsky, A. A. Savchenkov, and V. S. Ilchenko, "Ultimate Q of optical microsphere resonators," Optics Letters **21**, 453–455 (1996).

[52] Y. Li, S. Park, M. McLamb, M. Lata, S. Schöche, D. Childers, I. D. Aggarwal, M. K. Poutous, G. Boreman, and T. Hofmann, "UV to NIR optical properties of IP-Dip, IP-L, and IP-S after two-photon polymerization determined by spectroscopic ellipsometry," Optical Materials Express **9**, 4318–4328 (2019).

[53] M. Schmid, D. Ludescher, and H. Giessen, "Optical properties of photoresists for femtosecond 3D printing: refractive index, extinction, luminescence-dose dependence, aging, heat treatment and comparison between 1-photon and 2-photon exposure," Optical Materials Express **9**, 4564–4577 (2019).

[54] M. Borselli, K. Srinivasan, P. E. Barclay, and O. Painter, "Rayleigh scattering, mode coupling, and optical loss in silicon microdisks," Applied Physics Letters **85**, 3693–3695 (2004).

[55] M. Borselli, T. J. Johnson, and O. Painter, "Beyond the Rayleigh scattering limit in high-Q silicon microdisks: theory and experiment," Optics Express **13**, 1515–1530 (2005).

[56] J. M. Gérard, B. Sermage, B. Gayral, B. Legrand, E. Costard, and V. Thierry-Mieg, “Enhanced spontaneous emission by quantum boxes in a monolithic optical microcavity,” Physical Review Letters **81**, 1110–1113 (1998).

[57] M. Sumetsky, Y. Dulashko, and R. S. Windeler, “Super free spectral range tunable optical microbubble resonator,” Optics Letters **35**, 1866–1868 (2010).

[58] V. Van, *Optical Microring Resonators* (CRC Press, Boca Raton, 2016).

[59] K. Okamoto, *Fundamentals of Optical Waveguides* (Elsevier, Amsterdam, Boston, Heidelberg, 2006), 2. edition.

[60] M. Borselli, “High-Q Microresonators as Lasing Elements for Silicon Photonics,” Dissertation, California Institute of Technology (2006).

[61] D. F. Floess, “Numerische Analyse optischer Flüstergalerieresonatoren zur Biodetektion,” Diploma thesis, Karlsruhe Institute of Technology (KIT) (2011).

[62] O. Karayel, “Temperaturinduzierte variable Kopplung von Flüstergaleriemoden-Resonatoren auf flüssigkristallelastomeren Substraten,” Master’s thesis, Karlsruhe Institute of Technologie (KIT) (2020).

[63] D. V. Strekalov, C. Marquardt, A. B. Matsko, H. G. L. Schwefel, and G. Leuchs, “Nonlinear and quantum optics with whispering gallery resonators,” Journal of Optics **18**, 123002 (2016).

[64] M. Hauser, “Mikroresonatoren aus Glas und Polymeren als optische Flüstergalerien,” Dissertation, Karlsruhe Institute of Technologie (KIT) (2011).

[65] T. Grossmann, “Whispering-Gallery-Mode Lasing in Polymeric Microcavities,” Dissertation, Karlsruhe Institute of Technology (KIT) (2012).

[66] T. Beck, “Polymer-Mikroresonatoren hoher Güte als optische Sensoren,” Dissertation, Karlsruhe Institute of Technologie (KIT) (2013).

[67] S. Krämmer, “Dye-Doped Polymeric Lasers for Sensing Applications,” Dissertation, Karlsruhe Institute of Technology (KIT) (2016).

[68] F. Ruf, “TiO2 beschichtete Flüstergalerieresonatoren als Sensoren : Simulation und Experiment,” Master’s thesis, Karlsruhe Institute of Technology (KIT) (2015).

[69] P. Forster, “Photonisch-plasmonische Hybridmoden in silberbeschichteten keilförmigen Flüstergalerie-Resonatoren,” Master’s thesis, Karlsruhe Institute of Technology (KIT) (2017).

[70] A. B. Matsko, A. A. Savchenkov, D. Strekalov, V. S. Ilchenko, and L. Maleki, “Review of Applications of Whispering-Gallery Mode Resonators in Photonics and Nonlinear Optics,” IPN Progress Report **42**, 1–51 (2005).

[71] V. S. Ilchenko and A. B. Matsko, “Optical resonators with whispering-gallery modes - Part II: Applications,” IEEE Journal on Selected Topics in Quantum Electronics **12**, 15–32 (2006).

[72] C. G. B. Garrett, W. Kaiser, and W. L. Bond, “Stimulated Emission into Optical Whispering Modes of Spheres,” Physical Review **124**, 1807–1809 (1961).

[73] S. I. Shopova, G. Farca, A. T. Rosenberger, W. M. S. Wickramanayake, and N. A. Kotov, “Microsphere whispering-gallery-mode laser using HgTe quantum dots,” Applied Physics Letters **85**, 6101 (2004).

[74] D. Yan, T. Shi, Z. Zang, S. Zhao, J. Du, and Y. Leng, “Stable and low-threshold whispering-gallery-mode lasing from modified CsPbBr3 perovskite quantum dots@SiO2 sphere,” Chemical Engineering Journal **401**, 126066 (2020).

[75] J. Renner, L. Worschech, A. Forchel, S. Mahapatra, and K. Brunner, “Whispering gallery modes in high quality ZnSe/ZnMgSSe microdisks with CdSe quantum dots studied at room temperature,” Applied Physics Letters **89**, 091105 (2006).

[76] M. Pelton and Y. Yamamoto, “Ultralow threshold laser using a single quantum dot and a microsphere cavity,” Physical Review A **59**, 2418 (1999).

[77] K. Djordjev, S. J. Choi, S. J. Choi, and P. D. Dapkus, “Microdisk tunable resonant filters and switches,” IEEE Photonics Technology Letters **14**, 828–830 (2002).

[78] S. V. Boriskina, T. M. Benson, P. Sewell, and A. I. Nosich, “Tuning of Elliptic Whispering-Gallery-Mode Microdisk Waveguide Filters,” Journal of Lightwave Technology **21**, 1987– (2003).

[79] F. Monifi, J. Friedlein, Ş. K. Özdemir, and L. Yang, “A Robust and Tunable Add–Drop Filter Using Whispering Gallery Mode Microtoroid Resonator,” Journal of Lightwave Technology **30**, 3306–3315 (2012).

[80] F. Monifi, Ş. K. Özdemir, and L. Yang, “Tunable add-drop filter using an active whispering gallery mode microcavity,” Applied Physics Letters **103**, 181103 (2013).

[81] Q. Xu, B. Schmidt, S. Pradhan, and M. Lipson, “Micrometre-scale silicon electro-optic modulator,” Nature **435**, 325–327 (2005).

[82] Q. Xu, S. Manipatruni, B. Schmidt, J. Shakya, and M. Lipson, “12.5 Gbit/s carrier-injection-based silicon micro-ring silicon modulators,” Optics Express **15**, 430–436 (2007).

[83] M. Pöllinger and A. Rauschenbeutel, “All-optical signal processing at ultra-low powers in bottle microresonators using the Kerr effect,” Optics Express **18**, 17764–17775 (2010).

[84] W. Yoshiki, Y. Honda, T. Tetsumoto, K. Furusawa, N. Sekine, and T. Tanabe, “All-optical tunable buffering with coupled ultra-high Q whispering gallery mode microcavities,” Scientific Reports **7**, 1–8 (2017).

[85] D. O’Shea, C. Junge, M. Pöllinger, A. Vogler, and A. Rauschenbeutel, “All-optical switching and strong coupling using tunable whispering-gallery-mode microresonators,” Applied Physics B **105**, 129–148 (2011).

[86] H. Mabuchi and A. C. Doherty, “Cavity Quantum Electrodynamics: Coherence in Context,” Science **298**, 1372–1377 (2002).

[87] D. W. Vernooy, A. Furusawa, N. P. Georgiades, V. S. Ilchenko, and H. J. Kimble, “Cavity QED with high-Q whispering gallery modes,” Physical Review A **57**, R2293 (1998).

[88] H. Walther, B. T. H. Varcoe, B.-G. Englert, and T. Becker, “Cavity quantum electrodynamics,” Reports on Progress in Physics **69**, 1325 (2006).

[89] S. Haroche and D. Kleppner, “Cavity Quantum Electrodynamics,” Physics Today **42**, 24 (2008).

[90] E. M. Purcell, “Spontaneous emission probabilities at radio frequencies,” Physical Review **69**, 681–681 (1946).

[91] B. Gayral and J. M. Gérard, “Photoluminescence experiment on quantum dots embedded in a large Purcell-factor microcavity,” Physical Review B **78**, 235306 (2008).

[92] F. Liu, A. J. Brash, J. O’Hara, L. M. P. P. Martins, C. L. Phillips, R. J. Coles, B. Royall, E. Clarke, C. Bentham, N. Prtljaga, I. E. Itskevich, L. R. Wilson, M. S. Skolnick, and A. M. Fox, “High Purcell factor generation of indistinguishable on-chip single photons,” Nature Nanotechnology **13**, 835–840 (2018).

[93] T. Siegle, J. Kellerer, M. Bonenberger, S. Krämmer, C. Klusmann, M. Müller, and H. Kalt, “Comparison of various excitation and detection schemes for

dye-doped polymeric whispering gallery mode micro-lasers," Optics Express **26**, 3579–3593 (2018).

[94] J. U. Fürst, D. V. Strekalov, D. Elser, A. Aiello, U. L. Andersen, C. Marquardt, and G. Leuchs, "Quantum Light from a Whispering-Gallery-Mode Disk Resonator," Physical Review Letters **106**, 113901 (2011).

[95] M. Förtsch, J. U. Fürst, C. Wittmann, D. Strekalov, A. Aiello, M. V. Chekhova, C. Silberhorn, G. Leuchs, and C. Marquardt, "A versatile source of single photons for quantum information processing," Nature Communications **4**, 1–5 (2013).

[96] K. Xia, F. Sardi, C. Sauerzapf, T. Kornher, H.-W. Becker, Z. Kis, L. Kovacs, R. Kolesov, and J. Wrachtrup, "High-Speed Tunable Microcavities Coupled to Rare-Earth Quantum Emitters," arXiv:2104.00389 (2021).

[97] B. E. Little, S. T. Chu, H. A. Haus, J. Foresi, and J. P. Laine, "Microring resonator channel dropping filters," Journal of Lightwave Technology **15**, 998–1005 (1997).

[98] B. E. Little, H. A. Haus, and S. T. Chu, "Second-order filtering and sensing with partially coupled traveling waves in a single resonator," Optics Letters **23**, 1570–1572 (1998).

[99] J. V. Hryniewicz, P. P. Absil, B. E. Little, R. A. Wilson, and P. T. Ho, "Higher order filter response in coupled microring resonators," IEEE Photonics Technology Letters **12**, 320–322 (2000).

[100] B. E. Little, S. T. Chu, W. Pan, and Y. Kokubun, "Microring resonator arrays for VLSI photonics," IEEE Photonics Technology Letters **12**, 323–325 (2000).

[101] A. A. Savchenkov, V. S. Ilchenko, A. B. Matsko, and L. Maleki, "High-order tunable filters based on a chain of coupled crystalline whispering gallery-mode resonators," IEEE Photonics Technology Letters **17**, 136–138 (2005).

[102] F. Xia, L. Sekaric, M. Rooks, and Y. Vlasov, "Ultra-compact high order ring resonator filters using submicron silicon photonic wires for on-chip optical interconnects," Optics Express **15**, 11934–11941 (2007).

[103] J. Poon, J. Scheuer, S. Mookherjea, G. T. Paloczi, Y. Huang, and A. Yariv, "Matrix analysis of microring coupled-resonator optical waveguides," Optics Express **12**, 90–103 (2004).

[104] J. K. S. Poon, J. Scheuer, Y. Xu, and A. Yariv, “Designing coupled-resonator optical waveguide delay lines,” Journal of the Optical Society of America B **21**, 1665–1673 (2004).

[105] A. Melloni, F. Morichetti, and M. Martinelli, “Linear and nonlinear pulse propagation in coupled resonator slow-wave optical structures,” Optical and Quantum Electronics **35**, 365–379 (2003).

[106] A. Yariv, A. Scherer, R. K. Lee, and Y. Xu, “Coupled-resonator optical waveguide: a proposal and analysis,” Optics Letters **24**, 711–713 (1999).

[107] J. K. Poon, L. Zhu, G. A. DeRose, and A. Yariv, “Transmission and group delay of microring coupled-resonator optical waveguides,” Optics Letters **31**, 456–458 (2006).

[108] N. L. Kazanskiy and P. G. Serafimovich, “Coupled-resonator optical waveguides for temporal integration of optical signals,” Optics Express **22**, 14004–14013 (2014).

[109] H. Cao and J. Wiersig, “Dielectric microcavities: Model systems for wave chaos and non-Hermitian physics,” Reviews of Modern Physics **87**, 61–111 (2015).

[110] M.-A. Miri and A. Alù, “Exceptional points in optics and photonics,” Science **363** (2019).

[111] C. M. Bender, “Making sense of non-Hermitian Hamiltonians,” Reports on Progress in Physics **70**, 947 (2007).

[112] W. D. Heiss, “Exceptional points of non-Hermitian operators,” Journal of Physics A: Mathematical and General **37**, 2455–2464 (2004).

[113] W. D. Heiss, “The physics of exceptional points,” Journal of Physics A: Mathematical and Theoretical **45**, 444016 (2012).

[114] M. Brandstetter, M. Liertzer, C. Deutsch, P. Klang, J. Schöberl, H. E. Türeci, G. Strasser, K. Unterrainer, and S. Rotter, “Reversing the pump dependence of a laser at an exceptional point,” Nature Communications **5**, 1–7 (2014).

[115] E. Lafalce, Q. Zeng, C. H. Lin, M. J. Smith, S. T. Malak, J. Jung, Y. J. Yoon, Z. Lin, V. V. Tsukruk, and Z. V. Vardeny, “Robust lasing modes in coupled colloidal quantum dot microdisk pairs using a non-Hermitian exceptional point,” Nature Communications **10**, 1–8 (2019).

[116] H. Hodaei, A. U. Hassan, S. Wittek, H. Garcia-Gracia, R. El-Ganainy, D. N. Christodoulides, and M. Khajavikhan, “Enhanced sensitivity at higher-order exceptional points,” Nature **548**, 187–191 (2017).

[117] W. Chen, Ş. K. Özdemir, G. Zhao, J. Wiersig, and L. Yang, “Exceptional points enhance sensing in an optical microcavity,” Nature **548**, 192–195 (2017).

[118] J. Wiersig, “Review of exceptional point-based sensors,” Photonics Research **8**, 1457–1467 (2020).

[119] M. Y. Nada, M. A. K. Othman, and F. Capolino, “Theory of coupled resonator optical waveguides exhibiting high-order exceptional points of degeneracy,” Physical Review B **96**, 184304 (2017).

[120] M. Y. Nada, M. A. Othman, O. Boyraz, and F. Capolino, “Giant resonance and anomalous quality factor scaling in degenerate band edge coupled resonator optical waveguides,” Journal of Lightwave Technology **36**, 3030–3039 (2018).

[121] F. Capolino and M. Y. Nada, “Exceptional point of sixth-order degeneracy in a modified coupled-resonator optical waveguide,” Journal of the Optical Society of America B **37**, 2319–2328 (2020).

[122] L. Lu, J. D. Joannopoulos, and M. Soljačić, “Topological photonics,” Nature Photonics **8**, 821–829 (2014).

[123] T. Ozawa, H. M. Price, A. Amo, N. Goldman, M. Hafezi, L. Lu, M. C. Rechtsman, D. Schuster, J. Simon, O. Zilberberg, and I. Carusotto, “Topological photonics,” Reviews of Modern Physics **91**, 015006 (2019).

[124] M. Segev and M. A. Bandres, “Topological photonics: Where do we go from here?” Nanophotonics **10**, 425–434 (2020).

[125] M. Hafezi, S. Mittal, J. Fan, A. Migdall, and J. M. Taylor, “Imaging topological edge states in silicon photonics,” Nature Photonics **7**, 1001–1005 (2013).

[126] J. H. Choi, W. E. Hayenga, Y. G. Liu, M. Parto, B. Bahari, D. N. Christodoulides, and M. Khajavikhan, “Room temperature electrically pumped topological insulator lasers,” Nature Communications **12**, 1–7 (2021).

[127] J. Zhu, Ş. K. Özdemir, H. Yilmaz, B. Peng, M. Dong, M. Tomes, T. Carmon, and L. Yang, “Interfacing whispering-gallery microresonators and free space light with cavity enhanced Rayleigh scattering,” Scientific Reports **4**, 1–7 (2014).

[128] J. C. Knight, G. Cheung, F. Jacques, and T. A. Birks, “Phase-matched excitation of whispering-gallery-mode resonances by a fiber taper,” Optics Letters **22**, 1129–1131 (1997).

[129] M. Cai, O. Painter, and K. J. Vahala, “Observation of critical coupling in a fiber taper to a silica-microsphere whispering-gallery mode system,” Physical Review Letters **85**, 74–77 (2000).

[130] Y. Xu, Y. Li, R. K. Lee, and A. Yariv, “Scattering-theory analysis of waveguide-resonator coupling,” Physical Review E **62**, 7389–7404 (2000).

[131] F. C. Blom, D. R. van Dijk, H. J. Hoekstra, A. Driessen, and T. J. Popma, “Experimental study of integrated-optics microcavity resonators: toward an all-optical switching device,” Applied Physics Letters **71**, 747–749 (1997).

[132] M. Soltani, V. Ilchenko, A. Matsko, A. Savchenkov, J. Schlafer, C. Ryan, and L. Maleki, “Ultrahigh Q whispering gallery mode electro-optic resonators on a silicon photonic chip,” Optics Letters **41**, 4375–4378 (2016).

[133] H. A. Haus, *Waves and fields in optoelectronics* (Prentice Hall, Englewood Cliffs, NJ, 1984), 2. edition.

[134] H. A. Haus, W. P. Huang, S. Kawakami, and N. A. Whitaker, “Coupled-Mode Theory of Optical Waveguides,” Journal of Lightwave Technology **5**, 16–23 (1987).

[135] B. Peng, Ş. K. Özdemir, J. Zhu, and L. Yang, “Photonic molecules formed by coupled hybrid resonators,” Optics Letters **37**, 3435–3437 (2012).

[136] C. Manolatou, M. J. Khan, S. Fan, P. R. Villeneuve, H. A. Haus, and J. D. Joannopoulos, “Coupling of modes analysis of resonant channel add-drop filters,” IEEE Journal of Quantum Electronics **35**, 1322–1331 (1999).

[137] T. Beck, S. Schloer, T. Grossmann, T. Mappes, and H. Kalt, “Flexible coupling of high-Q goblet resonators for formation of tunable photonic molecules,” Optics Express **20**, 22012–22017 (2012).

[138] C. Klusmann, J. Oppermann, P. Forster, C. Rockstuhl, and H. Kalt, “Identification of Dielectric, Plasmonic, and Hybrid Modes in Metal-Coated Whispering-Gallery-Mode Resonators,” ACS Photonics **5**, 2365–2373 (2018).

[139] G. Brambilla, V. Finazzi, and D. J. Richardson, “Ultra-low-loss optical fiber nanotapers,” Optics Express **12**, 2258–2263 (2004).

[140] T. A. Birks and Y. W. Li, "The Shape of Fiber Tapers," Journal of Lightwave Technology **10**, 432–438 (1992).

[141] P. Brenner, "Herstellung ausgedünnter Glasfasern," Bachelor's thesis, Karlsruhe Institute of Technologie (KIT) (2011).

[142] P. Rietz, "Charakterisierung und Optimierung variabler Kopplung von Flüstergalerieresonatoren : Experiment und Simulation," Master's thesis, Karlsruhe Institute of Technologie (KIT) (2020).

[143] C. Schmidt, "Mode dynamics in coupled disk optical microresonators," Dissertation, Friedrich-Schiller-Universität Jena (2013).

[144] F. Vollmer and D. Yu, *Optical Whispering Gallery Modes for Biosensing* (Springer Nature, 2020).

[145] E. Kaiser, "Polarisationsabhängiges Modenverhalten von durchstimmbaren Flüstergalerieresonatoren," Bachelor's thesis, Karlsruhe Institute of Technologie (KIT) (2019).

[146] R. Ulrich, S. C. Rashleigh, and W. Eickhoff, "Bending-induced birefringence in single-mode fibers," Optics Letters **5**, 273–275 (1980).

[147] K. Okamoto, T. Hosaka, and A. Edahiro, "Stress Analysis of Optical Fibers by a Finite Element Method," IEEE Journal of Quantum Electronics **17**, 2123–2129 (1981).

[148] A. J. Barlow and D. N. Payne, "The Stress-Optic Effect in Optical Fibers," IEEE Journal of Quantum Electronics **19**, 834–839 (1983).

[149] J. N. Ross, "The rotation of the polarization in low birefringence monomode optical fibres due to geometric effects," Optical and Quantum Electronics **16**, 455–461 (1984).

[150] D. Chowdhury and D. Wilcox, "Comparison between optical fiber birefringence induced by stress anisotropy and geometric deformation," IEEE Journal on Selected Topics in Quantum Electronics **6**, 227–232 (2000).

[151] S. Pfleging, "Hysterese der spektralen Modenpositionen durchstimmbarer Flüstergalerieresonatoren aus Flüssigkristallelastomeren," Bachelor's thesis, Karlsruhe Institute of Technologie (KIT) (2020).

[152] F. L. Kien, J. Q. Liang, K. Hakuta, and V. I. Balykin, "Field intensity distributions and polarization orientations in a vacuum-clad subwavelength-diameter optical fiber," Optics Communications **242**, 445–455 (2004).

[153] M. H. Alizadeh and B. M. Reinhard, “Highly efficient and broadband optical polarizers based on dielectric nanowires,” Optics Express **25**, 22897–22904 (2017).

[154] M. Joos, A. Bramati, and Q. Glorieux, “Complete polarization control for a nanofiber waveguide using the scattering properties,” Optics Express **27**, 18818–18830 (2019).

[155] G. Tkachenko, F. Lei, and S. N. Chormaic, “Polarisation control for optical nanofibres by imaging through a single lens,” Journal of Optics **21**, 125604 (2019).

[156] F. Lei, G. Tkachenko, J. M. Ward, and S. Nic Chormaic, “Complete Polarization Control for a Nanofiber Waveguide Using Directional Coupling,” Physical Review Applied **11**, 064041 (2019).

[157] T. J. Kippenberg, S. M. Spillane, D. K. Armani, B. Min, L. Yang, and K. J. Vahala, “Fabrication, Coupling and Nonlinear Optics of Ultra-High-Q Micro-Sphere and Chip-Based Toroid Microcavities,” in “Optical Microcavities,” (World Scientific, 2004), p. 177–238.

[158] J. Hessenauer, “Durchstimmbare polymere Flüstergalerieresonatoren aus aktuierbaren Flüssigkristallelastomeren,” Master’s thesis, Karlsruhe Institute of Technologie (KIT) (2019).

[159] L. Mall, “Fotolithografische Herstellung von Flüstergalerie-Mikroresonatoren auf aktuierbaren flüssigkristallinen Elastomersubstraten,” Master’s thesis, Karlsruhe Institute of Technologie (KIT) (2019).

[160] B. Wenger, N. Tétreault, M. E. Welland, and R. H. Friend, “Mechanically tunable conjugated polymer distributed feedback lasers,” Applied Physics Letters **97**, 193303 (2010).

[161] P. Görrn, M. Lehnhardt, W. Kowalsky, T. Riedl, and S. Wagner, “Elastically Tunable Self-Organized Organic Lasers,” Advanced Materials **23**, 869–872 (2011).

[162] H. Feng, W. Shu, H. Xu, B. Zhang, B. Huang, J. Wang, W. Jin, and Y. Chen, “Two-Directional Tuning of Distributed Feedback Film Dye Laser Devices,” Micromachines **8**, 362 (2017).

[163] A. Berdin, H. Rekola, O. Sakhno, M. Wegener, and A. Priimagi, “Continuously tunable polymer membrane laser,” Optics Express **27**, 25634–25646 (2019).

[164] J. Wang, Y. Yin, Q. Hao, S. Huang, E. S. G. Naz, O. G. Schmidt, and L. Ma, "External Strain Enabled Post-Modification of Nanomembrane-Based Optical Microtube Cavities," ACS Photonics **5**, 2060–2067 (2018).

[165] P. Gutruf, C. Zou, W. Withayachumnankul, M. Bhaskaran, S. Sriram, and C. Fumeaux, "Mechanically Tunable Dielectric Resonator Metasurfaces at Visible Frequencies," ACS Nano **10**, 133–141 (2015).

[166] T.-W. Lu, C.-C. Wu, C. Wang, and P.-T. Lee, "Compressible 1D photonic crystal nanolasers with wide wavelength tuning," Optics Letters **42**, 2267–2270 (2017).

[167] Y. Chen, H. Li, and M. Li, "Flexible and tunable silicon photonic circuits on plastic substrates," Scientific Reports **2**, 1–6 (2012).

[168] G. Saerens, I. Tang, E. Bloch, K. Frizyuk, M. R. Escalé, C. Renaut, F. Timpu, V. Vogler-Neuling, I. Shtrom, E. Semenova, E. Lebedkina, A. Bouravleuv, Z. Sadrieva, G. Cirlin, M. Petrov, R. Grange, and M. Timofeeva, "Semiconductor III-V Nanowires as Building Blocks for Flexible Nonlinear Photonic Components," in "2020 Conference on Lasers and Electro-Optics (CLEO)," (OSA, Washington, D.C., 2020).

[169] S. Geiger, J. Michon, S. Liu, J. Qin, J. Ni, J. Hu, T. Gu, and N. Lu, "Flexible and Stretchable Photonics: The Next Stretch of Opportunities," ACS Photonics **7**, 2618–2635 (2020).

[170] T. Siegle, S. Schierle, S. Krämmer, B. Richter, S. F. Wondimu, P. Schuch, C. Koos, and H. Kalt, "Photonic molecules with a tunable inter-cavity gap," Light: Science & Applications **6**, e16224 (2017).

[171] C. A. Spiegel, M. Hippler, A. Münchinger, M. Bastmeyer, C. Barner-Kowollik, M. Wegener, and E. Blasco, "4D Printing at the Microscale," Advanced Functional Materials **30**, 1907615 (2020).

[172] L. Tan, A. C. Davis, and D. J. Cappelleri, "Smart Polymers for Microscale Machines," Advanced Functional Materials **31**, 2007125 (2021).

[173] M. O. Saed, A. Gablier, and E. M. Terentjev, "Exchangeable Liquid Crystalline Elastomers and Their Applications," Chemical Reviews **120**, 261 (2021).

[174] Z. He, G. Tan, D. Chanda, and S.-T. Wu, "Novel liquid crystal photonic devices enabled by two-photon polymerization," Optics Express **27**, 11472–11491 (2019).

[175] A. Kotikian, C. McMahan, E. C. Davidson, J. M. Muhammad, R. D. Weeks, C. Daraio, and J. A. Lewis, “Untethered soft robotic matter with passive control of shape morphing and propulsion,” Science Robotics **4**, 7044 (2019).

[176] A. Kotikian, J. M. Morales, A. Lu, J. Mueller, Z. S. Davidson, J. W. Boley, and J. A. Lewis, “Innervated, Self-Sensing Liquid Crystal Elastomer Actuators with Closed Loop Control,” Advanced Materials **33**, 2101814 (2021).

[177] H. Zeng, P. Wasylczyk, C. Parmeggiani, D. Martella, M. Burresi, and D. S. Wiersma, “Light-Fueled Microscopic Walkers,” Advanced Materials **27**, 3883–3887 (2015).

[178] D. Martella, S. Nocentini, D. Nuzhdin, C. Parmeggiani, and D. S. Wiersma, “Photonic Microhand with Autonomous Action,” Advanced Materials **29**, 1704047 (2017).

[179] E. Sungur, L. Mager, A. Boeglin, M.-H. Li, P. Keller, and K. D. Dorkenoo, “Temperature tunable optical gratings in nematic elastomer,” Applied Physics A **98**, 119–122 (2009).

[180] S. Nocentini, D. Martella, C. Parmeggiani, S. Zanotto, and D. S. Wiersma, “Structured Optical Materials Controlled by Light,” Advanced Optical Materials **6**, 1800167 (2018).

[181] S. Zanotto, F. Sgrignuoli, S. Nocentini, D. Martella, C. Parmeggiani, and D. S. Wiersma, “Multichannel remote polarization control enabled by nanostructured liquid crystalline networks,” Applied Physics Letters **114**, 201103 (2019).

[182] P. de Gennes, “A semi-fast artificial muscle,” Comptes Rendus De L’Academie De Sciences - Serie Iib **324**, 343–348 (1997).

[183] P.-G. de Gennes and J. Prost, *The Physics of Liquid Crystals* (Oxford University Press, London, 1974).

[184] M. Warner and E. M. Terentjev, *Liquid Crystal Elastomers (International Series of Monographs on Physics)* (Oxford University Press, 2009).

[185] M. A. Stuart, W. T. Huck, J. Genzer, M. Müller, C. Ober, M. Stamm, G. B. Sukhorukov, I. Szleifer, V. V. Tsukruk, M. Urban, F. Winnik, S. Zauscher, I. Luzinov, and S. Minko, “Emerging applications of stimuli-responsive polymer materials,” Nature Materials **9**, 101–113 (2010).

[186] M. Wei, Y. Gao, X. Li, and M. J. Serpe, “Stimuli-responsive polymers and their applications,” Polymer Chemistry **8**, 127–143 (2017).

[187] K. D. Dorkenoo, E. Sungur, H. Bulou, G. Taupier, and A. Boeglin, "Monitoring the Contractile Properties of Optically Patterned Liquid Crystal Based Elastomers," in "Advanced Elastomers - Technology, Properties and Applications," (IntechOpen, 2012), p. 37–60.

[188] S. Nocentini, "Tunable polymeric photonic structures," Dissertation, Universita degli Studi di Firenze (2016).

[189] H. Wermter and H. Finkelmann, "Liquid crystalline elastomers as artificial muscles," E-Polymers **1**, 013 (2001).

[190] D. Liu and D. J. Broer, "Liquid Crystal Polymer Networks: Preparation, Properties, and Applications of Films with Patterned Molecular Alignment," Langmuir **30**, 13499–13509 (2014).

[191] M. E. McConney, A. Martinez, V. P. Tondiglia, K. M. Lee, D. Langley, I. I. Smalyukh, and T. J. White, "Topography from Topology: Photoinduced Surface Features Generated in Liquid Crystal Polymer Networks," Advanced Materials **25**, 5880–5885 (2013).

[192] B. A. Kowalski, V. P. Tondiglia, T. Guin, and T. J. White, "Voxel resolution in the directed self-assembly of liquid crystal polymer networks and elastomers," Soft Matter **13**, 4335–4340 (2017).

[193] H. Zeng, P. Wasylczyk, G. Cerretti, D. Martella, C. Parmeggiani, and D. S. Wiersma, "Alignment engineering in liquid crystalline elastomers: Free-form microstructures with multiple functionalities," Applied Physics Letters **106**, 111902 (2015).

[194] Y. Guo, H. Shahsavan, and M. Sitti, "3D Microstructures of Liquid Crystal Networks with Programmed Voxelated Director Fields," Advanced Materials **32**, 2002753 (2020).

[195] C. C. Tartan, P. S. Salter, T. D. Wilkinson, M. J. Booth, S. M. Morris, and S. J. Elston, "Generation of 3-dimensional polymer structures in liquid crystalline devices using direct laser writing," RSC Advances **7**, 507–511 (2017).

[196] A. Münchinger, V. Hahn, D. Beutel, S. Woska, J. Monti, C. Rockstuhl, E. Blasco, and M. Wegener, "Multi-Photon 4D Printing of Complex Liquid Crystalline Microstructures by In Situ Alignment Using Electric Fields," Advanced Materials Technologies **??**, 2100944 (2021).

[197] I. Dierking, *Textures of Liquid Crystals* (Wiley-VCH, Weinheim, 2003).

[198] M. Migeot, “Aktuierbare Elastomere als Bausteine für durchstimmbare polymerbasierte photonische Bauelemente,” Master’s thesis, Karlsruhe Institute of Technology (KIT) (2018).

[199] P. Ball, “Curtains for LCD rubdown?” Nature (2001).

[200] J. Chen, W. Cranton, and M. Fihn, eds., *Handbook of Visual Display Technology* (Springer, Berlin, Heidelberg, 2012).

[201] H. M. Wu, J. H. Tang, Q. Luo, Z. M. Sun, Y. M. Zhu, Z. H. Lu, and Y. Wei, “Liquid-crystal alignment of rubbed polyimide films: A microscopic investigation,” Applied Physics B **62**, 613–618 (1996).

[202] J. Stöhr, M. G. Samant, A. Cossy-Favre, J. Díaz, Y. Momoi, S. Odahara, and T. Nagata, “Microscopic Origin of Liquid Crystal Alignment on Rubbed Polymer Surfaces,” Macromolecules **31**, 1942–1946 (1998).

[203] J. Stöhr and M. G. Samant, “Liquid crystal alignment by rubbed polymer surfaces: a microscopic bond orientation model,” Journal of Electron Spectroscopy and Related Phenomena **98-99**, 189–207 (1999).

[204] M. E. Becker, R. A. Kilian, B. B. Kosmowski, and D. A. Mlynski, “Alignment Properties of Rubbed Polymer Surfaces,” Molecular Crystals and Liquid Crystals **132**, 167–180 (2011).

[205] K. Weiss, C. Wöll, E. Böhm, B. Fiebranz, G. Forstmann, B. Peng, V. Scheumann, and D. Johannsmann, “Molecular Orientation at Rubbed Polyimide Surfaces Determined with X-ray Absorption Spectroscopy: Relevance for Liquid Crystal Alignment,” Macromolecules **31**, 1930–1936 (1998).

[206] D. Nuzhdin, “High-Q microcavities: characterization and optomechanical applications,” Dissertation, Universita degli Studi di Firenze (2018).

[207] D. E. Schaub, “Dynamically Tunable Photonic Bandgap Materials,” Dissertation, University of Manitoba (2010).

[208] M. H. Kim, J. D. Kim, T. Fukuda, and H. Matsuda, “Alignment control of liquid crystals on surface relief gratings,” Liquid Crystals **27**, 1633–1640 (2000).

[209] T. Frenzel, J. Köpfler, A. Naber, and M. Wegener, “Atomic scale displacements detected by optical image cross-correlation analysis and 3D printed marker arrays,” Scientific Reports **11**, 1–7 (2021).

[210] MathWorks Deutschland, “Find circles using circular Hough transform - MATLAB imfindcircles,” `https://de.mathworks.com/help/images/ref/imfindcircles.html`. Accessed: 2021-07-30.

[211] A. Buguin, M.-H. Li, P. Silberzan, B. Ladoux, and P. Keller, “Micro-Actuators: When Artificial Muscles Made of Nematic Liquid Crystal Elastomers Meet Soft Lithography,” Journal of the American Chemical Society **128**, 1088–1089 (2006).

[212] H. Yang, A. Buguin, J.-M. Taulemesse, K. Kaneko, S. Méry, A. Bergeret, and P. Keller, “Micron-Sized Main-Chain Liquid Crystalline Elastomer Actuators with Ultralarge Amplitude Contractions,” Journal of the American Chemical Society **131**, 15000–15004 (2009).

[213] S. Schuhladen, F. Preller, R. Rix, S. Petsch, R. Zentel, and H. Zappe, “Iris-Like Tunable Aperture Employing Liquid-Crystal Elastomers,” Advanced Materials **26**, 7247–7251 (2014).

[214] J. Fischer and M. Wegener, “Three-dimensional optical laser lithography beyond the diffraction limit,” Laser and Photonics Reviews **7**, 22–44 (2013).

[215] V. Hahn, P. Kiefer, T. Frenzel, J. Qu, E. Blasco, C. Barner-Kowollik, and M. Wegener, “Rapid Assembly of Small Materials Building Blocks (Voxels) into Large Functional 3D Metamaterials,” Advanced Functional Materials **30**, 1907795 (2020).

[216] P. Kiefer, V. Hahn, M. Nardi, L. Yang, E. Blasco, C. Barner-Kowollik, and M. Wegener, “Sensitive Photoresists for Rapid Multiphoton 3D Laser Micro- and Nanoprinting,” Advanced Optical Materials **8**, 2000895 (2020).

[217] N. Lindenmann, G. Balthasar, D. Hillerkuss, R. Schmogrow, M. Jordan, J. Leuthold, W. Freude, and C. Koos, “Photonic wire bonding: a novel concept for chip-scale interconnects,” Optics Express **20**, 17667–17677 (2012).

[218] M. Schumann, T. Bückmann, N. Gruhler, M. Wegener, and W. Pernice, “Hybrid 2D–3D optical devices for integrated optics by direct laser writing,” Light: Science & Applications **3**, e175 (2014).

[219] T. Gissibl, S. Thiele, A. Herkommer, and H. Giessen, “Sub-micrometre accurate free-form optics by three-dimensional printing on single-mode fibres,” Nature Communications **7**, 1–9 (2016).

[220] P.-I. Dietrich, M. Blaicher, I. Reuter, M. Billah, T. Hoose, A. Hofmann, C. Caer, R. Dangel, B. Offrein, U. Troppenz, M. Moehrle, W. Freude, and

C. Koos, “In situ 3D nanoprinting of free-form coupling elements for hybrid photonic integration,” Nature Photonics **12**, 241–247 (2018).

[221] H. Gehring, M. Blaicher, W. Hartmann, P. Varytis, K. Busch, M. Wegener, and W. H. P. Pernice, “Low-loss fiber-to-chip couplers with ultrawide optical bandwidth,” APL Photonics **4**, 010801 (2019).

[222] H. Gao, G. F. R. Chen, P. Xing, J. W. Choi, H. Y. Low, and D. T. H. Tan, “High-Resolution 3D Printed Photonic Waveguide Devices,” Advanced Optical Materials **8**, 2000613 (2020).

[223] J. B. Müller, “Exploring the Mechanisms of 3D Direct Laser Writing by Multi-Photon Polymerization,” Dissertation, Karlsruhe Institute of Technology (KIT) (2015).

[224] Nanoscribe GmbH, “NanoGuide,” `https://support.nanoscribe.com/hc/en-gb`. Accessed: 2020-09-18.

[225] S. Woska, P. Rietz, O. Karayel, and H. Kalt, “Tunable coupling of chip-scale photonic molecules via thermal actuation,” Optical Materials Express **11**, 3194–3207 (2021).

[226] C. C. Tartan, P. S. Salter, M. J. Booth, S. M. Morris, and S. J. Elston, “Localised polymer networks in chiral nematic liquid crystals for high speed photonic switching,” Journal of Applied Physics **119**, 183106 (2016).

[227] S. T. Wu, “Birefringence dispersions of liquid crystals,” Physical Review A **33**, 1270–1274 (1986).

[228] J. Li, S. T. Wu, S. Brugioni, R. Meucci, and S. Faetti, “Infrared refractive indices of liquid crystals,” Journal of Applied Physics **97**, 073501 (2005).

[229] G. Abbate, V. Tkachenko, A. Marino, F. Vita, M. Giocondo, A. Mazzulla, and L. De Stefano, “Optical characterization of liquid crystals by combined ellipsometry and half-leaky-guided-mode spectroscopy in the visible-near infrared range,” Journal of Applied Physics **101**, 073105 (2007).

[230] B. Richards and E. Wolf, “Electromagnetic diffraction in optical systems, II. Structure of the image field in an aplanatic system,” Proceedings of the Royal Society of London. Series A. Mathematical and Physical Sciences **253**, 358–379 (1959).

[231] P. Yeh, “Electromagnetic propagation in birefringent layered media,” Journal of the Optical Society of America **69**, 742–756 (1979).

[232] T. Carmon, L. Yang, and K. J. Vahala, “Dynamical thermal behavior and thermal self-stability of microcavities,” Optics Express **12**, 4742–4750 (2004).

[233] H. S. Choi and A. M. Armani, “Thermal nonlinear effects in hybrid optical microresonators,” Applied Physics Letters **97**, 223306 (2010).

[234] L. Chen, M. G. Wood, and R. M. Reano, “12.5 pm/V hybrid silicon and lithium niobate optical microring resonator with integrated electrodes,” Optics Express **21**, 27003–27010 (2013).

[235] A. Guarino, G. Poberaj, D. Rezzonico, R. Degl’Innocenti, and P. Günter, “Electro–optically tunable microring resonators in lithium niobate,” Nature Photonics **1**, 407–410 (2007).

[236] I. M. White, N. M. Hanumegowda, H. Oveys, and X. Fan, “Tuning whispering gallery modes in optical microspheres with chemical etching,” Optics Express **13**, 10754–10759 (2005).

[237] R. Henze, C. Pyrlik, A. Thies, J. M. Ward, A. Wicht, and O. Benson, “Fine-tuning of whispering gallery modes in on-chip silica microdisk resonators within a full spectral range,” Applied Physics Letters **102**, 041104 (2013).

[238] E. Gil-Santos, C. Baker, A. Lemaître, S. Ducci, C. Gomez, G. Leo, and I. Favero, “Scalable high-precision tuning of photonic resonators by resonant cavity-enhanced photoelectrochemical etching,” Nature Communications **8**, 1–7 (2017).

[239] A. Rastelli, A. Ulhaq, S. Kiravittaya, L. Wang, A. Zrenner, and O. G. Schmidt, “In situ laser microprocessing of single self-assembled quantum dots and optical microcavities,” Applied Physics Letters **90**, 073120 (2007).

[240] S. Woska, J. Hessenauer, C. Klusmann, M. Migeot, A. Münchinger, and H. Kalt, “Full Tunability of Whispering-Gallery-Modes in Resonators made from Liquid-Crystal Elastomers,” in “NATO Advanced Study Institute on Nanophotonics: Light-Matter Interactions Towards the Nanoscale,” (2019).

[241] S. Woska, O. Karayel, P. Rietz, J. Hessenauer, R. Oberle, E. Kaiser, S. Pfleging, C. Klusmann, T. Siegle, and H. Kalt, “Flexible Photonics Based on Whispering-Gallery-Mode Resonators and Liquid-Crystal-Elastomers,” in “2020 Conference on Lasers and Electro-Optics (CLEO),” (2020).

[242] S. Arnold, J. Comunale, W. B. Whitten, J. M. Ramsey, and K. A. Fuller, “Room-temperature microparticle-based persistent hole-burning spectroscopy,” Journal of the Optical Society of America B **9**, 819–824 (1992).

[243] S. Arnold and S. Holler, “7. Microparticle photophysics: Fluorescence microscopy and spectroscopy of a photonic atom,” Experimental Methods in the Physical Sciences **40**, 227–253 (2003).

[244] T. Cai, R. Bose, G. S. Solomon, and E. Waks, “Controlled coupling of photonic crystal cavities using photochromic tuning,” Applied Physics Letters **102**, 141118 (2013).

[245] H. Du, X. Zhang, G. Chen, J. Deng, F. S. Chau, and G. Zhou, “Precise control of coupling strength in photonic molecules over a wide range using nanoelectromechanical systems,” Scientific Reports **6**, 1–9 (2016).

[246] W. Ahn, S. V. Boriskina, Y. Hong, and B. M. Reinhard, “Photonic-plasmonic mode coupling in on-chip integrated optoplasmonic molecules,” ACS Nano **6**, 951–960 (2012).

[247] Y. Li, F. Abolmaali, K. W. Allen, N. I. Limberopoulos, A. Urbas, Y. Rakovich, A. V. Maslov, and V. N. Astratov, “Whispering gallery mode hybridization in photonic molecules,” Laser and Photonics Reviews **11**, 1600278 (2017).

[248] Y. Sato, Y. Tanaka, J. Upham, Y. Takahashi, T. Asano, and S. Noda, “Strong coupling between distant photonic nanocavities and its dynamic control,” Nature Photonics **6**, 56–61 (2012).

[249] S. Kapfinger, T. Reichert, S. Lichtmannecker, K. Müller, J. J. Finley, A. Wixforth, M. Kaniber, and H. J. Krenner, “Dynamic acousto-optic control of a strongly coupled photonic molecule,” Nature Communications **6**, 1–6 (2015).

[250] M. Zhang, C. Wang, Y. Hu, A. Shams-Ansari, T. Ren, S. Fan, and M. Lončar, “Electronically programmable photonic molecule,” Nature Photonics **13**, 36–40 (2019).

[251] S. Woska, P. Rietz, O. Karayel, and H. Kalt, “Transmission Switching of Coupled Whispering Gallery Mode Resonators on Flexible Substrates,” in “2021 Conference on Lasers and Electro-Optics (CLEO),” (2021).

[252] S. Woska, P. Rietz, O. Karayel, and H. Kalt, “Tunable Coupling of Photonic Molecules on Flexible Elastomer Substrates,” in “CLEO/EUROPE-EQEC 2021,” (2021).

[253] B. S. Lee, M. Zhang, F. A. S. Barbosa, S. A. Miller, A. Mohanty, R. St-Gelais, and M. Lipson, “On-chip thermo-optic tuning of suspended microresonators,” Optics Express **25**, 12109–12120 (2017).

[254] F. Wang, L. Shao, Q. Bai, X. Che, B. Liu, and Y. Wang, “Photo-Induced Vertical Alignment of Liquid Crystals via In Situ Polymerization Initiated by Polyimide Containing Benzophenone,” Polymers **9**, 233 (2017).

[255] W. Huang and K. M. de Payrebrune, “Experimental investigation on the thermal length expansion of direct laser writing material,” Proceedings in Applied Mathematics & Mechanics **19**, e201900485 (2019).

Closing words

Finally, I'd like to express my great gratitude to all the people who supported me in the pursuit of the present work at the Institute of Applied Physics:

- Prof. Dr. Heinz Kalt for the opportunity to work in his research group on this intriguing subject. Furthermore for his topical and general support as well as the creative freedom to pursue my own ideas.
- Priv.-Doz. Dr. Michael Hetterich for agreeing to act as co-examiner, his helpful ideas in various discussions and his support regarding experimental issues.
- My friends and colleagues Dr. Fabian Ruf, Dr. Jasmin Seeger and Dr. Markus Neuwirth for scientific and emotional support, great teamwork and wonderful times in- and outside the institute.
- Dr. Carolin Klusmann for taking a lot of time to teach me about whispering gallery mode resonators and how to deal with them.
- My former colleagues Dr. Mario Lang and Dr. Tobias Siegle for enthusing me for experimental lab work in general as well as for this intriguing subject. Also for their later support regarding experimental issues.
- My students Jannis Hessenauer, Lukas Mall, Osman Karayel, Roman Oberle, Evelyn Kaiser, Stefan Pfleging, Lukas Rebholz and Pascal Rietz for the great cooperation and their commitment. It was a pleasure working with all of you!
- The whole research group for a warm welcome, a cheerful atmosphere, and great times both at the institute and elsewhere.
- Alexander Münchinger for countless and fruitful discussions on liquid crystal elastomers and their preparation.
- The electronics and mechanics workshop for their competent and fast support regarding all kinds of technical issues and special requests.

- Heinz Leonhard for the preparation of numerous CAD drawings.
- Ursula Mösle, Monika Brenkmann, Claudia Alaya and Petra Bauer for their tireless support regarding all administrative topics.
- Oswald Speck at the Institute of Photonics and Quantum Electronics for the fast and reliable preparation of optical fibers.
- The whole team of the Nanostructure Service Laboratory for their support. Special thank goes to Dr. Silvia Diewald for her support regarding SEM images and the e-beam structuring of PMMA resonators, to Patrice Brenner for preparing FIB cuts, Lucas Radtke for numerous helpful tips on deep-UV lithography and Dr. Marc Hippler for constant support regarding 3D laser printing.
- Alexander Münchinger, Dominik Beutel, Prof. Dr. Eva Blasco, Prof. Dr. Carsten Rockstuhl and Prof. Dr. Martin Wegener for the fruitful cooperation on the development on novel fabrication processes.
- Prof. Dr. Martin Wegener for the possibility to use the polarizing-optical microscope.
- The Karlsruhe School of Optics and Photonics for financial support as well as numerous opportunities for networking and scientific exchange.
- All the people who have been proof reading this thesis.
- All my friends, fellow students, and roommates who made the last 10 years as great as they have been.

My final and most important thank goes to Ann-Kathrin as well as my parents and my sister. Thanks to all of you for supporting and encouraging me in everything I do. I love you!